3D-PRINTED SURROGATE LOWER LIMB FOR TESTING ANKLE-FOOT ORTHOSES

Alexis Thibodeau

A thesis submitted in partial fulfillment of the requirements for the

MASTER OF APPLIED SCIENCE

Degree in Mechanical Engineering

Ottawa-Carleton Institute for Mechanical and Aerospace Engineering
Faculty of Engineering
University of Ottawa

Abstract

Traditionally, the mechanical testing of ankle-foot orthoses (AFOs) has been performed with simple limb surrogates, typically with a single axis ankle joint and rigid foot and shank components. Since many current AFO designs allow 3D motion, a surrogate lower limb (SLL) that provides anatomically similar motion in all planes is needed to enable realistic load testing and cyclic testing in a controlled manner. The aim of this thesis was to design, fabricate and test a novel SLL that provides anatomically realistic 3D foot motion, based on a consensus of the passive lower limb range of motion (RoM) found in the literature.

The SLL design was inspired by the Rizzoli model, sectioning the lower limb into five segments (shank, hindfoot, midfoot, forefoot, toes). Ball and socket joints were used for the shank-hindfoot, hindfoot-midfoot, and midfoot-forefoot. Forefoot-toes used a hinge-type joint. 3D printed flexible thermoplastic polyurethane (TPU) snap-fit connectors connected the 3D printed nylon foot blocks. A threaded ball stud connected the shank shaft and hindfoot. This shank shaft was surrounded by a 3D printed polylactic acid (PLA) shank cover. The foot was cast in silicone rubber to emulate soft tissue, with a PLA custom mould based on a Össur prosthetic foot cover model.

The SLL was successfully designed for easy fabrication using readily available techniques, materials, and components. Only the metal shaft required additional machining. 3D printed components used an affordable 3D printer (Artillery Sidewinder X1), and readily available nylon, PLA, and TPU.

Using motion capture testing, SLL foot rotation angles were found to be within standard deviation of mean foot passive rotation angle ranges found in the literature, showing that most joints were within 5° of target maximum rotation angles. With load testing, the SLL was shown to survive static loads representing 1.5 times body weight for a 100 kg individuals and cyclic loads representing normal gait loading for 500,000 cycles.

Acknowledgments

Firstly, I would like to acknowledge and thank Dr. Patrick Dumond and Dr. Edward Lemaire, for help and guidance on this adventure. Their help and guidance elevated this thesis to proper engineering standards. They stayed patient throughout the process, guiding me steadily. Secondly, I would like to thank Joongho Kim for his assistance in 3D printing, providing his personal equipment and expertise. His feedback and time to create the core of the thesis is highly appreciated. Without his help, the countless constructions would have taken ages to complete, with a steeper cost.

I would also like to thank Gottics Inc. and the uOttawa machine shop team (Mr. Paul Burberry, Mr. James Kent, Mr. Jacques Audet, and Mr. Stanley Weedmark) for their time ensuring that the components requested were done with high quality. I would also like to thank Mr. Leo Denner for his assistance with the Instron technologies used for this thesis, providing expertise in their operation. I would like to thank Össur Inc. for providing a prosthetic foot cover digital file, enabling ideal casting for the mould creation. I would like to thank NSERC for providing funding towards this thesis.

I would like to thank my family for supporting me through the thesis, helping me focus on the work ahead. Finally, I would like to thank my wonderful partner, Meghan Delve, who supported me through it all. She was a steady pillar, helping me stay sane and healthy during the worst of it, supporting me while COVID-19 changed everything.

Table of Contents

List of Figures

List of Tables

Nomenclature

2D	Two dimensional
3D	Three dimensional
A_{bolt}	Bolt area
A_s	Shaft area
A_t	Thread tensile stress area
ABS	Acrylonitrile butadiene styrene
AFC	Ankle-foot complex
AFO	Ankle foot orthosis
AISI	American Iron and Steel institute
AM	Additive manufacturing
AR	Augmented reality
BAR-M	Biomechanics augmented reality -
BRUCE	Bi-articular Reciprocating Universal Compliance Estimator
BW	Body weight
C_b	bolt load distribution
C_m	Material load distribution
CAD	Computer aided design
CAI	Chronic ankle instability
CL	Cover length
D	Buckling loading condition
D_i	Inner diameter
D_o	Outer diameter
E	Young's Modulus

$\varepsilon_{permisible}$	Permissible strain
F_a	Alternating force
F_m	Mean force
F_{mating}	Mating force
F_o	Overload force
F_x	Radial force
F_y	Axial force
F_y	Radial force
FBD	Free body diagram
FDM	Fused deposition modelling
FEA	Finite element analysis
FL	Foot Length
FS	Factor of safety
FS_f	Fatigue safety factor
FT	Forefoot-Toes
G	Shear modulus
GRF	Ground reaction force
HM	Heel-Midfoot
I	Moment of inertia
I_t	Total moment of inertia
IDEO	Intrepid Dynamic Exoskeleton Orthosis
ISO	International organization for standardization
J	Polar moment of inertia
k_a	Surface condition factor
k_{bolt}	Bolt spring constant

k_bolt equation	Size modification factor
k_c	Primary load factor
k_d	Temperature factor
k_e	Reliability factor
k_f	Miscellaneous factor
k_{shaft}	Shaft spring constant
$k_{torsion}$	Torsional stiffness
l_o	Original length
l_t	Length threaded
L_{toe}	Toe connector bending length
l_{total}	Total length
M	Moment
M_w	Moment at shaft proximal end
MCL	Medial collateral ligament
MF	Midfoot-Forefoot
MTP	Metatarsophalangeal
μ	Coefficient of friction
ν	Poisson ratio
OFM	Oxford foot model
P	Deflection force
P_{cr}	Buckling critical load
PLA	Polylactic acid
PVA	Polyvinyl Acetate
QR	Quick response
r	Radius

RFM	Rizzoli foot model
RoM	Range of motion
S	Arc length
S_b	ISO foot offset
S_e	Endurance strength
S'_e	Endurance limit test specimen
S_{ut}	Ultimate strength
SAE	Society of automotive engineers
SD	Standard deviation
SH	Shank-Hindfoot
SLL	Surrogate lower limb
SR	Silicone rubber
T	Torsion
T_{toe}	Toe connector bending thickness
θ_{dorsi}	Dorsiflexion angle
$\theta_{plantar}$	Plantarflexion angle
TMT	Metararsalotarsal
TPU	Thermoplastic polyurethane
u	Vector 2
UNC	Unified national coarse threads
UNF	Unified national fine threads
UV	Ultraviolet
v	Vector 1
W_{toe}	Toe connector bending width
X_w	Connector geometric factor

y_c	Centroid height
σ_a	Alternating stress
σ_{axial}	Axial stress
$\sigma_{bending}$	Bending stress
$\sigma_{effective}$	Effective stress
σ_m	Mean stress
σ_{proof}	Proof strength
σ_{shear}	Shear stress

Chapter 1

Introduction

Most people consider walking a natural or mundane activity; something that requires little effort or thought. However, walking is a complex process that involves the entire body working together to achieve locomotion. If any part fails to operate correctly, the entire system might collapse. For example, people with hemiplegia have difficulty walking because one side is partially paralyzed [1] and people with chronic ankle instability can have unnatural gait, possibly leading to falls [2]. One approach for treating lower limb instability or paralysis is the use of an ankle-foot orthosis (AFO): a brace that connects to the shank and foot (Figure 1-1).

An AFO generally assists and controls motion by providing additional stiffness. AFOs come in a variety of designs, including devices that require power and controls (e.g. sensors, motors, controllers, etc.), and passive designs that rely on the device's mechanical properties to control motion, with solid non-articulating leaf springs or joints with moving parts [3]. AFOs have immediate gait benefits, such as preventing drop-foot, foot-slap, and improving stability during mid-stance. However, non-articulated AFOs could also limit beneficial motions during gait [3]. Articulated AFOs could also limit these movements, but to a lesser degree. Regardless of design, the mechanical properties of AFOs have a direct affect on lower limb motion control. Since AFOs are highly diverse in their designs, creating a customizable surrogate lower limb that enables consistent testing of these various designs is greatly needed.

Figure 1-1: Simple passive leaf-spring AFO

1.1 Motivation

With so many designs, comparing and evaluating AFO effectiveness consistently across devices is not currently possible. Moreover, no AFO testing standards exist. Several testing methods have been developed, but each has its own complex apparatus, methodology, and limited purpose. These elements make comparisons of AFO performance difficult. AFO testing should enable better clinical and research decision-making with respect to AFO design.

AFO testing should reflect realistic device behaviour while in use. However, realistic conditions that reflect human usage are not attained if methodologies test AFOs by themselves, without a lower limb. These testing methodologies do not reflect the supportive nature of AFOs, as devices are never used without the supported lower limb. In real use cases, the load is shared between the limb and device and AFO motion is dependant on the lower limb, which differs between individuals and their respective conditions. While some tests involving human limbs can be performed, cyclical and destructive tests are not possible with a participant. The use of cadaver limbs for orthosis testing is limited due to cost, availability, inappropriateness for long term repeated loading, and test setup complexity. A fabricated and customizable

surrogate lower limb (SLL) could provide the necessary replacement for testing purposes. However, existing SLL designs do not replicate accurate anatomy or behaviour.

Currently, multiple AFO designs offer three-dimensional (3D) support, which would require a SLL that can move in 3D. Existing SLL designs focus on ankle sagittal rotation, with a single-axis joint at the ankle. Complex foot joints that provide flexibility and stability are not considered in these designs. Several ankle-foot pathologies also produce highly variable foot movement ranges that must be accommodated by the AFO. As such, SLL designs should be versatile, adequately reproducing the individual's anatomy and ranges of motion (RoM). Modifications would be done on the digital files before fabrication, changing desired RoMs and joint stiffnesses to better represent the individual's limb.

Many AFO designs are available on the market, but end-users have little information to help choose the optimal device for their need other than the manufacturer's product details and specifications. A cost-efficient SLL made from readily available materials and fabrication techniques would facilitate appropriate AFO testing, with the test outcomes informing prescribers when selecting an AFO that best suits the end-user's needs. The emergence of low-cost 3D printing has created multiple opportunities, granting more people the ability to create devices, including medical tools. 3D printing could be used for highly versatile and customizable SLL production with proper material selection. There is a gap in the market for a low-cost SLL design that would allow AFO testing to be conducted, while still meeting end-user needs.

1.2 Objectives

Design and evaluate a SLL that replicates 3D anatomical limb movement and that can be used with an AFO for load and cyclic testing. The SLL should be easy to fabricate using readily available equipment, materials, and components to enhance access. The SLL model should scale to accommodate a large range of foot and AFO sizes.

1.3 Thesis Contributions

This thesis makes important contributions to orthosis testing and surrogate foot-ankle design, including:

- Creating a novel, easily manufactured SLL that reproduces 3D anatomical motion and that can be used for AFO testing.
- Proving that a four-segment foot model is a viable surrogate design for AFO testing.
- Creating a versatile SLL design that allows lower-limb rotations beyond a simple walking motion, enabling a wider range of scenarios, such as inclined walking surfaces, running, etc.
- Creating a highly customizable SLL design that could allow changeable RoM features for different pathologies, thereby emulating a wide range of human lower limbs.
- Designing an SLL that can be fabricated with readily available 3D printing equipment and materials, using commonly available hardware, and minimizing components requiring machining. This makes this surrogate limb accessible to a range of people who require appropriate orthosis testing and evaluation.
- Proving that the SLL can withstand static and cyclic loading suitable for AFO testing.
- Developing a SLL computer-aided design (CAD) model that is fully scalable to foot size.
- Demonstrating that fiducial marker-based motion tracking using a smartphone, developed by Basiratzadeh et al. [4], can reduce the equipment required for multi-segment angle and distance measurements.

1.4 Thesis Outline

Chapter 2 provides a literature review, including relevant anatomy background, gait analysis, and previous AFO testing methods. Chapter 3 specifies the SLL design criteria, including relevant ISO standards and joint RoM angles. Chapter 4 highlights the overall SLL design, providing justification for each important element, including flexible and rigid connectors, RoM limiting features, lower limb sections, and soft tissue emulator. Chapter 5 covers additive manufacturing, highlighting 3D printing equipment, material, software, and settings used in this study. Chapter 6 highlights the motion testing process, covering methodology, results, and discussion. Chapter 7 highlights the load testing process, highlighting

methodology, results, and discussion. Chapter 8 provides a summative discussion of the project, conclusions and areas for future work.

Chapter 2

Literature Review

2.1 Motion Terminology

Several terms are used throughout this thesis to discuss human motion and planes of motion. The primary planes are frontal, sagittal, and transverse (horizontal) (Figure 2-1).

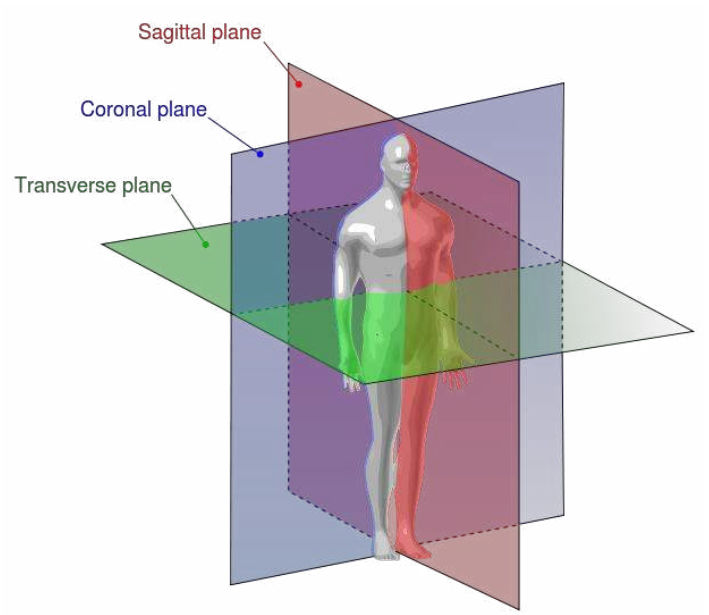

Figure 2-1: Anatomy planes [5]

In the foot-ankle sagittal plane, dorsiflexion moves the foot upward and plantarflexion moves the foot downward (Figure 2-2). Frontal plane rotations are eversion and inversion, and transverse plane rotations are abduction and adduction. Eversion and abduction rotate the foot away from the body's midline in their respective plane, while inversion and adduction rotates the foot towards this midline (Figure 2-2) [6]. The right and left foot have mirrored frontal and transverse rotations.

Supination and pronation are rotation combinations that move obliquely. Supination involves plantarflexion, inversion, and adduction, while pronation involves dorsiflexion, eversion, and abduction [7].

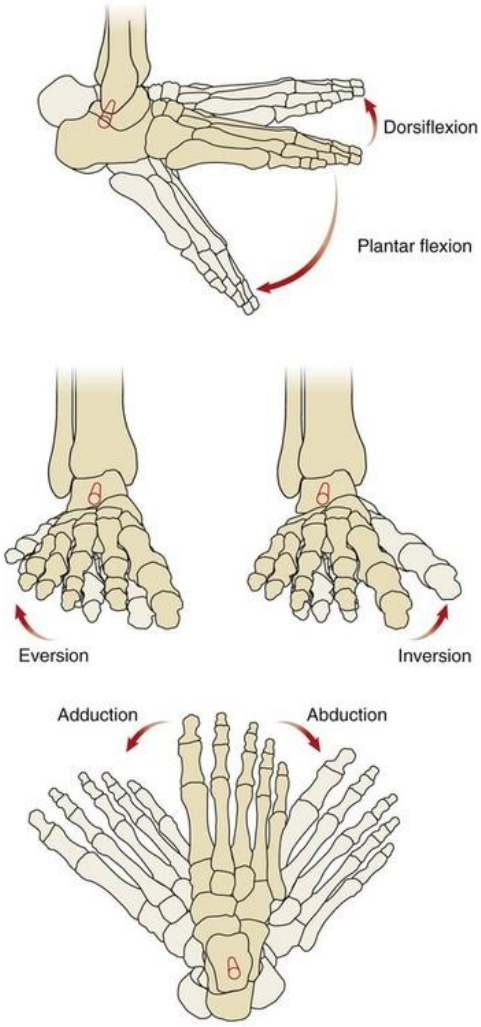

Figure 2-2: Right foot rotations [8]

2.2 Ankle Anatomy

To properly replicate the lower limb, its structure must be understood. The human lower extremity is a complex region comprising 28 bones (Figure 2-3). The tibia and fibula create the shank. The tarsals include the talus, calcaneus, navicular, cuboid, and the medial, intermediate, and lateral cuneiform bones. The five metatarsals are small, long bones, forming the forefoot. Each toe has three phalanges, except for the hallux, or big toe, which has only two bones.

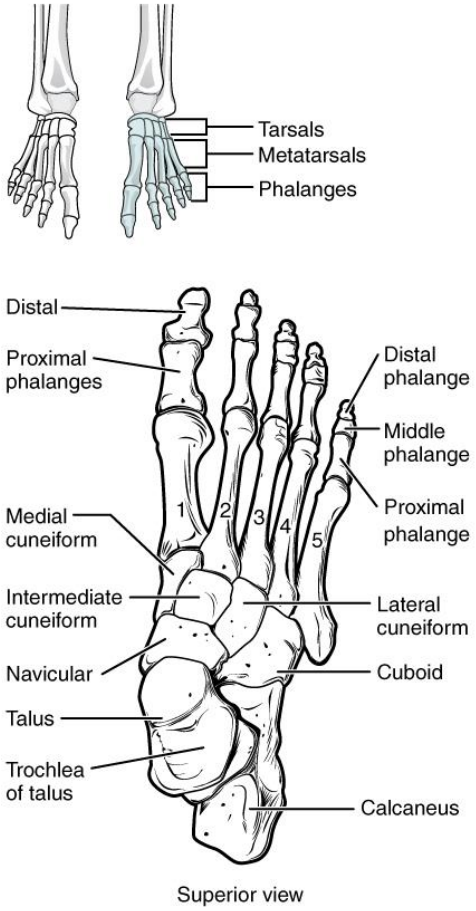

Figure 2-3: Ankle and foot bones [9]

The foot and ankle bones are linked by age network of ligaments, muscles, and tendons to provide controlled transfer of forces from the lower limb to the ground [10]. Joint motions during walking are created by gliding, rotating, and sliding together. Skin and other soft tissues surround the joints to protect the skeleton from the outside environment. Each of these organic tissues play a vital role in lower limb mechanics. Understanding tissue behaviour guides SLL material selection, to achieve more realistic behaviour and properties.

2.2.1 Bones

Bones have several functions, one of which is to support the body. As such, bones need to be strong and sturdy. Most bones have two sections: an inner component called trabecular (also called spongy) bone and an outer shell named cortical bone. Trabecular bone is made of a porous and light matrix of bone cells

randomly oriented, with a porosity of 30% to 90% [11]. Cortical bone has a denser matrix of bone cells, forming an outer shell with 5% to 30% porosity [11]. Cortical bone cells are arranged in an anisotropic structure, with excellent compressive axial strength, but weaker radial strength due to the required average body load. The combination of cortical and trabecular bone forms a composite material that mitigates weaknesses.

Bones are viscoelastic, behaving somewhat elastically while being dependent on the loading rate. Furthermore, bones can remodel themselves based on stress. If a bone is exposed to a different loading condition, the bone matrix will change its strength accordingly over time. For example, after an extended trip in space, an astronaut must be rehabilitated since their bones become weaker due to a lack of body weight in the microgravity environment. Bones can also gain strength if they need to support an increased load.

While multiple factors affect the mechanical properties of bone, average data from the literature can be used for design. The Young's modulus (E) of an average human tibia of a young adult (20-39 years old) is provided as 18.4 GPa, with an ultimate strength of 174 MPa, and an ultimate elongation of 1.50% [11].

2.2.2 Ligaments and Tendons

Ligaments and tendons are made of collagen and elastin fibres. These flexible connective tissues transfer forces to enable motion in some directions and prevent motion in others. While similar in composition, ligaments are more isotropic than tendons because ligament collagen fibres are arranged along more random orientations [12]. Tendon fibres are organized to provide strength in one orientation. Ligaments connect bones to bones and assist in guiding motion, while tendons connect bones to muscles, transferring the muscle's pull [12].

Ligaments and tendons behave visco-elastically. Under a constant strain rate, the stress-strain behaviour can be divided into exponential behaviour (body operates under natural activity), semi-linear (backup strength for more extreme activity), and non-linear (where tissue fibres fail and eventually rupture), as shown in Figure 2-4 [12]. The semi-linear Young's modulus is a good approximation of physiologic

conditions. A human medial collateral ligament (MCL) has a 17.1 ± 1.5% ultimate strain, a 38.6 ± 4.8 MPa tensile strength, and a 332.2 ± 58.3 MPa tangent modulus [13].

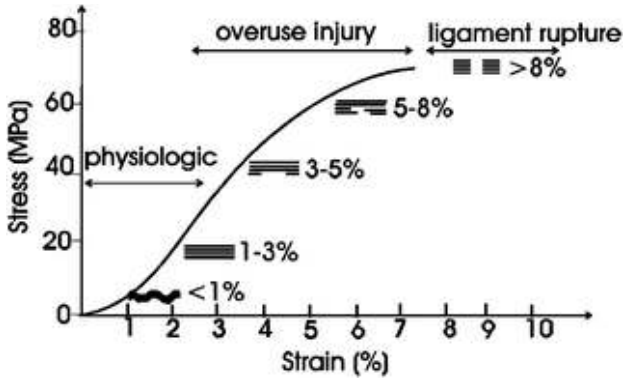

Figure 2-4: Stress-strain behaviour of ligaments under constant strain [11]

The ankle-foot complex (AFC) has several ligaments with varying geometries and alignments that, together, offer proper support to the corresponding joint. The first group is the tibiofibular syndesmosis, which consist of three sections: anterior, posterior, and interosseous ligaments. These control the fibula and tibia rotation while the lower limb moves [7]. The medial collateral ligaments, also known as the deltoid ligaments, connect the tibia to the tarsals. The medial collateral ligaments are fan-shaped, connecting the tibia to the calcaneus, navicular, and talus. The fibula is connected through the lateral collateral ligaments to the calcaneus and talus [7].

2.2.3 Muscles

The major AFC muscles are extrinsic, meaning that they are outside the AFC. This allows the AFC to be less bulky and more maneuverable (e.g. large calf muscles would not fit well inside the foot). The twelve main muscles can be divided into four groups.

Anterior muscles (tibialis anterior, extensor hallucis longus, extensor digitorum longus, peroneus terius) create an ankle dorsiflexion moment. Tibialis anterior, extensor hallucis longus, and peroneus terius create a foot eversion moment. The lateral muscles (peroneus longus, peroneus brevis) produce ankle plantarflexion and foot eversion moments [7]. The posterior muscles (gastrocnemius, soleus, plantaris)

generate a plantarflexion moment on the ankle. Deep posterior muscles (tibialis posterior, flexor digitoum longus, flexor hallucis longus) perform ankle plantarflexion and foot inversion moments [7].

2.2.4 Skin

Skin is the body's largest organ, separating internal organs from the outside environment. Skin controls heat and water transfer through sweat and blood flow and provides sensory inputs with touch. The skin structure is layered, with the epidermis as the exterior layer, the dermis in the middle, and the hypodermis as the internal layer (Figure 2-5). Epidermis is very thin (20-150 µm), except for the palms and soles. The dermis is thicker at 1 to 4 mm, consisting of collagen and keratin fibres that provide strength to the whole skin structure. The hypodermis is a layer of fat, absorbing impact and insulating the internal organs [14].

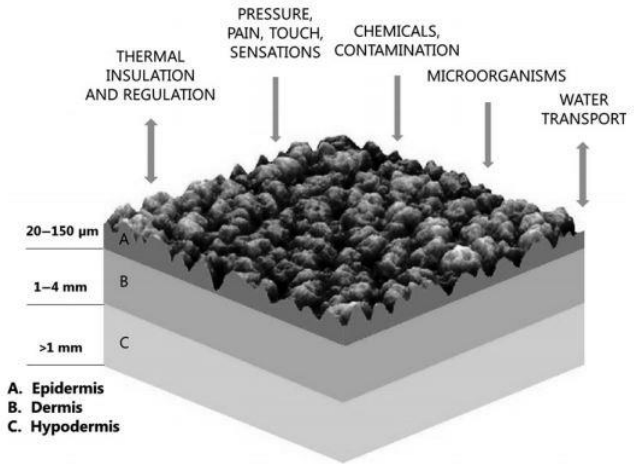

Figure 2-5: Layer structure of skin, with skin purposes [14]

The mechanical properties of skin vary based on location. For example, the sole is harder and more durable due to the frequent, large loads that are applied. Aging also affects skin properties, becoming less elastic over time, along with reduced cell production. The sole's hardness ranges between 20 and 30 Shore 00 for young adults, increasing to 23-35 Shore 00 hardness [15].

2.2.5 Anthropometry

Since body dimensions vary in size and shape because length, width, and height ratios are unique to individuals, assumptions and simplifications are necessary when studying body measurements of multiple people. Anthropometry uses statistical analysis to define body measurements under static and dynamic

conditions [16]. The dimensional ratios provided through research will enable the SLL design to scale in size and be representative of more individuals.

Limb dimensions can be linked to an individual's height (Figure 2-6). The US army, and more recently volunteer Iranian students, performed AFC measurements to obtain anthropometric data [17], [18]. Dimensions, average values, and proportion to foot length (*FL*) are listed in Table 2-1.

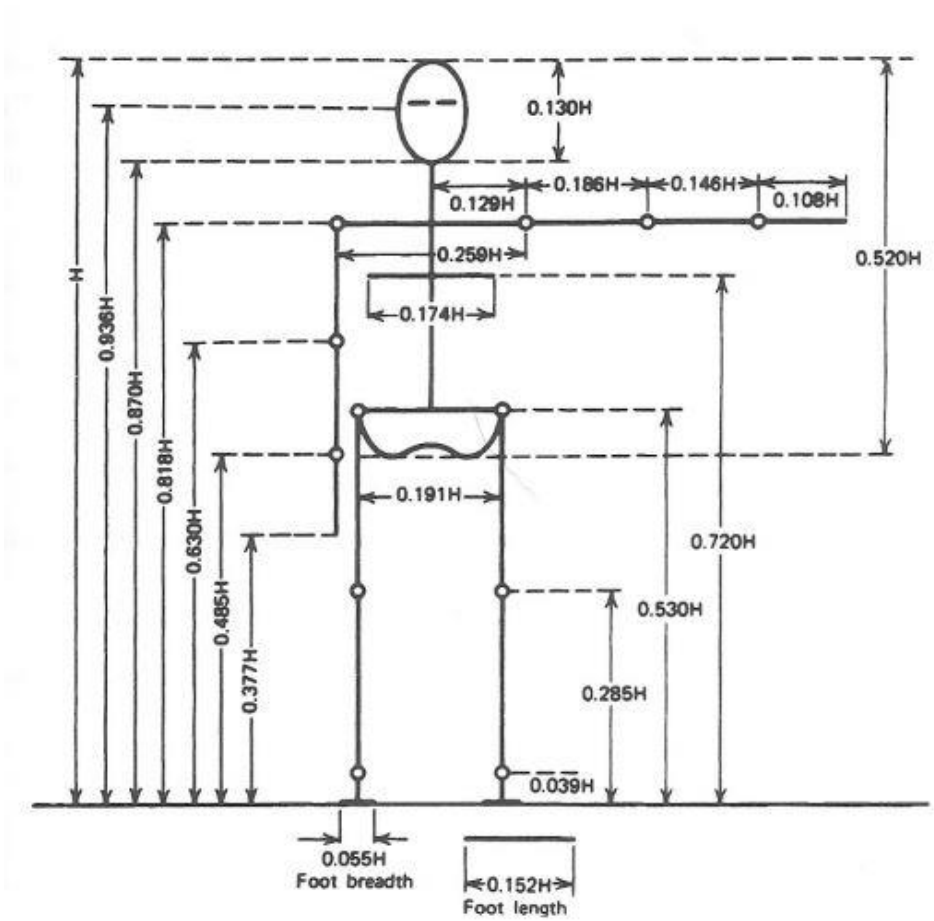

Figure 2-6 Body lengths [19]

Table 2-1: Foot dimensions and proportional relationship to FL for males [18]

Name	Mean (mm)	Proportion to FL
First toe length	270.03	N/A
Second toe length	266.86	99%
Third toe length	258.47	96%
Fourth toe length	247.89	92%
Fifth toe length	233.23	86%
Arch length	195.67	73%
Heel to medial malleolus	83.65	31%
Heel to lateral malleolus	70.19	26%
Heel width	70.71	26%
Foot width	100.44	37%
Bimalleolar Width	74.36	28%
Mid-foot width	92.96	34%
Medial malleolus height	76.96	29%
Lateral malleolus height	66.67	25%
Height at 50%-$\boldsymbol{FL}$	55.96	21%
Ball Girth	248.71	92%

The relationships in Table 2-1 are scaled to FL. Therefore, shoe size could be used to define population-relevant foot measurements. The foot's multiple variables, such as foot and heel width, or heel height and forefoot length, can be simplified to be linearly dependant on FL. This allows model scaling with one variable. The smallest US male adult shoe size is 6 (FL = 235 mm) and the largest is 16 (FL = 318 mm) [20]. Therefore, the model in this thesis should be scalable for size 6 to 16 shoes.

2.3 Ankle-Foot Complex Joints

Joints are points where two or more bone extremities meet and where limb motion is possible [21]. The SLL must match passive RoM angles to behave realistically. The ankle and foot joints can be divided into the ankle, subtalar, and tarsal-metatarsal-phalanges [22]. Other joints are the transverse tarsal joints, metatarsalotarsal (TMT) joints, and interphalangeal joints. All pertinent RoM angles are summarized in Table 2-2. The ankle rotates obliquely, causing movement in all three planes [23], shown in Table 2-3. With many irregular bones, each interacting with several neighbours, joints have many different behaviours and

RoMs. Some joints are also heavily restricted, so relative motion between neighbouring bones can be neglected.

2.3.1 Ankle Joint

The ankle joint, (also known as the talocrural joint) connects the tibia, fibula, and talus. While the fibula is not directly connected to the talus, the fibula is connected to the tibia as an important stabilizer. The talocrural joint moves with the subtalar joint like a mitred hinge (Figure 2-7). Therefore, talocrural joint rotation forces the subtalar joint to rotate [22]. The ankle joint rotates in the sagittal plane with 15°-25° dorsiflexion and 40°-50° plantarflexion [24], [25]. Due to bone geometry, the axis of rotation is oblique. The axis orientation is highlighted in Table 2-3.

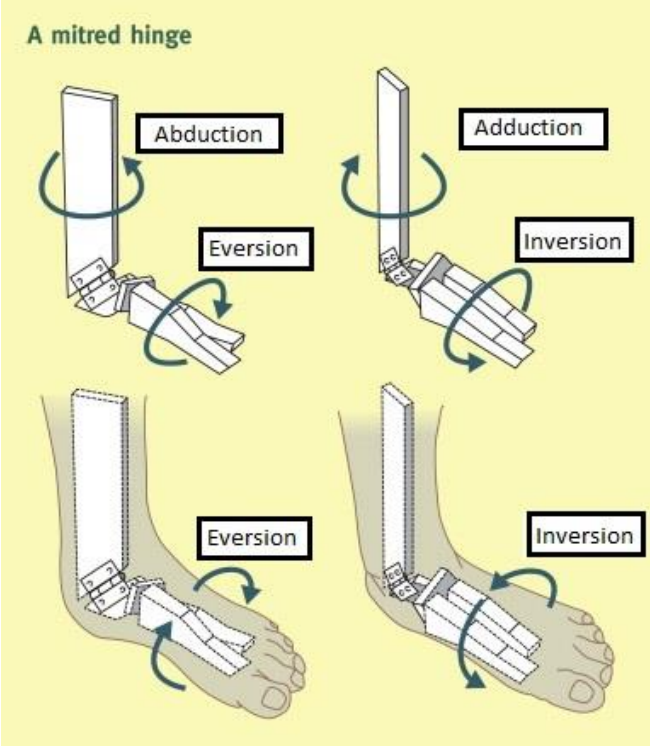

Figure 2-7: "Mitred hinge" motions [26]

2.3.2 Subtalar Joint

The subtalar joint lies inferior to the talocrural joint and involves the talus and calcaneus (also known as the heel bone). These bones connect on the posterior side, between the inferior talus and superior

calcaneus [22]. The joint creates frontal planar motion (inversion and eversion) on the mitred hinge (Figure 2-7), with a passive RoM of 10°-21° eversion and 30°-35° inversion [25], [27]. The joint axis is oblique, with the orientation highlighted in Table 2-3. Due to the mitred hinge, 1° of subtalar motion would result in 1° of tibia rotation, and vise-versa [22], [28].

2.3.3 Tarsal-Metatarsal-Phalange Complex

2.3.3.1 Midtarsal Joints

The midfoot gives the foot its versatility, providing rigidity and flexibility as required. The talonavicular and calcaneocuboid joints are often grouped together as the Chopart joints, transverse tarsal joints, or midtarsal joints. Interactions between the talus and navicular can be described as a ball and socket joint, allowing the foot to rotate in three dimensions [22]. The calcaneus-cuboid joint is much more limited, affecting talonavicular joint RoM. Midtarsal joint RoM is small, measured using cadaver research [29] (Table 2-2).

The midtarsal section has two joints and two independent axes, one oblique and another longitudinal to the foot. The longitudinal axis provides mostly frontal motion, while the oblique axis provides roughly the same sagittal and transverse rotations at once [28]. Both axes orientations are highlighted in Table 2-3.

2.3.3.2 Metatarsalotarsal Joints

The tarsals and metatarsals joints, also known as the Lisfranc joint, connect along a slanted line (Figure 2-8), because the 3rd-5th metatarsal proximal ends are closer to the ankle than the 1st or 2nd metatarsal joints.

Bones are labelled by rays, with the first ray being medial for the hallux. Since metatarsals are linked together, separating the RoM of each ray is difficult. As such, researchers have focused on the first ray's RoM (Table 2-2). The first ray's joint axis is shown in Table 2-3. The orientation creates dorsiflexion, inversion, and some adduction at the same time, while plantarflexion, eversion, and abduction move simultaneously [28].

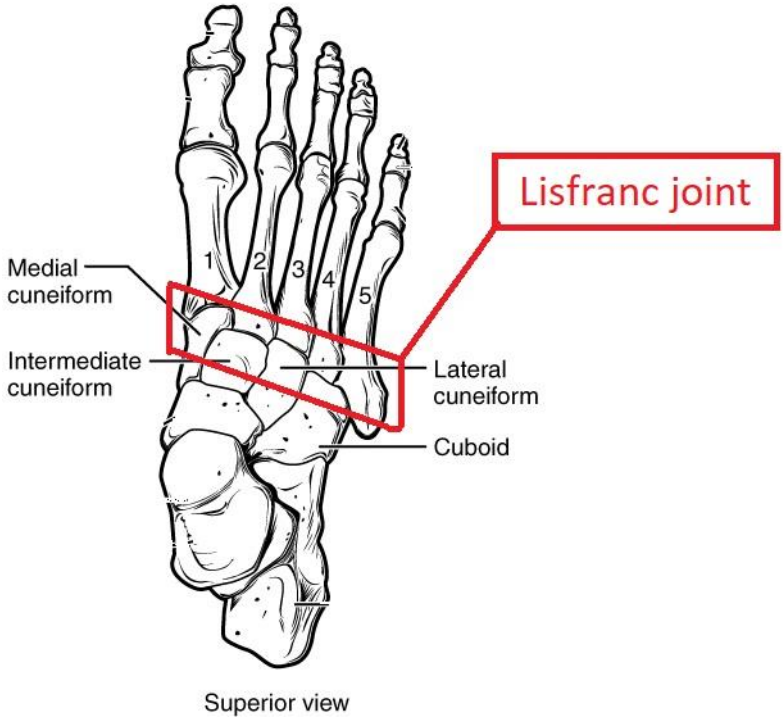

Figure 2-8: Lisfranc joint [9]

2.3.3.3 Metatarsophalangeal Joints

Metatarsophalangeal joints (MTP joints) are vital for locomotion because the centre of pressure passes quickly through the joints while walking, assisting with balance during stance [30]. These joints are located at the metatarsals' anterior line, interlocking with the phalanges' posterior line. These biaxial joints have the largest RoM compared to other foot joints, with 30° plantarflexion and 70°-90° dorsiflexion. This RoM allows the foot to push off during terminal stance, which is vital for walking [22]. MTP RoM was reported as 98.2-99% in the sagittal plane, 0.3-4.4% in the transverse plane, and 0-0.4% in the frontal plane [31].

2.3.3.4 Interphalangeal Joints

The interphalangeal joints constitute the toes. Each toe has three small bones, except the hallux (big toe) that has only two phalanges. The proximal and intermediate phalanges are miniature long bones, while the distal bones are small nubs. The toes support and stabilize, not bearing much weight during gait [22]. Hallux phalangeal joint RoM is 73° dorsiflexion and 86° plantarflexion [32].

Table 2-2: AFC joint RoM

Joint	Dorsiflexion	Plantarflexion	Eversion	Inversion
Talocrural	15°-25° [24], [25]	40°-50° [24], [25]	N/A	N/A
Subtalar	N/A	N/A	10°-20.8° [25], [27]	30°-35° [25], [27]
Midtarsal	4.47° [29]		6.01° [29]	
Metatarsal-tarsal	6.47° [33]	6.12° [33]	2.97° [33]	2.96° [33]
MTP	70°-90° [24], [25]	30°-50° [24], [25]	N/A	N/A

Table 2-3: AFC joint axes offset from primary planes

Joint name	Frontal offset	Sagittal offset	Transverse offset
Talocrural	20°-30° [12]	82° [12]	8° [12]
Subtalar	48° [12]	16°-23° [12]	42° [12]
Midtarsal (longitudinal)	38° [28]	57° [28]	52° [28]
Midtarsal (oblique)	75° [28]	9° [28]	15° [28]
Metatarsotarsal	45° [28]	45° [28]	9° [28]

2.4 Foot Modelling

To simplify AFC motion analysis, researchers have segmented the lower limb into multiple rigid bodies (Figure 2-9) and ignored certain joints. The Oxford Foot Model (OFM) [34], Rao et al. model [35], and Rizzoli Foot Model (RFM) [36] accurately and effectively record lower limb motion during gait [37], using 3D body landmark coordinates. While designed for motion capture, these models could be the basis for a SLL CAD model, since these valid motion capture models simplify the anatomy into linked rigid bodies.

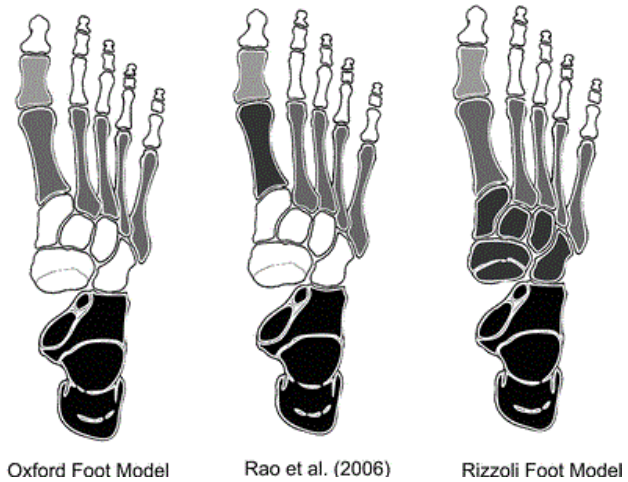

Figure 2-9: Multi-segmented foot models [38]

2.4.1 Oxford Foot Model

The OFM separates the AFC into four rigid body segments (Figure 2-10): tibia, hindfoot, forefoot, and hallux [39]. The hindfoot involves both the calcaneus and talus and the forefoot combines the five metatarsals. The navicular, cuneiforms and cuboid bones are not considered in this model. The hallux segment is the big toe's proximal phalanx [39].

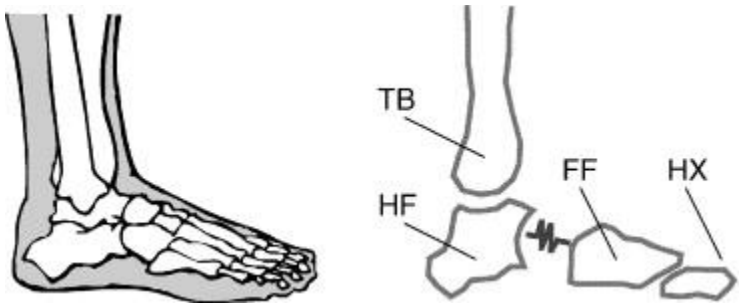

Figure 2-10: OFM segments: TB=tibia, FF=forefoot, HF=hindfoot, HX=hallux [39]

The simplification allows for a viable motion analysis marker set during walking. However, not all internal foot motion is captured. Since more joints are fused into a single rigid body, error related to motion accuracy increases because the segments are more likely to stray away from the rigid body assumption [40]. This error is less than 5° under normal conditions. Depending on selected rigid segments, the error can be diminished. Nester et al. tested several models and found that combining the navicular, cuneiforms, cuboid, and all five metatarsals produced the greatest error due to the rigid body assumption [40].

For this reason, the OFM is not ideal for the ankle-foot surrogate application since the lack of a midfoot causes some motion to be lost.

2.4.2 Rao et al. Foot Model

The Rao model [35] contains tibial, rearfoot, and hallux sections, similar to the OFM. However, the forefoot is divided into two segments, with the first metatarsal and the other four metatarsals (labeled forefoot) separated into two bodies. Furthermore, the rearfoot includes the calcaneus but not the talus [35].

Calcaneus motion relative to the shank encompasses the subtalar and ankle joints. This assumption was validated on cadaver studies, where most dorsiflexion-plantarflexion was attributed to the ankle joint and

eversion-inversion was mainly provided by the subtalar joint [35]. Since the two rotations are bound together in a mitred hinge arrangement, the combination is reasonable. However, the first metatarsal's separation from the other four is unnecessary because the first metatarsal-calcaneus rotation behaves similarly to the forefoot-calcaneus (Figure 2-11). The similarities extend to the first metatarsal and forefoot global motions (Figure 2-12). A limited relative difference exists between the two graphics, and separation between the first metatarsal and the other four seems redundant. As such, the Rao model is also not the ideal choice for a SLL.

2.4.3 Rizzoli Foot Model

The RFM, based on a design by Leardini et al. [36], includes rearfoot and forefoot sections, but also a midfoot section that encompasses the navicular, cuneiforms, and cuboid bones [36]. The rearfoot represents the calcaneus, while the forefoot includes the metatarsals. The hallux is also studied, but as a vector instead of a full segment. Considering the midfoot allows for better analysis, with fewer bone motion limitations (Figure 2-13). Foot kinematics relative to the shank, along with forefoot kinematics relative to the heel, can be used to study the foot's longitudinal arch [36]. For this thesis, important motions include the shank-calcaneus, calcaneus-midfoot, and midfoot-forefoot.

Like Rao's model, the RFM adds one segment to better define foot movements when compared to the OFM. Separating the metatarsals from the tarsals may be more valuable than separating the metatarsals themselves. Unlike Rao's model, calcaneus-midfoot rotation is different than midfoot-forefoot (Figure 2-13). This difference indicates that the midfoot should be included in a model, leaving only the smaller phalanges from the analysis. Including a midfoot section also allows for an easier construction of a physical model. As such, the RFM was chosen as the basis for the CAD model in this thesis.

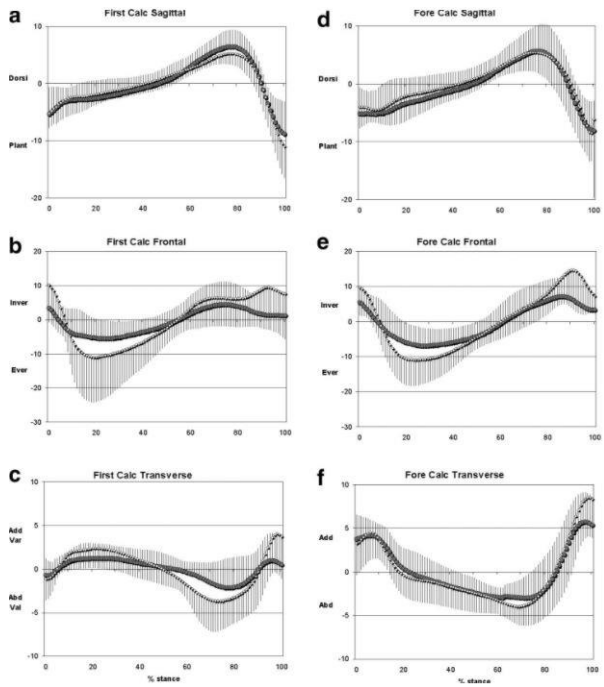

Figure 2-11: Relative rotations of Rao's model rigid bodies, for both individuals with diabetes mellitus (circles) and control individuals (diamond), with error bar representing 1 standard deviation [35]

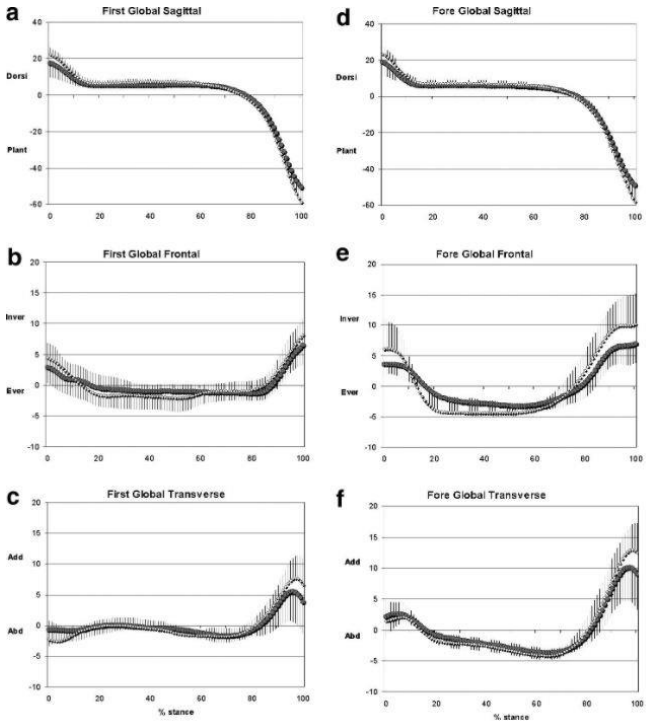

Figure 2-12: Global motion of first metatarsal and forefoot using Rao's model, , for both individuals with diabetes mellitus (circles) and control individuals (diamond), with error bar representing 1 standard deviation [35]

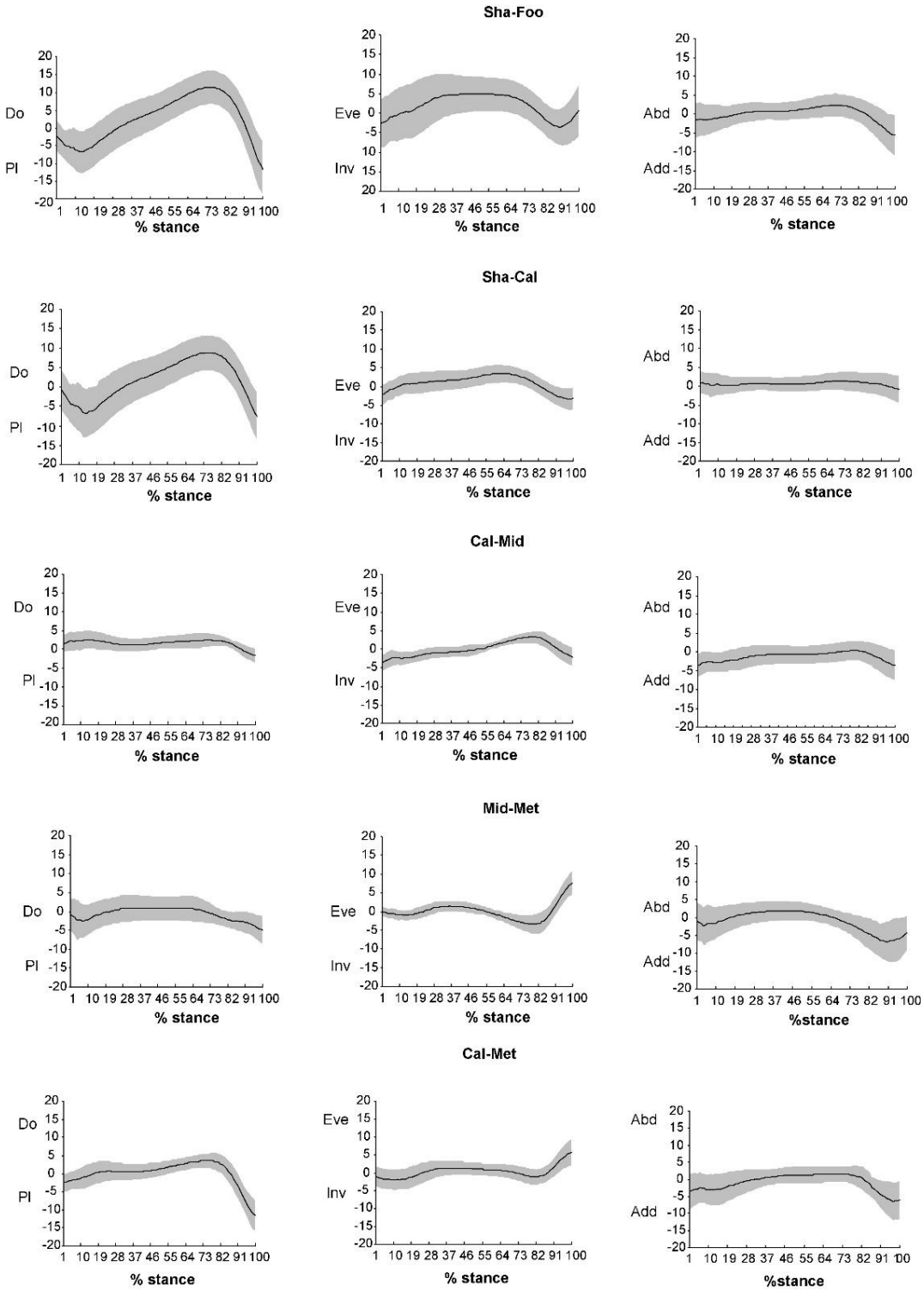

Figure 2-13: RFM planar motion during stance [36]. Do=dorsiflexion, Pl=plantarflexion, Eve=eversion, Inv=inversion, Abd=Abduction, Add=adduction, Sha=shank, foo=Foot, Cal=Calcaneus, Mid=midfoot, Met=metatarsals.

2.5 AFO Testing

Ankle foot orthoses control the foot and ankle during gait, often to keep the toes raised during swing phase and avoid inappropriate foot-ground contact as the leg passes under the body. Therefore, AFO design and mechanical properties are directly linked to performance. Multiple AFO designs are available. These designs require testing to empirically quantify device performance. Test methods can be classified as functional, computational simulations, and bench tests.

2.5.1 Functional Tests

Functional tests compare AFO walking kinematics while in use to gait without the device on or when wearing another AFO design. Moments and rotations can be used to calculate stiffness as a function of torque per rotation (Nm/° or Nm/rad). Some studies used strain gages to measure AFO stress and strain while in use [41].

New AFO designs are constantly being developed, including different manufacturing methods [42]–[44] or other custom designs [45], [46]. Testing these AFO approaches on users is a good way to validate design efficacy. Other studies have focussed on the effect of AFO for groups with different disabilities. These include hemiplegia, hemiparetic, multiple sclerosis, crouch gait, lower limb salvage, and cerebral palsy [45], [47]–[51].

While these tests are helpful, the results cannot be generalized because testing conditions rely heavily on the person's specific pathology [52]. As such, methods have been developed to remove inter-person variations.

2.5.2 Computational Simulations

Computational simulations, such as finite element analysis (FEA), can be used to estimate AFO properties when external loads are applied [41], [53]. FEA segments a surface into a mesh of small geometric objects that can be used to calculate mechanical behaviour at interceptive points. Numerical computations enable fast results, with coarser meshes being faster, but less accurate [54].

FEA was used to study the stress caused by dorsiflexion and plantarflexion on a polypropylene AFO. The ankle trimline was found to support the highest stress [53]. In some studies, a lower limb was introduced in the simulation to better evaluate how an AFO reacts when used in a supportive manner and when connected to the AFC. Unfortunately, the lower limb is complex and the simulations were time consuming to set up and execute. Moreover, organic tissues are viscoelastic, making the AFO-lower limb system hard to simulate. One study simplified anatomy by having bone and cartilage as elastic and homogeneous models, ligaments and tendons as linear elastic structures for tension forces only, and only soft tissues programmed with non-linear viscoelastic properties. These simplifications eased force distribution calculations throughout the AFO-lower limb system, allowing bone and tendon stresses to be calculated [53]. Another study simulated the entire AFO-lower limb system as linear, elastic and isotropic to find peak stresses in the system [53].

Such simplifications speed up the simulation by reducing the complexity, but increases potential inaccuracies due to behavioural difference artifacts. Computational simulations are useful since they allow AFO testing without material and production costs. However, simulations must be validated with physical testing of AFOs to ensure accurate results.

2.5.3 Bench Tests

Bench tests use a variety of testing apparatuses to reproduce a desired condition. Several methods for testing AFO designs and mechanical properties exist. Although most focus on sagittal stiffness, each testing method is unique.

Cappa et al. [55] developed an automatic method of testing an AFO's stiffness in multiple planes. Their first attempt was semi-automatic and could measure force to displacement in both frontal and sagittal planes. This initial apparatus consisted of sliding shafts for the shank and a footplate to secure the AFO foot section (Figure 2-14). Cappa el al. [55] decided against reproducing a full SLL, including soft tissue and a compliant foot, because these properties vary with each individual. Two slider screws measured the x-y

displacement across the transverse plane and two load cells measured the applied load. The researchers performed several trials, first by limiting rotation to one direction, then allowing both rotations.

AFO stiffness was derived from moments in plantar flexion/extension (α) and eversion/inversion (ß) directions, along with angular displacements. Results showed non-symmetrical behaviour, matching previous literature. The calculation uncertainties resulted in roughly 4% error due to the testing apparatus and operator skill [55].

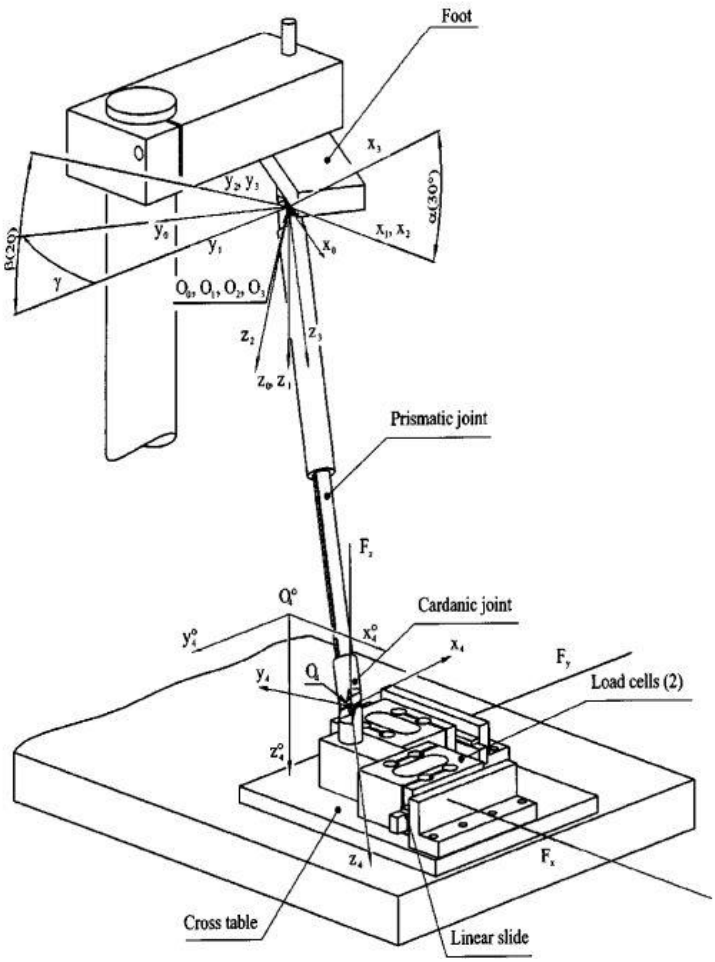

Figure 2-14: Cappa et al. two dimensional (2D) semi-automatic AFO testing apparatus [55]

Cappa et al. [56] subsequently developed an automatic testing apparatus that could work in all three planes and was designed to decrease errors associated with calculations. An industrial Cartesian x-y robot was used, moving the device in the transverse plane. The robot could apply a steady 500 N load (Figure 2-15). The displacement created by the robot was known, with either a quasi-static behaviour or a static

load. The apparatus allowed both α and β to change freely, while keeping the vertical rotation (γ) fixed. γ had only three position options: -15°, 0°, 15° [56]. The researchers tested each AFO five times, and the tests lasted approximately 15 minutes each.

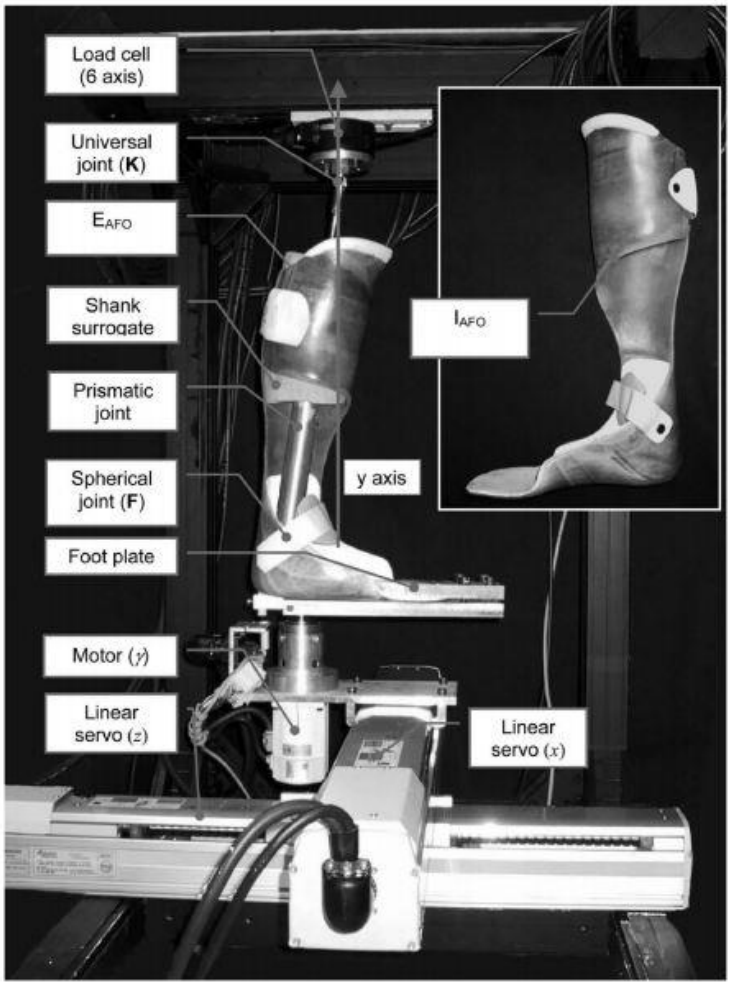

Figure 2-15: Cappa et al. continuous 3D testing apparatus [56]

The AFO remained bare, like the semi-automatic apparatus. The validation process showed that the apparatus was able to reduce error to 1%. Flexibility was greater in the frontal plane than in the sagittal plane, with inversion and dorsiflexion less stiff than eversion and plantarflexion, highlighting the importance of 3D AFO testing [56].

DeToro et al. also designed an AFO testing rig, but included a SLL [57]. This lower leg model was based on a volunteer's anatomy (Figure 2-16), with the leg's inside built from a plywood core surrounded by rigid polyurethane foam. The surface was laminated with polyester resin, over a layer of nylon stockinet.

This SLL was made in a neutral position, with a single axis hinge joint at the transmalleolar region and another single axis joint at the MTP location. Enough material was removed near the joint to allow 20° in both dorsiflexion and plantarflexion. Eight custom-made AFOs and 10 prefabricated AFOs were tested, after being bolted to the SLL at the calf along their back, while the foot moved freely.

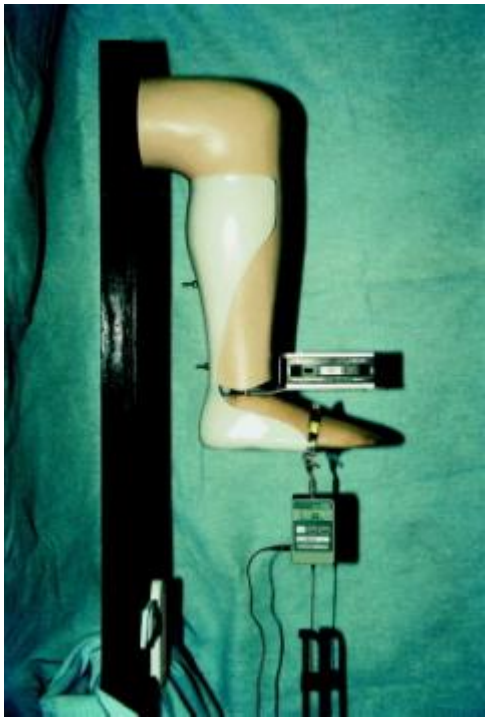

Figure 2-16: De Toro et al. wood-foam SLL [57]

The test required applying a load to a stainless-steel band, 10” anterior to the ankle joint via a screw drive. This screw drive created rotation in increments of 1°, up to 10° plantarflexion. Each AFO was tested 10 times. A secondary test was done in a similar fashion, after permanently reshaping the AFO to 10° dorsiflexion without applying a load.

AFO stiffnesses were characterized into three categories: plantarflexion stop, plantarflexion resistance and non-ambulatory. Plantarflexion stop required a high applied force to deflect the AFO from its initial position. This category drastically limited user RoM. Plantarflexion resistance required 44.5-71.2 N (10-16 pounds) of force to create deflection. The resistance reduced motion but did not completely limit movement. Non-ambulatory offered less than 22.2 N of resistance. These AFOs would work best at keeping a neutral position when lying down.

Golay et al. [58] studied the effects of malleolar protrusions on non-articulating polypropylene AFOs. To decrease pressure on the malleoli, some AFOs have protrusions designed for the ankle's medial and lateral bony prominences. However, these modifications can lead to undesired stress concentrations and result in buckling. In this case, the researchers used a below-knee prosthesis as a SLL. 12 custom-made AFOs were separated into four groups, where each group had increasingly larger protrusions at the malleoli within the range of 0-19.05 mm (3/4") in increments of 6.35 mm (1/4").

The testing apparatus involved a SLL, with an articulation at the ankle (Figure 2-17). A winch was used to apply loads and was controlled using a cable and a pulley to keep the load perpendicular to the prosthetic leg's tibial axis at 25.4 cm (10"). A long pin showed orthosis rotation.

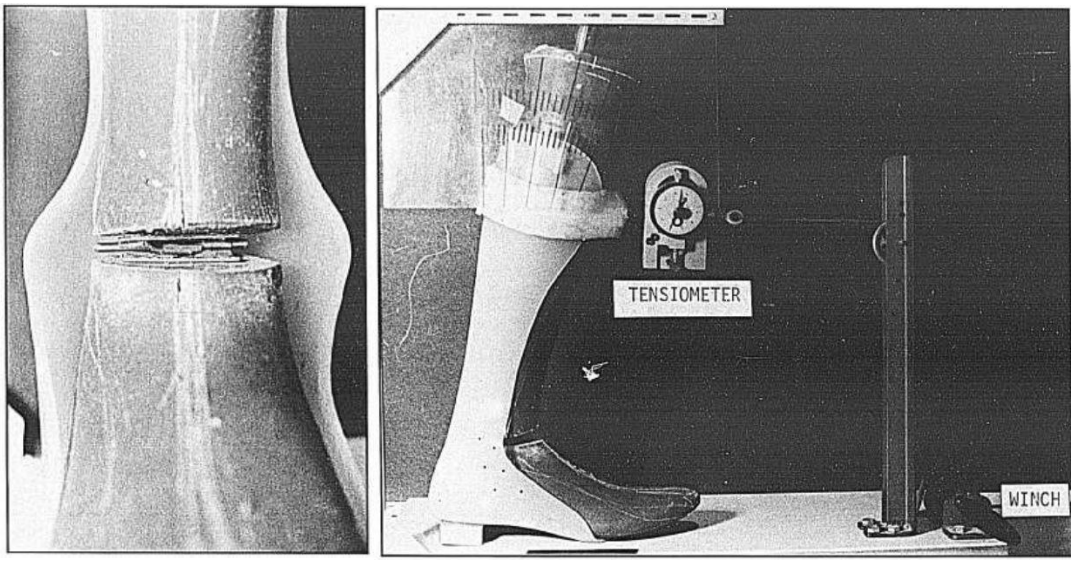

Figure 2-17: Golay et al. ankle joint and full testing apparatus [58]

Change of medial-lateral malleoli width was used as a measure of buckling strain, measured before load application then after each increment of 2°, up to 16°. This protocol was done three times for each AFO, with one hour between every test on any specific AFO to limit plastic deformation.

Malleolar protrusions reduced AFO stiffness, with a 16% reduction for 6.35 mm protrusions, 52% for 12.7 mm protrusions, and 60% for 19.05 mm protrusions, when compared to the AFO without protrusions. The load required to create deformations decreased with larger protrusions, but the strain was also reduced. Larger protrusions created a "pre-buckling" effect, reducing the deformation required to rotate [58].

Most of the previous test apparatuses damaged or physically compromised the tested AFO when securing the device to the SLL, limiting AFO reusability after testing. Kobayashi et al. designed an apparatus that would forgo this requirement, and still allowed dynamic data to be collected for measuring sagittal stiffness [59]. Their setup used a rack and pinion system, along with a torque meter to induce AFO rotation (Figure 2-18).

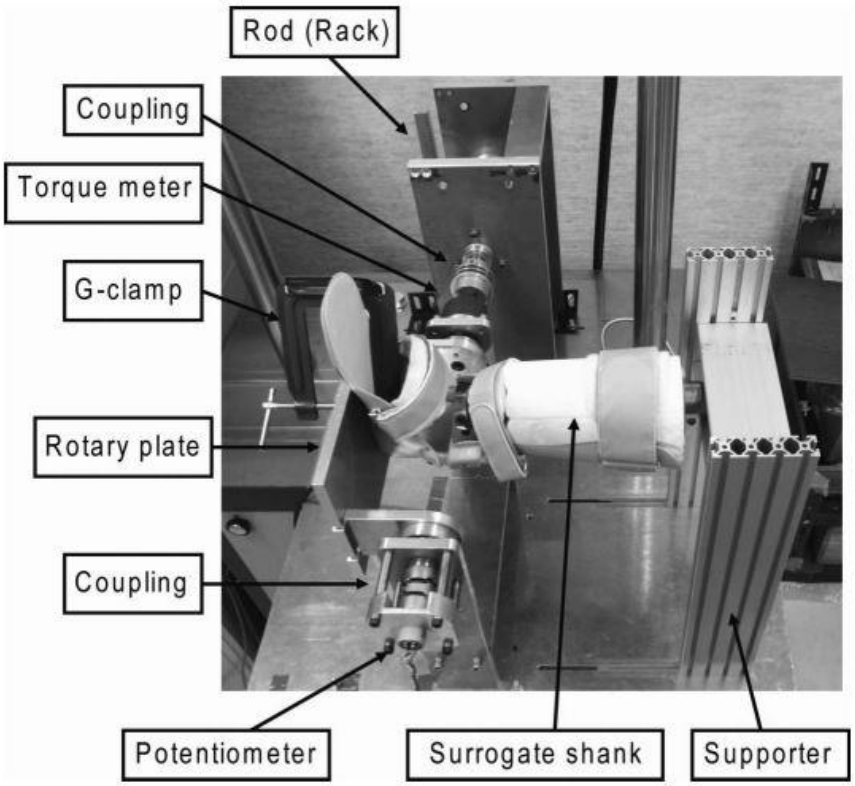

Figure 2-18: Kobayashi et al. testing apparatus [59]

The apparatus also included a partial SLL, created from a prosthetic pylon surrounded by plaster, moulded from a calf model, but without a foot. This apparatus accurately measured the articulated AFO stiffness within a range of 15° dorsiflexion to 15° plantarflexion, at an error of 8%. This error was within the torque meter's range of error, and deemed acceptable [59].

Wach et al. [60] cyclically tested seven different AFO types to understand the effect of mechanical properties (i.e. structural stiffness, rotational motion, strut deflection) on assistance provided. The test rig used a SLL, based on a person's lower limb. One single axis articulation was located at the ankle. The SLL

was based on a prosthetic leg, with rigid foam surrounding an aluminum shank and an external gel liner to replicate soft tissues (Figure 2-19).

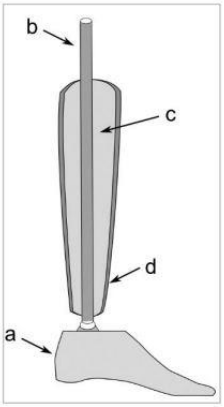

Figure 2-19: Wach SLL a) single axis prosthetic foot-ankle, b) pylon, c) foam shank, d) gel liner [60]

Each AFO was attached to the SLL and tested for 10 quasi-static cycles to emulate gait loading. The load settings were set by an able-bodied person's weight and data. Throughout the tests, markers tracked anatomical landmarks and a force plate measured the applied load. While the initial five cycles were not considered to avoid pre-conditioning effects, hysteresis accounted for some energy loss. Foot displacement was non-linearly related to force, while displacement increased later in the stance, with most displacement occurring in pre-swing. The Intrepid Dynamic Exoskeletal Orthosis (IDEO) had lower hysteresis and RoM than other AFO designs, and higher posterior strut displacement, signaling possible column buckling [60].

Bregan et al. designed a bi-articular reciprocating universal compliance estimator (BRUCE) (Figure 2-20) that mimicked real ankle-foot motion during gait [61]. Integrated sensors provided data to calculate AFO stiffness, regardless of AFO size, and determined the AFO neutral axis, which varied based on the AFO's design. BRUCE's ankle joint covered 10° plantarflexion to 20° dorsiflexion and the MTP joint covered 0° to 30° dorsiflexion [61]. Having two joints is useful because AFO designs can put emphasis on either joint, or a combination of both, depending on the desired effect.

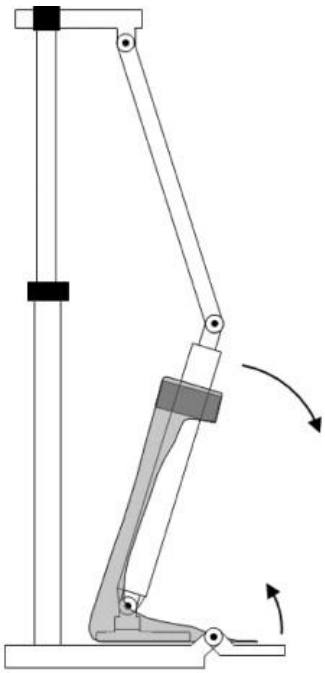

Figure 2-20: BRUCE testing apparatus [61]

BRUCE has six anthropomorphic sized leg models for testing AFOs of various lengths. The AFO can be secured using non-destructive clamping, so that the AFO can be re-used after testing. Furthermore, the AFO can be tested while equipped with normal sized footwear. However, footwear thickness is somewhat limited because the MTP joint was not designed to move vertically. Nonetheless, Bregman et al. indicated that normal footwear should not pose problems since normal shoe thickness does not add too much height [61]. Reliable results were achieved on several tests under varying load conditions.

2.6 Additive Manufacturing

Since the SLL design needs to be easily fabricated, additive manufacturing (AM), commonly known as 3D printing, is explored. AM is a manufacturing method that has evolved to become a practical and readily available fabrication method. While not typically used for mass production, AM is versatile, allows for customizable designs and uses less material overall than other manufacturing processes. AM has been used in construction and biomechanics [62]. While various 3D printing approaches exist, each method creates solid 3D objects directly based on provided digital models. These processes can create objects with complex geometries that are challenging to produce using other methods without additional processes since

objects are “grown” layer by layer. However, each part can take hours to complete, based on the desired volume and complexity.

2.6.1 Fused Deposition Modelling

The most common AM method is fused deposition modelling (FDM), also known as fused filament fabrication. FDM pushes thermoplastic filaments into a nozzle, melts the filament into a semi-liquid state, and then applies the semi-liquid filament on a smooth platform. The nozzle moves freely in a 2D plane, laying the filament layer by layer [62]. The nozzle follows a pre-programmed path for each layer, based on a sliced digital model. Once a layer is completed, the platform moves down (or the nozzle moves up) and the nozzle adds the next layer onto the previous one, which solidifies as the filament cools to room temperature. The final product is anisotropic, based on classic laminate theory [63]. The mechanical properties are dependant on multiple settings, including layer thickness, filament orientation inside the layer, and object infill percentage (percentage of each layer covered in filament, Figure 2-21). Infill patterns can be aesthetic or structural (e.g. honeycombs and zig-zags). However, the outer shell is always set to 100% infill. FDM can only print thermoplastic polymers. Acrylonitrile Butadiene Styrene (ABS) and Polylactic Acid (PLA) are the two most common filaments, but nylons and other flexible thermoplastics can be also used [64].

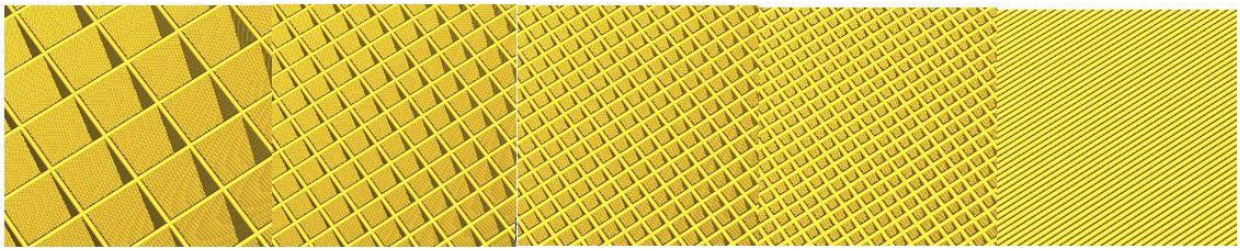

Figure 2-21: Infill ratios in 3D printed material, 20% to 100% in 20% increase intervals

The process is simple and cost effective, making FDM common and popular. However, FDM typically has poor mechanical properties due to the laminated nature of its layers, as well as limited material selection (restricts applications) and a rougher surface finish when compared to other AM approaches [62].

2.6.2 Filaments

FDM thermoplastics come in spools of filaments, usually a few millimeters in diameter. Thermoplastics are lightweight and recyclable [65]. Thermoplastics can be repeatedly molten and modeled into desired shapes while solidifying quickly [66]. Several thermoplastic filaments can be reinforced with carbon fibres or wood particles before being spooled. Unfortunately, compared to thermoset plastics, thermoplastics require higher pressure during processing due to their high viscosity [65].

PLA is a common material for 3D printing since the polymer is made from low-cost and environmentally friendly materials such as cornstarch or sugar cane. As such, PLA is biodegradable and can be used for biomedical purposes [66], [67]. PLA has a low melting temperature and fast cooling rate, which allows the FDM platform to remain at room temperature [68]. However, PLA prints are brittle, reducing their applications.

Polyamide, more commonly known as nylon, can also be used for FDM manufacturing. Nylon has several grades, based on chemical composition and carbon content [69]. Nylon offers flexibility and strength, as well as being resistant in several aspects: chemical, fatigue, impact [70]. Unfortunately, nylon can absorb water in the air, which weakens its structure and permits greater elongation. Nylon 6 is more susceptible to this than other forms of nylon [69]. Nylon can be treated (via curing or heat treating to evaporate the water) so that water has a smaller effect on the filament before, during, or after FDM manufacturing.

While most thermoplastics offer rigid final products, some thermoplastics remain flexible after printing. Thermoplastic polyurethanes (TPU) can remain flexible due to their chemical composition. The main polymer chains have equal distributions of diol and diisocyanate blocks. One offers rigidity while the other has elastic properties [71]. TPU offers great flexibility and elongation, reaching up to 600% elongation at break. However, TPU can be challenging to use in FDM since the push system that feeds the nozzle is often at a distance from the nozzle, which can cause TPU filaments to buckle or slip, damaging the material before reaching the nozzle. This leads to prints having patchy or empty layers, producing failed and

unusable prints. Thankfully, this problem can be reduced if the nozzle is designed to pull the filament directly. Harder TPU grades are easier to push or pull through the nozzle, at the cost of less flexibility.

Chapter 3

Methodology

For a SLL to be acceptable, the design must conform to several criteria and a quantitative validation process. These criteria must be based on scientific evidence.

3.1 Overall Aim

This thesis aims to develop a SLL that can be used for testing AFOs. This SLL should move and rotate similarly to the anatomical AFC, with kinetics and kinematics of a healthy male without pathological problems. The design should be modifiable before fabrication to represent pathological limitations involving a reduced RoM. The SLL design and construction should allow clinicians, industry experts, and researchers to safely use the device during AFO testing. Materials and fabrication processes should be readily available, and components should be cost-effective and easily procured (i.e. avoid specialty components if possible). Since cost is often a limiting factor in research, special care will be taken to reduce fabrication costs during the design phase.

The SLL should work with most AFO designs and foot sizes. As such, the design model should scale anthropometrically with the desired AFO size. To simplify, only one dimension, FL, should be required to scale the digital model before production. The SLL should scale from a FL of 235 mm (male size 6) to 318 mm (male size 16), covering most adult shoe sizes [20].

The proposed SLL must withstand critical loads during AFO testing without damage, including loads corresponding to an average Canadian adult male weighing 86.8 kg [72]. Furthermore, when used in conjunction with an AFO, the SLL should survive critical loads (further discussed in section 3.2) inspired by ISO 10328:2016.

3.2 SLL Load Requirements

3.2.1 Lower Limb Behaviour

A major design factor affecting the SLL is the required strength and expected loads. Since the surrogate needs to replicate anatomical behaviour, the design should be able to sustain whatever loads the anatomical limb would normally experience. The ground reaction force (GRF) is the load transferred up each leg during gait, which is measured through force plates and gait analysis [73]. The load can be normalized by an individual's body weight (BW) to easily compare results between individuals (Figure 3-1). As the locomotion speed increases, the peak loads increase due to the additional kinetic energy and muscle activity. GRF helps in understanding normal lower limb loading.

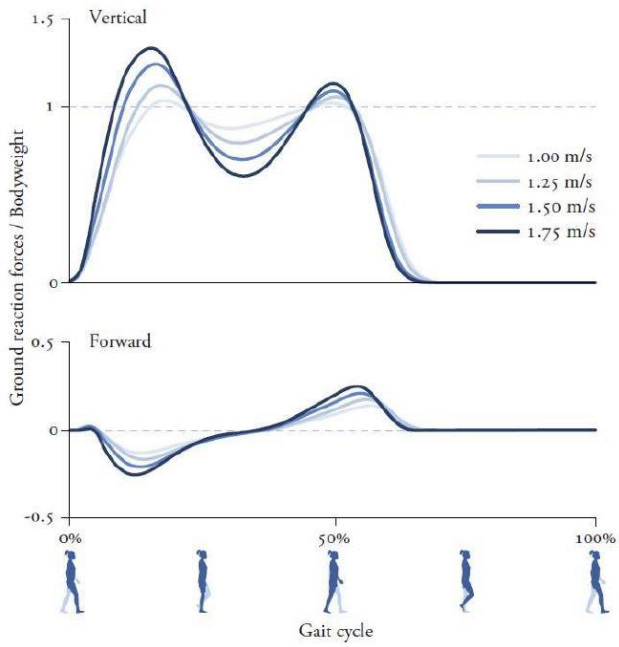

Figure 3-1: Normalized GRF over gait cycle for different speeds [73]

Knowing BW and the GRF for a given speed, the expected load on a lower limb (and matching SLL) can be determined. The average healthy adult walking speed is between 1.2 and 1.4 m/s, with a cadence of 2 steps/s [73]. Typically, AFO user walking speed and cadence decreases due to their medical conditions. One study found that a hinged AFO changed the walking speed of a user from 0.18 m/s when unassisted to

0.25 m/s with the device. Cadence likewise increased from 0.88 steps/s to 1.04 step/s [74]. A study focused on GRFs for males found that 1.5 m/s walking speed resulted in a 1.23 BW load. Higher walking speeds increased the load up to 1.62 BW [75]. These datapoints will be useful in creating a reliable SLL.

3.2.2 Existing Testing Protocol: ISO 10328:2016

AFO testing standards do not currently exist. However, the International Organization for Standardization (ISO) is working on a protocol to test the strength and reliability of lower limb orthoses, which is in the committee draft stage, having already cleared the preliminary, proposal, and preparatory stages [76]. Since this thesis focuses on the design of a SLL for testing AFOs, ISO 10328:2016 was used as a reference because the protocol includes testing methods for ankle-foot prosthetics [77]. The standard is an appropriate starting point because the lower limb prosthetic test loads are related to expected user activity with the lower limb assistive device. Designing the SLL with ISO 10328:2016 in mind should ensure that reasonable static and cyclic loading conditions are considered when used to test an AFO.

ISO 10328:2016 standardizes the prosthetic lower limb testing procedure, including the whole leg, knee, and ankle-foot sections. Guidelines are provided for each section. The testing procedure mimics the stance phase since stance bears BW. ISO 10328:2016 includes a proof static test, ultimate static test, and cyclic test [78]. There are several sections within the protocol, but the relevant section is 17.2, for separated ankle-foot devices and foot units, which include its own static proof, ultimate static, and cyclic test protocol.

Each ankle-foot test has a heel and forefoot component. The testing protocol uses a standard orientation for the ankle-foot devices (Figure 3-2). The ankle joint centre is defined as a point equally distant from the foot's medial and lateral sides, at a distance of $0.25 \cdot FL$ from the calcaneal tuberosity edge or equivalent. The forefoot loading point is equally distant from the foot's medial and lateral sides, with a specific offset (S_B) from the ankle joint centre (Figure 3-2). S_B is defined by the prosthetic user weight [77]. The foot's longitudinal axis is defined by the ankle joint centre and S_B.

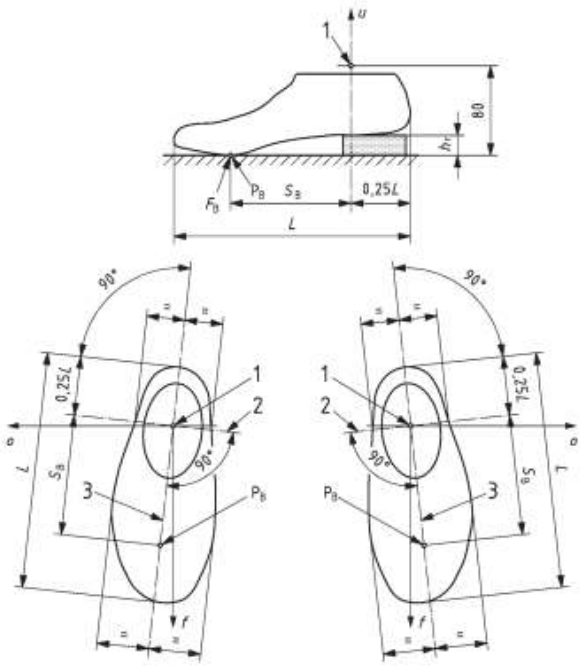

Key

1	effective ankle-joint centre	L	foot length
2	effective ankle-joint centreline	P_B	bottom load application point on forefoot (test loading condition II)
3	longitudinal axis of foot corresponding to 6.7.2	S_B	combined bottom offset of bottom load application point P_B on forefoot from u-axis
h_r	heel height		

Figure 3-2: ISO 10328:2016 foot coordinates and axes [78]

According to the ISO standard, the heel must be loaded at 15° (α) from the vertical axis and the forefoot must be loaded at -20° (β) from the vertical axis (Figure 3-3). The foot's longitudinal axis must be -7° (γ) from the forward horizontal axis.

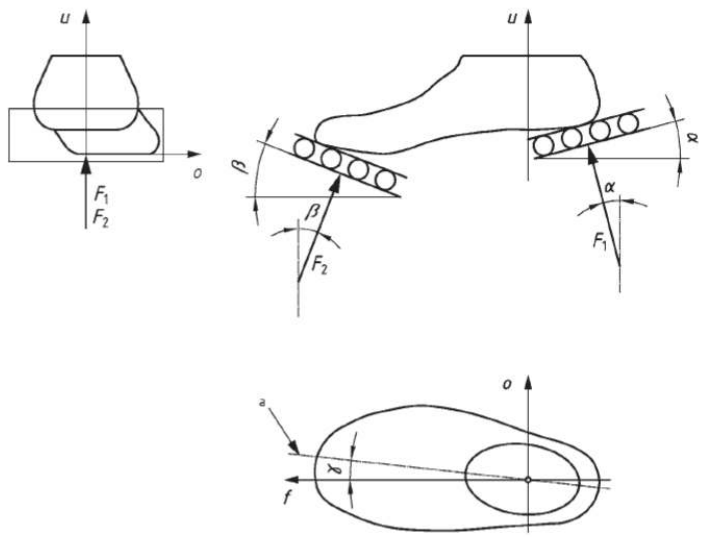

FIGURE 3-3: ISO 10328:2016 FOOT LOAD ORIENTATION [78]

3.2.2.1 Test Load Conditions

All loading conditions are based on user weight ranges. P3 is for people under 60 kg, P4 for 60 to 80 kg, and P5 for 80 to 100 kg. Test specifications are also set for users above 100 kg, with loads of up to 175 kg. For this thesis, the P5 specifications (Table 3-1) were examined since the average Canadian adult male weighs 86.8 kg [72], too high for P4. As a result, the SLL loads were designed to replicate a majority of potential AFO users. According to the standard, at P5, S_B is 130 mm.

Table 3-1: ISO 10328 P5 loads

Test name	Force (N)
Proof static test (heel, forefoot)	2240
Ultimate static test, lower bound (heel, forefoot)	3360
Ultimate static test, upper bound (heel, forefoot)	4480
Minimum cyclic load (heel, forefoot)	50
Maximum cyclic load (heel, forefoot)	1330
Final static load (heel, forefoot)	2240

3.2.2.2 Proof Static Test

The proof static test is intended to apply a higher load than would normally be seen by the device, which could happen occasionally during use. The load is applied first at the heel, at a constant rate, ranging

from 100 N/s to 250 N/s, then held in position for 30 (±3) s. Afterward, a forefoot load is applied at a constant rate, with the same range, for the same duration. Two samples from the same production batch need to pass the test. To pass, the load must be held for the entire duration and inclination without any deformation or structural damage. A replacement is possible, under specific conditions [78].

The ISO load is for prosthetics, where the device replaces the limbs. Since lower limbs can experience high loads in some conditions, such as running or jumping, the replacement must survive matching loads. Running loads can reach 2.38 BW for adult males running at 6 m/s [75] and can be higher when jumping. As such, a static proof load of 2240 N is reasonable for a prosthesis, which could be used for running. However, AFOs are not typically used for running and since the SLL is always intended to be used in conjunction with an orthosis for testing, this load magnitude is excessive. Because the SLL is designed to mimic the lower limb, walking loads should suffice. A 1500 N load, 1.5 BW for a 100 kg individual, is reasonable for static loading since this exceeds the normal walking load. The remaining protocol components are sound since holding the load for 30 seconds can be required in AFO testing to simulate standing.

3.2.2.3 Ultimate Static Test

The ultimate static test reproduces a single catastrophic event scenario. This test aims to find the device's maximum sustainable load, within pre-defined bounds, before becoming unusable. The load is applied at a constant rate, ranging from 100 N/s to 250 N/s. Force is increased until failure, or the upper limit is reached. If the sample survives, the forefoot is loaded in a similar fashion. To pass this test, either the device remains functional after reaching the upper limit in either heel or forefoot loading conditions or the device's maximum sustainable load (device retains its structural integrity) is above the lower limit in either the heel or the forefoot loading conditions.

The SLL is not designed to be tested until failure, since AFOs are not usually used for destructive testing. As such, ISO ultimate static load protocols are not used in this thesis.

3.2.2.4 Cyclic Test

The cyclic test is designed to reproduce performance under normal usage. This test has two parts, an initial cyclic load test followed by a final static test to ensure that the device still functions correctly. For the cyclic load test, the heel and forefoot are loaded alternatively in a pulsating fashion (Figure 3-4a-d). Figure 3-4d shows the most realistic walking behaviour, with the forefoot sequentially loaded after the heel. The heel and forefoot load functions are designed to be identical, but with the forefoot load delayed to mimic load transfer during midstance.

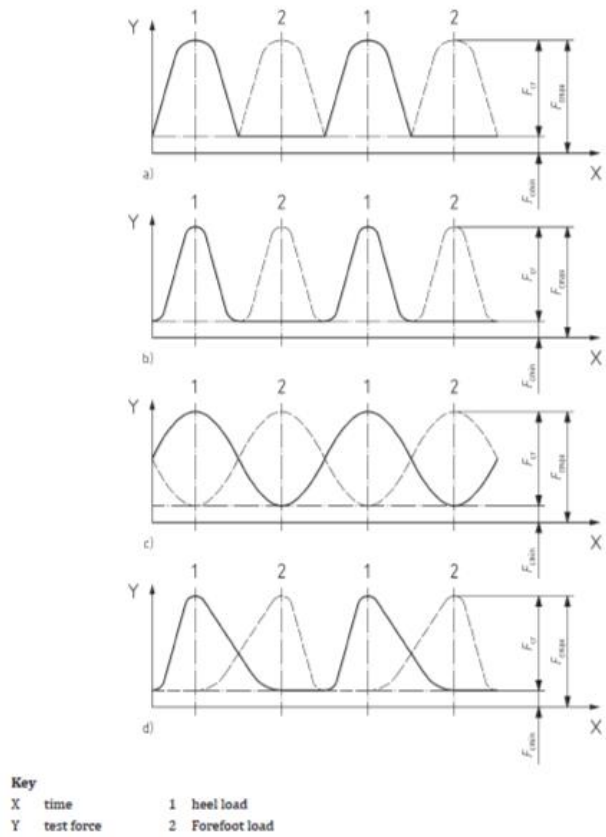

Figure 3-4: ISO cyclic test patterns

The testing apparatus should settle at the desired frequency, ranging from 0.5 to 3 Hz, with a 69 N applied force (10% of the peak cyclic value). Once the desired loading frequency is achieved, the test runs for $2 \cdot 10^6$ cycles to allow both forefoot and heel components to be tested 1 million times, or until the device breaks. If the device does not break during the cyclic test, a static proof test is applied at the heel

first, at a constant rate, ranging from 100 to 250 N/s. 2240N is applied for 30 (±3) seconds. The forefoot is then loaded in an identical fashion. Two samples from the same batch must pass the test to be considered compliant [78].

Testing the AFO and SLL cyclically is vital since orthoses will be loaded repeatedly during locomotion. The ISO protocol requires two million cycles to ensure that the prosthesis will survive an expected lifetime. Since an AFO would also be subjected to a lot of repeated wear, cyclic testing should also include two million cycles. For initial SLL cyclic testing, 500,000 cycles will be performed in each position to confirm that the design can handle cyclic loading.

The ISO cyclic load of 50 N to 1330 N is reasonable, taken that 1330 N is 1.33 times BW for 100 kg individuals, which is slightly higher than normal walking load [75]. Testing the device's structural integrity after undergoing fatigue testing through a final sustained load is also reasonable since the AFO and SLL should be able to survive both. The sustained load will indicate if any potential creep or cracking occurred during cyclic testing. However, the 2240 N load remains excessive for testing a device intended for walking, so 1500 N as a final static proof load is used.

3.2.3 SLL Testing Conditions

The SLL should be subjected to static and cyclic tests, to ensure that the device can withstand typical lower limb behaviour. The static test will apply a load on the combined SLL and AFO from 0 to 1500 N at 200 N/s. The load will then be held for 30 seconds, and removed at -200 N/s. This process will be done first in the heel position with the load angled at 15°, then in the forefoot position with the load angled at -20°.

The cyclic test will differ from the ISO protocol due to the available loading apparatus. The Instron device available for this thesis cannot perform two sequential loads as per the ISO standard. As such, the heel will be loaded first, from 50 N to 1330 N for $0.5 \cdot 10^6$ cycles at a frequency of 1 step/s, one half a healthy adult cadence [73] since only one leg is tested. Afterward, the forefoot position will be loaded in an identical matter.

Table 3-2: Anatomical joint rotation angles required by the SLL design

Joint	Dorsiflexion	Plantarflexion	Eversion	Inversion	Abduction	Adduction
Talocrural	20°	50°	-	-	-	-
Subtalar	-	-	20°	30°	-	-
Midtarsal	4.5°		6.0°		0.5°	3.8°
Metatarsal-tarsal	6.5°	6.1°	3.0°	3.0°	2.0°	6.5°
MTP	80°	30°	-	-	-	-

3.3 Design Criteria

The SLL design criteria are:

- The SLL must survive all load and test procedures, for 100 kg loads.
    - Static test: 1500 N, held for 30 seconds at both heel and forefoot positions.
    - Cyclic test: $0.5 \cdot 10^6$ cycles alternating between 50 N and 1330 N, at both heel and forefoot, followed by static proof test of 1500 N, for 30 s.
- Scalable design:
    - Accommodate FL from 235 mm (US male 6 shoe) to 318 mm (shoe size US male 16).
- Fabrication:
    - Use readily available 3D printing material and equipment and easily sourced components.
- RoMs should match maximum rotation angles in Table 3-2.

Chapter 4

SLL Design

4.1 Overall Design

This chapter focuses on the design of the SLL components, shown in Figure 4-1.

Figure 4-1: Fully Assembled SLL

To simplify the SLL anatomy and fabrication process, fewer segments than real lower limbs were used while retaining anatomical RoM where required. Using the RFM reduced the moving components from 28 bones to 5 major segments [36]. The design involved five main elements (Figure 4-2):

- Shank, contained a shaft representing both the tibia and fibula
- Hindfoot: combining the calcaneus and talus

- Midfoot: combining the remaining tarsals
- Forefoot: merging the metatarsals
- Toes: phalanges coalesced and hallux separated from the smaller toes at the distal end.

The foot segments were designed to scale anthropometrically with FL. The five segments were connected using four joints: the shank-hindfoot (SH) mimicking the combined talocrural and subtalar joints; the hindfoot-midfoot (HM) simulating the midtarsal joints; the midfoot-forefoot (MF), mimicking the metatarsal-tarsal joints; and the forefoot-toes (FT) representing the MTP joints.

The foot components used FDM nylon to represent the bones since nylon is strong, durable, and easy to print into specific shapes. TPU connected the main foot blocks, acting as ligaments since the material could bend and be easily shaped as well. These TPU connectors were specifically designed and dimensioned to control stiffness based on joint passive stiffness. Torsional stiffness was also controlled through rails on the HM and MF connectors. Silicone rubber (SR) surrounded the foot segment to provide an anatomical shape and emulate soft tissue. SRs can match skin mechanical properties [14]. A mould was 3D printed based on a prosthetic foot cover file provided by Össur™ to cast the SR around the foot. The mould included metal pins to elevate the foot above the mould's inner surface, creating a cavity that could be filled by the SR, encapsulating the foot. These pins were created by machining the length of flat headed nails. The shank shaft used metal for its strength, surrounded by a 3D printed shank cover to provide the appropriate anatomical shape.

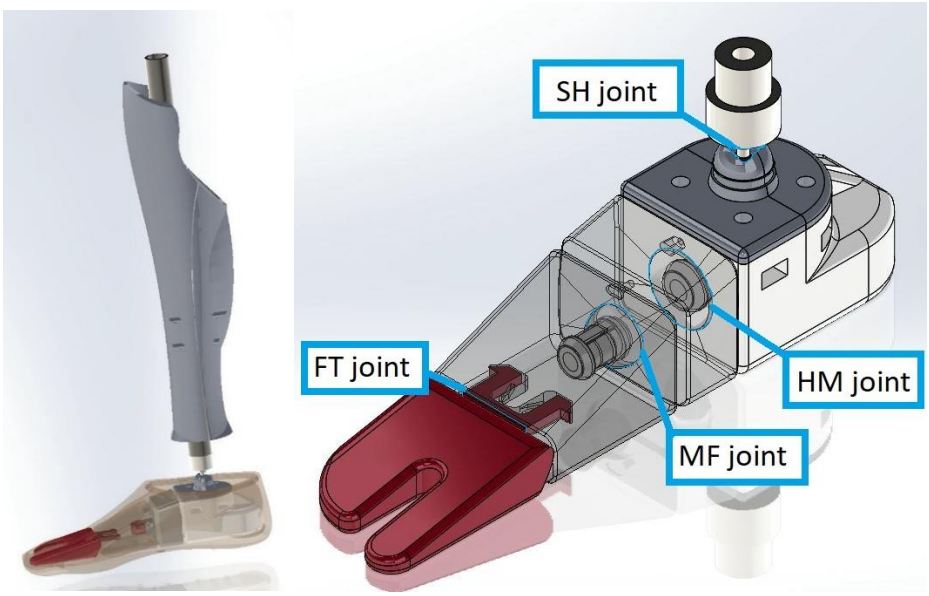

Figure 4-2: full SLL assembly (left), SLL foot (right)

4.1.1 Joint Design

Ball and socket joints were used for the SH, HM, and MF joints because the required motions were across multiple planes. Since the MTP joint only rotates in the sagittal plane, the joint was designed using a hinge-type joint, consisting of double cantilever snap-fit connectors to ensure a secure connection.

There were two different ball and socket joints used for the SLL design, both designed to replicate their respective anatomies. The SH involved a metal ball stud that sat inside a nylon socket (Figure 4-2). The socket was sectioned into three components (the heel base and two heel plate halves) so that the ball stud could be properly inserted, due to the ball stud's integrated nut. The HM and MF ball and socket joints were integrated inside the foot components, replicating the midtarsal and metatarsal-tarsal joints (Figure 4-3). These joints were centred on the foot segments' proximal and distal surfaces to better control all 3D rotation and accommodate all motion-defining features. These two ball and sockets were secured with annular snap-fit connectors, preventing separation, but allowing rotation via the bending action of the connector. Joint stiffness was related to the connectors' material properties and connector geometry.

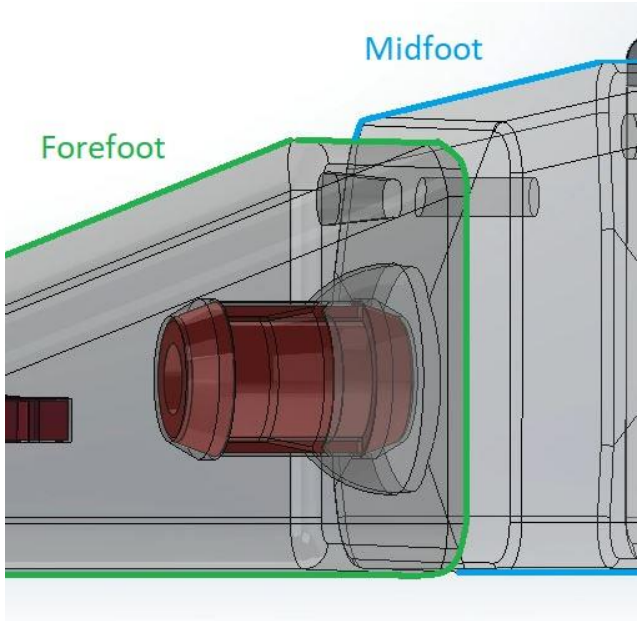

Figure 4-3: Midfoot (blue outline) meshing with forefoot (green outline) to form the MF joint

Each SLL joint was designed with features constraining motion to match anatomical RoMs. These features were defined by maximum RoM, divided by planar directions (Table 4-1). These features involved tapered openings, angled surfaces, guiding pins, and flexible connectors.

Table 4-1: SLL 3D maximum joint rotation values

	SH	HM	MF	FT
Eversion	20.0°	3.5°	6.5°	-
Inversion	30.0°	3.2°	7.0°	-
Dorsiflexion	20.0°	2.2°	6.5°	80.0°
Plantarflexion	50.0°	2.2°	6.1°	30.0°
Abduction	-	0.5°	6.5°	-
Adduction	-	3.8°	2.0°	-

4.1.1.1 SH Tapered Opening

The SH socket was created with an opening to let the ball stud neck through. This opening tapered in a manner that would allow the neck to move with the desired RoMs (Figure 4-4). To create the tapered opening that dictated possible rotation angles, reference sketches were made in the upper socket's frontal and sagittal planes (Figure 4-5), showing the desired rotation angles in all planes by the ball stud neck.

These sketches show reference points at equal height to the hemisphere's outer radius. For a secure connection, the reference sketches used a 2.6 mm stem radius.

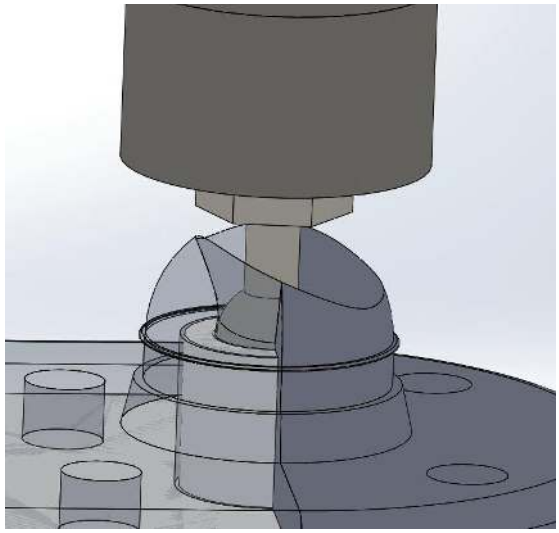

Figure 4-4: Close-up side view of the SH ball and socket joint

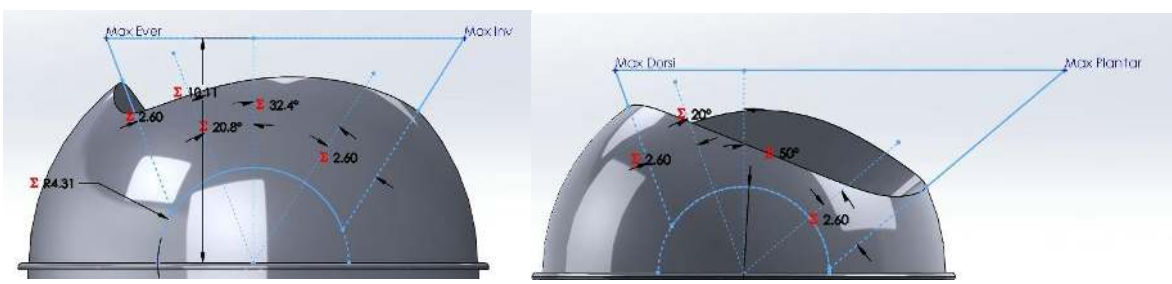

Figure 4-5: SH upper socket reference sketches: frontal plane (left) and sagittal plane (right)

The plantarflexion and inversion points were used as x-y coordinates to create a fifth point, while dorsiflexion and eversion created a sixth point. These six points were used to create an irregular oval (Figure 4-6) which guided the tapered opening. The opening enabled the shank to rotate with respect to the heel in the appropriate manner, replicating talocrural and subtalar behaviour.

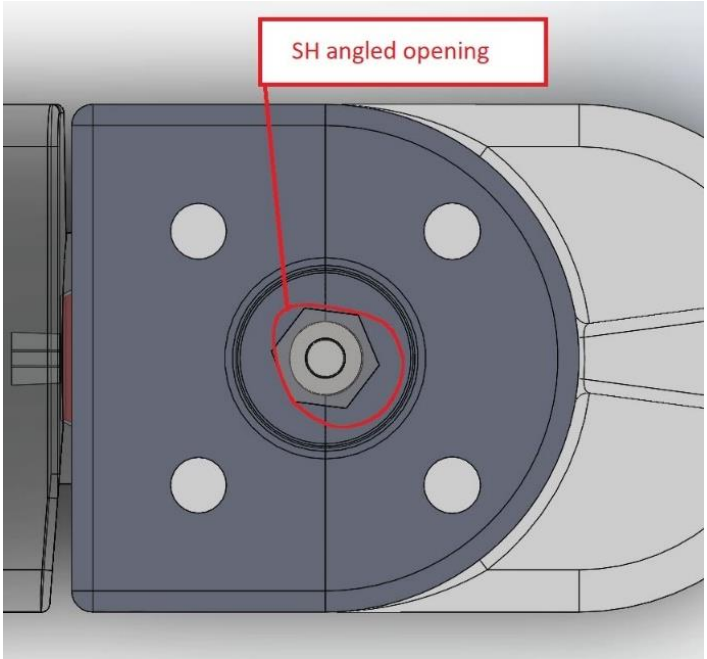

Figure 4-6: Heel plate top view, with max rotation spline highlighted

4.1.1.2 HM and MF Angled Surfaces

To enable proper sagittal and transverse motion, the material surrounding the HM and MF joints were tapered inward (Figure 4-7 and Figure 4-8). These surfaces were created by removing triangular wedges from the midfoot digital file, centred on the joints, and extending to the outer edges. The cuts were defined by the relevant motion for that joint in Table 4-1. All these motion defining features were added on the midfoot so that if the RoM required alterations, fewer segments would need to be modified. These cuts created an asymmetric pyramid on each side since some wedges were shallower than others. The cuts were created first, then the joints' protruding ball features were added afterward so that the balls properly connected to the angled surfaces. These angled surfaces enable rotation while preventing overextension.

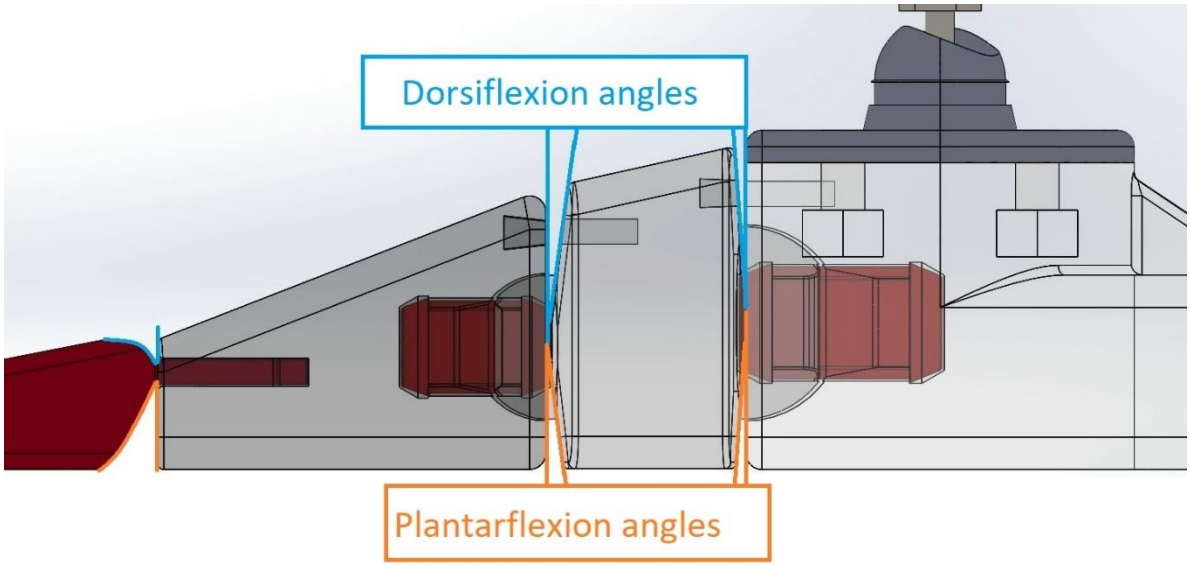

Figure 4-7: SLL side view with HM and MF angled surfaces highlighted (dorsiflexion-plantarflexion)

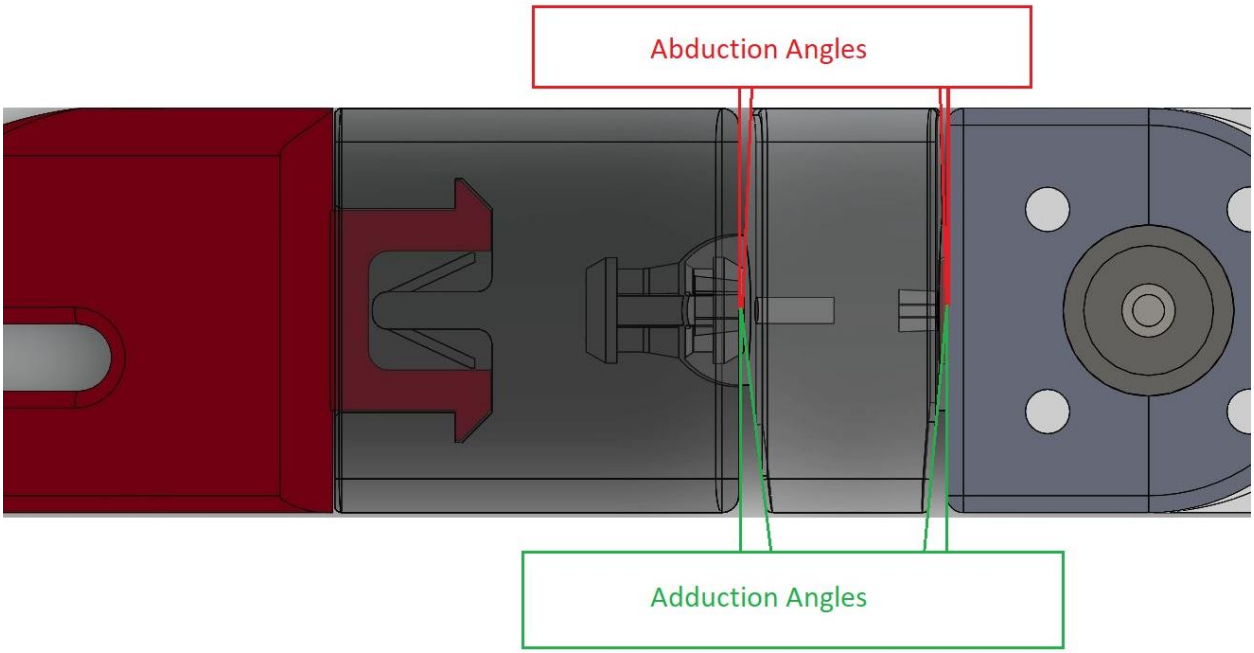

Figure 4-8: SLL top view with HM and MF angled surfaces highlighted (abduction and adduction)

4.1.1.3 Guiding Pins

The HM and MF angled surfaces were designed to define maximum sagittal and transverse rotations, but another feature was required for frontal motion. The maximum planar rotation was constrained by guiding pins above the ball and socket joints. On the proximal surfaces, a pin protruded above the ball and

socket joint. On the distal surfaces, a groove was created above the socket at a matching height. The groove curved around the joint, with the curvature centred on the joint. The curvature extended on each side by the desired maximum eversion and inversion rotation angles shown in Table 4-1. When frontal motion would occur, only the desired motion was performed, without overextension.

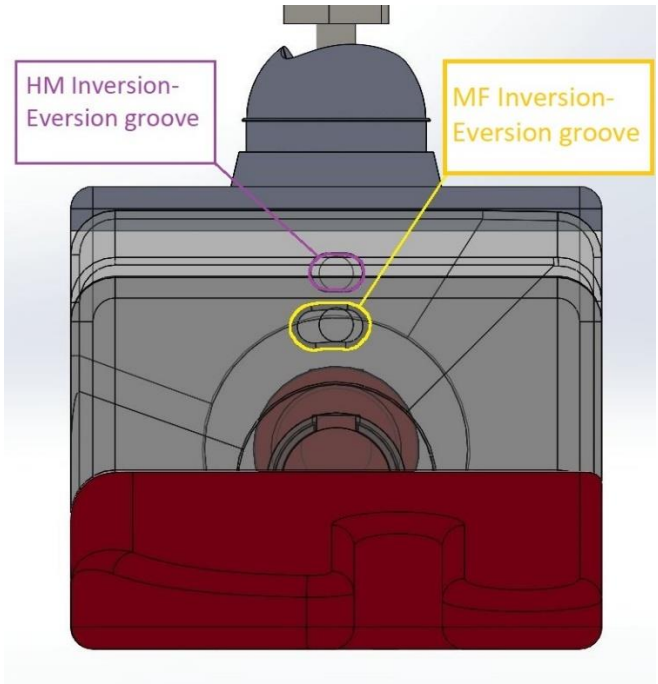

Figure 4-9: SLL front view with HM and MF guiding grooves highlighted (eversion and inversion)

Given the pin's protruding length, the guiding groove widened internally so that when the joint rotated in sagittal or transverse planes, the pin's tilt would be accommodated for as well.

4.1.1.4 Cantilever snap-fit Connectors

The toe segment integrated both motion defining features and connecting segments. To constrain the FT RoM, the toe segment's proximal surface facing the forefoot was rounded according to a specific

geometry that would allow the appropriate rotational motion (Figure 4-10). From the apex of the curved surface, two cantilever snap-fit connectors protruded out, connecting the toes to the forefoot.

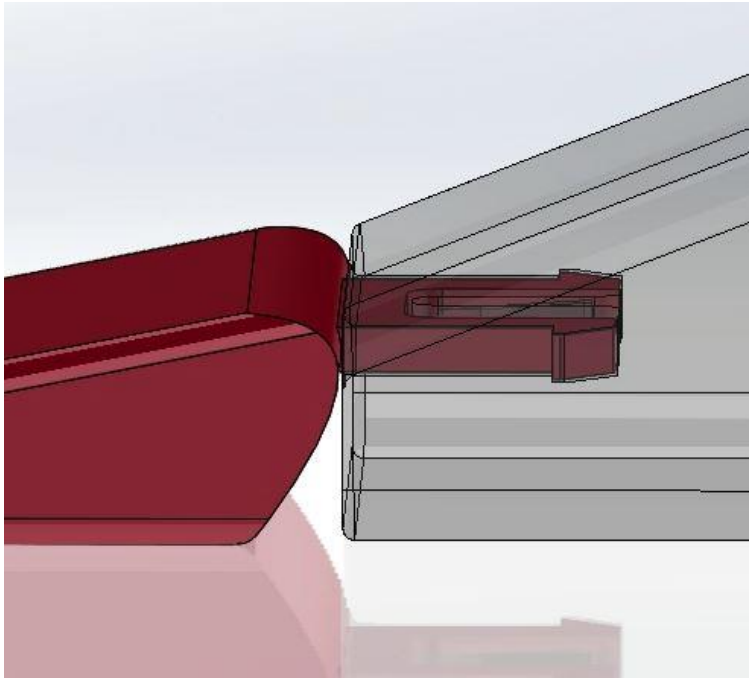

Figure 4-10: Toe segment (red) and forefoot segment (gray) forming the FT joint

The curvature's apex height and length were calculated based on the known angle of rotation and arc length, as shown in Figure 4-11. The arc length S remained constant for both dorsiflexion and plantarflexion Therefore, the joint height (acting as arc radii) determined the possible RoM. The desired rotation angles were 80° dorsiflexion (θ_{dorsi}) and 30° plantarflexion ($\theta_{plantar}$), and the total height was defined as $FL/13.5$ based on the toe's maximum height (explained in section 4.4.3). Given these properties, the joint height was calculated to be $FL/18.5625$ using equation (4-1). The arc length was calculated as $FL \cdot \frac{8\pi}{891}$. The surface curvature was created and added to the main toe segment based on these results.

The FT connector was elevated to the joint height, extending posteriorly (Figure 4-12). The connectors involved two back to back snap fit cantilever beams (Figure 4-12 point A and B). Given that snap-fit hooks are not intended to move once installed, the two connectors were attached to a bending strip (Figure 4-12 point C), which enabled FT joint rotation. The bending strip's dimensions were designed to replicate MTP joint stiffness. Marabelle's et al. determined that MTP joint stiffness can vary between 0.66 to 56 $Nmm/°$

[79]. The average stiffness measured by an experienced worker was 13.75 $Nmm/°$ [79]. Based on this value and equation (4-2) , several possible dimensions were available for the bending strip. However, stiffness does not scale linearly with respect to geometrical dimensions. As a result, the connector's dimensions were fixed, not scaling to FL because the linear anthropometric scaling could not be made to match stiffness scaling. The width (W_{toe}) was set to 30 mm minus Nylon-TPU clearance, to ensure that when the FL was small, the connector did not interact with either ends. The thickness (T_{toe}) was set to 4 mm minus Nylon-TPU clearance to keep a lip above the joint on the forefoot surface. With these dimensions and a modulus of elasticity of 26 MPa [80], the required strip length (L_{toe}) was calculated to be 5.28 mm using equation (4-2).

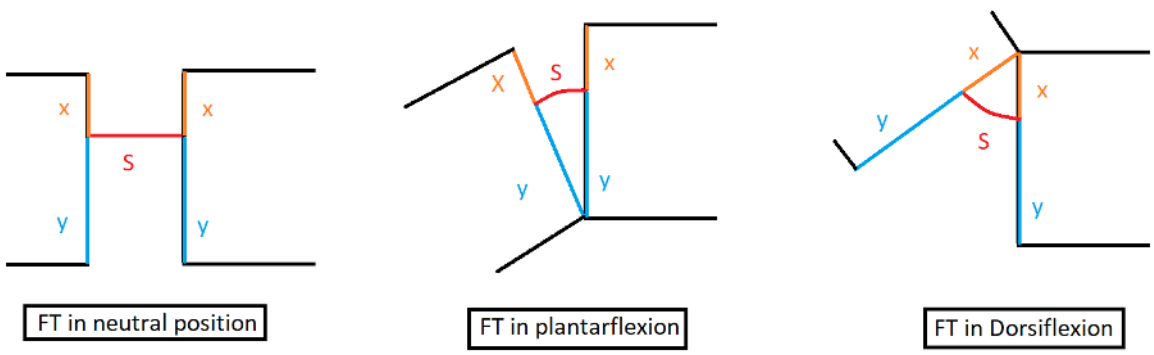

Figure 4-11: Arc length diagram for FT motion constraints

$$S = \theta_{dorsi} \cdot x = \theta_{plantar} \cdot y, \qquad x + y = FL/13.5 \tag{4-1}$$

For the cantilever snap-fit dimensions themselves, the driving factors were the highest permissible deflection and associated force calculated in equation (4-3) [81]. The permissible deflection would also define the notch lengths (Figure 4-12point D and E). The deflection occurred on the transverse plane, along the segment's width. The cantilevers' width was the same dimension as the bending strip's thickness. Similarly, the cantilever height h was along the bending strip's width. This height was set at a fixed 6 mm to enable enough deflection without interacting with the other connector. The cantilever lengths were set at 12 mm plus Nylon-TPU clearance, to ensure a solid connection with the forefoot without interfere with the

MF joint. For the relevant material properties, the permissible strain ($\varepsilon_{permisible}$) was taken as half the yield strain, which was provided by the manufacturer's data sheet. TPU has a yield strain of 55%. Therefore, $\varepsilon_{permisible}$ is 27.5% [81]–[83]. The estimated secant modulus was 18.2 MPa, assumed as 70% of the full modulus of elasticity [82]. Given these dimensions and material properties, the permissible deflection (y) was calculated as 4.42 mm while the deflection force P was calculated as 60.1 N, both using equation (4-3). As such, the notches were set at 4.42 mm long.

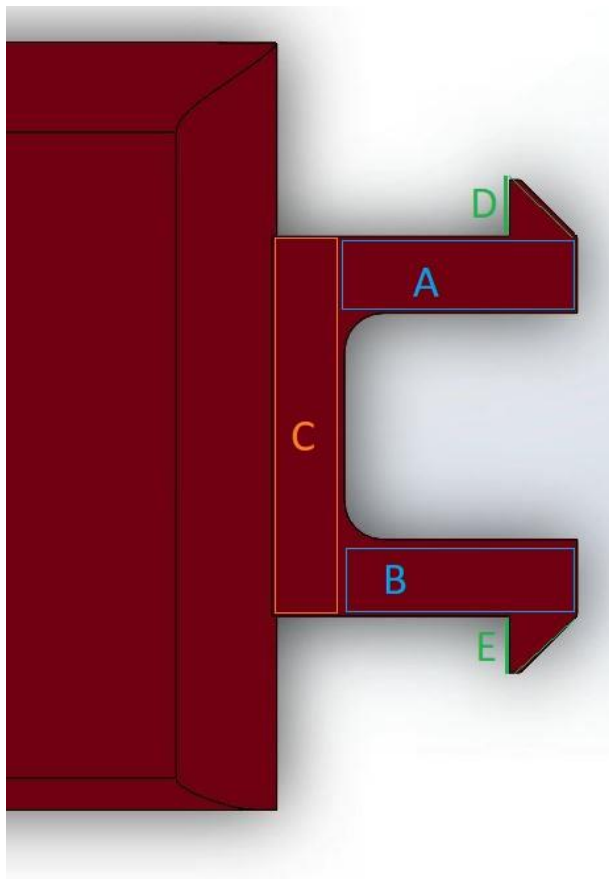

Figure 4-12: FT connector top view, with main features highlighted

$$k\left(\frac{N \cdot mm}{rad}\right) = \frac{M}{\theta} = \frac{EI}{L_{toe}}, \qquad I = \frac{W_{toe}T_{toe}^3}{12} \tag{4-2}$$

The mating force (F_{Mating}) was the force required to insert the component properly inside the hole, calculated using equation (4-4). This force was dependant on the deflection force, friction between the two materials, and the mating angles, α and β. The friction coefficient (μ) for TPU ranges between 0.2 and 0.25 [84]. To account for the rougher TPU-nylon interaction, the higher value of 0.25 was used. The initial mating angle α was set at 45° to keep the mating angle low yet keep dimensions reasonable, while the return angle β was set at 90° to prevent removal. The initial mating force was calculated as 100.1 N. The return force was not calculated given that equation (4-4) cannot be used at 90°. The edges connecting the cantilever beams to the bending strips were filleted to reduce bending stresses.

$$h = \frac{0.67\varepsilon_{permissible} l^2}{w}, \qquad P = \frac{Tw^3}{6} \cdot \frac{E_s \varepsilon_{permissible}}{l} \tag{4-3}$$

$$F_{Mating} = P \cdot \frac{\mu + \tan(\alpha)}{1 - \mu \cdot \tan(\alpha)} \tag{4-4}$$

4.1.1.5 Annular Connectors

The HM and MF ball and socket joints required a connector to hold both components together during rotation. These connectors were designed to be inside the ball joints themselves, allowing rotation in all anthropometric directions, while defining the stiffness of the joints from within. These connectors were made circular to allow rotation in the frontal plane. The connectors had three main sections (Figure 4-13): a solid middle section that defined the bending and torsional stiffness of each join, notched ends which would lock the connectors in place, and torsion rails preventing free rotation in the frontal plane.

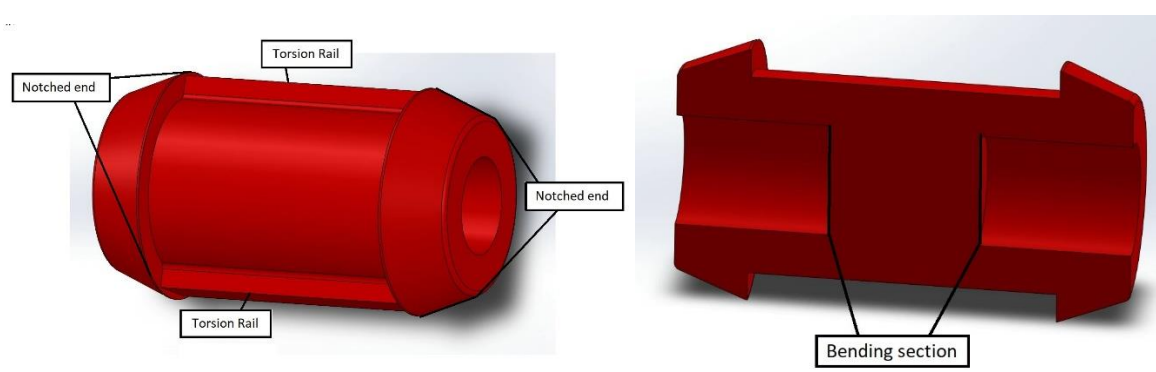

Figure 4-13: Annular connector, main features

Both HM and MF connectors were dimensioned to create identical bending stiffnesses, based on a male ankle stiffness of 100 $Nmm/°$ [85] and equation (4-2). Ankle stiffness was selected due to lack of data on TMT or midtarsal joint stiffnesses. Since the same material was used for the toe segment and connectors, the modulus of elasticity was 26 MPa. Due to the circular connector body, the moment of inertia was calculated using equation (4-5). While both connectors had identical stiffnesses, the outer diameters (D_O) were different because the respective ball and sockets were designed to be of different sizes. After testing multiple dimensions, the HM D_O was set to 14.56 mm minus Nylon-TPU clearances, resulting in a length of 10.01 mm. Similarly, the MF D_O was set to 12.25 mm minus Nylon-TPU clearances, which produced a length of 5.02 mm.

$$I = \frac{\pi D_O^4}{64} \tag{4-5}$$

The snap connector notches at both ends of the connectors involved a hollow cylinder with an angled protruding notch at the outer edge (Figure 4-13). When pushed in, the notch would deflect inside the hollow cylinder then snap back into place once seated. The hollow cylinder had a D_O matching the connector's middle section diameter, and an inner diameter (D_I) large enough to accommodate the notch when pushed in. The notch diameter length was dictated by the material's maximum permissible deflection (y) and corresponding deflection force (P), calculated using equation (4-6) and (4-7) [81]. From the permissible strain $\varepsilon_{persmisible}$ and the D_O, deflection was calculated. The required HM notch diameter was calculated to be 4.01 mm, while the MF notch diameter was 3.37 mm. As such, half the notch diameter was added all around the hollow cylinder.

$$y = \varepsilon_{permisible} \cdot D_O \tag{4-6}$$
$$P = y \cdot D \cdot E_s \cdot X_w \tag{4-7}$$

For the deflection force calculations, a geometric factor was used (X_W), obtained from graphs in literature [81], proportional to the connector D_I-D_O ratio. Using the TPU filament secant modulus E_s and diameter D, HM connector deflection force was found to be 251.2 N and MF connector force was found to

be 160.9 N, both using equation (4-7). To reduce the mating force calculated by equation (4-4), the initial mating angles were made as low as possible. In this case, a mating angle of 22° was used for the HM snap-fit connector and 20° for the MF snap-fit connector. With a coefficient of friction of 0.25, the mating force was calculated to be 201 N for the HM connector and 120 N for the MF connector. Like the toe snap-fit connectors, the decoupling angle ß was set at 90° to prevent disassembly. The overall snap-fit connector lengths were 31 mm (HM) and 22.5 mm (MF), which ensured appropriate bending without interference from other components.

Along the connector lengths, two rails were added to provide torsional resistance during HM and MF eversion-inversion. These rails prevented the connectors from freely rotating inside their sockets during frontal motion. These rails were dimensioned to add some stiffness. The rail widths were set as a third of the connector D_O, while the heights were set as the maximum diagonal to the notch lip. These dimensions prevented slipping or shearing. Holding the connectors in place during frontal rotation created torsional stiffness $k_{torsion}$ within the joints, based on equation (4-8). The shear modulus G was calculated using equation (4-9), where ν is Poisson's ratio, with a value of 0.48 for TPU [86]. As such, the shear modulus of TPU was calculated as 8.78 MPa. The polar moment of inertia J was calculated using equation (4-10) and determined to be 4410 mm^4 for the HM connector and 2210 mm^4 for the MF connector. The length was taken as the middle section exposed to torsion. However, given that the connector rails are made of flexible material, this length could be longer. Nonetheless, taking the solid middle section length of the connector was deemed to be an appropriate approximation. Given these values, the HM torsional stiffness was calculated as 210 Nm/° while the MF torsional stiffness was calculated as 105 Nm/°, both using equation (4-8). These values cannot be easily compared to anatomical stiffness for tarsal-metatarsal joints, given a lack of data on these joints. However, adding stiffness to frontal rotation was essential, given that anatomical behaviour would still present some resistance to rotation in this plane.

$$k_{torsion} = \frac{T}{\theta} = \frac{G \cdot J}{L} \tag{4-8}$$

$$G = \frac{E}{2(1+\nu)} \tag{4-9}$$

$$J = \frac{\pi \cdot D_O^4}{32} \tag{4-10}$$

Both connector dimensions and CAD drawings are provided in Appendix B.12.

4.1.2 Anthropometric Scaling and Ratios

Since the SLL should accommodate a large variety of limb sizes, SLL foot component dimensions were set to scale proportionally to FL (i.e. overall model block dimensions were defined as ratios of FL as a global variable). Joint locations, such as HM and MF spheres and pin heights, were also scaled proportionally. However, machined or purchased components were designed to accommodate all FLs without needing to be scalable (i.e. bolt, washer, nut, dimensions were fixed for all FLs). All three connectors were also designed as a fixed size acceptable for all FLs because the geometries were based on non-linear stiffness functions. As such, the connector stiffnesses were not designed to scale, given that the connectors were dimensionally fixed. Appendix B provides an overview of all component equations related to design scalability.

The mould used for the SR is based on a prosthetic foot cover CAD file provided by Össur™ and was also set to scale anthropometrically. However, while the main SLL components scale directly with FL, the mould and some mould features scale linearly with foot cover length rather than FL, including the mould length and supporting pin locations.

While the SLL foot was composed of 4 main blocks, the length was sectioned into three equal parts. The forefoot and midfoot combined length was a third of FL through allometric measurements [87]. The rearfoot was a third of FL, so that the SH joint could be located at a fourth of FL, recommended by ISO 10328:2016 standards [78]. The toe segment was one third FL, slightly longer than the difference between FL and arch length to fully house the ball of the foot [18].

Several CAD dimensions were reduced to enable proper fit inside the Össur prosthetic foot cover and allow even SR coverage. The foot width was kept constant at 22.2% FL to ensure every component fit properly in the mould. The forefoot, midfoot, and forefoot upper surface sloped down to fit inside the prosthetic foot cover. The forefoot and midfoot slopes were shared, while the toes slope was less pronounced.

4.1.3 Clearance

In engineering, "clearance is the distance for one object to clear another, or the clear space between them" [88]. Clearance must be considered in every manufacturing process since inaccuracies are inevitable. Clearance is a major factor for FDM processes because final product dimensions are highly sensitive to the cooling process (material shrinkage) or flow variations [89]. Unwanted nozzle motion can also affect model dimensions. FDM clearance depends on the material, printer, and settings used. As such, testing was required to understand the variability and to characterize the clearances created by specific 3D printer setups used in this thesis.

Since each FDM filament required specific settings, clearances for any design combining two or more different objects, 3D printed or otherwise, changed depending on the materials used. As such, each combination of filaments and material in this thesis were tested for their particular clearance characteristics.

Pylons with identical dimensions (10 mm diameter) were made using PLA, Nylon 230, and TPU (Figure 4-14a). Four sets of fused rings were made, two using PLA and two using Nylon 230 (Figure 4-14b). The two hexagonal ring sets were designed to mate with the pylons, while the smaller ring sets were tested with 3.25 mm diameter nails for the mould creation, and 3.175 mm (1/8") metal pins for general foot assembly. Each set of rings was designed with an increasing ring diameter (increments of 0.1 mm). The smallest rings were those nearest the hexagonal rings (Table 4-2). The hole dimensions were measured and recorded to contrast how materials behaved when 3D printed, showing dimensional inaccuracy in the inner diameter. The circles were imperfect, with bumps where the machine stopped, which created small overflow. These bumps reduced the minimal diameters, affecting clearance.

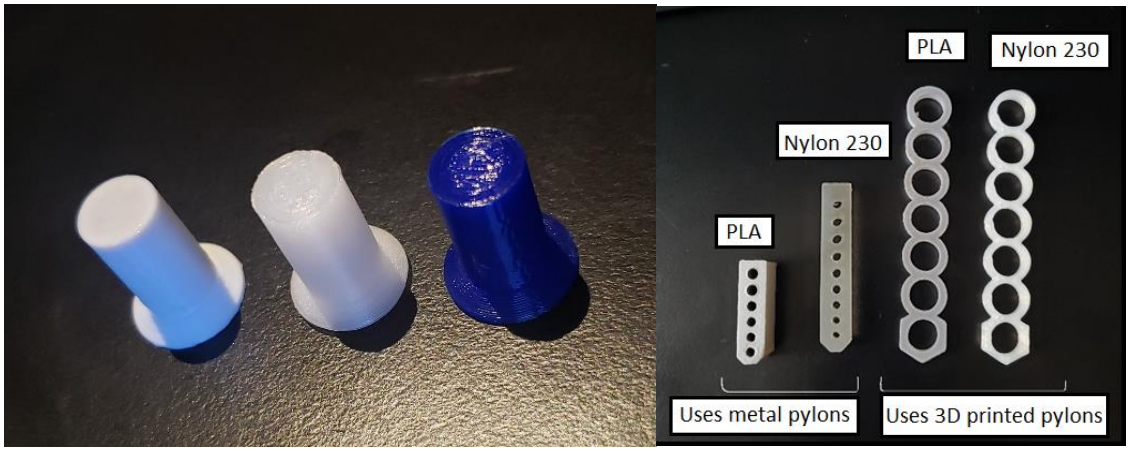

Figure 4-14: Clearance test components: PLA, Nylon 230 and TPU pylons (left), test rings (right)

TABLE 4-2: FDM CLEARANCE TEST RING DIAMETERS (ALL MM)

Hole	PLA-metal rings		Nylon-metal rings		PLA-pylon rings		Nylon-pylon rings	
	CAD	Measured	CAD	Measured	CAD	Measured	CAD	Measured
1st	3.25	2.88	3.175	2.41	10.1	9.63	10.1	9.80
2nd	3.35	2.97	3.275	2.52	10.2	9.69	10.2	9.88
3rd	3.45	3.12	3.375	2.63	10.3	9.95	10.3	9.92
4th	3.55	3.24	3.475	2.73	10.4	10.03	10.4	10.13
5th	3.65	3.29	3.575	2.92	10.5	10.25	10.5	10.23
6th	3.75	3.37	3.675	3.05	10.6	10.33	10.6	10.32
7th	-	-	3.775	3.17	10.7	10.38	10.7	10.39
8th	-	-	3.875	3.22	-	-	-	-
9th	-	-	3.975	3.26	-	-	-	-

Pylons and metal pins were inserted into each set of rings to find the best fit and which hole fit best was recorded. The hole number showed how much clearance should be added to CAD model connecting dimensions to reproduce the optimal fit for each material combination. These clearance values are reported in Table 4-3.

Table 4-3: Clearance value for each material combination

Connection type	Clearance required for best fit (mm)
Nylon-Nylon	± 0.5
Nylon-TPU	± 0.3
Nylon-Metal	± 0.7
PLA-PLA	± 0.6
PLA-metal	± 0.8

Since various material combination interfaces are used, each SLL CAD component was designed with several global variables that could be used to drive the dimensional requirements at these interfaces, based on clearances. Each main SLL block had three nylon-related variables: Nylon-Metal, Nylon-TPU, and Nylon-Nylon. The foot mould segments used to cast SR had two PLA-related clearance variables: PLA-Metal and PLA-PLA. Since future SLL production might use different FDM equipment, settings, or occur under different environmental conditions that would affect clearances, global variables enable fast and efficient changes to the whole CAD design that would accommodate these differences.

When designing connections between components, male part dimensions were reduced by half the clearance value for the particular material combination, while the related female dimensions were enlarged by half the clearance value, providing additional clearance between components. Splitting the clearance between the two interfacing components accommodated variations on both sides. However, metal components could not be modified. Therefore, female interface dimensions connecting to metal parts were widened by the full clearance factor.

Two examples are the HM and SH ball and socket diameters. The original HM diameter was 30.0 mm. Given a clearance factor of 0.5 mm for nylon to nylon, the ball diameter was reduced to 29.75 mm while the socket diameter was increased to 30.25 mm. The overall gap between the components was, therefore, 0.5 mm, split evenly across both features. For the SH ball and socket, the original diameter was 8.61 mm and the connection was metal ball in a nylon socket. As such, only the nylon socket diameter was increased to 9.31 mm, given a full clearance value of 0.7 mm.

In addition to affecting connections, several features related to the RoM were affected by material clearances. Abduction-adduction and dorsiflexion-plantarflexion angled surfaces on the midfoot were increased by the nylon-nylon clearance to ensure that no overflow affected maximum rotation. For the eversion-inversion guiding grooves in both the midfoot and forefoot blocks, nylon-metal clearance was subtracted from the desired range.

While most connecting components were affected by clearance, several model dimensions were not altered. Overall width, height, and length were not modified since small variations do not affect model

performance. The "heel plate-heel base" surface interface was not modified to account for clearance because the bolts create a tight connection regardless of differences in thickness. Appendix B shows all equations used for the CAD component models, showing how clearance was integrated.

4.2 Shank

The shank used a simpler design than the foot because the shank contains no articulations. The shank's structure was designed to have a core metal shaft, surrounded by a 3D printed cover representing typical calf geometry. A ball stud was threaded into the metal shaft's lower extremity, while the upper extremity was threaded into a test machine adapter, which in turn was connected to a test machine (e.g. Instron load testing machine). The metal components were machined or purchased according to design requirements.

4.2.1 Shank Ball Stud

The ball stud was a critical component for the SH joint, connecting the 3D printed foot to the metal shank. This piece consisted of a ball and neck, an integrated hex nut, and a threaded end (Figure 4-15). The threads meshed with the shank shaft, while the ball was secured to the rearfoot SH socket using heel plates.

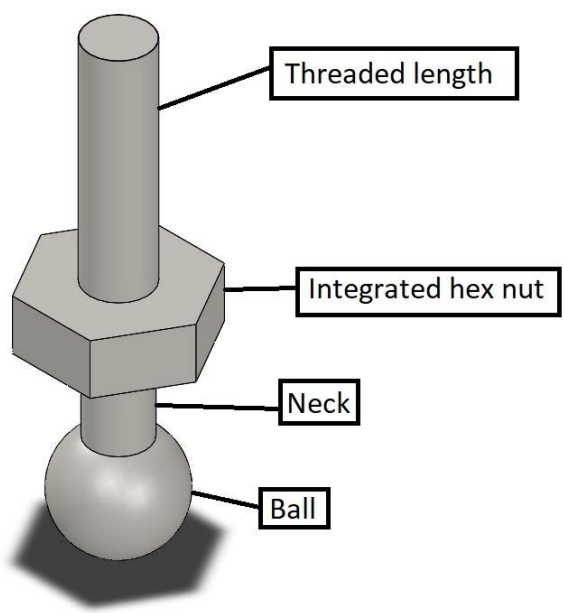

Figure 4-15: Ball stud features

The ball stud dimensions were evaluated to ensure that the ball stud dimensions could handle cyclic and static loads, as defined by section 3.3. Although the loads were applied at an angle, thread calculations assumed that the loads were axial. The thread's effective area was used to determine the appropriate thread size. Thread dimensions used the Unified National standards, while material strength was defined by the Society of Automotive Engineers (SAE) standards [77], [90]. The tensile stress area A_t was calculated using equation (4-11), where F_O was the overload force applied on the thread and σ_{proof} was the bolt's material proof strength, slightly lower than yield strength [90], [91]. The overload force was calculated using equation (4-12), where F_y was the axial force applied on the ball stud, defined in section 3.3 (static proof load of 1500 N) and a reasonable factor of safety (FS). For this application, the FS was set to 3, to ensure that the device could survive potential higher loading conditions. The calculated overload force was therefore 4500 N.

$$A_t = \frac{F_o}{\sigma_{proof}} \tag{4-11}$$

$$F_o = F_y \cdot FS \tag{4-12}$$

Ball studs available in the market are composed of carbon steel. However, the steel's grade was not provided. Therefore, the weakest grade was assumed: SAE grade 1. This steel has a proof yield strength of 33 ksi (227.5 MPa), a yield strength of 36 ksi (248.2 MPa), and an ultimate strength of 60 ksi (413.7 MPa) [90]. Using equation (4-11), the resulting minimum tensile stress area required was 19.78 mm^2. Anything equal to this or bigger was deemed acceptable and would handle the static proof load. To reduce sizing issues with the shank shaft, 5/16"-24 unified fine-pitch threads (UNF) were selected, with a tensile stress area of 37.42 mm^2 (0.058 in^2). The real stress and FS were calculated using the new area, giving a static axial stress of 40.1 MPa and a FS of 6.19 when using a yield strength of 248.2 MPa [90].

Fatigue calculations required a slightly different process, involving both the shaft and bolt. Since the bolt and surrounding material shared the load, calculating the load distribution (C_b) was important for determining fatigue stresses. The load distribution was determined by the two material spring constants: k_{bolt} for the bolt and k_{shaft} for the shaft. The bolt's weighted distribution was calculated using equation

(4-13). The surrounding shaft load distribution was calculated using equation (4-14) used to calculate shaft stress, ensuring that the load did not damage the shaft either.

$$C_b = \frac{k_{bolt}}{k_{bolt} + k_{shaft}} \tag{4-13}$$

$$C_s = 1 - C_b \tag{4-14}$$

Both spring constants were calculated using axial deflection beam theory, given in equation (4-15). The term A_s was the shaft area affected by the load, $E_{b,m}$ was the modulus of elasticity and l_t was the threaded length. A_s was set as a hollow circle of 1" outer diameter (25.4 mm), with an inner diameter of 5/16" (7.94 mm), as explained in section 4.2.2. SAE grade 1 steel bolt and shaft moduli of elasticity were assumed to be 200 GPa, [91]. The ball stud threads were shorter than the shaft internal threads. Therefore, only the ball stud thread length was considered for load calculations. Taking a threaded length of 17.30 mm (0.681"), the bolt's spring constant was calculated to be 432 MN/m, the shaft's spring constant was calculated as 5445 MN/m, both from equation (4-15). As such, C_b was calculated to be 0.074 using equation (4-13), and C_s was 0.926 from equation (4-14).

$$k_{bolt} = \frac{A_t E_b}{l_t}, \qquad k_{shaft} = \frac{A_s E_s}{l_t} \tag{4-15}$$

Bolt and shaft cyclic stresses were calculated using equation (4-16) and the load distribution. The alternating (F_a) and mean (F_m) forces, as specified by the cyclic loads in section 3.3 (Table 4-4), generated corresponding alternating (σ_a) and mean (σ_m) stresses. While some bolts are pre-loaded to create an initial force and stress affecting cyclic strength, the ball stud threads were not pre-loaded. Table 4-4 provides the resulting stresses for both the shaft and the ball stud's threads.

$$\sigma_a = C \cdot \frac{F_a}{A}, \qquad \sigma_m = C \cdot \frac{F_m}{A} \tag{4-16}$$

Table 4-4: Ball thread fatigue induced stresses

	Initial loads	Thread stresses	Shaft stresses
Alternating stress	640 N	1.26 MPa	1.30 MPa
Mean stress	690 N	1.36 MPa	1.40 MPa

Fatigue strength (FS_f) was then calculated using equation (4-17), where S_e was the endurance strength and S_{ut} was the ultimate strength.

$$FS_f = \frac{S_e(S_{ut})}{S_{ut}\sigma_a + S_e(\sigma_m)} \tag{4-17}$$

Endurance strength was difficult to determine for grade 1 steel, and therefore, was estimated as 15 ksi (105 MPa), lower than other grades given in literature (e.g. SAE grade 5 steel has an endurance strength of 18.6 ksi [91]). With an ultimate strength of 60 ksi (413.7 MPa), the resulting FS_f was 64.7 for the threads and 62.8 for the shaft, showing that the threads and the surrounding shaft should handle cyclic loads.

Another critical ball stud element was the neck connecting the ball to the integrated hex nut and threads, since this region was thinnest and would be a weak point. Buckling and bending were the two major factors that could affect the neck due to the angled force applied to the shank. The critical load that would induce buckling was calculated using equation (4-18) [91]. The loading condition term D, was set as ¼ given that the ball stud, along with the shank shaft, was under a free-fixed condition. The modulus of elasticity of carbon steel is 200 GPa, and for a neck diameter of 5.81 mm the moment of inertia I was calculated as 55.9 mm^4. The neck length l was measured as 6.55 mm, resulting in a critical load P_{cr} of 643 kN. Anything below this would not induce buckling, indicating that the ball stud is strong enough.

$$P_{cr} = \frac{D \cdot \pi^2 \cdot E \cdot I}{l^2} \tag{4-18}$$

The bending moment was calculated using equation (4-19) for static, alternating, and mean perpendicular loads, after breaking the loads into cartesian components. Then the corresponding bending stresses were calculated using equation (4-20), where the term r was the neck radius of 2.91 mm. The moments and stresses are listed in Table 4-4. The static FS was calculated as a ratio of yield strength to static bending stress, while fatigue FS was calculated using equation (4-21). The resulting static FS are listed in Table 4-5 for each condition, showing that the ball stud neck would survive the bending load.

$$M = F \cdot l \tag{4-19}$$

$$\sigma_{bending} = \frac{M \cdot r}{I} \tag{4-20}$$

$$FS_f = \left(\frac{\sigma_a}{S_e} + \frac{\sigma_m}{S_{ut}}\right)^{-1} \tag{4-21}$$

Table 4-5: Ball stud neck bending moment and stress

Loading condition	Bending moment (Nm)	Bending stress (MPa)
Heel static	2.5	132.1
Heel alternating	1.1	56.3
Heel mean	1.2	60.8
Forefoot static	3.4	174.5
Forefoot alternating	1.4	74.5
Forefoot mean	1.5	80.3

Table 4-6: Ball stud neck FS

Loading condition	Resulting FS
Heel static	1.88
Heel fatigue	2.39
Forefoot static	1.42
Forefoot fatigue	1.80

A quick disconnect ball stud was selected with 5/16”-24 UNF threads from Speedway Motors™ [92]. Ball stud details are provided in Appendix B.1.

4.2.2 Shank Shaft

The shaft was designed to connect the ball stud and the testing apparatus, as well as transfer the SLL load, akin to a shank. The shaft had both ends tapped with different thread sizes to connect the ball stud at the bottom and a threaded rod at the top (Figure 4-16).

The load was initially applied on the foot, on either heel or forefoot (Figure 3-2). In each case, the load was transferred through the ball stud into the shaft. The shank was treated as a cantilever beam with the proximal end fixed and unloaded, while the distal end was free to move and loaded. Due to the angled force, the shaft was subjected to both an axial load and a bending moment. The cantilever beam’s reaction forces and moment at the fixed end (point *w*) were calculated to ensure the axial and bending stresses were not destructive. These reaction forces are visualized as a 2D free-body diagram (FBD) in Figure 4-17.

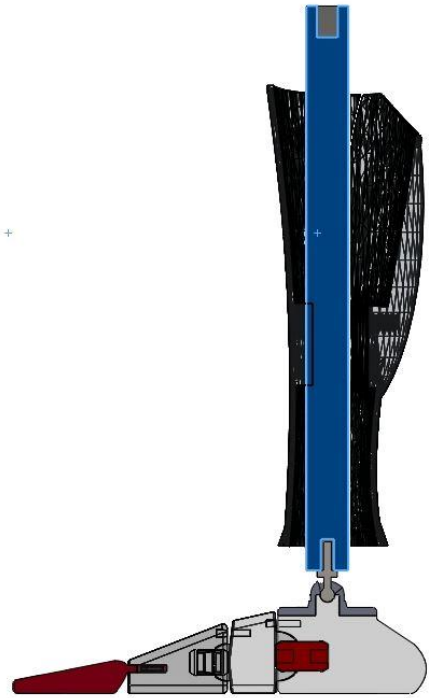

Figure 4-16: SLL cross-section with highlighted (blue) shaft

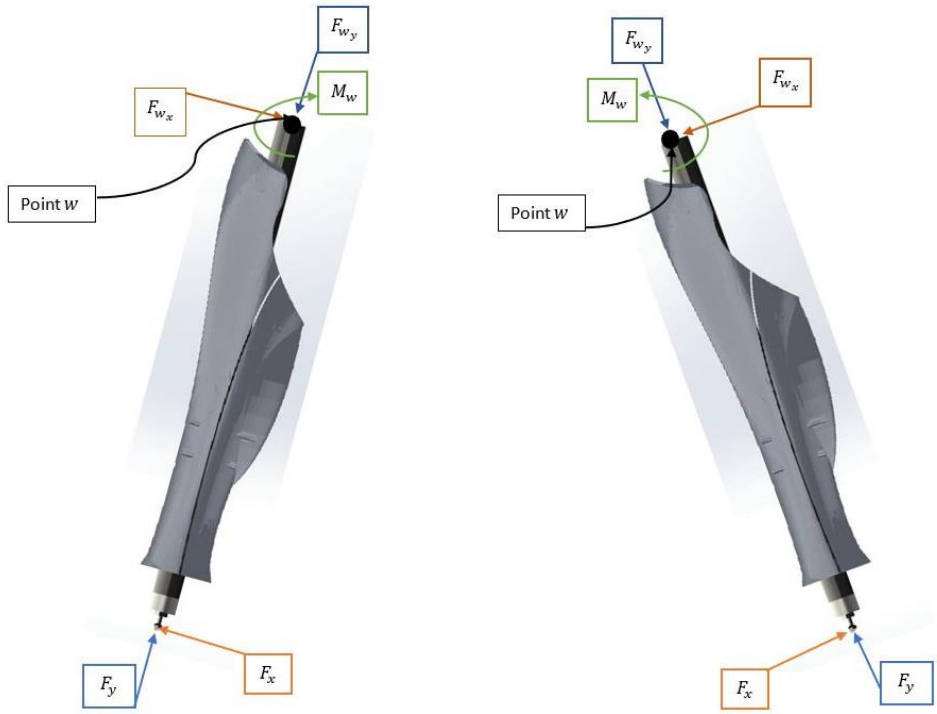

Figure 4-17: Shank FBD in heel position (left) and forefoot position (right)

The load components were calculated by dividing the load into Cartesian coordinates, using angle α for heel loads (15°) or ß for forefoot loads (20°) to create axial load F_y and radial load F_x. The moment was calculated by multiplying the radial load by the shaft length. This length was set as 13.5" (342.9 mm) so that when fully assembled, the SLL was taller than the AFO used for testing. Table 4-7 and Table 4-8 show the resulting forces and moments at the shaft's proximal end, at point w for static and cyclic loads.

Table 4-7: FBD calculation results for heel load conditions at point *w*

	Static	**Alternating**	**Mean**
F_{w_x} (N)	388.2	165.6	178.6
F_{w_y} (N)	1448.9	618.2	666.5
M_w (Nm)	133.1	56.8	61.2

Table 4-8: FBD calculation results for forefoot load conditions at point *w*

	Static	**Alternating**	**Mean**
F_{w_x} (N)	513.0	218.9	236.0
F_{w_y} (N)	1409.5	601.4	648.4
M_w (Nm)	175.9	75.1	80.9

With M_w and $F_{w_{x,y}}$ known, the axial stress was calculated using equation (4-22), while the bending stress was calculated using equation (4-20). Several shafts dimensions were assessed, and a 1" (25.4 mm) outer diameter was found to be acceptable. The FS were calculated using equation (4-23) [91], where σ_e was the effective stress, a combination of both axial and bending moment, used for static, alternating, and mean stresses. Table 4-9 shows the calculated stresses.

$$\sigma_{axial} = \frac{F_y}{A_s} \tag{4-22}$$

Table 4-9: Calculated SLL shaft effective stress created by common load conditions

	Axial stress (MPa)	**Bending stress (MPa)**	**Effective stress (MPa)**
Heel static	2.9	82.7	85.6
Heel alternating	1.2	35.3	36.5
Heel mean	1.3	38.1	39.4
Forefoot static	2.8	109.3	112.1
Forefoot alternating	1.2	46.7	47.8
Forefoot mean	1.3	50.3	51.6

The material chosen was cold-drawn 1045 steel, with an ultimate strength of 625 MPa [93]. The endurance strength S_e was calculated using equation (4-24) [91]. The term S_e' was the endurance limit for the test specimen, being half the ultimate strength (312.5 MPa). The k terms represented several factors affecting the endurance limit. The first two, k_a for surface condition and k_b for size modification, were calculated via equation (4-25) and (4-26), respectively. Given a cold-drawn metal, the terms of equation (4-25) were 4.51 for a and -0.265 for b, resulting in a surface factor of 0.819. Given a 25.4 mm diameter, the size factor was calculated to be 1.837. The term k_c was 1 for the primary load method, bending. The temperature factor k_d was also 1 since loading occurred at room temperature. The reliability factor k_e was provided based on several reliability goals, such as 50%, 95%, etc. For a reliability of 95%, the factor was 0.868. The final factor k_f represented miscellaneous effects [91]. Given that the shaft included threaded ends, a factor of 0.7 was selected to account for the stress concentrations. Given all factors, the endurance stress was calculated as 286 MPa, enabling FS_f to be calculated. All FS for the shaft are reported in Table 4-10, showing that the shaft should survive both static and cyclic loading.

$$FS = \frac{S_{ut}}{\sigma_e}, \qquad FS_f = \left(\frac{\sigma_{e_a}}{S_e} + \frac{\sigma_{e_a}}{S_u}\right)^{-1} \tag{4-23}$$

$$S_e = k_a k_b k_c k_d k_e k_f \cdot S'_e \tag{4-24}$$

$$k_a = a \cdot S_u^b, \qquad a = 4.51, b = -0.265 \tag{4-25}$$

$$k_b = 1.24 \cdot d^{(-0.107)} \tag{4-26}$$

Table 4-10: SLL shank shaft factors of safety created by common loading conditions

Loading condition	**Factor of Safety**
Heel static	7.30
Heel fatigue	5.24
Forefoot static	5.57
Forefoot fatigue	4.00

Another factor to consider for the shank shaft was buckling due to the load's compressive nature. The critical load P_{cr} was calculated using equation (4-18). Similarly to the ball stud neck, the loading condition was a free-fixed cantilever beam, resulting in a D factor of ¼. The modulus of elasticity of American Iron

and Steel Institute (AISI) 1045 steel is 206 GPa [93]. With a moment of inertia of 20400 mm^4 and a length of 13.5" (342.9 mm), the critical load was found to be 88.3 kN, showing that buckling would not be an issue for the SLL during testing. The shank shaft's details are shown in Appendix B.2

4.2.3 Top Adapter

The SLL required a secure connection to the testing apparatus, an Instron hydraulic servo frame model 1332. The shaft's upper end connected to a top adapter and supporting collar, while the foot segment rested on a moving plate adapter (further discussed in section 4.2.4), as shown in Figure 4-18.

As discussed in section 3.2.2, positioning the SLL at specific angles was an essential component of load testing. As such, the top adapter was designed with angled surfaces providing two options for proper arrangement: 15° for the heel position and 20° for the forefoot position (Figure 4-19). The shank shaft connected to these angled surfaces through a threaded rod perpendicular to the angled surfaces.

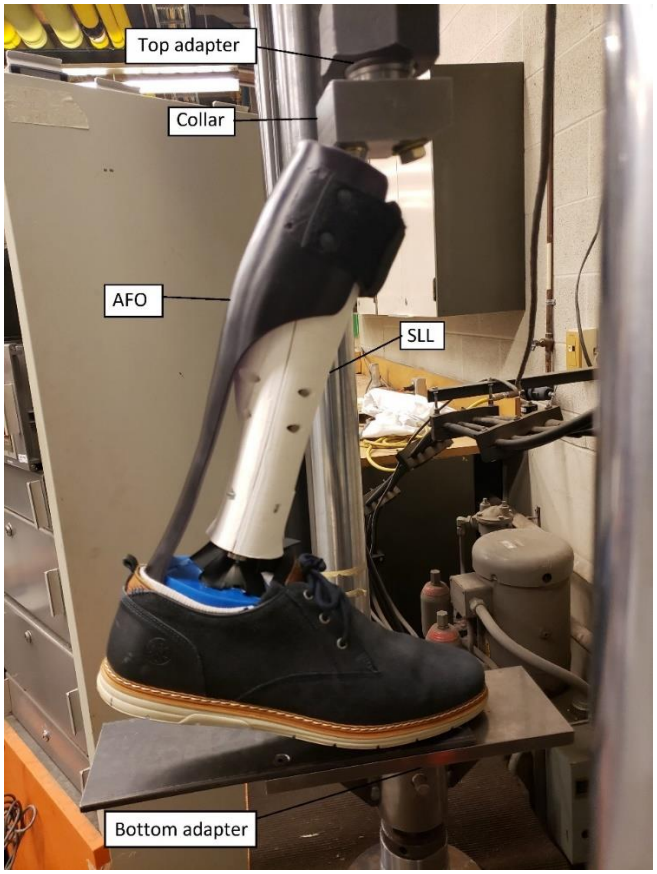

Figure 4-18: SLL on the testing apparatus in the forefoot position

Figure 4-19: Instron-SLL top adapter, with angled surfaces

The adapter was made to be 2” (50.8 mm) in diameter so that the shank shaft was completely supported on either angled surface. The adapter’s upper section was designed thinner, to be inserted inside the Instron pylon. A pin secured the adapter to the Instron socket. A 2”-4½ unified national coarse threads (UNC) hex nut was threaded to the adapter’s lower half to keep the adapter in place. A thread relief was inserted to ensure the angled surfaces were not affected. The adapter was machined using 44W hot rolled steel.

To distribute the bending load to the shank shaft and threaded rod safely, two supporting collars were designed with the top adapter (Figure 4-20). These collars sat below the adapter, with a circular socket for the angled surfaces. The collars included two angled holes, one for the shank shaft and one for a bolt to lock the collar to the adapter. The bolt sat on an angle surface parallel to the adapter angled surface to get uniform tension. One collar was made for the shaft in the forefoot position and the bolt on the other side, while a second collar was made for the shaft in the heel position due to the bolt and shaft diameter differences. CAD drawing for the top adapter is shown in Appendix B.4 and collars details are shown in Appendix B.6.

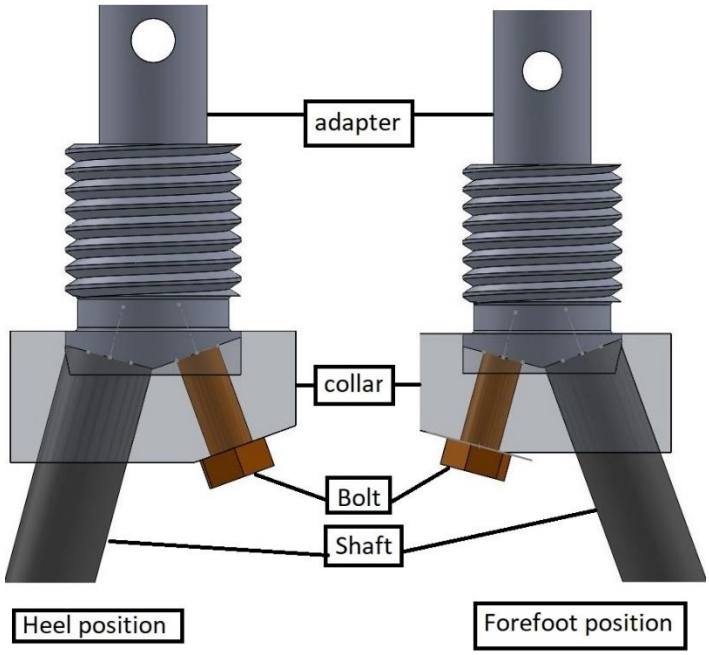

Figure 4-20: Top adapter and collar in both heel and forefoot positions

A ½”-13 UNC threaded rod 1.5” in length made from SAE grade 8 steel was used to connect the adapter to the shank shaft. A bolt with matching threads and metal was used for securing the collar to the adapter.

4.2.4 Bottom Adapter

The SLL foot components needed to be loaded by the Instron evenly. To do so, a plate adapter was designed to fit with the Instron’s lower pylon. The bottom adapter required a secure connection to the Instron pylon while offering a flat surface to apply the forefoot or heel position loads.

Unlike the top adapter, which was inserted inside the Instron pylon, the bottom adapter fit above the Instron pylon. A pin secured the adapter to the Instron pylon in a similar fashion to the top adapter. The adapter involved three main elements (Figure 4-21): tubing connected to the Instron pylon, a plate with appropriate dimensions to hold the foot in both forefoot and heel positions, and gussets to ensure appropriate strength and minimize deflection. Cold drawn 1018 steel was chosen due to its welding properties.

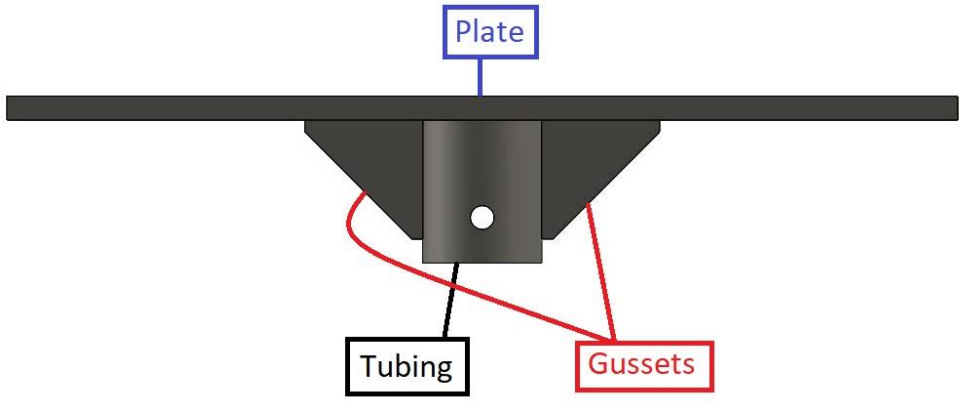

Figure 4-21: Plate adapter with highlighted features

The tubing section, initially a solid rod, was welded to a plate with triangular gussets, then hollowed out to fit the Instron pylon. This sequential fabrication mitigated welding warping. The plate width was 4" (101.6 mm) to ensure that the foot's full width would be supported by the plate width, given that the SLL foot measured 95.82 mm wide. Geometric calculations were done to measure the minimum plate length using the SLL dimensions, from the shaft's top to the foot loading point in either position. The reference lengths (Table 4-11) were positioned with the top adapter angled surface dimensions, aligned to the plate's centre to find the furthest distance (Figure 4-22). The heel loading distance, at point A, was 155.85 mm away from the adapter centre, while the forefoot distance, at point B, was found to be 200.78 mm from the plate centre. To ensure the foot load was not on an edge during loading, the plate was set 254 mm (10") from the centreline in one direction, with the adapter able to rotate to match loading positions and reduce costs. After consultations with the University of Ottawa machine shop, a plate thickness of ½" (12.7 mm) was used to mitigate upward curling due to gusset welding. The bottom adapter CAD drawings can be found in Appendix B.5.

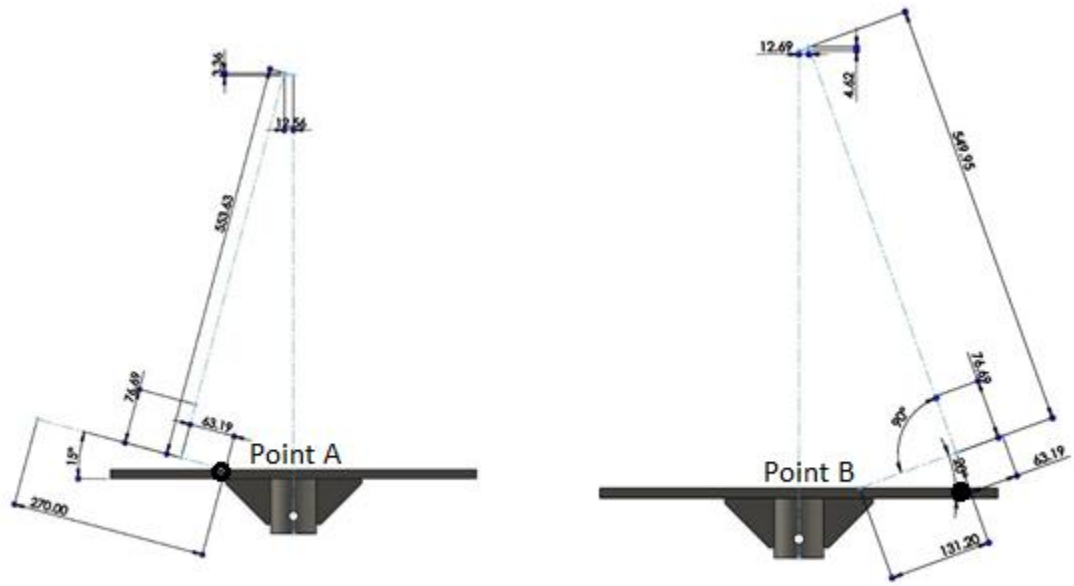

Figure 4-22: Bottom adapter with heel and forefoot reference sketches

Table 4-11: SLL measurements for bottom adapter references

	Forefoot load (mm)	**Heel load (mm)**
SLL X distance	131.20	63.19
SLL Y distance	549.95	533.63
Adapter x distance	12.69	12.56
Adapter y distance	4.62	3.36

The maximum bending stress at the gusset-tubing edge was calculated to ensure that the dimensions were adequate for the application. The bending moment along the adapter length (M_r) was calculated using equation (4-27), where F was the force and l was the length. Taking a static force of 1500 N (selected in section 3.3) and the furthest load length, point B to the gusset edge, 169.09 mm, the moment was calculated as 254 Nm.

$$M_r = F \cdot l \tag{4-27}$$

The bending stress was calculated using equation (4-28) where y_c was the centroid height and I_t was the maximal moment of inertia for both the gusset and plate combined. The centroid height was calculated using equation (4-29), using a weighted ratio of both gusset and plate centroids (Figure 4-23) [94]. The

gusset and plate dimensions (Table 4-12) resulted in a centroid height of -2.72 mm from the origin, located at the plate-gusset intersection (Figure 4-23). The total moment of inertia was calculated as 598,797 mm^4 using equation (4-30) [94] and adapter cross-sectional dimensions. A maximum stress of 25.7 MPa was calculated and was found to be located at the gusset's lowest point (y = -63.5 mm). Given that cold drawn 1018 steel has a yield stress of 370 MPa [88], the resulting FS was calculated as 14.4, showing that the plate adapter would handle SLL testing loads.

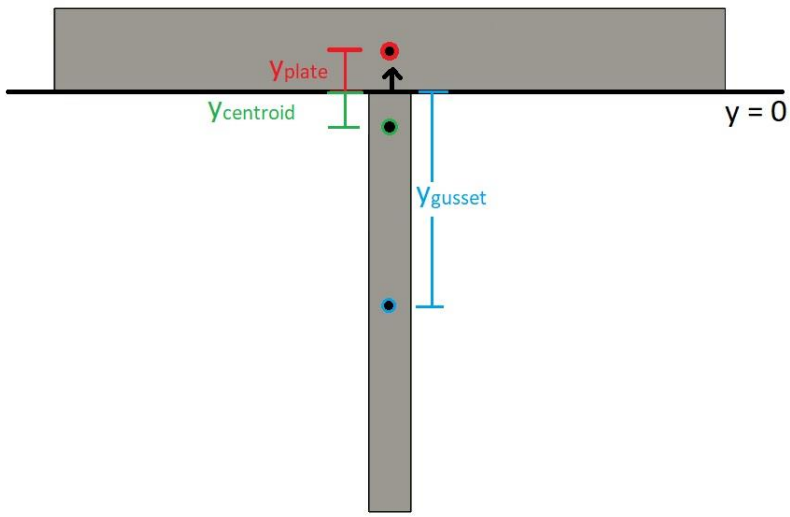

Figure 4-23: Bottom adapter cross-section at weld

Table 4-12: Bottom adapter geometric factors

	Gusset geometric factors	**Plate geometric factors**
Centroid height (mm)	-31.8	6.4
Area (mm^2)	403.2	1,290.3
Moment of Inertia (mm^4)	13,492.0	17,343.0

$$\sigma_b(y) = \frac{M_r(y - y_c)}{I_t} \tag{4-28}$$

$$y_c = \sum y_n \cdot A_n = \frac{y_g A_g + y_p A_p}{A_g + A_p} \tag{4-29}$$

$$I_t = I_g + A_g \cdot (y_g - y_c)^2 + I_p + A_p \cdot (y_p - y_c)^2 \tag{4-30}$$

4.2.5 Shank Cover and Components

While the shank shaft offered strength, another solution was required to recreate the shank's anatomical geometry. A shank cover was included in the design to provide the required shape. An open-source shank cover CAD file was obtained from Thingiverse [96] and modified to provide two halves, secured by bolts to the shank shaft (Figure 4-24).

Figure 4-24: Open-source shank cover CAD model

Since the load was supported by the shank shaft, the cover only bore the load created by the AFO's stiffness, transferring the force to the shaft. Given that AFO stiffness and load are intended to be low and not injure users, the shank was not designed around this load. Therefore, cover geometry was the only relevant factor. The initial geometry was slightly modified to allow a better connection to the shaft (Figure 4-25).

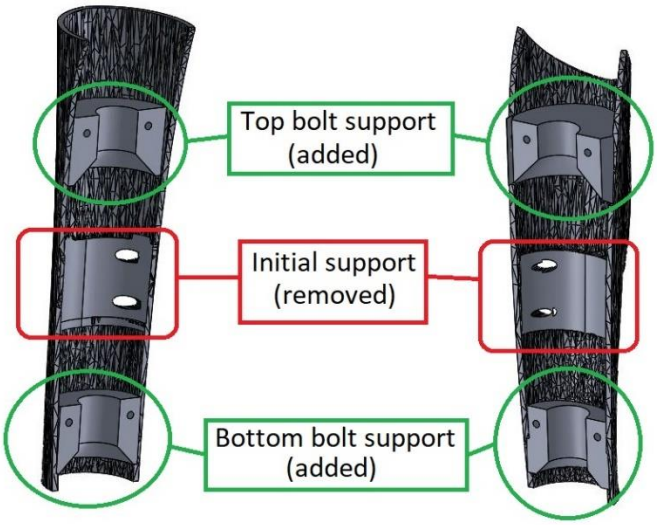

Figure 4-25: shank cover with modifications highlighted

The shaft connection areas, where bolts were inserted, were changed to be closer to the knee and ankle ends of the shank cover, preventing cover rotation during testing. The original connecting section was removed. The upper and lower supports were 40 mm thick each, with a 45° slant for easy FDM fabrication (Figure 4-26). These bands had a central half circle cut measuring 12.7+0.3 mm in radius to accommodate the shaft.

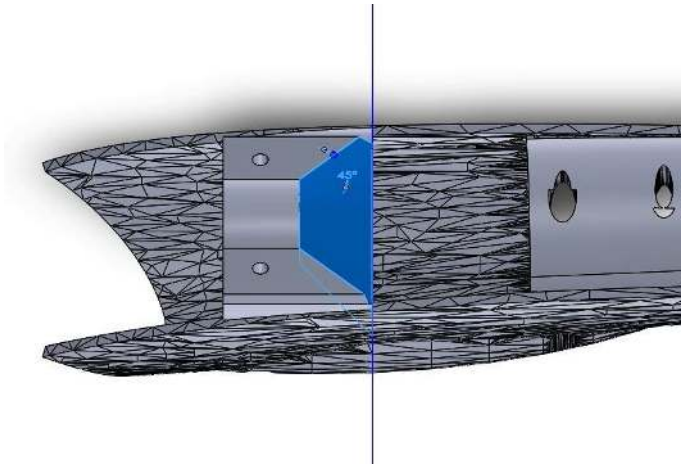

Figure 4-26: Shank cover back interior

The bands included two holes for bolts to secure the two halves together. On the front cover, these circular holes were enlarged to accommodate the bolt heads, while the back cover included hexagonal holes to hold nut during tightening. Full cover dimensions are provided in Appendix B.3.

4.3 Rearfoot

The rearfoot connected the shank to the forefoot. This section supported the ball stud, allowing SH rotation, and was designed to absorb heel loads. The rearfoot supported the SH and HM joints. To properly secure the SH ball stud on the top, the rearfoot was designed as three separate components, including the heel base, front-heel plate and back-heel plate (Figure 4-27). The three were secured using bolts and a zip-tie to prevent separation.

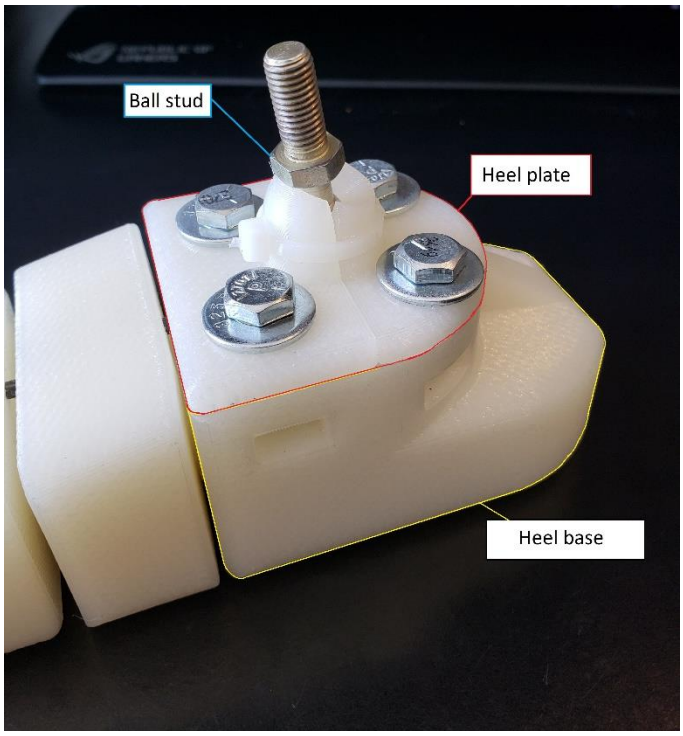

Figure 4-27: Rearfoot components

4.3.1 Heel Base

The rearfoot's main component was the heel base, which housed both the SH and HM sockets (Figure 4-28). The base was designed to support the entirety of the vertical load during testing. The heel base was designed to feature a long and sturdy rounded lower half to mimic the calcaneal tuberosity (point A) enabling realistic heel strike loading. The tuberosity was supported by a gusset (point B) connecting the

tuberosity to the main body, reducing stress concentrations between the upper and lower halves. Both upper and lower halves had rounded posteriorities to replicate the heel's rounded back.

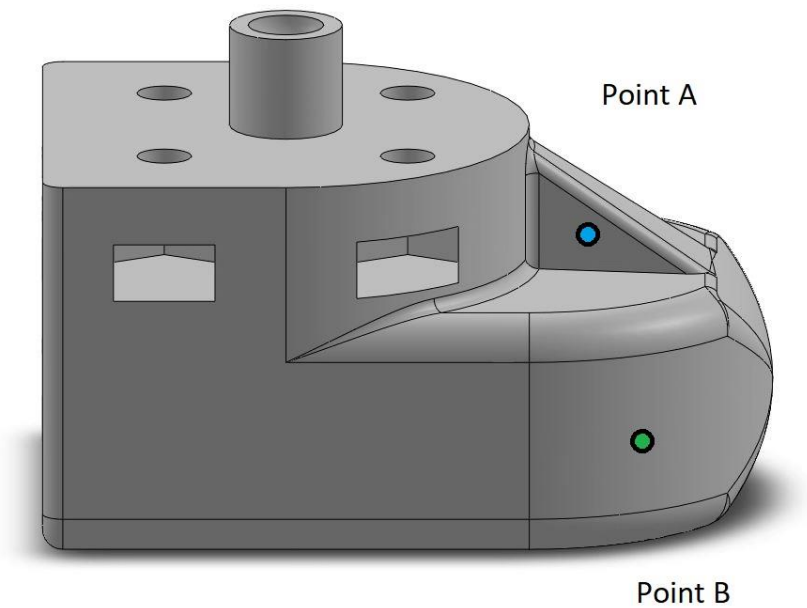

Figure 4-28: Heel base

On the heel base's anterior surface, a socket was created to house the HM joint (Figure 4-29). The socket diameter was set to match the ball diameter, further discussed in section 4.4.1. To accommodate the 1/8" (3.175 mm) eversion-inversion guiding pinhole above the socket and to have enough material surrounding the joint, the socket was set at $FL/36$ from the heel base sole. Centred inside the socket was another hole dimensioned to accommodate one half of the HM annular connector. The hole slightly tapered outward to enable rotation.

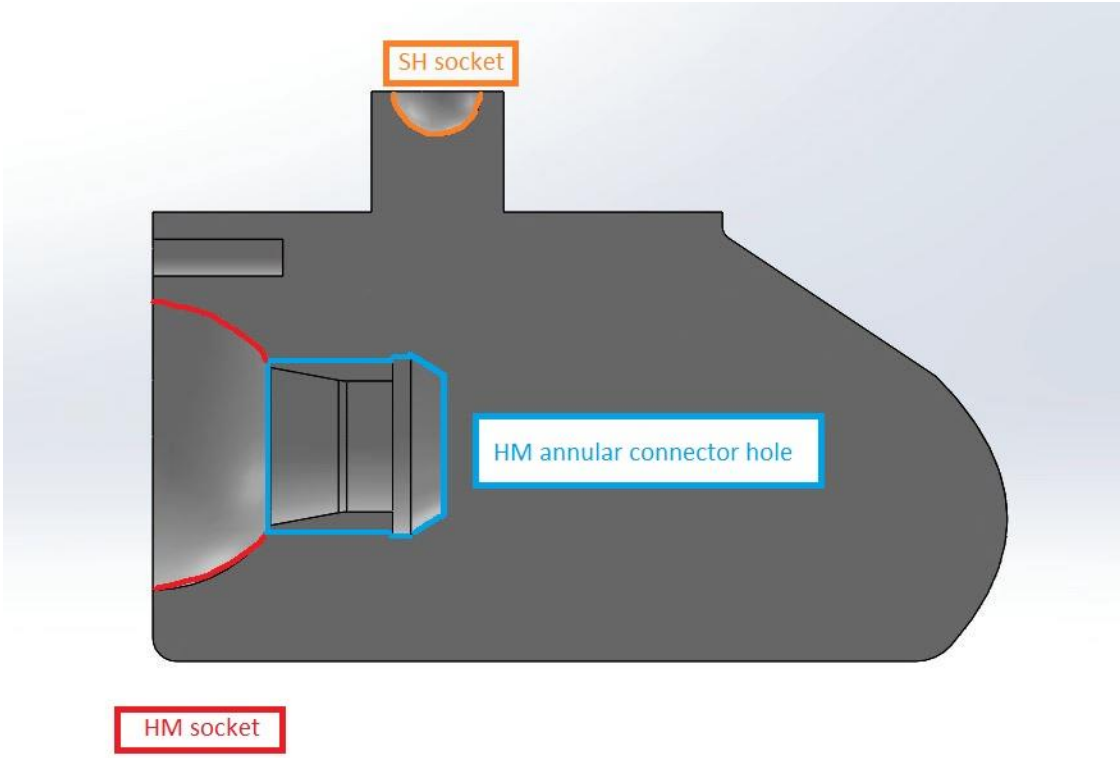

Figure 4-29: Heel base CAD model cross-section with sockets highlighted

The SH socket was elevated above the main body to ensure that the ball stud and shank shaft did not interfere with the heel base during rotation. This elevation was created by a stem centred on the upper section, wide enough to have the socket surrounded by 2.3 mm of material all around. To account for the SR creating a sole underneath the heel base, the SH joint height was set to $FL/4.5$, lower than anthropometric measurements (26% FL [18]). The SH joint was also set to $FL/4.5$ away from the calcaneus tuberosity length-wise to accommodate the SR, which would bring the total length to $FL/4$, a ratio provided by ISO 10328:2016 [78]. On the heel base upper section, four holes and hexagonal insertion grooves were created to house bolts and hex nuts, discussed in section 4.3.3, which secured the heel plate to the base. These holes were located at equidistant points from the SH stem, scaling with the entire segment. CAD drawing and scaling ratios are provided in Appendix B.7.

4.3.2 Heel Plate

The heel plate was designed to prevent the SH ball from being dislocated and limit rotation determined by anatomical data (Figure 4-30). As such, the heel plate consisted of a hollow hemisphere with the SH tapered opening, discussed in section 4.1.1.1. The hemisphere's inner diameter matched the ball stud's diameter plus Nylon-Metal clearance, while the outer diameter was set at 10.11 mm to fit below the ball stud's nut. This hemisphere was integrated with a plate having an identical profile as the heel base upper section through a hollow tube. Given that this tube surrounded the heel base SH stem, the inner diameter matched the stem's outer diameter, while the outer diameter matched the hemisphere outer diameter.

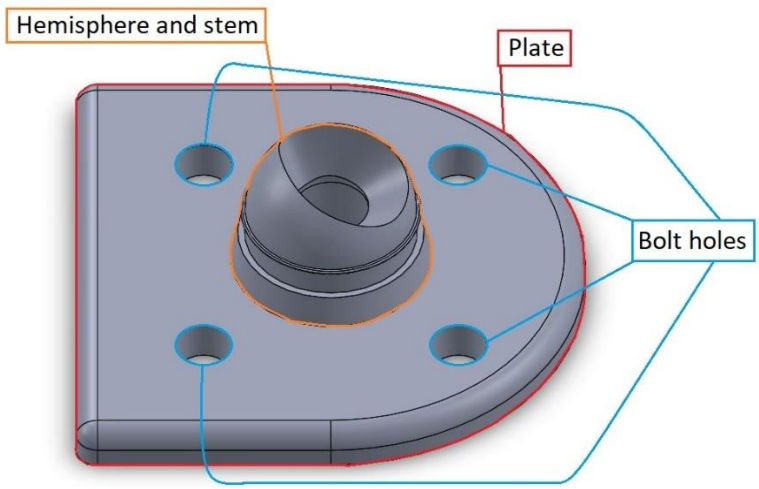

Figure 4-30: Heel plate features

To secure the heel plate around the ball stud and its integrated hex nut, the heel plate was split along the frontal plane, creating front and back sections. To prevent the two halves from splitting apart under load, a groove was added on both halves for a zip-tie to be installed near the hemisphere (Figure 4-31). This groove included a small notch at the top to keep the zip-tie in place, while the hollow tube widened slightly below the groove. The groove height matched the zip-tie's width of 3.50 mm. Heel plate CAD drawings and scaling ratios are provided in Appendix B.8.

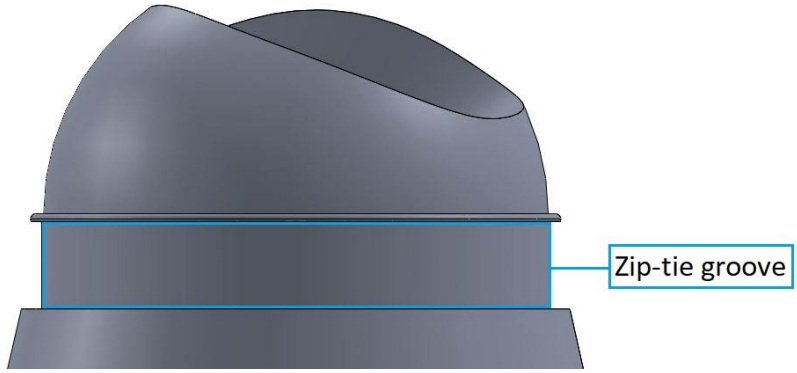

Figure 4-31: Heel plate zip-tie groove

4.3.3 Heel Plate Bolts, Nut, and Washers

Four bolts and hex nuts were introduced to secure the heel plates to the heel base. Two bolts held each heel plate half (Figure 4-30). Calculations were done to ensure that the bolts would survive expected loads. Since the load applied on the bolts came directly from the heel plate, which held the ball stud in place, the load was primarily perpendicular to the bolts. As such, shear resistance was verified. Given that two bolts held the heel plate at any given time, the perpendicular force F_x was assumed to be shared equally between the bolts. The shear stress was calculated using equation (4-31) for static, alternating, and mean loads.

$$\sigma_{shear} = \frac{F_x}{A_{bolt}} \tag{4-31}$$

¼”-20 bolts were selected with a minor diameter of 0.1887” (4.793 mm) [90]. The area was determined based on the bolt minor diameter. The calculated stresses are listed in Table 4-13 for each loading condition. Similar to the ball stud neck, the static FSs were taken as a ratio of yield strength, while the fatigue FSs were calculated using equation (4-21). SAE grade 5 bolts were the most widely available bolts, which had a yield strength of 92 ksi (634.3 MPa), an ultimate strength of 120 ksi (827.4 MPa), and an endurance strength of 18.6 ksi (128.2 MPa) [90]. The resulting FSs are listed in Table 4-14, which showed that the bolts would work great for this application.

Table 4-13: Shear stress on heel plate bolts

Loading condition	Shear Stress (MPa)
Heel static	10.8
Heel alternating	4.6
Heel mean	4.9
Forefoot static	14.2
Forefoot alternating	6.1
Forefoot mean	6.5

Table 4-14: Heel plate bolt FSs

Loading condition	Factor of Safety
Heel static	59.0
Heel fatigue	23.9
Forefoot static	44.6
Forefoot fatigue	18.1

4.3.4 Ankle Elastic

While the heel plate limited SH joint rotation, another solution was required to provide joint stiffness. For this, four elastics were introduced, one end attached to the shank shaft using a hose clamp while the other end secured underneath the heel plate bolts (Figure 4-32). Washers were added to the heel bolt to maximize the area holding the elastic in place. The elastic bands were extended from the washer's distal edge to increase each elastic's moment arm.

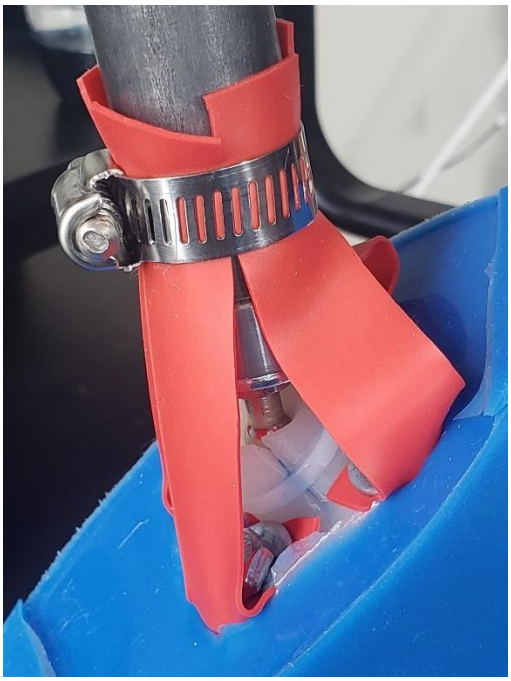

Figure 4-32: SH elastics with hose clamp

Each elastic band were cut from extra-heavy resistance bands made by Haquno [97], having a resistance of 10.4 N/mm, measured experimentally. This stiffness was selected for its ability to hold the weight of the foot. The four elastics covered the shaft's circumference, separated by a small gap to prevent overlap. Since the shank shaft circumference divided by four is 19.95 mm, each elastic's width was 19.05 mm (3/4"). The full elastic length was 82 mm, so that 50 mm would stretch, while 12.7 mm (1/2") length was held by the hose clamp and 19.05 mm (3/4") length was secured by the washers. A hole was cut in the centre of the bottom section of each elastic to allow bolt insertion.

4.4 Forefoot Blocks

The SLL's forefoot was designed using three segments: the midfoot, the forefoot, and the toes. These segments were designed to transfer forces from the ground to the shank during loading. Connectors were inserted inside each segment to prevent separation and to reproduce maximum anatomical rotation angles.

4.4.1 Midfoot

The midfoot simulated the tarsals and incorporated the ball aspects for both the HM and MF joints (Figure 4-33). As discussed in section 4.1.1.2, the midfoot involved several motion-defining features. The segment also partially housed the HM and MF annular snap-fit connectors, which held the balls in their sockets.

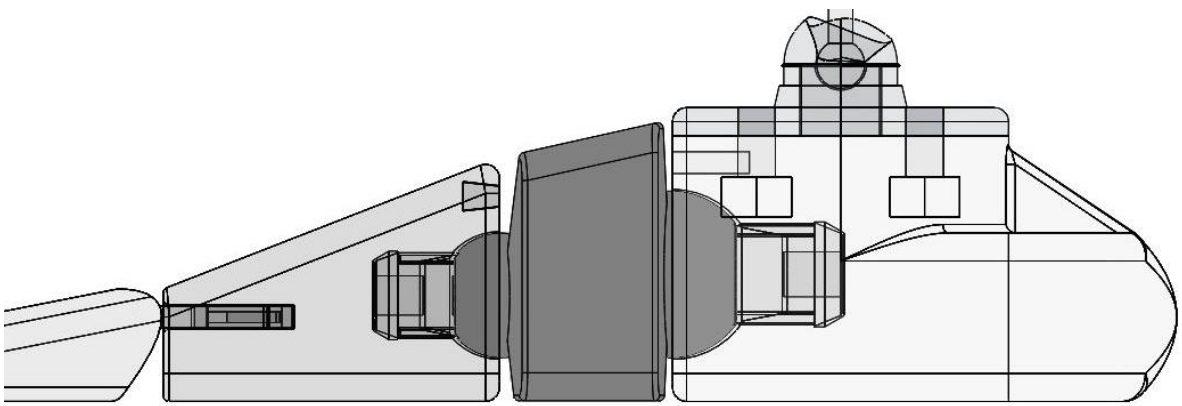

Figure 4-33: Midfoot in SLL assembly

The midfoot plus forefoot length was set to $FL/3$ [87], with the midfoot being shorter, matching the short cuneiform bone lengths. As such, the midfoot length was set to $FL/9$ to ensure that the internal features did not overlap. The midfoot and forefoot heights were designed to slope down, as per their respective anatomy. After measuring prosthetic foot covers, the maximum midfoot height was set to 50 mm, scaling with a ratio of $FL/5.4$, sloping down to a max toe height of 20 mm, with a ratio of $FL/13.5$. The lower midfoot height was extrapolated from the total forefoot-midfoot length to create an appropriate slope. From equation (4-32), the slope required a decrease in distal height of 6.7 mm, at a ratio of $FL/40.5$, from the upper surface as illustrated in Figure 4-34, point A.

$$\frac{FL/13.5}{FL/3} = \frac{X}{FL/9}, X = FL/40.5 \tag{4-32}$$

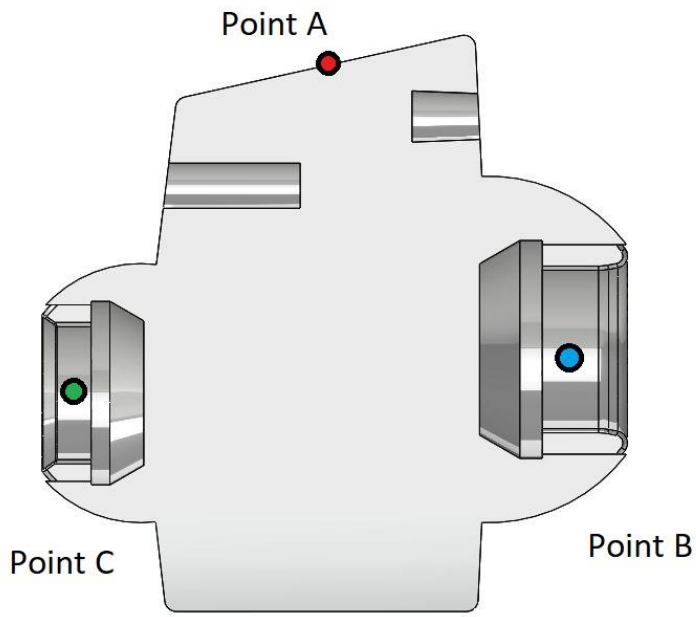

Figure 4-34: Midfoot cross-section

Both balls were centred on the foot width and had their lowest point $FL/36$ above the sole to ensure enough material would support the joint. The ball diameters were set to be slightly more than half the midfoot heights to account for the surrounding material and the inversion-eversion pins above the spheres. The HM ball diameter was set to a ratio of $FL/9$ minus Nylon-Nylon clearance, while the MF ball diameter ratio was $FL/12$ minus Nylon-Nylon clearance. Centred on the ball, a hole was created inside the balls for the annular snap-fit connectors, shown by point B and C in Figure 4-34. The annular snap-fit connector insertion holes matched the connector dimensions, enlarged by the Nylon-TPU clearance, as discussed in section 4.1.3. Midfoot CAD drawing and scaling ratios are provided in appendix B.9.

4.4.2 Forefoot

The forefoot was designed as a connecting block between the midfoot and the toes, mimicking the anatomy of the metatarsals (Figure 4-35). The forefoot segment housed the MF socket on the proximal surface (point A) and a hole with locking leaflets for the FT joint cantilever snap-fit connector on its distal end (point B). A guiding groove was set above the MF socket to control the joint's frontal rotation (point C).

The block length was set to $FL/4.5$ so that the combined midfoot-forefoot length was $FL/3$. The forefoot was longer to better replicate the metatarsal lengths. The maximum height was set to $FL \cdot \frac{13}{81}$ to properly match the midfoot's lower height calculated by equation (4-32).

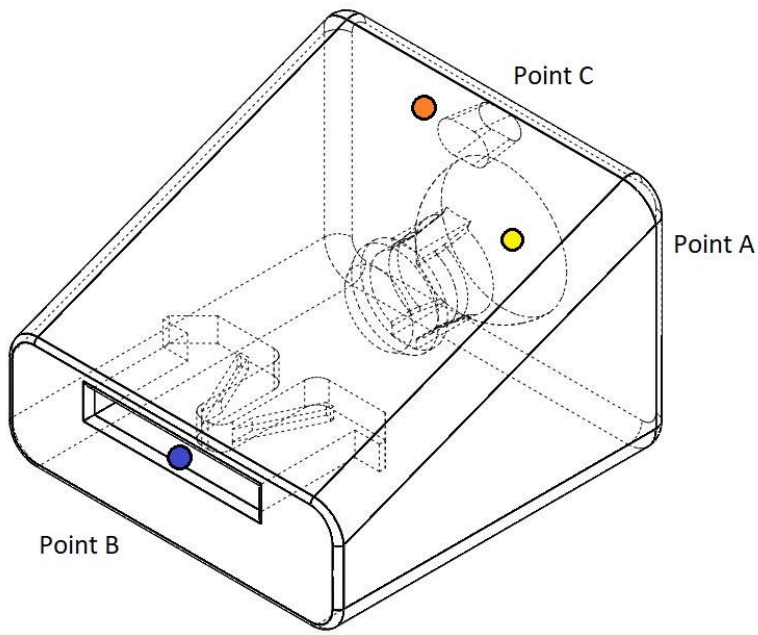

Figure 4-35: Forefoot segment mesh view

On the proximal surface, a socket was created, centred with the MF ball (Figure 4-35 point A), highlighted in section 4.4.1. This socket's diameter matched the ball's diameter plus Nylon-Nylon clearance, accounting for dimensional inaccuracies. Like for the HM joint socket in Figure 4-29, the MF socket extended internally for an annular snap-fit connector. The hole's dimensions matched the connector's dimensions, enlarged by the Nylon-TPU clearance. The hole tapered outward near the extremity to allow bending of the connector to occur during socket rotation.

To house the FT connector, a rectangular hole was created at an appropriate height. This hole extended to match the two cantilever snap-fit connectors (Figure 4-35 point B). However, to enable the connectors to fully go through the holes, the hole was enlarged for each beam and notch. To prevent the connectors from slipping out once inserted, a locking leaflet was placed on each side (Figure 4-36 Point D and E).

To lock the connectors in place, the leaflets bent internally during initial insertion, then returned to their original positions once the connectors slipped into place. The leaflets were set on the internal walls nearest to the foot midline, in the middle of the connector hole. The dimensions were dictated by the available space inside the FT connector hole, avoiding being too close to the internal surfaces since the leaflets could accidently fuse with other internal surfaces due to 3D printing dimensional variation issues. To ease bending, the leaflets were angled 25° away from the interior walls, enabling a deflection of 4.42 mm, equivalent to the connector notch length. The angled surface also helped guide the connector fully into the hole. All forefoot dimensions and scaling ratios are provided in Appendix B.10.

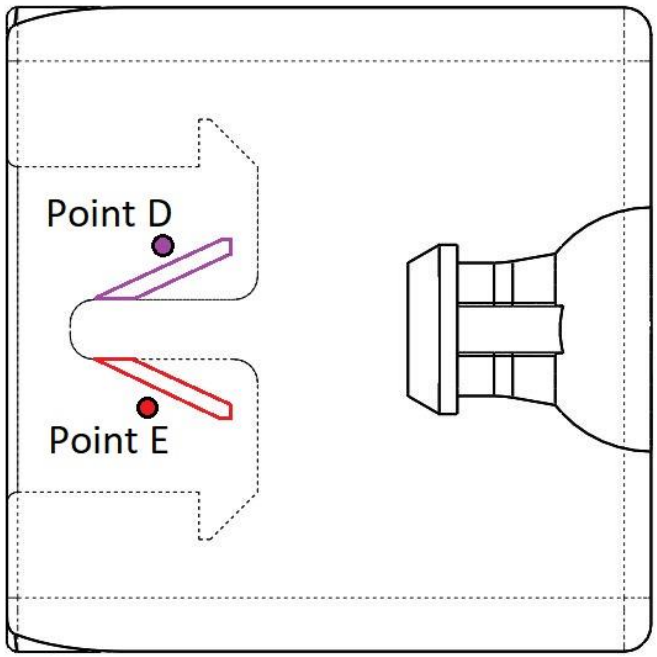

Figure 4-36: Forefoot mesh top view

4.4.3 Toes

The toe segment was designed to enable FT joint rotation and represent the phalanges (Figure 4-37). This segment was designed to have the hallux separated from the other smaller toes, matching the design of many prosthetic foot covers (e.g. the FSTM26R provided by Össur™). This separation served two purposes: this design enabled a wider array of footwear to fit the SLL, and the hallux could reproduce more

accurately certain behaviours such as foot pivoting or turning if desired. The whole segment required flexibility to enable the toes to bend, which would replicate the interphalangeal joints. As such, the segment was designed with TPU, a flexible FDM filament (further explained in section 5.1.2). To reduce complexity, the FT connector was integrated with the toe segment design (Figure 4-37 point A). The toes also included a curved surface which helped control the rotation according to desired anatomical rotations (Figure 4-37 point B).

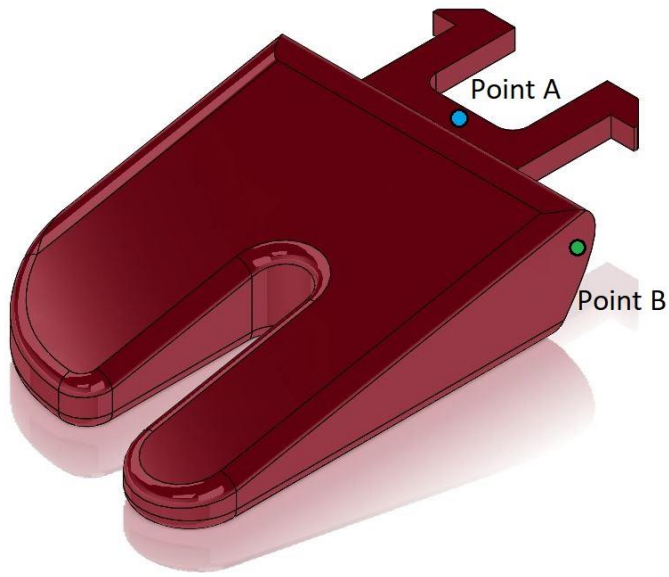

Figure 4-37: Toe segment

The main body had a sloped top, replicating anatomy. The maximum proximal height was set to $FL/13.5$, matching the forefoot's minimal height. The smallest height was set to $FL/42.7$ while the main segment length was set to $FL/3.86$, both enabling proper fit in the prosthetic foot cover. Appendix B.11 highlights all toe dimensions, scaling equations, and CAD drawings.

4.5 SSL Foot Shell

To encapsulate the inner foot structure, soft tissue needed to be emulated with a material that could withstand repeated loading [14]. Therefore, the shell material required compliance to allow the foot joints to move appropriately, while remaining structurally sound during cyclic loading. Furthermore, the foot shell provided an anatomical structure to accommodate the AFO and shoe.

4.5.1 Silicone Rubber

Two material types can emulate the mechanical properties of soft tissue: elastomers and gelatinous substances. Gelatinous substances such as gelatine allow good skin density, can withstand high speed impact, but are less representative of skin behaviour at low speeds [14]. Agar is occasionally used but is not stable for long durations. Elastomers such as SR and polyurethane are more durable with the desired density, hardness, and malleability. SR can be obtained in a form that has a closer stiffness to soft tissue than polyurethanes [98], and therefore, was chosen as the shell material for this study.

Hardness was a major criterion when selecting the proper silicone. While the sole's soft tissue ranges from Shore 00-20 to 00-30 [15], a harder silicone was chosen to help endure cyclic loads. While skin is soft, the organ has regenerative properties to repair damage after loading. Because SR is not self-healing, a harder material were required. As a result, 30 A hardness was chosen as a medium level between compliance and hardness. Smooth-On™ products were selected for their worldwide availability and their large selection of SRs and polyurethanes. Platinum cure SRs were chosen for their durability. Mold Star 30™ was chosen for its hardness, while being simple to use during moulding and without requiring special equipment for curing. Two components were mixed at equal volume, to cure and solidify into the appropriate shape. The chosen SR did not require degassing due to its lower viscosity, mitigating trapped air bubbles. The chosen SR also cured at room temperature, which reduced thermal complications for the mould and internal components. Mold star 30™ also provides a lengthy pot time of 45 minutes. This allowed for larger quantities of product to be mixed at a time. The chosen SR cures in a reasonable time of 6 hours. These properties were ideal for the SLL application at hand.

4.5.2 Silicone Rubber Supplements

While the intent was for the SR to surround the SLL components, the gap between joints had to remain free to allow proper rotation. As such, the joints were wrapped in "press-n-seal", a thin impermeable wrap, to cover the gaps and prevent liquid silicone from seeping in during casting. This wrap was thin and flexible, adding little additional joint stiffness.

The wrap was applied to the HM and MF joints, covering the entire midfoot and forefoot. Each end was taped on the heel base and toe segment, to ensure a tight connection while adding no joint resistance.

To help the SR detach from the mould after curing, a release agent (Ease Release 200™) was applied to the mould before casting [99].

4.5.3 Mould

To cast the SR around the 3D printed parts, a mould was designed and printed to shape the SR. A prosthetic foot shell CAD model was provided by Ossür (Figure 4-38). This model was used to create a negative mould, with the cover shape creating a gap with the desired volume (Figure 4-39). Because the cover had a separated hallux, the mould was divided into three parts: the front mould, the back-left mould, and the back-right mould. Because the foot components needed to be fully surrounded by the SR, pins were placed at strategic points around the mould to elevate the foot components.

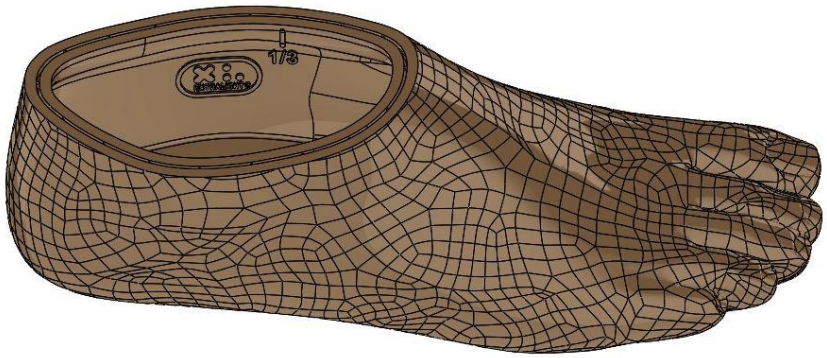

Figure 4-38: Össur prosthetic foot cover CAD file model FSTM26R

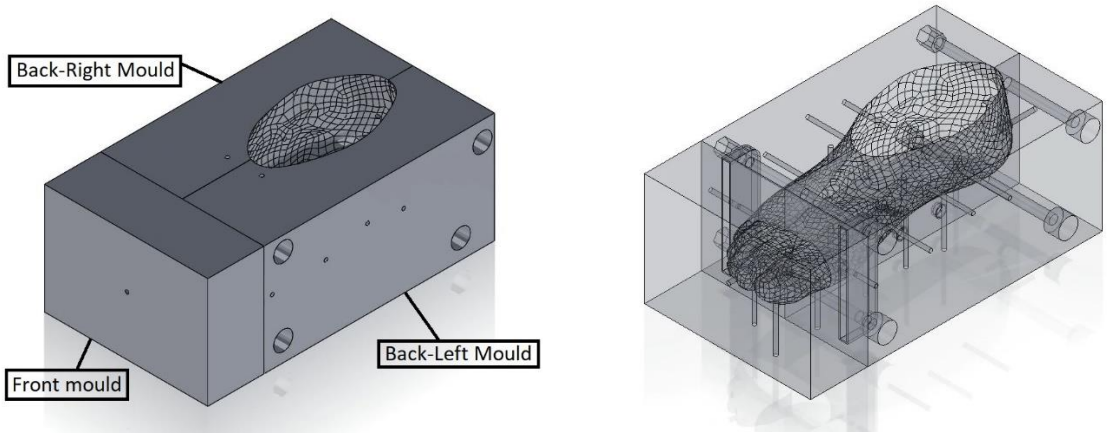

Figure 4-39: Mould components labelled (left) and transparent mould view (right)

Since the Össur cover was the driving mould element, all other features were scaled linearly to cover length CL instead of FL. However, the cover itself was scaled linearly to match FL for anthropometric scaling. Linking all mould features to CL enabled simpler calculations since the mould directly interacted with the cover, while still retaining FL as the primary dimension.

Reference lines and points were created on the model to properly align the cover on the SLL foot (Figure 4-40). Reference points were placed at the hallux peak, second toe peak, and heel peak. Using the hallux and heel point, a plane was set perpendicular to the cover's sagittal plane. The cover's longitudinal axis was defined with the ankle joint centre point and the forefoot offset point, both defined by Figure 3-2. A secondary plane was generated, perpendicular to the longitudinal axis and coincident to the ankle joint centre. The foot's vertical axis was set as a line directly on that plane.

The three mould segments surrounded the foot shell. The two back blocks covered from the heel to a point just before the hallux-toes separation. There was a 20 mm spacing between the posterior mould edge and the cover heel point for fasteners. The back block length scaled with CL so that when the cover increased in size, the hallux-toes separation would shift as well. This ensured that the split toe would be easy to remove once casting was complete.

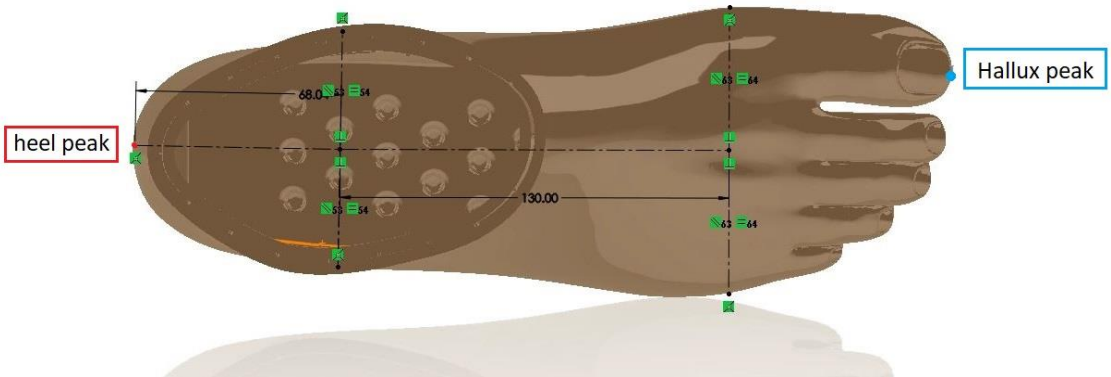

Figure 4-40: Foot cover reference sketch

The blocks were aligned to the cover then a cavity was created from the prosthetic foot shell to generate a negative mould, split across all three blocks. Then the three cover reference points were reproduced on the mould blocks so that every feature was aligned properly.

To ensure that no leaks occurred during casting, bolts held the mould blocks together tightly. Bolt selection was based on availability and overall length, to accommodate mould width. 6” long (152.4 mm) 5/16”-18 threads were chosen. The bolt holes were 8 mm, slightly larger than the 5/16” (7.94 mm) bolts.

For the two back blocks, bolt holes were located at the four corners (Figure 4-41). These holes were enlarged at the end for the bolt heads and hex nuts; one end widened to a 20 mm diameter circular cut to fit a socket wrench while the other end widened to a 12.7 mm (½”) hexagonal cut to restrain the hex nut. The enlarged shapes were inset 15 mm to allow the 6” bolts to go through the mould blocks, with enough room for the hex nut.

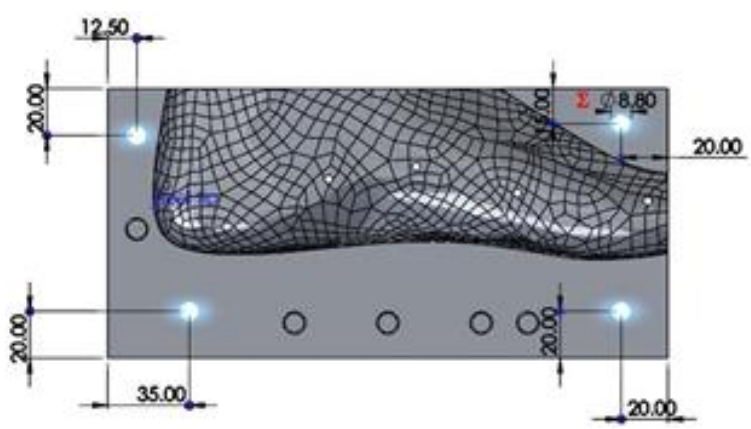

Figure 4-41: Back-left mould side view with bolt hole locations

To ensure that the front block was secured by the bolts, the segment included two leaf lock extrusions, which inserted into matching cuts on each back block (Figure 4-42). These leaf-locks incorporated matching bolt holes aligned with the main holes. The bolts were then used hold all three segment together.

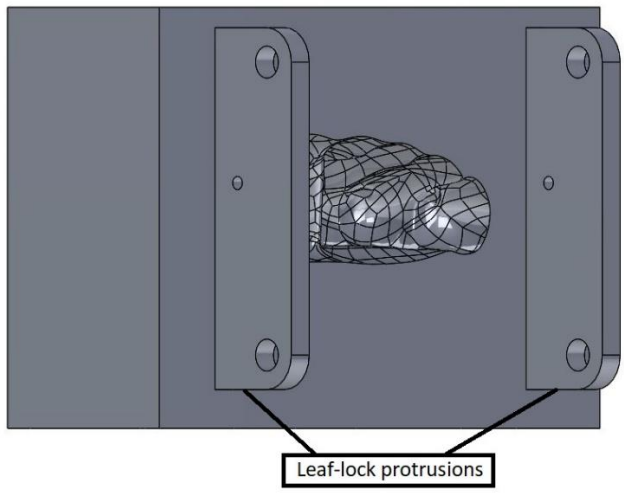

Figure 4-42: Front mould with leaf-lock protrusions

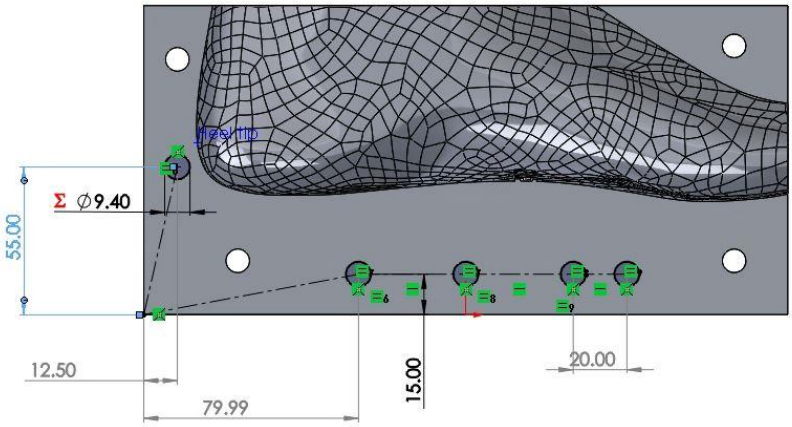

Figure 4-43: Mould alignment bump locations

To help align the mould halves, bumps were added on the back-left block's internal length, around the foot shell cavity (Figure 4-43). These bumps were simple 10 mm minus PLA-PLA clearance cylinders extending 5 mm minus PLA-PLA clearance from the mould surface. On the back-right block, holes were made for insertion, located at matching locations, with 10 mm plus PLA-PLA clearance diameter and

5 mm plus PLA-PLA clearance deep. These bumps assisted the bolts and ensured that the cavity was properly aligned at the seams.

Since the SR needed to surround the 3D printed foot, the components were supported away from the mould walls using twenty-four mounted pins, in five directions during casting. These pins were alphabetized and then placed on strategic points on the SLL foot surfaces, in the middle of flat surfaces, except for the front and back pins, due to curvature of those parts. Eleven pins (A-K) were placed across the sole's surface (Figure 4-44). Eight pins (L-S) were on the medial and lateral sides (Figure 4-45). One was in the front (T), two (U and V) were on the back (Figure 4-46), and two (W and X) supported the top (Figure 4-44).

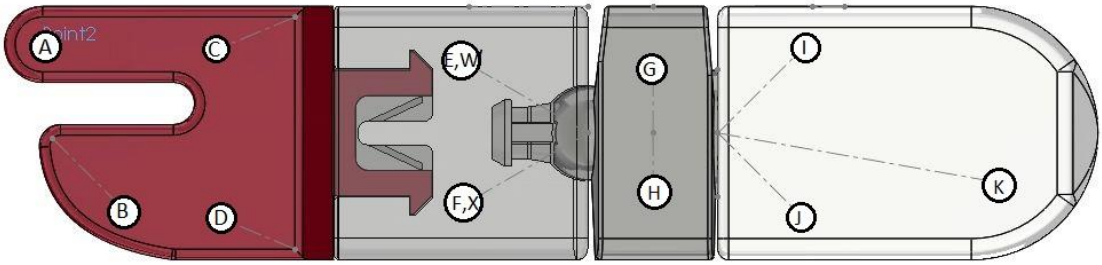

Figure 4-44: Sole pin locations

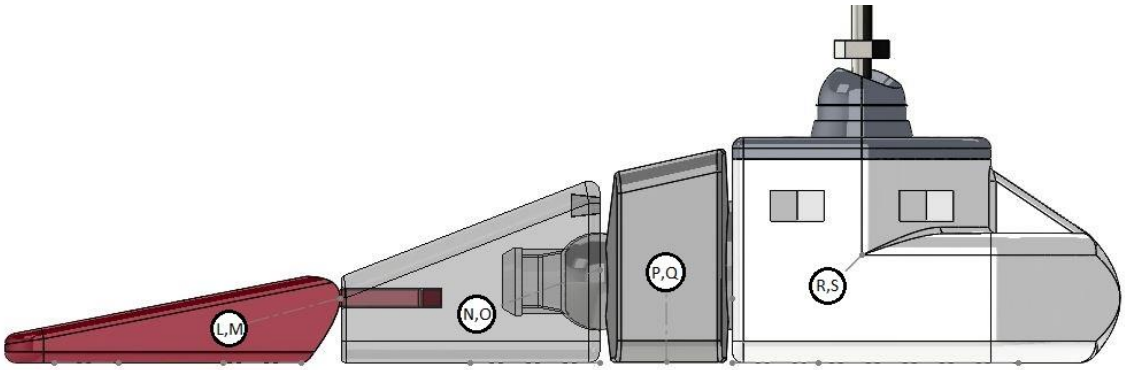

Figure 4-45: Lateral-medial pin locations

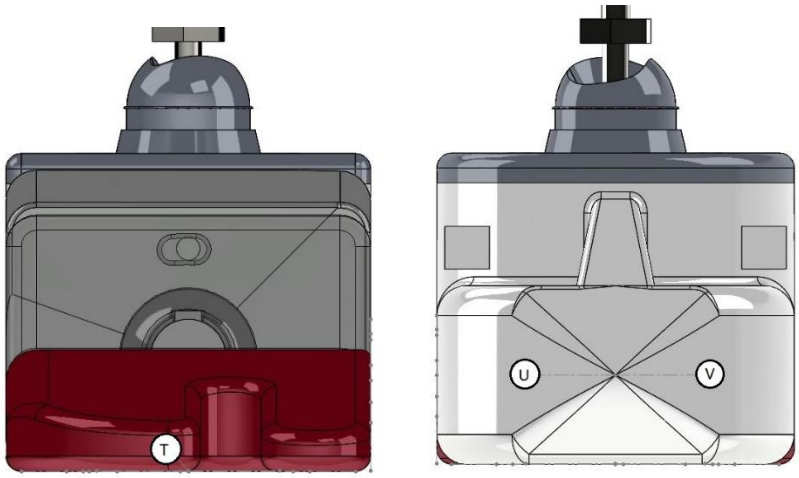

Figure 4-46: Front and back pin locations

A plastic plate 6.35 mm (1/4") thick and 295 mm by 170 mm was placed on top of the assembled mould to hold the foot down during casting. This plate had an opening for the heel top components and to allow casting of the SR.

Each pin was machined to support the 3D printed parts at the required height. To calculate this height, the Ossur prosthetic foot shell was fixed to the SLL CAD model, aligned so that everything would be covered with SR. The shell's longitudinal axis was aligned 2° away from the CAD midline to have proper toe separation. The foot shell was then lowered and adjusted to support the sole. Each point was placed manually, with distances from reference points measured and scaled appropriately (Table 4-15). These reference points were the heel point for the mould's left and right sides, and hallux tip for the front mould. Some values are negative to indicate direction with respect to those reference points. Initial location for pin C, D, L, and M required small displacement in addition to anthropometric scaling, given their proximity to the seam between the front and back mould segments. The displacement ensured that increasing or decreasing FL would keep the pin fully within one block. Appendix B.13 shows all three mould dimensions, scaling equations, and CAD drawings.

Table 4-15: Support point location with respect to reference points

Pin letter	Reference point	X length (mm)	Y length (mm)	Z length (mm)
A	Hallux tip	$CL \cdot (-0.058)$	-	$CL \cdot (-0.014)$
B	Hallux tip	$CL \cdot (-0.117)$	-	$CL \cdot (+0.125)$
C	Heel tip (left)	$CL \cdot (+0.791) - 3.5$	-	$CL \cdot (+0.088)$
D	Heel tip (right)	$CL \cdot (+0.796) - 3.5$	-	$CL \cdot (-0.059)$
E	Heel tip (left)	$CL \cdot (+0.579)$	-	$CL \cdot (+0.071)$
F	Heel tip (right)	$CL \cdot (+0.584)$	-	$CL \cdot (-0.056)$
G	Heel tip (left)	$CL \cdot (+0.414)$	-	$CL \cdot (+0.057)$
H	Heel tip (right)	$CL \cdot (+0.418)$	-	$CL \cdot (-0.053)$
I	Heel tip (left)	$CL \cdot (+0.284)$	-	$CL \cdot (+0.071)$
J	Heel tip (right)	$CL \cdot (+0.290)$	-	$CL \cdot (-0.76)$
K	Heel tip (right)	$CL \cdot (+0.118)$	-	$CL \cdot (-0.052)$
L	Heel tip (left)	$CL \cdot (+0.786) - 2.5$	$CL \cdot (+0.011)$	-
M	Heel tip (right)	$CL \cdot (+0.785) - 2.5$	$CL \cdot (+0.011)$	-
N	Heel tip (left)	$CL \cdot (+0.572)$	$CL \cdot (+0.023)$	-
O	Heel tip (right)	$CL \cdot (+0.571)$	$CL \cdot (+0.023)$	-
P	Heel tip (left)	$CL \cdot (+0.413)$	$CL \cdot (+0.064)$	-
Q	Heel tip (right)	$CL \cdot (+0.411)$	$CL \cdot (+0.066)$	-
R	Heel tip (left)	$CL \cdot (+0.274)$	$CL \cdot (+0.045)$	-
S	Heel tip (right)	$CL \cdot (+0.273)$	$CL \cdot (+0.045)$	-
T	Hallux tip	-	$CL \cdot (-0.011)$	$CL \cdot (-0.084)$
U	Heel tip (left)	-	$CL \cdot (+0.036)$	$CL \cdot (+0.056)$
V	Heel tip (right)	-	$CL \cdot (+0.036)$	$CL \cdot (-0.054)$
W	Heel tip (left)	$CL \cdot (+0.579)$	-	$CL \cdot (+0.071)$
X	Heel tip (right)	$CL \cdot (+0.584)$	-	$CL \cdot (-0.056)$

Chapter 5

SLL Additive Manufacturing

5.1 FDM

Due to the SLL's component geometries, AM was selected for creating the foot segments. In addition to its ability to fabricate complex parts, AM can be used to create custom parts due to the ability to modify parameters and digital files between fabrication instances. These modifications can include AM settings, such as infill and layer height, but also modifications to the CAD objects themselves, such as scaling size or orientation. Furthermore, many AM equipment requires minimal training, providing wider accessibility. Moreover, for low production volumes, this process can be cost-efficient. Therefore, AM is an ideal candidate for SLL fabrication.

FDM was selected over other AM processes for its low-cost, low barriers to entry, and wider availability. FDM printing material is affordable and widely available while offering favourable mechanical properties. While FDM does have limitations, none were found to be a major constraint for this design. FDM component surface finishes were deemed to be appropriate since the SLL foot is cast in SR after printing, which is in turn covered by footwear during AFO testing. While FDM material options are limited to thermoplastics, a wide variety of materials offering adequate strength and stiffness properties are available for this project.

5.1.1 Rigid Filament Selection

The main material used in the fabrication of SLL components was Nylon 230, made by taulman3D [100]. This material is stronger and less brittle than the more widely used PLA. Nylons are also easier to use than other strong thermoplastics, such as ABS, because toxic fumes are not emitted during printing. Furthermore, nylons offer higher fatigue resistance than either material [70], [101].

Nylon 230 was specifically chosen for its smoother filament and lower printing temperatures. Some nylon filaments, such as Onyx™ [102], have carbon fibre integrated within its length, making the prints stronger. However, these special filaments require speciality printers, with abrasive resistant nozzles and hot-ends capable of reaching temperatures above 275 °C. Nylon 230 was specifically developed for 3D printers with lower temperature capabilities (228-235 °C), and is non-abrasive, making this nylon the most accessible choice [99].

Nylon 230 does have some issues that required care and consideration. Nylon is hygroscopic, meaning that the material will absorb moisture in the air over time. Drying the filament before 3D printing is required so that water molecules do not affect the material while the filament is fed and heated through the nozzle [101]. This process was done consistently before every nylon print to ensure print quality. After printing, the nylon components were dried a second time to ensure that minimal moisture was present before casting. To prevent warping, nylon components were printed on a heated bed and the printer was placed in an enclosure to minimize the difference between the ambient temperature and the nozzle's hot-end. To prevent model surface delamination or accidental motion during printing, a thin layer of polyvinyl acetate (PVA) glue was applied to the print surface to promote adhesion.

While nylon was used for the load bearing components, PLA was used for some components that did not require the strength that nylon provided. The shank cover and mould share one main purpose: obtaining a specific shape, achievable quickly via FDM. As such, a high strength material is not required for these larger components. PLA is low-cost and easy to print, as well as a commonly available FDM printing material.

5.1.2 Flexible Filament Selection

While most components required rigid bodies, three parts required complex geometries and flexibility. The two annular connectors and the toe segment were printed using TPU filaments. TPU varies in hardness, with harder materials being stiffer but easier to print. Most FDM printers push on the filaments to feed the nozzle, usually near the filament spool and not near the nozzle. However, pushing on flexible filament can

be difficult since the motor can slip and wear down the filament causing inconsistent flow resulting in unwanted gaps within layers. Another issue is filament buckling, where the flexible material bends while being pressed through the nozzle and causing a blockage. Thankfully, these issues can be fixed, with a feeding motor near the nozzle that pulls filament instead of pushing, and an adjustable grip on the filament to prevent slip.

To further mitigate these problems, a good balance between hardness and flexibility is required. For this design, Cheetah™ filament from NinjaTek was chosen after experimental prints. This particular filament's hardness was 95 on the shore hardness A scale, which was found to print easily, but also allowed adequate bending within the dimensional constraints of the SLL design.

5.2 FDM Settings

5.2.1 Hardware and Software

An Artillery Sidewinder X1 printer was used for this thesis (Figure 5-1). This FDM printer has a large, 300 mm by 300 mm in the x/y plane and up to 400mm in height, print volume. This device also features a bed that can heat up to 130°C. The printer includes several fault detections. If the power or filament runs out, work is halted and can be recovered once the conditions are restored [103].

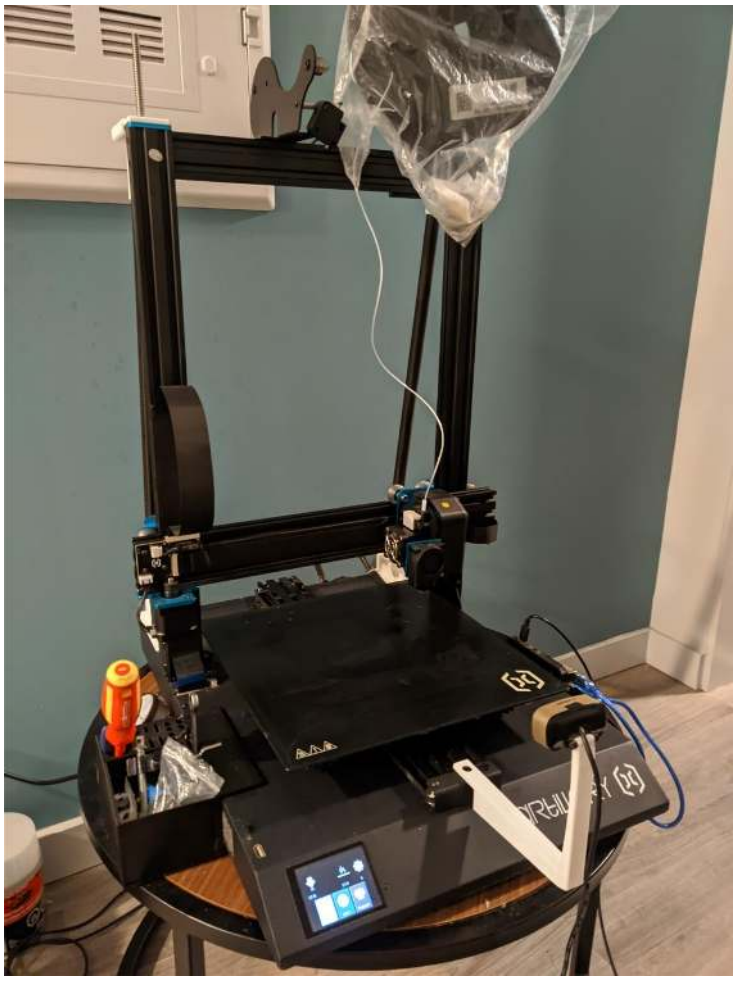

Figure 5-1: Sidewinder X1 FDM printer by Artillery

The Sidewinder X1 can take spools of filaments 1.75 mm in diameter, up to 3 kg in weight. The 0.4 mm diameter nozzle has a direct drive filament extruder directly above the hot-end assembly, which is ideal for flexible filaments. The nozzle can travel at 250 mm/s, with a maximum printing speed of 150 mm/s. A maximum layer resolution of 0.1 mm allows precise prints. Files can be uploaded via USB connections or micro SD cards [103]. The printer's full specifications are listed in Appendix D.1.

To prepare the CAD models for 3D printing, Cura™ v4.8.1 from Ultimaker was used to slice the model into layers and generate a planned nozzle path for each layer. Cura™ is free to download and simple to use and implement. While primarily designed for Ultimaker brand FDM printers, this software is compatible with other FDM printers. The software allows both 1.75 mm and 2.85 mm filament settings, which are the two most common filament sizes. Once the settings are ready, Cura converts a mesh file into a ".gcode"

file, to be exported and transferred to the FDM printer. Cura provides a layer-by-layer preview, showing the programmed path for each layer. Estimates for print time and material used are also generated, based on the chosen settings [104]. The object can be moved, rotated, and scaled to improve the print quality. Furthermore, internal settings such as layer dimensions, outer wall dimensions, and infill can be modified along with nozzle speed and temperature. Depending on the build and orientation, removable scaffolding might be required as well, since filament needs to be deposited on a surface to properly finish a layer. Overhang angles 45° or lower are generally acceptable for FDM, because at least half the filament deposited near the edges is supported without scaffolding [105]. This maximum overhang angle limit is dependant on the printer and can therefore be greater than 45°. Scaffolding is typically designed to be easy to remove, using different settings than those for the actual part to be printed.

5.2.2 Component Settings

Due to the different materials and orientations used, specific printer parameters were considered for each SLL component. While some settings remained the same throughout, some key differences were required across print materials. Table 5-1 summarizes the settings for all three filaments.

5.2.2.1 Nylon Component Settings

Nylon was used for the heel base, heel plates, midfoot, and forefoot. Nylon layers were set to 0.2 mm because noticeable strength losses are found to occur when layer height is set to more than 50% of the nozzle diameter [106]. However, higher layer heights typically reduce print times, reducing the likelihood of moisture absorption during the print. Each line was set to 0.6 mm wide because line widths of 150% of the nozzle diameter are found to produce stronger parts [107]. The outer shell was set to a thickness of 0.8 mm on top and bottom layers (4 layers thick) and 1.2 mm thick on the sides (2 lines thick). Since the nylon parts are load bearing, the internal area infill was set to 85% to increase strength. Infill percentages above this value were found to “overflow” a given layer. The “cubic” pattern, described as cubes tilted and stacked together, was used for the nylon infill (Figure 5-2) since the three-dimensional pattern offers strength in all directions [108].

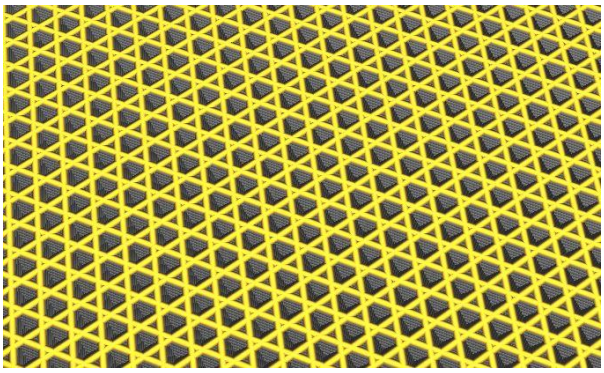

Figure 5-2: Cubic pattern at 85% infill, layered view

The nozzle temperature was kept constant at 235 °C during prints and the build plate was heated to 60 °C to ensure a warm ambient temperature and prevent warping. In this case, the cooling fan was disabled, since the cooling fan could introduce temperature gradients that could encourage warping. The nozzle's speed was set to 60 mm/s for the infill section and was 30 mm/s for the support and walls, ensuring proper flow for those vital areas.

Nylon support was set to the same layer height as the main object for consistency. The chosen support pattern was "zig-zag" at 10% infill for easy removal (Figure 5-3). The support's offset was set to 0.4 mm in the z-axis and 1.2 in the x/y-axis, providing an appropriate distance between the scaffolding and the main print to prevent support fusing with the object. However, the infill increased to 90% near the scaffold's top edge, with a concentric pattern to create a solid interface. This scaffold interface is a floating surface enabling proper layer deposition for the main object's overhanging features, providing better scaffolding. Creating such scaffolding can sometimes be hard to separate from the main object due to unwanted fusion between scaffolding and main prints [109]. However, after experimental trials, scaffold removal was found to be easy. Appendix D.2 provides nylon print settings.

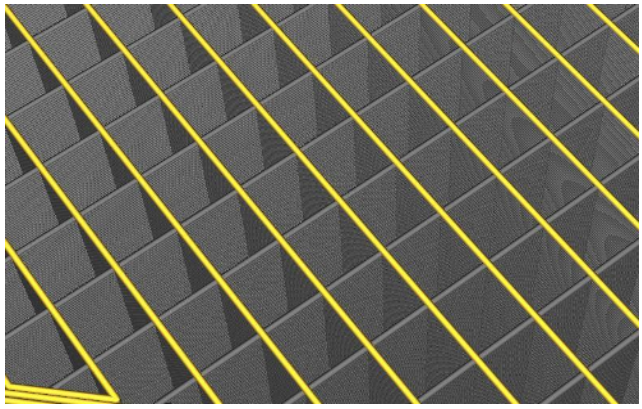

Figure 5-3: Zig-zag pattern at 10% infill, layered view

Part orientations were selected to improve quality, minimize supports, and avoid major defects. The forefoot was placed with the distal face down and internal scaffolds supporting the FT leaf locks (Figure 5-4). The midfoot was placed with the sole down, with the extruding balls supported on both sides. The heel base was set on its side, to reduce support near the bolt holes. However, the ball stud stem did require support, as well as the posterior support beam (Figure 5-5). The heel plates were built in their natural orientation, with internal support for the ball socket.

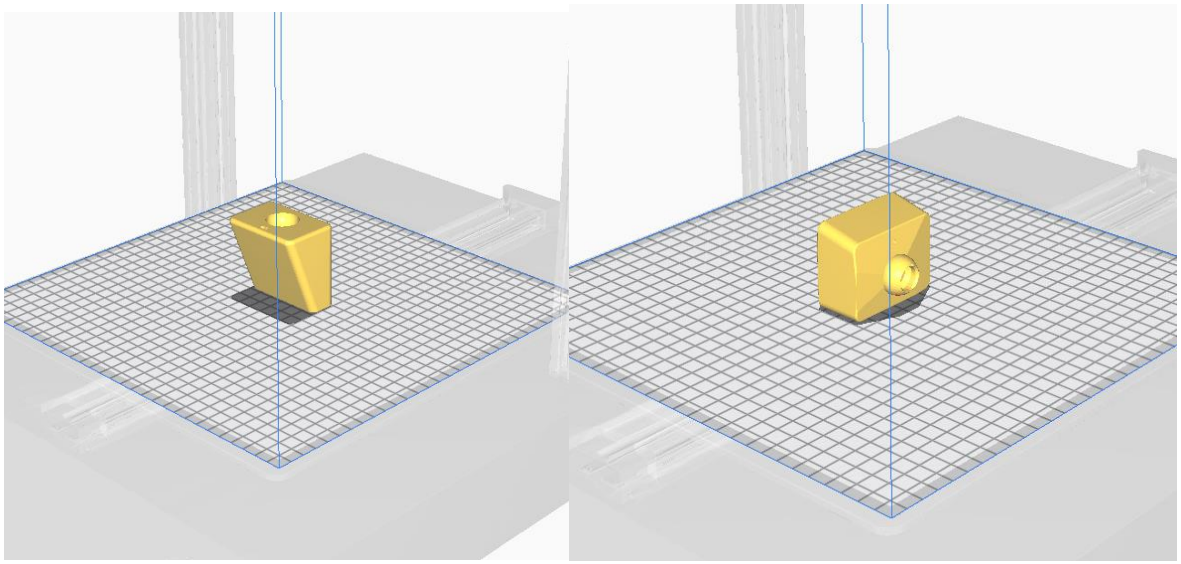

Figure 5-4: Forefoot and midfoot printing orientation

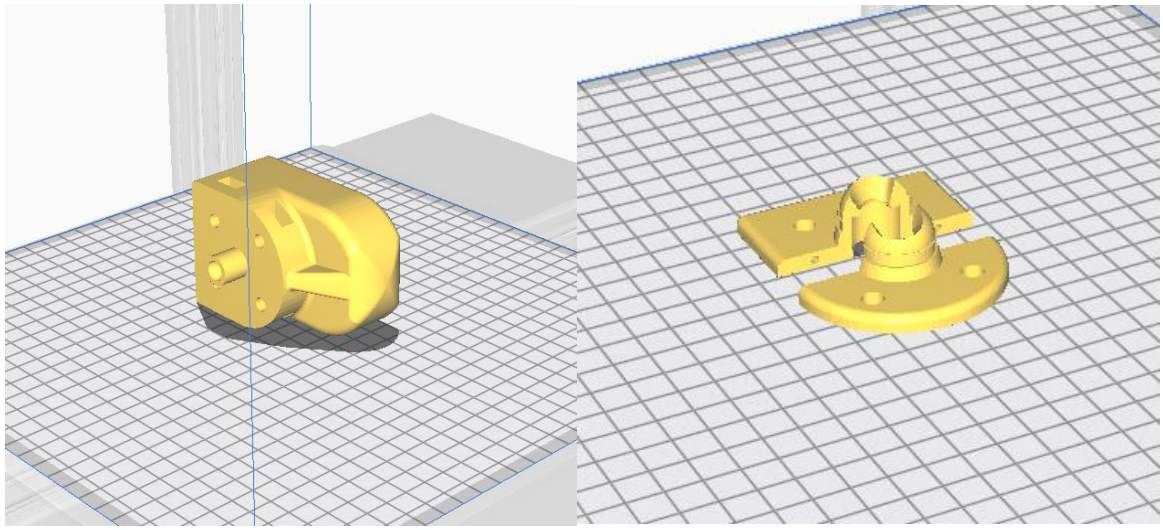

Figure 5-5: Heel base and heel plates print orientations

5.2.2.2 TPU Component Settings

The three TPU components included the toes and the two annular connectors. Most settings were identical to those used for nylon. The infill was raised to 100% following a concentric pattern because the snap-fit calculations assumed that the objects were solid. Furthermore, the snap-fit connectors were not designed to take load in three dimensions, therefore a cubic pattern was not required.

Unlike for the nylon, cooling was required for TPU to help the filament from solidifying once deposited. The fans were set to spin at full speed once the print had completed three full layers. This delay prevented the fan from interfering with the initial phase of the print, crucial for anchoring the print to the building plate.

The toe block was printed with its sole on the ground, with scaffolds for the cantilever snap-fit connectors (Figure 5-6). The support settings are consistent with those used for nylon. Appendix D.3.1 provides the toe segment settings. The annular connectors were oriented with one circular surface on the ground, printed as a column (Figure 5-7). As such, supports were not required for the connectors and settings were slightly different (Appendix D.3.2).

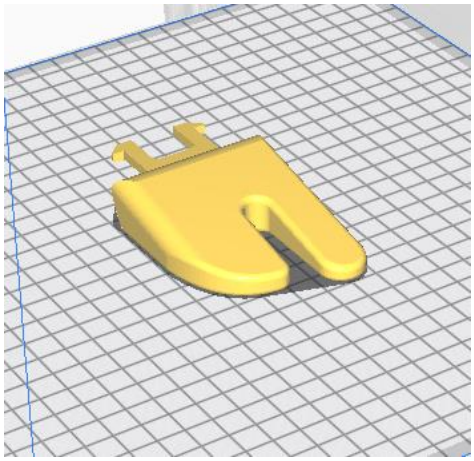

Figure 5-6: Toe segment print orientation

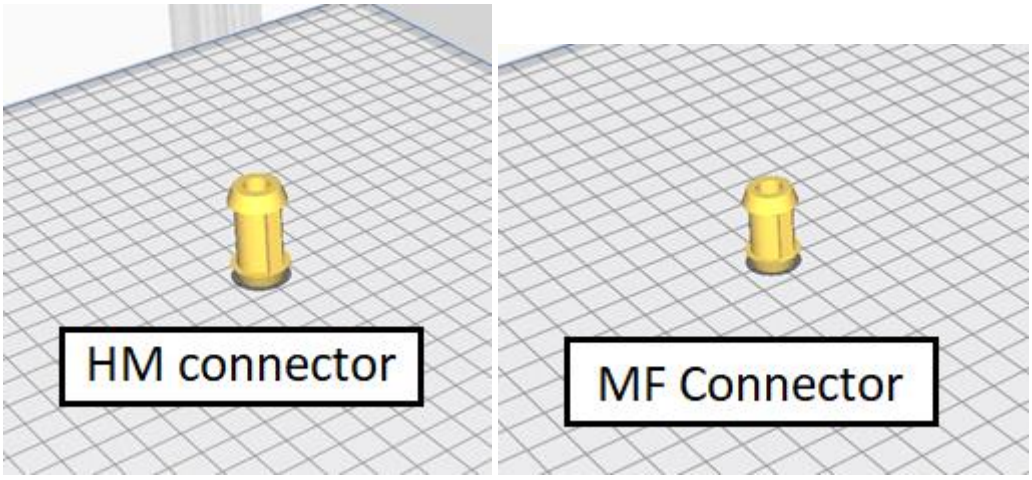

Figure 5-7: HM and MF annular snap-fit connectors print orientations

5.2.2.3 PLA Component Settings

The three mould sections and the two shank cover halves were made using PLA. The mould segments used different settings than the shank covers. Since PLA parts were not designed to bear load, the layer heights were set at 0.32 mm to reduce the numbers of layers and print time at the cost of strength. The line width was the same as those used for nylon and TPU (0.6 mm).

The mould's outer shell line count was equal to previous settings. The mould components were made with low infill to prevent waste (5% infill following a "gyroid" pattern, Figure 5-8). The gyroid pattern was selected because of its faster printing time and lower material usage. The nozzle's temperature was lowered to 200°C. PLA also required cooling, with fan settings identical to those used for TPU.

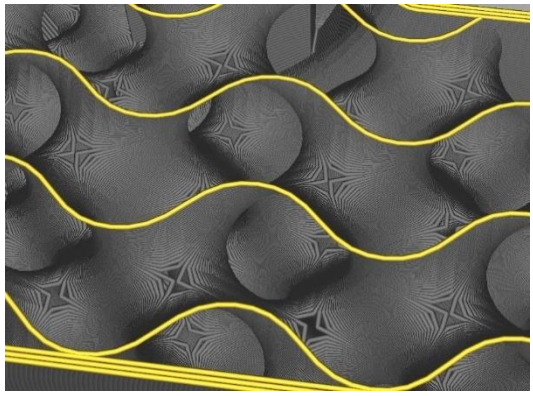

Figure 5-8: Gyroid pattern at 5% infill, layered view

The front and back-right mould blocks did not require support (Figure 5-9), while the back left mould block did. However, to prevent scaffolds being generated in the back mould's pinholes, a support blocker was generated (Figure 5-10). In this case, the intersecting volume would not generate scaffolding. Therefore, the offset was set to 4.25 mm in the x-axis and -5 mm in the y-axis, allowing supports for the overhanging curved region and the alignment extrusions. The back left mould settings are listed in Appendix D.4.1, while the front and back right mould part settings are given in Appendix D.4.2.

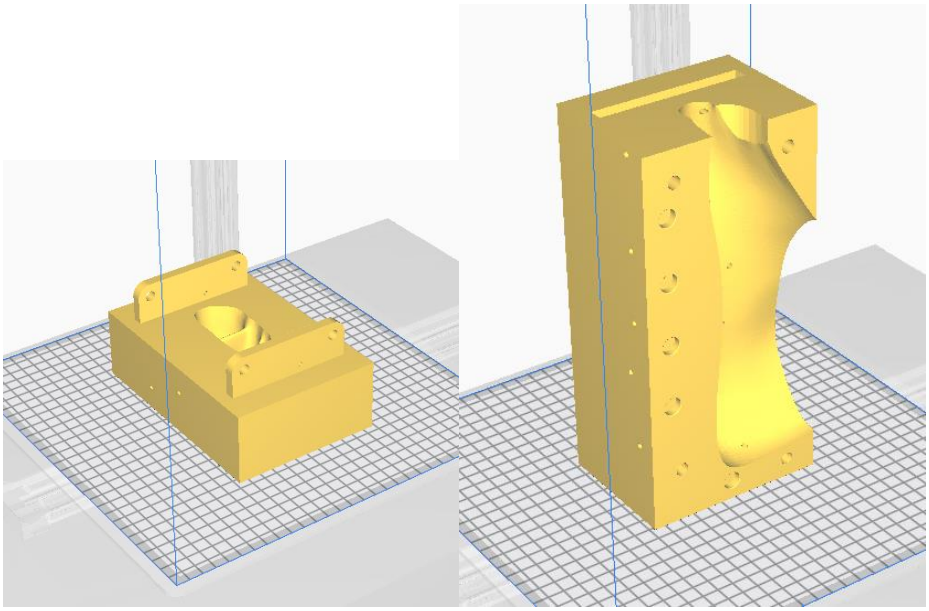

Figure 5-9: Front and back right mould block print orientations

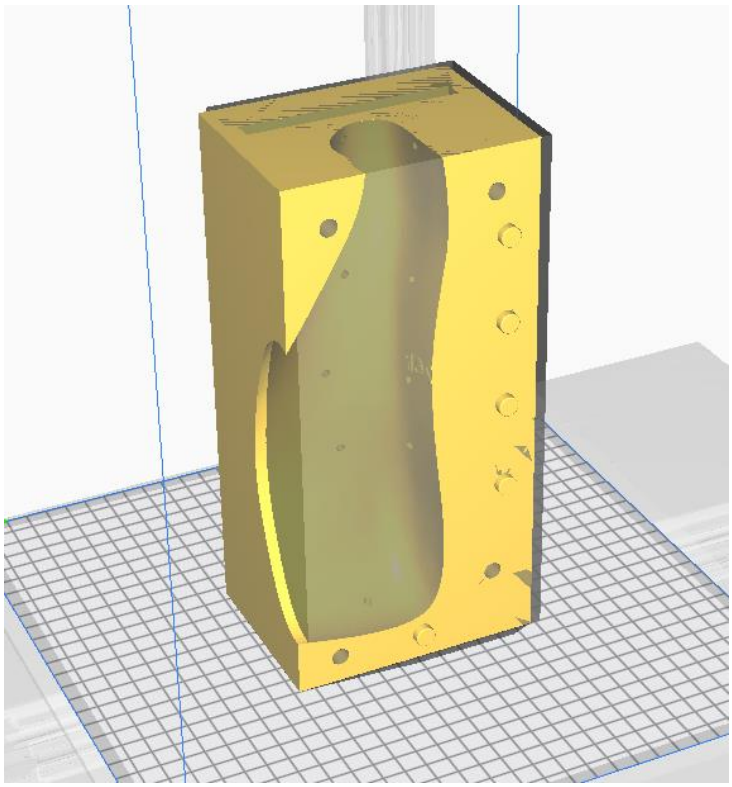

Figure 5-10: Back left mould block print orientation with overlapping grey support blocker

The shank cover outer shell line count was increased to 3, and the bottom and top thicknesses were increased to 4 layers. The shank cover halves were made at 15% infill to remain economical, yet stronger than the mould. The infill pattern used was cubic, to provide three-dimensional strength. As with TPU and other PLA parts, cooling was required. Both halves required support. Scaffold settings were similar to those used for TPU and PLA components, but had a lower overhanging angle threshold at 43°. The two halves were printed upright (Figure 5-11). The shank cover settings are listed in Appendix D.4.3.

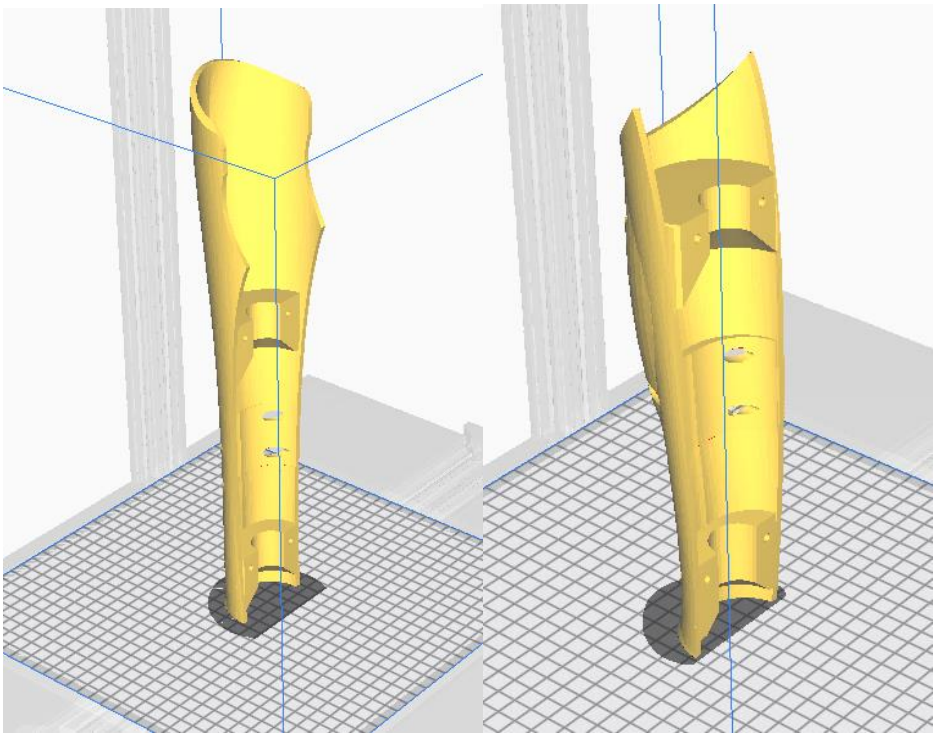

Figure 5-11: Front and back shank cover print orientations

Table 5-1: FDM print settings summary

	Nylon settings	**TPU settings**	**PLA settings**
Layer height	0.2 mm	0.2 mm	0.32 mm
Line width	0.6 mm	0.6 mm	0.6 mm
Bottom-top shell thickness	4 lines	4 lines	3 lines
Wall thickness	2 lines	2 lines	2 lines
Infill percent	85%	100 %	5%
Infill pattern	Cubic	Concentric	Gyroid
Nozzle temperature	235 °C	235 °C	200 °C
Bed temperature	60 °C	60 °C	60 °C
Cooling fan status	Off	On	On
Nozzle speed	60 mm/s	60 mm/s	60 mm/s
Nozzle speed wall	30 m/s	30 mm/s	30 mm/s

Chapter 6

Motion Testing

Since a main objective of the thesis was to design a SLL that had accurate anatomical motion, testing this motion was essential. Each joint was tested for its respective motion using fiducial markers and motion capture software.

6.1 Fiducial Markers and Smartphone Application

SLL motion tracking involved fiducial markers, an Android phone (Samsung Galaxy 9 S plus™), and an application named "Biomechanics Augmented Reality – Marker" (BAR-M), which was developed by Basiratzadeh et al. [4]. Fiducial markers are patterns that can be attached to objects and accurately tracked by software using a camera. Fiducial markers include quick response (QR) tags and other patterned squares that can be placed in a video's field of view. AprilTag2 markers were used for this thesis. The Android smartphone application was previously shown to accurately locate the tag centre and corners of up to four tags simultaneously. The application was found to have an angular accuracy of 0.29° and a linear accuracy of 0.27 cm in controlled static conditions [4]. This application was selected for two reasons. First, due to motion laboratory access restrictions imposed by the COVID-19 pandemic. In this case, the BAR-M application required only paper markers, an android smartphone, and a single technician. Second, the application provided time-stepped digitized data for the entire measurement trial. SLL joint rotation angles were calculated by securing markers on the segment surfaces and aligning the smartphone parallel to the plane of motion being measured.

Apriltag2 markers were printed on rigid cardboard then laminated to create durable and reusable measurement tools (Figure 6-1). Three square sizes were produced, with white borders of 18.5 mm, 27.5 mm, or 36.1 mm. This allowed more flexibility during testing since marker size could be changed depending on the testing conditions. Larger markers provided similar benefits to those of a camera placed closer to the

test setup, providing better view of the marker, and therefore, better accuracy. However, the largest size were more cumbersome to place. Therefore, smaller markers could enable better positioning.

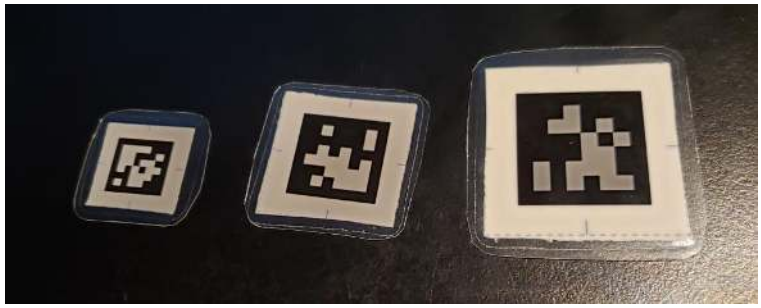

Figure 6-1: AprilTag2 markers on laminated cardboard

The BAR-M app produces marker corner locations in Cartesian coordinates for every recorded frame. From these coordinates, marker edges were converted into vectors using equation (6-1), where v_x and v_y are vector components. All vector directions were identical between tags for easy reference (Figure 6-2). Each vector was created from one corner point to the one directly beside: from point 1 to point 2 creating vector 2-1, and so on. The relative angle (α) was calculated between two vectors using equation (6-1), v being the vector for tag 1 and u for tag 2. To mitigate errors, the vector 2-1 and vector 3-2 were used for angle calculations. As such, 90° was subtracted from the initial calculations for same-plane rotation angles.

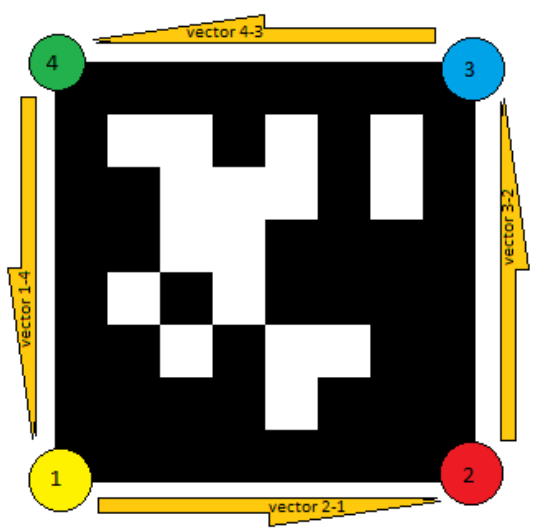

Figure 6-2: Vector directions across all marker coordinates

$$v_x = x_2 - x_1, v_y = y_2 - y_1 \tag{6-1}$$

$$\alpha = \cos^{-1}\left(\frac{(v_x \cdot u_x) + (v_y \cdot u_y)}{\sqrt{(v_x^2 + v_y^2)} + \sqrt{(u_x^2 + u_y^2)}}\right) - 90° \tag{6-2}$$

6.2 Test Methods

Several motion tracking tests ensured that rotation was adequate throughout the design process. Three main testing stages were established: an initial block test, a SLL foot test without SR (pre-casting), and a SLL foot test with SR (post-casting). This three step approach confirmed that rotation angles were valid before, during, and after SLL construction.

6.2.1 Initial Block Testing

6.2.1.1 Testing Component Production

Before 3D printing the main SLL foot components, smaller test blocks were made. The joint geometry remained, but the overall anthropometric geometry was removed. Four blocks were made, each one representing one joint, allowing testing for all relevant planar motions (Figure 6-3 and Figure 6-4). The SH test block included the heel plates, a simplified heel base, and the ball stud. Bolts and nuts secured the heel plates. Both HM and MF joints used unchanged annular snap-fit connectors, ball components, and socket components. These blocks included the eversion-inversion pin and groove, above the ball socket. To reduce waste, only a small rectangular section of the midfoot extended from the ball, while the socket component was made bigger to fully incorporate the annular connector. The FT test block included the forefoot FT socket and the toe cantilever snap-fit connectors, along with the proximal curved end. All blocks were made using the final product FDM settings.

Figure 6-3: SH, HM, MF, and FT test blocks

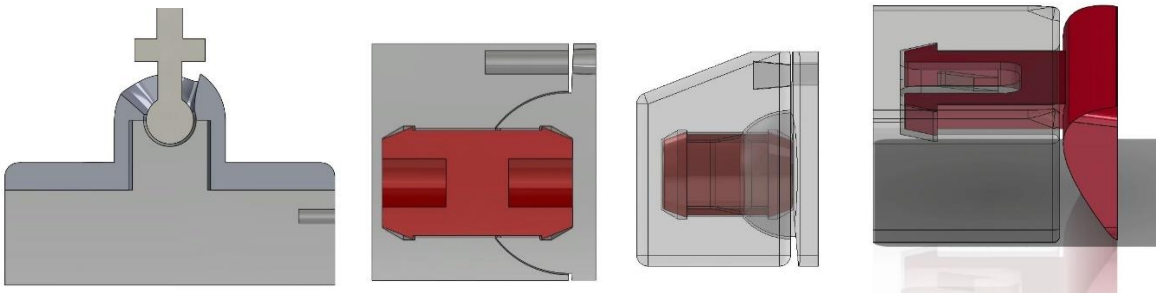

Figure 6-4: Cross-sectional and transparent view of the SH, HM, MF, and FT initial test blocks

6.2.1.2 Block Test Setup

For motion testing, each block was secured in a small vice, with the top surface level to the ground. The female components were fixed in place while the male components were above the vice, free to move. One marker was placed on the fixed surface, while another was placed on the free-moving surface (Figure 6-5). For SH tests, the free-moving component was the ball stud, and the marker was placed on the ball stud's integrated hex nut. For HM and MF, the free-moving components were the midfoot wedges. These wedges were placed above the socket block and rotated relative to the top surface, for both sagittal and transverse rotations. As such, the moving marker was placed on the wedges' small length as shown in Figure 6-5. For HM and MF frontal motion, the fixed marker was elevated above the block using sticks and tape behind the socket block, while the free-moving marker was placed on the midfoot wedge, parallel to the top surface. For the FT component, the free-moving marker was placed on the toe component medial side, while the fixed marker was placed on the forefoot medial side.

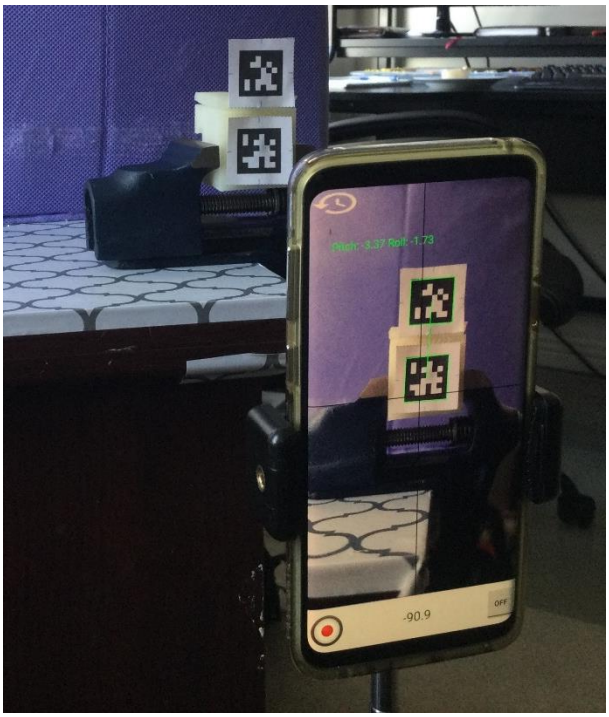

Figure 6-5: Initial block test setup

The smartphone was set on a tripod, in portrait orientation, back camera facing the block, phone level to the ground. The tripod was placed close to the vice to maximize marker size within the viewing area of the camera (Figure 6-5). To mitigate camera motion errors, interactions with the camera were minimal.

6.2.1.3 Block Testing Method

Three trials of the following protocol were completed consecutively for each joint's relevant motion planes:

1. Start with the joint in the neutral position for 5 s
2. Rotated the joint clockwise for 5 s
3. Released for 5 s to enable the joint to return to neutral
4. Rotated the joint counter-clockwise for 5 s
5. Released for 5 s to enable the joint to return to neutral

For SH rotation, the ball stud did not have a neutral rest position without load. As such, HM motion tests were performed from the maximum clockwise rotation angle to the maximum counter-clockwise rotation angle in both frontal and sagittal planes, skipping the return to neutral position steps.

6.2.1.4 Initial Motion Block Results and Discussion

The marker's corner coordinates were converted into vectors and graphed. The angles for each neutral or rotated position were averaged over 50 frames and standard deviations (SD) were calculated for each trial. Maximum rotation angles for each joint were calculated as the difference between neutral and rotated positions. Results from each trial were averaged. For SH motion, measurements showed full rotation within a plane due to the lack of a neutral position (i.e. from maximum dorsiflexion to maximum plantarflexion and from maximum eversion to maximum inversion).

Figure 6-6 shows a representative motion graph for one of the block rotation trials. Appendix E.1.1 provides all other motion graphs. Joint rotation angle results for all blocks are tabulated in Table 6-1.

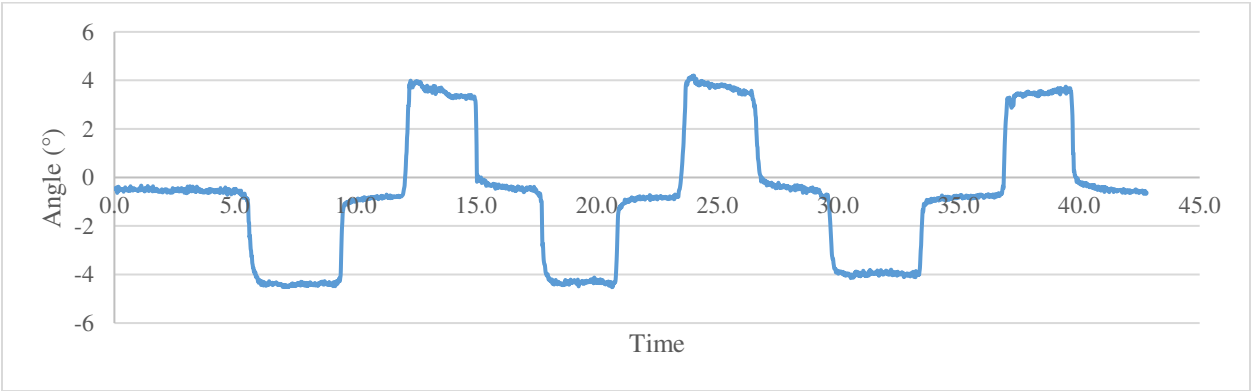

Figure 6-6: MF abduction (AB) to adduction (AD) motion graph example

Table 6-1: Ideal vs measured joint rotation angles for initial joint test blocks

	Ideal rotation	Measured rotation (SD)	Differences
SH frontal	50.0°	60.0° (2.53)	10.0°
SH sagittal	70.0°	57.4° (1.33)	-12.6°
HM abduction	0.5°	1.1° (0.12)	0.6°
HM adduction	3.8°	4.9° (0.37)	1.1°
HM dorsiflexion	2.2°	3.1° (0.18)	0.9°
HM plantarflexion	2.2°	2.6° (0.60)	0.4°
HM eversion	3.5°	5.4° (0.31)	1.9°
HM inversion	3.2°	3.8° (0.35)	0.6°
MF abduction	2.0°	3.8° (0.20)	1.8°
MF adduction	6.5°	4.3° (0.20)	-2.2°
MF dorsiflexion	6.5°	4.9° (0.21)	-1.6°
MF plantarflexion	6.1°	2.9° (0.21)	-3.2°
MF eversion	3.5°	3.3° (0.36)	-0.2°
MF inversion	7.0°	6.8° (0.61)	-0.2°
FT dorsiflexion	80.0°	80.3° (2.51)	0.3°
FT plantarflexion	30.0°	31.2° (0.64)	1.2°

Most initial tests showed results within 2° of the desired rotation angles. However, SH joint motion was found to be an outlier with a difference of at least 10° in both directions when compared to maximum ideal rotation angles. MF adduction and plantarflexion angles were also found to be slightly outside the 2° threshold.

Slight methodology errors and inaccuracies occurred during the testing process since even after leveling the foot and phone, the markers were not perfectly parallel to the smartphone. Therefore, some corners were a bit further or closer to the camera, causing the vector lengths to vary slightly, influencing the results. Furthermore, the load was manually applied by hand, resulting in some uneven motion and measurements. Due to the blocks' small geometry, some motions were unevenly induced. Ideally, future block testing would apply loads using hard surfaces like wood or metal. This would reduce small load variation and provide better force transfer. Overall, methodology errors were minor and the testing process was considered to be appropriate for verifying the joint design.

The main source of error present within all motion tests (including pre-cast and post-cast) was FDM dimensional inaccuracy. Since rotation angles depend on the printing features, over or under extrusion of the surface changes the gap dimensions between materials, changing the maximum permissible

rotation angle at that joint. Some motions were also affected by residual material from FDM scaffolding. The midfoot joint was more susceptible to dimensional inaccuracies due to residual scaffolding underneath the ball features. Even after polishing the features with sandpaper, some residue affected rotation. Higher precision FDM printing or other AM processes like stereolithography could mitigate the dimensional accuracy and RoM variations. However, using these higher quality printers would also reduce accessibility to fabrication equipment and increase the SLL fabrication cost.

For SH motions, the difference between the results and the expected results was high because the ball stud could easily dislocate from the socket when reaching maximum RoM. This was due to the required geometry of the socket based on the ball/neck ratio of the chosen ball stud. As a result, the SH motion tests could not be performed at maximum angles consistently. Furthermore, since the maximum rotation occurred in both frontal and sagittal planes, the moving marker was never parallel at either end, worsening results. A bigger ball to neck diameter ratio would increase the thickness of the socket material at the opening, creating a bigger lip to hold the joint together. The ball dislocation only occurred at maximum values and still showed a reasonable RoM before occurring. Even with all these sources of errors, the initial block testing results showed rotations within human variability and were deemed to be acceptable.

6.2.2 Pre-Cast 3D Printed SLL Testing

6.2.2.1 Methodology

After joint block tests were performed and proper rotation angles were confirmed, the full SLL foot blocks were printed and assembled. Two identical copies were made, to confirm that the results were indeed repeatable. One would be cast afterward to measure effects of SR on the motion and be used for load testing. Motion testing was then performed again. For testing the whole foot, a different vice was used, which could hold larger objects. Each joint was tested individually in all relevant planar motions. Marker locations were set to the mould pin locations given that these locations would also be used for post-casted motion testing.

For each test, one marker was placed on the proximal component, which was fixed. Another marker was placed on the distal component, free to move (Figure 6-7). For sagittal motions, the markers were placed on the foot's medial side, matching corresponding pin locations. For transverse motion, markers were placed on the sole, at corresponding pin locations. For frontal motions, both markers were attached to metal needles connected to relevant tested motions, level to medial pin locations.

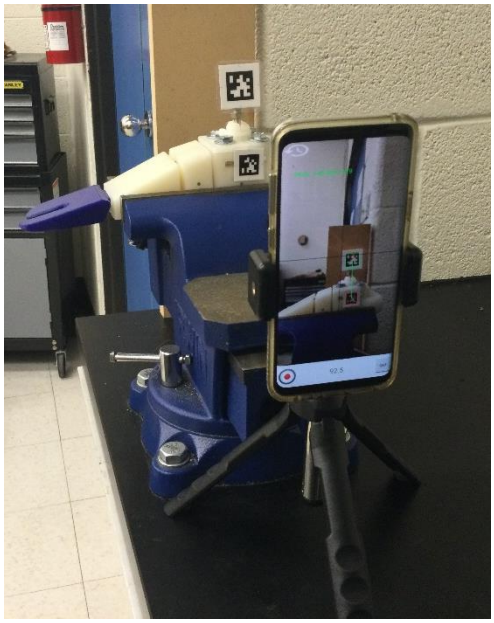

Figure 6-7: Pre-cast SLL SH sagittal testing configuration

The smartphone was positioned similarly to the initial test blocks conditions. However, for frontal motion the smartphone was repositioned so that the camera was in front of the foot. Rotation was induced in an identical manner to the initial test blocks: three cycles of 5 s in neutral position, 5 s rotated clockwise, 5 s neutral position, 5 s rotated counter-clockwise.

6.2.2.2 Results and Discussion

The raw coordinate data was converted into vectors and relative angles were calculated using equation (6-2). The resulting angles were graphed for every data point for both copies of the foot (Figure 6-8). Appendix E.1.2 shows all motion graphs for pre-cast feet. The maximum rotation during each trial was averaged over 50 datapoints and then all trials were averaged together, similarly to initial testing block data. Average rotation angles and standard deviations were summarized in Table 6-2.

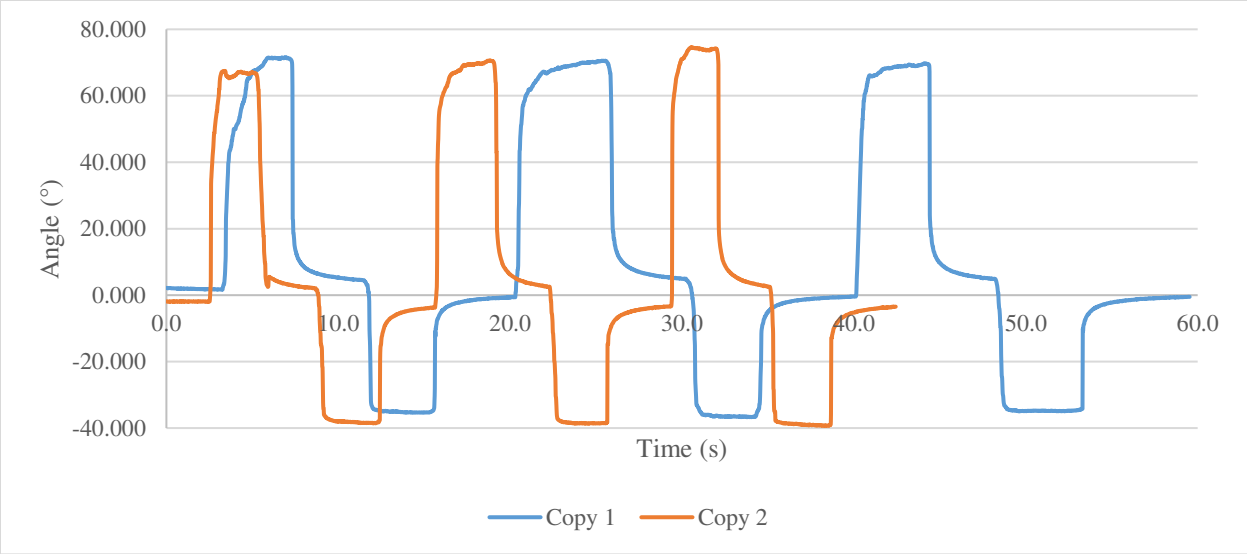

Figure 6-8: Pre-cast FT joint rotation angles (dorsi to plantar) for both SLL foot copies

Table 6-2: Pre-cast SLL feet planar motion measurements

		Copy 1		Copy 2	
Joint	**Ideal angle**	**Measured angle (SD)**	**Difference**	**Measured angle (SD)**	**Difference**
SH frontal	50.0°	43.9° (0.30)	-6.1°	41.8° (0.97)	-8.2°
SH sagittal	70.0°	71.3° (2.45)	1.3°	58.1° (0.98)	-11.9°
HM abduction	0.5°	3.0° (0.09)	2.5°	3.0° (0.15)	2.5°
HM adduction	3.8°	3.9° (0.25)	0.1°	3.8° (0.22)	0.0°
HM dorsiflexion	2.2°	2.5° (0.07)	0.3°	3.7° (0.33)	1.5°
HM plantarflexion	2.2°	3.1° (0.36)	0.9°	3.9° (0.35)	1.7°
HM eversion	3.5°	4.1° (0.58)	0.6°	5.2° (1.03)	1.7°
HM inversion	3.2°	5.1° (0.02)	1.9°	2.7° (0.95)	-0.5°
MF abduction	2.0°	4.7° (0.08)	2.7°	4.1° (0.07)	2.1°
MF adduction	6.5°	11.8° (0.40)	5.3°	8.0° (0.03)	1.5°
MF dorsiflexion	6.5°	10.1° (1.17)	3.6°	9.5° (0.45)	3.0°
MF plantarflexion	6.1°	10.5° (0.62)	4.4°	10.2° (0.67)	4.1°
MF eversion	3.5°	8.1° (0.58)	4.6°	10.7° (1.35)	7.2°
MF inversion	7.0°	9.7° (0.87)	2.7°	12.3° (1.47)	5.3°
FT dorsiflexion	80.0°	70.1° (0.66)	-9.9°	73.5° (4.55)	-6.5°
FT plantarflexion	30.0°	40.8 (0.8)	10.8°	41.4° (0.62)	11.1°

The assembled foot showed good rotation angle matching overall. All joint rotations were easily induced. Maximum HM rotation angles most closely matched expected results, followed by the MF joint. Some motion showed slight over-rotation, especially with the FT and SH joint. Some errors that were present during initial block testing remained with the SLL pre-cast foot testing, such as slightly uneven

markers with respect to the camera, dimensional inaccuracies, and SH dislocation. The second copy results showed more over-rotation compared to the first copy. This is likely because of dimensional inaccuracy. While settings were identical, the two versions were printed at slightly different times. Weather, temperature, and overall printer conditions could have accumulated in causing variability between prints, which affected the rotation values. However, while maximum rotation angles were generally larger for the 2nd copy, it was still found to behave as intended, with maximum rotation angles within 2° or less of the ideal values for the most part.

The MF joint over-rotation was created by a higher gap than desired between the midfoot and forefoot. This gap was likely due to imperfections in the forefoot MF connector hole. The only viable printing orientation for the FT leaf-locks caused unsupported overhang within the MF connector hole, which could not be polished easily. These imperfections were not prevalent in the initial test blocks even though printing orientation remained the same. The difference between the initial block and full SLL foot could be due to the increase in volume and therefore additional heat, which takes longer to dissipate. This additional heat buildup would certainly slow the solidification process and cause the overhang surfaces to deform more after printing. Furthermore, a longer print time could have affected the components, since more water could have been absorbed during the process. However, water absorption was a known factor throughout the study and mid-print filament dehydration was not feasible. The internal surfaces could be cleaned and polished using specialized hooked tools. Polishing the internal surfaces would reduce the unwanted joint gap and bring maximum rotation closer to ideal values.

In most cases, rotation angles were found to be within human variation. Human joint variations is affected by several factors, such as gender, body proportions and structure. One study showed that overall body joints were shown to have standard deviation greater than 5° for most joints due to numerous factors. The study also showed that ankle rotations showed a standard deviation of 6.5° across both females and males [110]. As such, most SLL joints being within 2° or less of the ideal target was deemed acceptable. Moreover, it was deemed appropriate to continue with the casting process, as the addition of SR was expected to reduce overall motion slightly, counteracting the over-rotations found here.

6.2.3 Post-Cast 3D Printed SLL Testing

6.2.3.1 Methodology

After SLL foot rotation angles were confirmed, the first SLL foot copy was cast in SR and its motion was tested to ensure that rotation angles were not impeded beyond expectations. The methodology was identical to pre-cast testing, with markers placed on mould pin locations as matching reference points to pre-cast conditions. To prevent the vice from damaging the SR, protective cardboard was inserted between the cast foot and the vice.

6.2.3.2 Results and Discussion

The coordinate raw data was analyzed in the same way as previous motion tests. Appendix E.1.3 shows all motion graphs for post-cast motion results. The averaged maximum joint planar rotation angles were listed in Table 6-3.

Table 6-3: Pre-cast vs post cast joint rotation angles

Joint	Ideal angle	Pre-cast angle (SD)	Post-cast angle (SD)	Difference Pre-Post	Difference Ideal-Post
SH frontal	50.0°	43.9° (0.30)	50.3° (2.60)	6.4°	0.3°
SH sagittal	70.0°	71.3° (2.45)	64.5° (2.53)	-6.8°	-5.5°
HM abduction	0.5°	3.0° (0.09)	1.9° (0.27)	-1.1°	1.4°
HM adduction	3.8°	3.9° (0.25)	2.7° (0.17)	-1.2°	-1.1°
HM dorsiflexion	2.2°	2.5° (0.07)	3.1° (0.18)	0.6°	0.9°
HM plantarflexion	2.2°	3.1° (0.36)	4.2° (0.43)	1.1°	2.0°
HM eversion	3.5°	4.1° (0.58)	4.4° (0.93)	0.3°	0.9°
HM inversion	3.2°	5.1° (0.02)	5.2° (0.01)	0.1°	2.0°
MF abduction	2.0°	4.7° (0.08)	6.7° (0.96)	2.0°	4.7°
MF adduction	6.5°	11.8° (0.40)	7.1° (0.19)	-4.7°	0.6°
MF dorsiflexion	6.5°	10.1° (1.17)	7.2° (1.69)	-2.9°	0.7°
MF plantarflexion	6.1°	10.5° (0.62)	7.1° (0.28)	3.4°	1.0°
MF eversion	3.5°	8.1° (0.58)	5.9° (0.72)	-2.2°	2.4°
MF inversion	7.0°	9.7° (0.87)	7.0° (0.35)	-2.7°	0.0°
FT dorsiflexion	80.0°	70.1° (0.66)	39.7° (4.14)	-30.4°	-40.3°
FT plantarflexion	30.0°	40.8 (0.8)	25.5° (0.30)	-15.3°	-4.5°

The post-casted foot behaved well. The SR held the shape well during joint rotation, stretching and then returning to original position without tear or deformation. The rotation was still easily performed, showing

that wrapping the foot before casting maintained the intended gap between components. The wrap kept the motion-defining features clear, easing joint rotation.

The post-casted joint motion showed improved motion accuracy when compared to desired results. Given that the pre-casted foot showed some level of over-extension, the SR's added resistance returned the joints closer to target maximum rotations angles: nine planar motions were improved, while four remained close, within human variability. One clear example was FT plantarflexion: there was a decrease of 15.3° after casting. However, given over-rotation in pre-cast testing, this decrease still brought the peak rotation closer to the desired RoM, improving overall results.

The main joint error was with the FT dorsiflexion, showing more than 40° difference. This disparity was caused by the SR, which added a lot of material to the dorsiflexion motion, increasing resistance even though the joint was wrapped before casting. The joint's dorsiflexion required more SR deformation than other joints due to the large RoM. The joint's geometry resulted in more material added in dorsiflexion than in plantarflexion or other joints. However, while normal MTP dorsiflexion is 80°-90°, normal dorsiflexion varies based on a person's condition. Nawoczenski et al. measured different passive dorsiflexion between weight-bearing (37±2.8°) and non-weight bearing patients (57±3.1°) [111], closer to post-casted results. Furthermore, since the load was manually applied to the SLL, pushing became more difficult past 40°. Machine loading would allow better control and likely could create more rotation.

SH motion had the same degree of difference between obtained and expected results, which was to be expected since this joint was not affected by casting. The other joints were still within human variability, less than 6.5° of variation [110], and were deemed acceptable (Table 6-3). Although FT joints had large differences from expected values, results were still close to weight-bearing dorsiflexion. Furthermore, machine loading would likely generate more rotation in FT dorsiflexion, reducing this difference further.

Chapter 7

Load Testing

Just as motion testing was essential for validating the SLL design, static and cyclic load testing was also necessary. Load testing involved the application of a load to the SLL with an AFO, as well as on some of its subcomponents. The SLL and its components were loaded to ensure adequate durability and strength.

7.1 Initial Compressive Tests

Before testing the full leg under static and cyclic load conditions, the weakest load bearing components (the nylon and the SR) were tested in compression to confirm that the material strength would be suitable for the application and would be worthy of further testing. A heel base, along with associated heel plates were printed and used in tandem with a ball stud for the nylon test. The heel base was chosen because this component would be subjected to the greatest compressive loads during testing. A small rectangular slab of Mold star 30™ was used for SR testing. These tests were used to validate that the selected material could sustain the maximum load before subjecting the entire SLL to prolonged loading.

7.1.1 Initial Compressive Test Methodologies

For the nylon heel base, the ball stud was included to better reproduce real loading. To prevent damaging threads, a hollow metal cylinder transferred the Instron compressive plate's load to the ball stud and integrated hex nut (Figure 7-1). The initial test speed was set to 0.1 mm/minute, loading up to 500 N. The second and third tests had a higher speed of 0.5 mm/minute. For the SR slab, loading was placed between a wooden block and the Instron compressive plate to create two flat surfaces (Figure 7-2). The initial loading rate was set to 0.1 mm/minute up to 100 N, then the other two tests had a loading rate of 1 mm/minute due to the higher compressibility of SR.

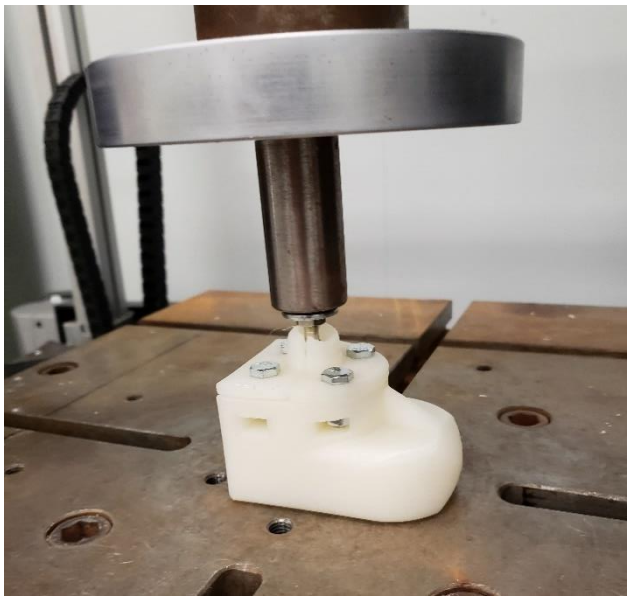

Figure 7-1: Heel base compressive test set up

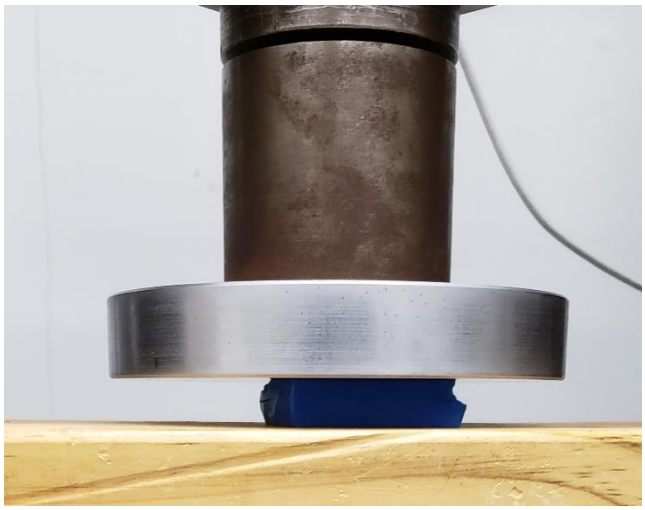

Figure 7-2: SR compressive test set up

An Instron Model 4482 was used to apply a controlled compressive load on each material. Three tests were performed for each material. The first test was conducted at a low loading rate up to a low load to properly set the loading condition, the second and third tests were conducted at faster rates. The second test went up to 1000 N, while the third test went up to 2000 N or up to the point of plastic deformation, whichever came first. This approach gradually checked the limits of the material. Going beyond the static load of 1500 N set in section 3.3 enabled the limits to be defined for each material beyond the required

static load. For all six tests, the time elapsed, material compression displacement, and load applied were recorded digitally and graphed.

7.1.2 Initial Compressive Test Results and Discussion

With the measured displacement and applied load, the strain and stress were calculated to properly evaluate each material's deformation. With the measured displacement d, the strain was calculated using equation (7-1), where l_o represented the original length, set at 4.305 mm for the nylon socket radius and 16 mm for the SR slab thickness. Axial stress was calculated using equation (4-22). The ball stud surface area was calculated to be 87.04 mm^2, while the SR slab area was calculated to be 2321 mm^2. The stress-strain curves were plotted for each test and material, as shown in Figure 7-3 and Figure 7-4.

$$\varepsilon = \frac{d}{l_o} \tag{7-1}$$

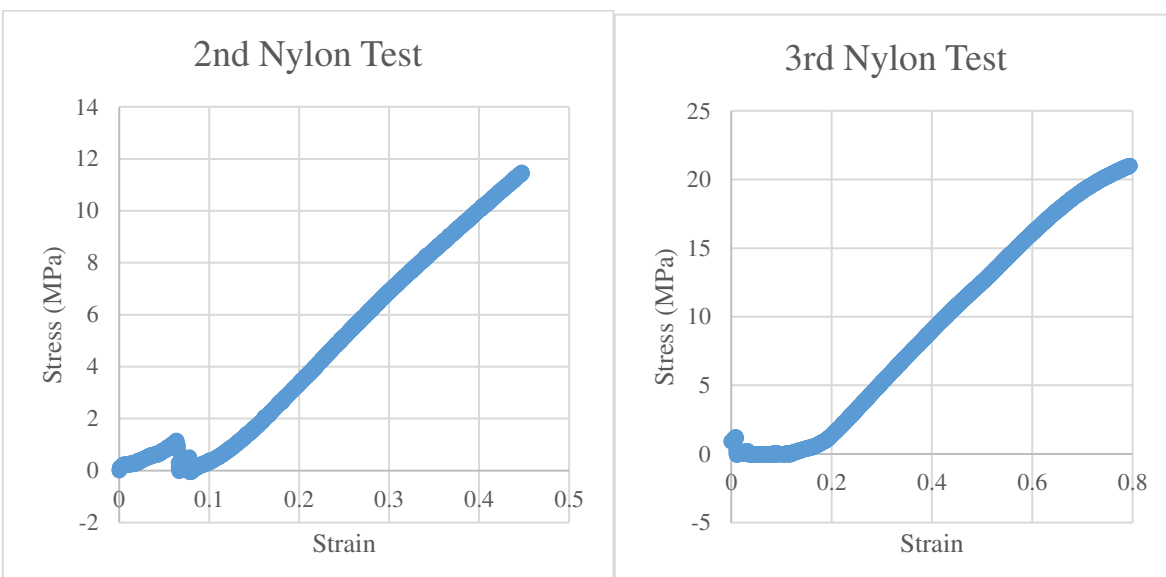

Figure 7-3: Initial compressive test stress versus strain graphs for the heel base

During the second Nylon test (Figure 7-3, left), the load was slightly misaligned and required adjustment at the beginning of data collection. This caused the unusual behaviour observed at the beginning of the test. Normal behaviour was observed after adjustment. The nylon stress-strain curve was found to be linear for most of the loading, with some plastic deformation observed after 1700 N. This was deemed to be acceptable given that the SLL would not be required to bear this much load during normal testing. The

maximum stress on the nylon block at 1500 N was approximately 17.2 MPa, lower than the ultimate strength provided by the nylon manufacturer [100]. Given that the SH ball socket was the most stressed nylon component, with the highest compressive load and smallest contact area, the material was deemed fit for further testing.

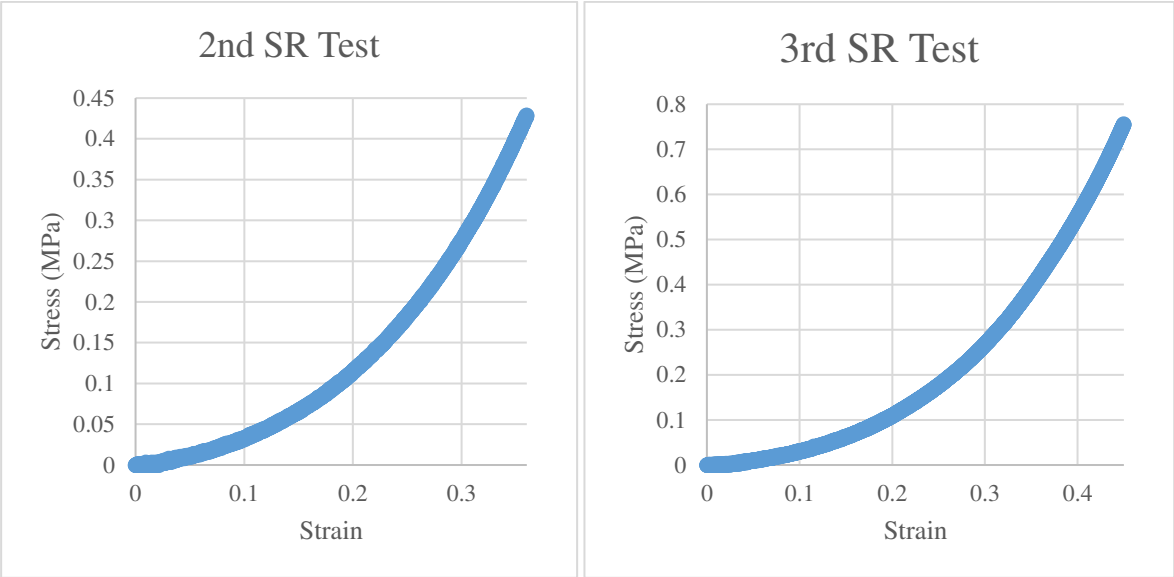

Figure 7-4: Initial compressive test stress vs strain graphs for the SR

The SR was loaded up to 2000 N without obvious plastic deformation. While the SR stress-strain curves were non-linear, the behaviour was repeatable and no visible damage on the test sample was observed after testing. The SR deformed more than the nylon component at 7.6 mm compared to 3.2 mm for the nylon. The SR deformation was fully elastic and, therefore, found fit for more testing.

7.2 SLL Static Loading

A static load test was set up to reproduce standing conditions, with the SLL angled in both the heel and forefoot positions for a fixed duration of time.

7.2.1 Static Loading Methodology

Before securing the SLL to the loading apparatus, the device was secured to a propylene non-articulated leaf spring AFO and footwear to recreate realistic loading conditions (Figure 7-5). The footwear consisted of an ankle sock and Europe size 46 (US 12 equivalent) shoe made by New Balance. The SLL was then

secured to the loading adapter, ensuring that the foot and SH elastics were positioned in the heel direction. The adapter was then secured to a Servo Hydraulic Frame Instron Model 1332 via the top adapter in the heel position (Figure 7-6).

Figure 7-5: SLL-AFO with sock only (left), then sock and shoe (right)

Figure 7-6: SLL in Instron

The Instron settings were set to properly load the SLL and record appropriate data. The maximum load capacity, 22 kip (97.8 kN), was set to 5% of its full range, showing ±1.1 kip (4.89 kN) at maximum voltage (10 V). The applied force was set as the controlling parameter while the displacement as auxiliary data.

The load was applied to the SLL in the heel position first. The load was increased manually by controlling the vertical stroke: a dial was manually turned to slowly raise the lower arm and bottom plate until the measured load reached the desired maximum static load of 1500 N. The arm position was then held for 30 s, then the load was removed by manually lowering the plate adapter. After the load was removed, the SLL was inspected visually for any defects, and the SLL was placed in the forefoot position. The load was applied again using identical settings. The load was removed and inspected again for signs of defects.

7.2.2 Static Loading Results and Discussion

The Instron control panel was connected to a computer, which recorded the voltage input and converted output voltages into displacement and load measurements through a LabView program (Appendix F.1.1) The program displayed and recorded applied load and lower arm vertical displacement at set time increments (1 s in this case). The vertical displacements and loads were then graphed separately to visualize the results (Figure 7-7 and Figure 7-8).

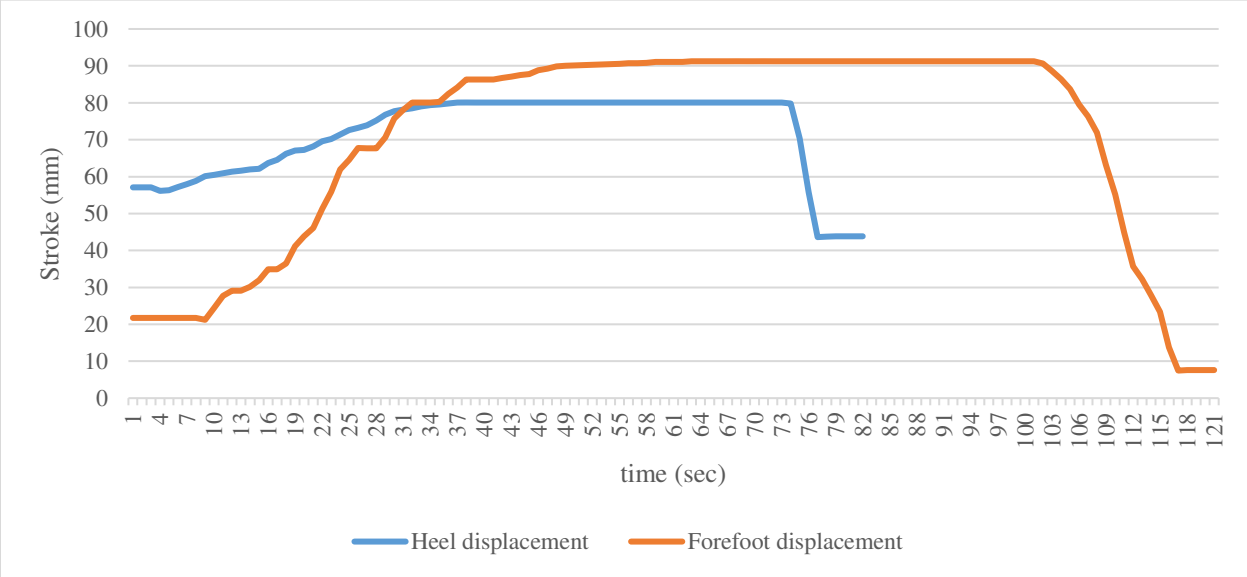

Figure 7-7: Static test vertical displacements

Given that the vertical displacement was the controlling unit, the motion was linear. Displacement was slowly increased as the load was measured. Given the higher angle, the forefoot required more vertical displacement to reach the desired load. The increase in required vertical motion was also due to the load-bearing elements with respect to the Instron motion arm. The heel had the SH joint almost directly beside the arm and only a small displacement was required to apply adequate pressure. The forefoot had the SH further away from the Instron arm, and therefore, required more vertical motion to apply appropriate load.

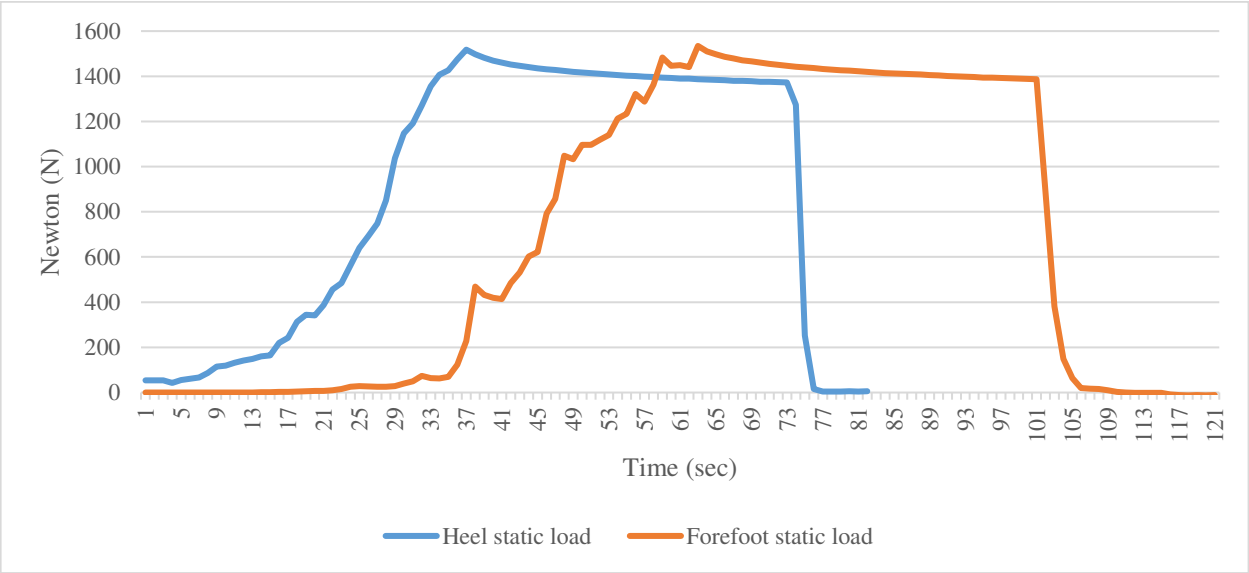

Figure 7-8: Measured static load applied on the SLL in both heel and forefoot positions

Once the Instron arm was raised to the adequate height, the desired load was reached. However, after motion stopped, the load did slowly decrease as the load was held. This decrease was likely caused by material relaxation, especially the SR and shoe sole, given their compliant and rubbery nature. While the load did decrease slightly during the held period, the load was still close to the desired load. As such, this slight decrease was deemed acceptable. Given the manual increase in vertical displacement, the initial loading response was not smooth. The vertical stoke was induced carefully with slower dial motions. This slow manual motion likely resulted in semi-stationary positions of the dial, especially for the forefoot build-up period, resulting in the jagged load increases observed in Figure 7-8. Stick-slip conditions in the SLL joints might also have been a factor, and should be investigated further.

Overall static load testing of the SLL was completed while retaining full structural integrity; The SR did not tear, the metal components remained structurally stable. The SLL was able to withstand more than 1400 N in both heel and forefoot positions for 30 s. When loaded, the foot supinated, slightly rotating medially. This could be due to several factors. The AFO's asymmetry (Figure 7-9) could have guided bending with a medial tendency. The load could also have been applied slightly more medially and created supination. Furthermore, the SLL foot could have had more space to supinate than pronate during loading, leading to the rotation. Testing the SLL with different AFOs and footwear could be considered, to confirm the rotation's cause.

While the rotation could lead to rolling ankles in real life situations, the loading apparatus prevents this potential issue for the SLL since the plate recreates an even footing with the flat plate. Furthermore, the constant compressive load prevents full ankle roll. Given the external factors affecting supination, the rotation was deemed acceptable for continued load testing.

Figure 7-9: AFO back profile

7.3 Cyclic Loading

Given that the lower limb is commonly used for cyclic loading, testing the SLL in a similar manner was essential for proper validation. As with static loading, the SLL was tested with an AFO and footwear. Once again, two tests were completed: one for the heel position and one in forefoot position.

7.3.1 Cyclic Loading Methodology

Cyclic tests were set up similarly to the static load tests, with the SLL loaded in the heel position first, then rotated to the forefoot position. The loads were produced by setting the load capacity to 5%, placing the setup in the appropriate load range. However, there were a few key differences between static and cyclic loading. In this case, the load was the driving setting, set to apply cyclic loads between 50 N and 1300 N. Both displacement and load controls were set to stop if the measurements reached a certain threshold. If the device tried to apply too much load or move too far due to component failure, the motion would stop automatically. The frequency for both positions was set to 0.8 Hz, replicating half of a 1.6 step/second gait [112]. 500,000 cycles were performed in each position.

Once heel position tests were completed, the device was removed and inspected for any potential creep or damage. The SLL was then re-attached to the Instron in the forefoot position and the cyclic load was repeated using identical settings.

7.3.2 Cyclic Loading Results Discussion

Data was recorded once again from the Instron machine using LabView. However, LabView (Appendix F.1.2) was set to only record the peak values for both vertical displacement and load at a set time interval. This time interval was increased from one second to one minute. The slower data sampling rate reduced the total data collected to a reasonable amount, given that cyclic loading would last a week in each position. While the recording rate was not synchronized with the loading frequency, the LabView program recorded the most recent maximum vertical motion and load peaks.

The data was then exported and plotted to visualize the results. Positive and negative peaks were plotted together to illustrate the amplitude for both load (Figure 7-10 and Figure 7-11) and vertical displacement (Figure 7-12 and Figure 7-13).

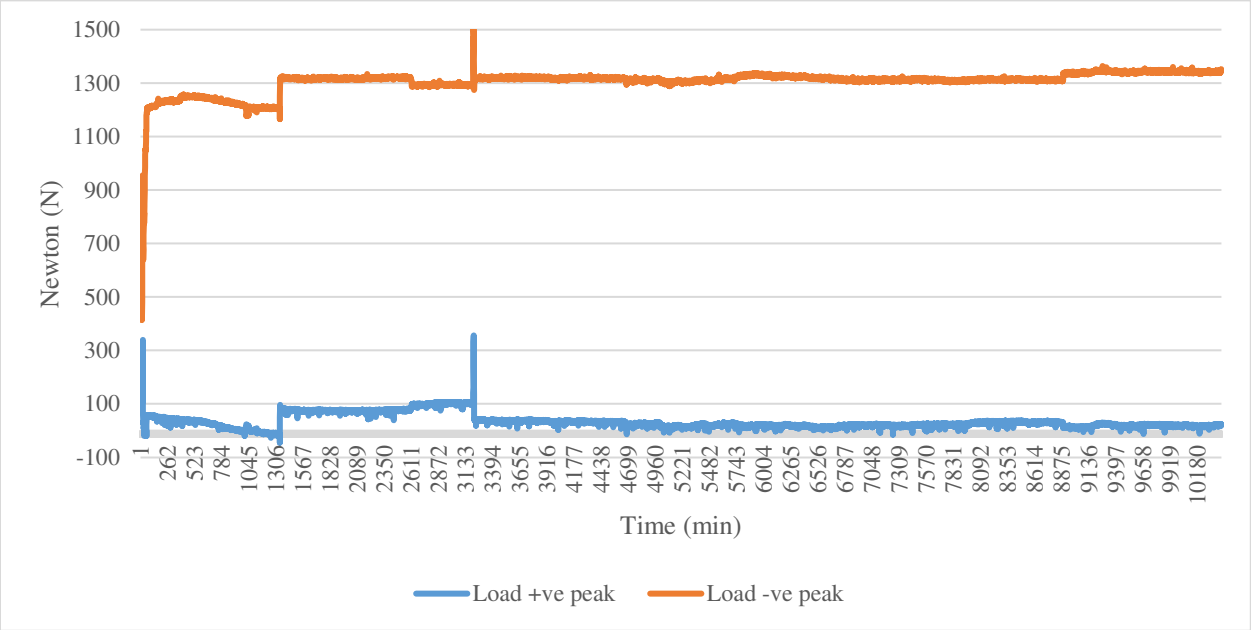

Figure 7-10: Measured maximum and minimum loads induced during cyclic testing in heel position

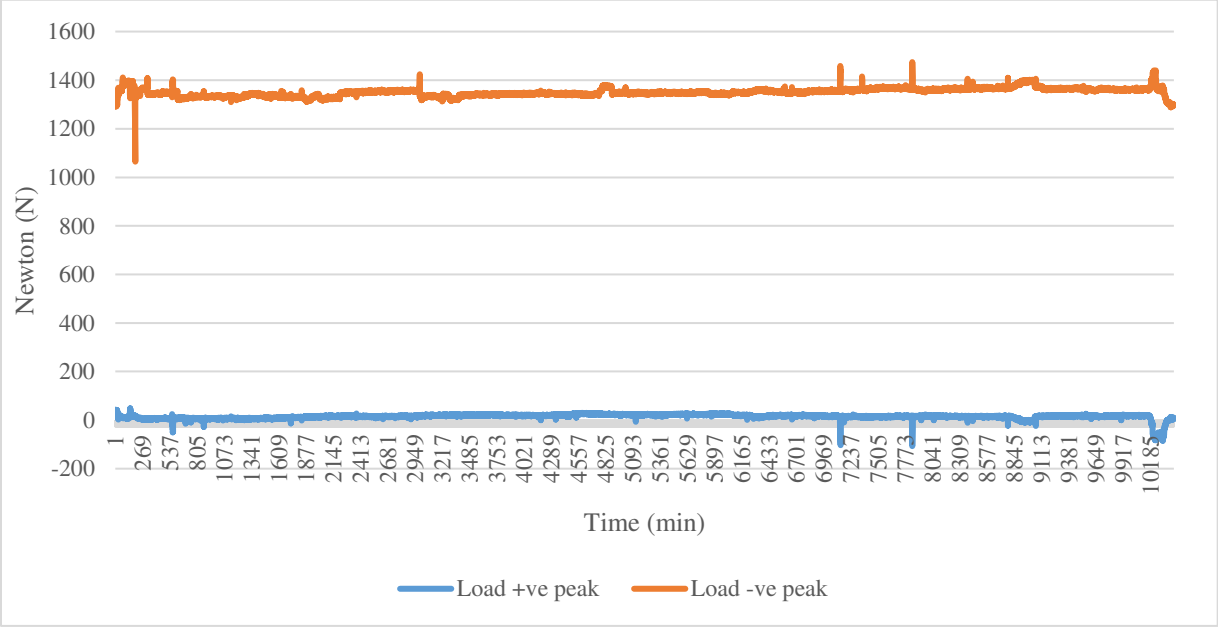

Figure 7-11: Measured maximum and minimum loads induced during cyclic testing in forefoot position

Given that the load was the control setting, the Instron machine aimed to create required loads by pushing on the SLL with the bottom adapter. Therefore, the load was steady, without much variation because the instructions were to create steady amplitude. However, there are small variations at the beginning that were created due to small tweaks and adjustments to the load control panel to get the load amplitude within its target range. The spike at minute 3210-3213 in Figure 7-10 was created by an over-adjustment of the control panel, to maintain the load at appropriate levels after the first overnight period of testing. This over-adjustment was quickly corrected and did not negatively affect further results. The other smaller spikes were caused by small adjustments to the SLL, which moved the upper Instron arm, where the sensors are located. However, given the low frequency of adjustments, the testing was not affected.

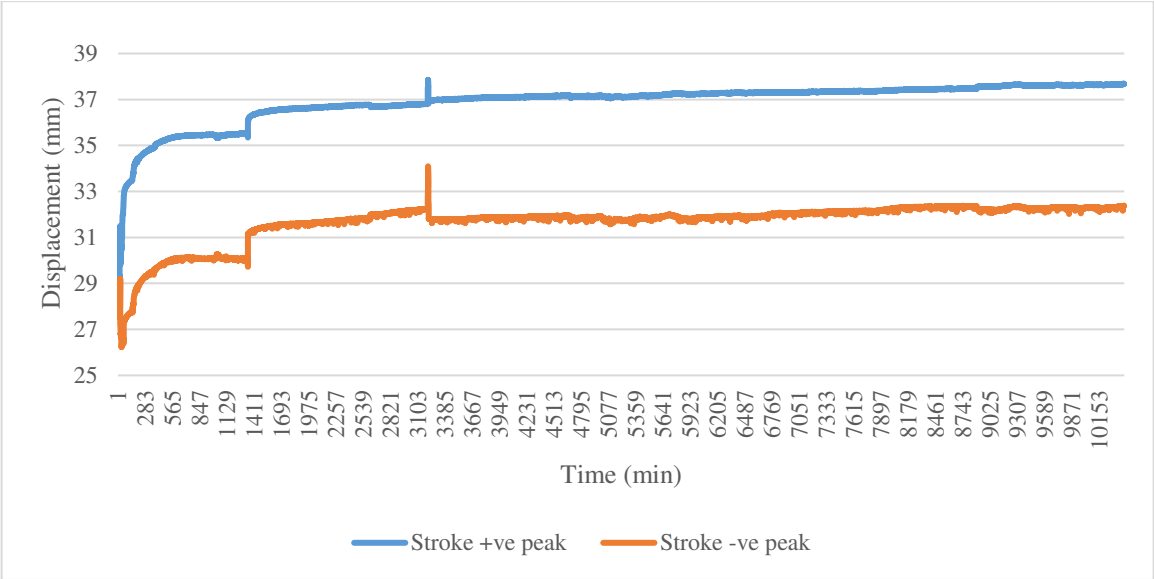

Figure 7-12: Measured maximum and minimum vertical positions during cyclic testing in the heel position

The vertical machine displacements showed mostly steady load, after initial small adjustments. As such, the load was induced with constant vertical displacement, showing that the SLL could take the cyclic loading. While the amplitude remained steady, there was a slight increase in peak vertical displacement. The vertical displacement peaks were 31.2 mm-37.0 mm after initial adjustments and increased to 32.2 mm-37.7 mm. The amplitude increased slowly by roughly 0.7 mm over the 500,000 cycles. This increase was caused by a higher required displacement over time to create consistent loads. The required increase was likely caused by microscopic deformation caused by fatigue. The vertical displacement

increase shows that fatigue was slowly affecting the SLL components, which was expected, given that most material are not immune to fatigue. The increase in vertical displacement showed that the SLL would have a fatigue limit. However, given the slow increasing rate of vertical displacement, this limit should only be attained after achieving reasonable cyclic test limits appropriate for AFO cyclic testing. Further testing would be required to quantify the actual fatigue limit of the SLL.

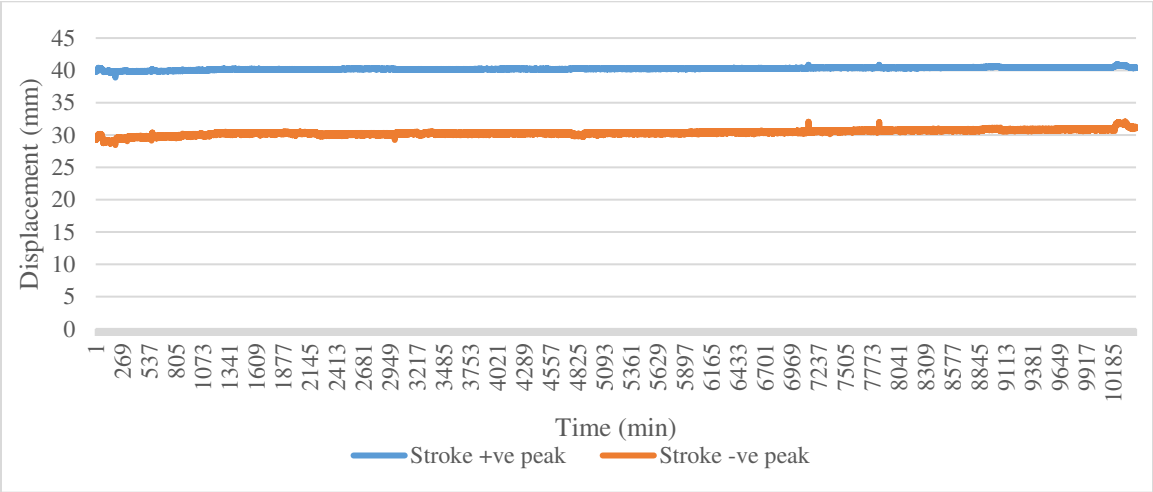

Figure 7-13: Measured maximum and minimum vertical positions during cyclic testing in the forefoot position

Overall, the SLL was shown to perform well in fatigue for both heel and forefoot positions. Most components were not affected or damaged by the test. As seen in Figure 7-10 and Figure 7-11, the load applied was mostly uniform, showing that the metal, nylon and TPU components handled cyclic loading well. The AFO and footwear definitively helped bear the load since the AFO distributed the load from the sole of the foot to the shank. The footwear also protected the foot from friction.

Nonetheless, there were a few components that were indeed affected by fatigue wear. The SR tore on the heel base medial side (Figure 7-14) during the heel test. This is likely due to foot supination, which pushed more into this side compared to the lateral side. The SR shell was found to be very thin in this region as well, with trapped air bubbles adding stress concentrations on this side. Increasing the thickness of the SR shell would likely prevent tearing. This thickness could be created by modifying the mould to include a larger void in this region or reducing the heel base volume at that location via a larger fillet or curved sole, providing more space for the SR. However, even with a tear in the SR, the shell did hold its shape and

could still function as intended. Moreover, the SH stiffness elastics did show partial tearing due to the hose clamp's edge and the distal washer edges. This would evidently be problematic during longer testing. Smoothing the SH elastic to hose clamp and washer connections would reduce the possibility of creating a tear initiation point.

Figure 7-14: Tearing after cyclic loading

The SH joint was under constant motion, and therefore, was the joint most affected by wear. The SH ball remained in its socket due to the constant compressive load on the foot. However, the small lip holding the ball in place was affected due to fatigue, as lateral forces caused the ball and socket joint to loosen over time. Increasing the SH ball diameter relative to the neck would create more material available to hold the ball in place, reducing the wear on this joint.

While some wear was present, the SLL design was shown to survive the specified loading conditions for at least 500,000 cycles in both heel and forefoot positions at a frequency of 0.8 Hz, mimicking average cadence. Further cyclic testing involving longer durations should be considered if the SLL's fatigue limit become important.

Chapter 8

Discussion, Conclusions and Future Work

8.1 Discussion

8.1.1 Positive Design Attributes and Improvements

Most SLL design aspects worked out as intended. Joints offered]large surfaces for load transfer while constraining the rotation to adequate RoM angles. The connectors provided resistance without completely impeding rotation. The SR offered compliance while demonstrating good fatigue strength, with only minor aesthetic tearing occurring at a thin section. This tearing could easily be mitigated by increasing the thickness of SR at the tear location.

The overall SLL fabrication process was simple and the SLL was found to be easy to assemble. Casting foot structure was also found to be simple, given the easy mixture and setting requirements for Mold Star 30™. However, some Bubbles were found to be trapped under the foot due to its positioning during casting. Nonetheless, these bubbles did not appear to have critical impact on the design. Furthermore, these bubbles could be mitigated greatly with adequate vibrations of the mould before curing, dislodging the trapped air under the foot. SH elastic connections were found to be difficult to install due to the testing apparatus and top adapter threads. The SH elastics needed to be altered so that the shaft could be rotated in the proper direction, then secured to the shaft. However, this process was simple, by loosening the hose clamp and rotating the shaft before re-tightening the clamp again. Future testing could use an adapter design that would not require rotation of the shaft during installation.

The total fabrication cost was found to be a positive attribute of the design, assuming that a 3D printer is already accessible to the user. The SR cost was reasonable at $45.00 per pint, which would enable one full SR shell. Nylon 230 and Cheetah™ TPU filament spools were both $59.95, while PLA was $39.95.

However, these prices are for full spools, being 1 kg for both nylon 230 and PLA, and 0.5 kg for TPU. Given that estimated filament used per SLL was 450 g for nylon 230, 81 g for TPU, and 1466 g for PLA, the real filament cost would be $26.98 for nylon, $9.71 for TPU, and $58.57 for PLA (requiring 2 spools). Shaft material and machining cost were approximately $150.00. Given the price of other components, such as bolts, nuts, elastic, etc (given in Appendix C), the total cost for one SLL was calculated to be approximately $370.00.

Time considerations are also important for cost calculations. The only relevant time to consider here was the 3D printing time and SR curing time. Most 3D prints only took a few hours. The exceptions were the shank cover, mould segments, and heel base, taking more than half a day each to make due to their size. Even with these larger prints, the entire assembly could be done within a week. SR curing would then take another 6 hours, as specified in section 4.5.1.

Another fabrication alternative would be to send the 3D prints to an external printing facility, such as HUBS, a major FDM service website. However, in this case costs can be much higher. A quote from HUBS, estimated a total cost of $1120.00. As such, using FDM printers locally remains an interesting option, if available.

A few design aspects require some improvement. FDM print variability remains an issue if highly accurate RoM results are sought, even after applying careful design considerations. FDM is affected by several factors including the conditions of the print environment. As such, moving FDM production to an environment with better controls over temperature, humidity, and air flow would likely result in more consistent prints.

Another aspect requiring improvement was the SH ball stud. Due to the ball stud's ball to neck diameter ratio, there was only a small lip that could be designed to hold the ball within the socket. As discussed in section 6.2.1.4, increasing that ratio with a bigger ball would minimize this issue. The shank cover used for this study was also found to be narrower than anatomical limbs found in the literature, requiring the AFO to be modified slightly to properly fit the SLL. While this was not an issue for testing, it would be important

to size the shank cover according to anthropometric values found in the literature if the SLL is to be used with existing AFO designs.

8.1.2 Modifications for Different Pathologies

The SLL CAD elements were designed to enable modifications to better represent various pathologies. These modifications were mostly focused on size and dimensions, by having the foot components increase or decrease to fit a large range of adult male shoe sizes. The modifications were also focused on making the motion-defining features discussed in section 4.1.1 easier to alter with global variables. As such, an individual with limited RoM could have an SLL designed to better represent their anatomy and specific RoM.

The HM, MF, and FT joint stiffnesses were defined by fixed component geometries and material properties. Changing these stiffnesses could be done by restructuring the connectors and respective holes to replicate specific stiffnesses instead of averaged values. Further engineering could enable simpler non-linear anthropometric scaling in the future. This change could also reflect female anatomical properties as well. The SH stiffness could be changed more easily, given that the elastics are external features. Different elastics could replace the current ones to change the overall stiffness across all directions. Additionally, elastics could be added to create a stiffer, or the elastic dimensions could be modified as well. Furthermore, given that there were four elastics present in design, each elastic could be chosen to represent a different stiffness in each rotational direction. For example, the SH joint could be made stiffer in plantarflexion by adding stiffer elastics anteriorly. Having four elastics enables a modular approach to SH stiffness, and therefore, greater flexibility for representing different pathologies.

8.1.3 Further Testing with AFO

This thesis focused on the design and validation of an SLL that could be used for AFO testing. However, the physical limitations of the SLL were not measured. The current adapter was not designed destructive loading of the SLL, given that the moment would be greatest at the top adapter. Initial compressive tests

were done to find some limit to the design, but only on the weakest components. The fully assembled SLL should be tested to understand the maximum compressive loads that can be supported.

Future SLL use will focus on AFO testing with different AFO designs to further validate the SLL presented in this thesis. To ensure appropriate testing of AFOs a rigorous test method using the SLL, similar to ISO 10328:2016, should be developed, including static, cyclic, and destructive tests.

Given that the SLL's RoMs and stiffnesses are known, AFO tests could focus on measuring the difference in these properties when using a given AFO. The level of support provided by a given AFO could then be measured for each individual.

8.2 Conclusions

This thesis studied the anatomical behaviour of the AFC, from biological composition to RoM and modelling, to create a SLL that would behave and move in a similar fashion to a real lower limb. The thesis then rationalized reasonable testing conditions and developed a SLL design using motion constraining features, realistic joint stiffnesses, and accessible fabrication processes. The SLL was then tested and results validated the design against the original requirements.

- The maximum rotation angles for most SLL foot joints were found to be within 2° of the normal human range for anatomical passive RoM. While more precise AM processes could be used to reduce RoM variations, the current design still showed adequate RoM for AFO testing within typical human variation.
- Static load testing performed on nylon and SR showed that the two weakest materials that were used for this study could withstand 1500 N, matching 1.5 BW load for a 100 kg individual. Full SLL static loading showed that the overall design could sustain this load as well. Cyclic loading with a simple leaf-spring AFO showed that the SLL could survive at least 500,000 load cycles from 50 N to 1300 N in both heel and forefoot positions. The cyclic tests were not found to damage the SLL in a way that prevented further testing.

- The SLL was successfully designed to be easy to fabricate using readily available equipment, materials, and components, enhancing its access to a broad range of people working with AFOs. Using FDM to create the foot components enabled cost effective fabrication using strong materials. The Artillery Sidewinder X1 and filaments were specifically selected for their properties and their wide availability. Most metal components were chosen from commonly available sources that can be found in most hardware stores. Only the shank shaft and mould pins required machining. However, the materials used for these components were easy to acquire and prepare.
- The SLL model was successfully designed to be parametric, accommodating a large range of common foot and AFO sizes, by adding anthropometric scaling ratios to vital dimensions across all CAD components. As such, the digital components could be changed easily based on the desired FL. The scaling also incorporated the mould and pin locations, based on the Össur prosthetic foot cover length. This enabled the SLL to be constructed to represent any FL from US size 6 to US size 16.

8.3 Future Work

In the future, several things could be done to improve the SLL design:

- Several AFO designs could be tested with the proposed SLL and compared to the performance of a healthy lower limb to validate anatomical behaviour.
- The design of the SLL shank cover should be improved to better match average anatomical calf dimensions. The cover model used for this study was acquired through an open-source CAD model repository and is thinner than a realistic shank. The radius could also be enlarged by adding a neoprene liner, as suggested by the orthosis expert.
- Full SLL scalability should also be confirmed experimentally. After printing the SLL in multiple sizes, testing should occur to confirm that the motion and strength design criteria are satisfied for the full design range specified herein.

- The FDM components could be printed using a higher precision printer to confirm that higher dimensional accuracy leads to less RoM differences between obtained and expected results.
- A copy of the SLL could be sent to Össur for testing on a purpose built prosthetic testing machine according to ISO cyclic testing standards. In this case, the AFO could be tested under sequential heel/forefoot cyclic loading conditions to ensure that results are as expected.
- The SH ball stud connection should be improved to prevent dislocation. A ball stud with a larger ball to neck ratio should be found and integrated into the design.

References

[1] M. Franceschini, M. Massucci, L. Ferrari, M. Agosti, and C. Paroli, "Effects of an ankle-foot orthosis on spatiotemporal parameters and energy cost of hemiparetic gait," *Clin. Rehabil.*, vol. 17, no. 4, pp. 368–372, Jun. 2003, doi: 10.1191/0269215503cr622oa.

[2] K. Monaghan, E. Delahunt, and B. Caulfield, "Ankle function during gait in patients with chronic ankle instability compared to controls," *Clin. Biomech.*, vol. 21, no. 2, pp. 168–174, Feb. 2006, doi: 10.1016/j.clinbiomech.2005.09.004.

[3] A. Daryabor, M. Arazpour, and G. Aminian, "Effect of different designs of ankle-foot orthoses on gait in patients with stroke: A systematic review," *Gait Posture*, vol. 62, pp. 268–279, May 2018, doi: 10.1016/j.gaitpost.2018.03.026.

[4] S. Basiratzadeh, E. D. Lemaire, M. Dorrikhteh, and N. Baddour, "Fiducial Marker Approach for Biomechanical Smartphone-Based Measurements," in *2019 3rd International Conference on Bio-engineering for Smart Technologies (BioSMART)*, Apr. 2019, pp. 1–4. doi: 10.1109/BIOSMART.2019.8734237.

[5] Gy. T. W. vector image was created with Inkscape, *English: Planes of human anatomy*. 2008. Accessed: Sep. 21, 2021. [Online]. Available: https://commons.wikimedia.org/wiki/File:Human_anatomy_planes.svg

[6] "Anatomical Terms of Movement - Flexion - Rotation - TeachMeAnatomy." https://teachmeanatomy.info/the-basics/anatomical-terminology/terms-of-movement/ (accessed Oct. 25, 2020).

[7] C. L. Brockett and G. J. Chapman, "Biomechanics of the ankle," *Orthop. Trauma*, vol. 30, no. 3, pp. 232–238, Jun. 2016, doi: 10.1016/j.mporth.2016.04.015.

[8] U. F. O. Themes, "Structure and Function of the Ankle and Foot," *Musculoskeletal Key*, Dec. 05, 2016. https://musculoskeletalkey.com/structure-and-function-of-the-ankle-and-foot/ (accessed Jul. 01, 2021).

[9] O. College, *English: Anatomy & Physiology, Connexions Web site. http://cnx.org/content/col11496/1.6/, Jun 19, 2013*. 2013. Accessed: Sep. 20, 2021. [Online]. Available: https://commons.wikimedia.org/wiki/File:812_Bones_of_the_Foot.jpg

[10] C. L. Riegger, "Anatomy of the Ankle and Foot," *Phys. Ther.*, p. 13.

[11] S. Pal, "Mechanical Properties of Biological Materials," in *Design of Artificial Human Joints & Organs*, S. Pal, Ed. Boston, MA: Springer US, 2014, pp. 23–40. doi: 10.1007/978-1-4614-6255-2_2.

[12] Y. C. Fung, *Biomechanics: Mechanical Properties of Living Tissues*. Springer Science & Business Media, 2013.

[13] S. C. Cowin and S. B. Doty, *Tissue Mechanics*, 2007 edition. New York: Springer, 2006.

[14] A. K. Dąbrowska *et al.*, "Materials used to simulate physical properties of human skin," *Skin Res. Technol.*, vol. 22, no. 1, pp. 3–14, 2016, doi: 10.1111/srt.12235.

[15] R. Periyasamy, S. Anand, and A. C. Ammini, "The effect of aging on the hardness of foot sole skin: A preliminary study," *The Foot*, vol. 22, no. 2, pp. 95–99, Jun. 2012, doi: 10.1016/j.foot.2012.01.003.

[16] I. Healthcare, *International Encyclopedia of Ergonomics and Human Factors - 3 Volume Set*. CRC Press, 2000.

[17] R. M. White, "Comparative Anthropometry of the Foot:," Defense Technical Information Center, Fort Belvoir, VA, Dec. 1982. doi: 10.21236/ADA126189.

[18] M. Hajaghazadeh, R. Minaei, T. Allahyari, and H. Khalkhali, "Anthropometric Dimensions of Foot in Northwestern Iran and Comparison with Other Populations," *Health Scope*, vol. In Press, Aug. 2018, doi: 10.5812/jhealthscope.14063.

[19] *Biomechanics and Motor Control of Human Movement*, 4 edition. Hoboken, N.J: Wiley, 2009.

[20] "Shoe Size Converter Charts." https://www.shoesizingcharts.com/ (accessed May 15, 2020).

[21] "Definition of JOINT." https://www.merriam-webster.com/dictionary/joint (accessed May 17, 2021).

[22] E. J. C. Dawe and J. Davis, "(vi) Anatomy and biomechanics of the foot and ankle," *Orthop. Trauma*, vol. 25, no. 4, pp. 279–286, Aug. 2011, doi: 10.1016/j.mporth.2011.02.004.
[23] J. M. Czerniecki, "Foot and Ankle Biomechanics in Walking and Running: A Review," *J. Phys. Med.*, vol. 67, no. 6, pp. 246–252, Dec. 1988.
[24] "Physical Therapy (PT) - Special Subjects," *MSD Manual Professional Edition*. https://www.msdmanuals.com/professional/special-subjects/rehabilitation/physical-therapy-pt (accessed Sep. 22, 2020).
[25] D. J. G. Stephen, G. W. Choy, and A. G. Fam, "7 - THE ANKLE AND FOOT," in *Fam's Musculoskeletal Examination and Joint Injection Techniques (Second Edition)*, G. V. Lawry, H. J. Kreder, G. A. Hawker, and D. Jerome, Eds. Philadelphia: Mosby, 2010, pp. 89–101. doi: 10.1016/B978-0-323-06504-7.10007-7.
[26] A. P. Monk, D. J. Simpson, N. D. Riley, D. W. Murray, and H. S. Gill, "Biomechanics in orthopaedics: considerations of the lower limb," *Surg. Oxf.*, vol. 31, no. 9, pp. 445–451, Sep. 2013, doi: 10.1016/j.mpsur.2013.07.002.
[27] P. Ball and G. Johnson, "Technique for the measurement of hindfoot inversion and eversion and its use to study a normal population," *Clin. Biomech.*, vol. 11, no. 3, pp. 165–169, Apr. 1996, doi: 10.1016/0268-0033(95)00059-3.
[28] S. F. A. FACFAOM D. P. M. ,. C. Ped and S. A. C. P. D. FHEA BSc (Hons), FCPodMed, FFPM RCPS (Glas), *Lower Extremity Biomechanics: Theory and Practice Volume 1*. Bipedmed, LLC, 2018.
[29] C. B. B. Ledoux Tracy J. Yuen, Bruce J. Sangeorzan, William R., "The Midtarsal Joint Locking Mechanism - C. Brian Blackwood, Tracy J. Yuen, Bruce J. Sangeorzan, William R. Ledoux, 2005," *Foot Ankle Int.*, Nov. 2016, Accessed: Sep. 22, 2020. [Online]. Available: http://journals.sagepub.com/doi/full/10.1177/107110070502601213
[30] Y. Kim, S. Kim, B. Jeong, and J. Son, *Metatarsophalangeal Joint Kinetics in Normal Walking*. 2012.
[31] T.-K. Ahn, H. B. Kitaoka, Z.-P. Luo, and K.-N. An, "Kinematics and Contact Characteristics of the First Metatarsophalangeal Joint," *Foot Ankle Int.*, vol. 18, no. 3, pp. 170–174, Mar. 1997, doi: 10.1177/107110079701800310.
[32] J. Joseph, "RANGE OF MOVEMENT OF THE GREAT TOE IN MEN," *J. Bone Joint Surg. Br.*, vol. 36-B, no. 3, pp. 450–457, Aug. 1954, doi: 10.1302/0301-620X.36B3.450.
[33] S. P. Tavara-Vidalón, M. Á. Monge-Vera, G. Lafuente-Sotillos, G. Domínguez-Maldonado, and P. V. Munuera-Martínez, "Static Range of Motion of the First Metatarsal in the Sagittal and Frontal Planes," *J. Clin. Med.*, vol. 7, no. 11, Art. no. 11, Nov. 2018, doi: 10.3390/jcm7110456.
[34] "Effect of Peroneal Electrical Stimulation Versus an Ankle-Foot Orthosis on Obstacle Avoidance Ability in People With Stroke-Related Foot Drop | Physical Therapy | Oxford Academic." https://academic.oup.com/ptj/article/92/3/398/2735246 (accessed Sep. 15, 2020).
[35] S. Rao, C. Saltzman, and H. J. Yack, "Segmental foot mobility in individuals with and without diabetes and neuropathy," *Clin. Biomech.*, vol. 22, no. 4, pp. 464–471, May 2007, doi: 10.1016/j.clinbiomech.2006.11.013.
[36] A. Leardini, M. G. Benedetti, L. Berti, D. Bettinelli, R. Nativo, and S. Giannini, "Rear-foot, mid-foot and fore-foot motion during the stance phase of gait," *Gait Posture*, vol. 25, no. 3, pp. 453–462, Mar. 2007, doi: 10.1016/j.gaitpost.2006.05.017.
[37] S. L. Carter, N. Sato, and L. S. Hopper, "Kinematic repeatability of a multi-segment foot model for dance," *Sports Biomech.*, vol. 17, no. 1, pp. 48–66, Jan. 2018, doi: 10.1080/14763141.2017.1343864.
[38] A. Leardini and P. Caravaggi, "Kinematic Foot Models for Instrumented Gait Analysis," in *Handbook of Human Motion*, B. Müller, S. I. Wolf, G.-P. Brueggemann, Z. Deng, A. McIntosh, F. Miller, and W. S. Selbie, Eds. Cham: Springer International Publishing, 2017, pp. 1–24. doi: 10.1007/978-3-319-30808-1_28-1.
[39] M. C. Carson, M. E. Harrington, N. Thompson, J. J. O'Connor, and T. N. Theologis, "Kinematic analysis of a multi-segment foot model for research and clinical applications: a repeatability analysis," *J. Biomech.*, vol. 34, no. 10, pp. 1299–1307, Oct. 2001, doi: 10.1016/S0021-9290(01)00101-4.

[40] C. J. Nester, A. M. Liu, E. Ward, D. Howard, J. Cocheba, and T. Derrick, “Error in the description of foot kinematics due to violation of rigid body assumptions,” *J. Biomech.*, vol. 43, no. 4, pp. 666–672, Mar. 2010, doi: 10.1016/j.jbiomech.2009.10.027.
[41] T. Kobayashi, A. K. L. Leung, and S. W. Hutchins, “Techniques to measure rigidity of ankle-foot orthosis: A review,” *J. Rehabil. Res. Dev.*, vol. 48, no. 5, p. 565, 2011, doi: 10.1682/JRRD.2010.10.0193.
[42] H. K. Banga, R. M. Belokar, P. Kalra, and R. Kumar, “Fabrication and stress analysis of ankle foot orthosis with additive manufacturing,” *Rapid Prototyp. J.*, vol. 24, no. 2, pp. 301–312, Jan. 2018, doi: 10.1108/RPJ-08-2016-0125.
[43] H. S. Mali and S. Vasistha, “Fabrication of Customized Ankle Foot Orthosis (AFO) by Reverse Engineering Using Fused Deposition Modelling,” in *Advances in Additive Manufacturing and Joining*, Singapore, 2020, pp. 3–15. doi: 10.1007/978-981-32-9433-2_1.
[44] S. Telfer, J. Pallari, J. Munguia, K. Dalgarno, M. McGeough, and J. Woodburn, “Embracing additive manufacture: implications for foot and ankle orthosis design,” *BMC Musculoskelet. Disord.*, vol. 13, no. 1, p. 84, May 2012, doi: 10.1186/1471-2474-13-84.
[45] E. A. Middleton, G. R. B. Hurley, and J. S. McIlwain, “The role of rigid and hinged polypropylene ankle-foot-orthoses in the management of cerebral palsy: a case study,” *Prosthet. Orthot. Int.*, vol. 12, no. 3, pp. 129–135, Dec. 1988, doi: 10.3109/03093648809079396.
[46] M. Bhadane-Deshpande, “Towards a Shape Memory Alloy Based Variable Stiffness Ankle Foot Orthosis,” University of Toledo, 2012. Accessed: Sep. 15, 2020. [Online]. Available: https://etd.ohiolink.edu/pg_10?0::NO:10:P10_ACCESSION_NUM:toledo1333750098
[47] N. S. Thompson, T. C. Taylor, K. R. McCarthy, A. P. Cosgrove, and R. J. Baker, “Effect of a rigid ankle-foot orthosis on hamstring length in children with hemiplegia,” *Dev. Med. Child Neurol.*, vol. 44, no. 1, pp. 51–57, 2002, doi: 10.1111/j.1469-8749.2002.tb00259.x.
[48] A. Doğğan, M. MengüllüoĞĞlu, and N. Özgirgin, “Evaluation of the effect of ankle-foot orthosis use on balance and mobility in hemiparetic stroke patients,” *Disabil. Rehabil.*, vol. 33, no. 15–16, pp. 1433–1439, Jan. 2011, doi: 10.3109/09638288.2010.533243.
[49] L. R. Sheffler, M. T. Hennessey, J. S. Knutson, G. G. Naples, and J. Chae, “Functional Effect of an Ankle Foot Orthosis on Gait in Multiple Sclerosis: A Pilot Study,” *Am. J. Phys. Med. Rehabil.*, vol. 87, no. 1, pp. 26–32, Jan. 2008, doi: 10.1097/PHM.0b013e31815b5325.
[50] “Ground reaction and solid ankle–foot orthoses are equivalent for the correction of crouch gait in children with cerebral palsy - Ries - 2019 - Developmental Medicine & Child Neurology - Wiley Online Library.” https://onlinelibrary.wiley.com/doi/full/10.1111/dmcn.13999 (accessed Sep. 16, 2020).
[51] E. Russell Esposito, R. V. Blanck, N. G. Harper, J. R. Hsu, and J. M. Wilken, “How Does Ankle-foot Orthosis Stiffness Affect Gait in Patients With Lower Limb Salvage?,” *Clin. Orthop. Relat. Res.*, vol. 472, no. 10, pp. 3026–3035, Oct. 2014, doi: 10.1007/s11999-014-3661-3.
[52] B. Stier, J.-W. Simon, and S. Reese, “Numerical and experimental investigation of the structural behavior of a carbon fiber reinforced ankle-foot orthosis,” *Med. Eng. Phys.*, vol. 37, no. 5, pp. 505–511, May 2015, doi: 10.1016/j.medengphy.2015.02.002.
[53] “Computational and experimental evaluation of the mechanical properties of ankle foot orthoses: A literature review - Alessio Ielapi, Malcolm Forward, Matthieu De Beule, 2019.” https://journals.sagepub.com/doi/full/10.1177/0309364618824452?casa_token=JsII2uYzNNkAAAAA%3AvwUg_jicBJ5Iavnw8tYaMCHmbJ_M1mN4TdlsPz6wheJFOhzDy4rW7-L7lpLVo9Mx7C1NTiN7fSQ5gQ (accessed Sep. 15, 2020).
[54] “What Is FEA | Finite Element Analysis? SimScale Documentation,” *SimScale*. https://www.simscale.com/docs/simwiki/fea-finite-element-analysis/what-is-fea-finite-element-analysis/ (accessed Oct. 12, 2020).
[55] Cappa, Patane`, and M. M. Pierro, “A Novel Device to Evaluate the Stiffness of Ankle-Foot Orthosis Devices,” *J. Biomech. Eng.*, vol. 125, no. 6, pp. 913–917, Dec. 2003, doi: 10.1115/1.1634993.

[56] P. Cappa, F. Patanè, and G. Di Rosa, "A Continuous Loading Apparatus for Measuring Three-dimensional Stiffness of Ankle-Foot Orthoses," *J. Biomech. Eng.*, vol. 127, no. 6, pp. 1025–1029, Nov. 2005, doi: 10.1115/1.2049313.
[57] W. DeToro, "Plantarflexion Resistance of Selected Ankle-Foot Orthoses: A Pilot Study of Commonly Prescribed Prefabricated and Custom-Molded Alternatives," *Jpo J. Prosthet. Orthot.*, vol. 13, no. 2, pp. 39–44, Jun. 2001.
[58] W. Golay, T. Lunsford, B. R. Lunsford, and J. Greenfield, "The Effect of Malleolar Prominence on Polypropylene AFO Rigidity and Buckling," *JPO J. Prosthet. Orthot.*, vol. 1, no. 4, pp. 231–241, Jul. 1989.
[59] T. Kobayashi, A. k. L. Leung, Y. Akazawa, H. Naito, M. Tanaka, and S. W. Hutchins, "Design of an Automated Device to Measure Sagittal Plane Stiffness of an Articulated Ankle-Foot Orthosis," *Prosthet. Orthot. Int.*, vol. 34, no. 4, pp. 439–448, Dec. 2010, doi: 10.3109/03093646.2010.495370.
[60] A. Wach, "Mechanical Characterization of Carbon Fiber and Thermoplastic Ankle Foot Orthoses," *Masters Theses 2009 -*, Oct. 2015, [Online]. Available: https://epublications.marquette.edu/theses_open/341
[61] D. J. J. Bregman, A. Rozumalski, D. Koops, V. de Groot, M. Schwartz, and J. Harlaar, "A new method for evaluating ankle foot orthosis characteristics: BRUCE," *Gait Posture*, vol. 30, no. 2, pp. 144–149, Aug. 2009, doi: 10.1016/j.gaitpost.2009.05.012.
[62] "Additive manufacturing (3D printing)_ A review of materials, methods, applications and challenges | Elsevier Enhanced Reader." https://reader.elsevier.com/reader/sd/pii/S1359836817342944?token=069EB2DB86AC0F7EBA94B6BBC810A2701E70E9D0CAC192B9FD4DC9A7C4CA1DE96F5C5AAE8155EF448B09B83394C798B1 (accessed Jan. 22, 2020).
[63] "FDM process parameters influence over the mechanical properties of polymer specimens: A review," *Polym. Test.*, vol. 69, pp. 157–166, Aug. 2018, doi: 10.1016/j.polymertesting.2018.05.020.
[64] "2019 Types of 3D Printing Technology," *All3DP*, Jul. 22, 2019. https://all3dp.com/1/types-of-3d-printers-3d-printing-technology/ (accessed Jan. 22, 2020).
[65] A. Dasari, "Thermoplastics," in *Structural Materials and Processes in Transportation*, John Wiley & Sons, Ltd, 2013, pp. 183–203. doi: 10.1002/9783527649846.ch5.
[66] V. R. Sastri, "Chapter 3 - Materials Used in Medical Devices," in *Plastics in Medical Devices*, V. R. Sastri, Ed. Boston: William Andrew Publishing, 2010, pp. 21–32. doi: 10.1016/B978-0-8155-2027-6.10003-0.
[67] Z. Tao, H.-J. Ahn, C. Lian, K.-H. Lee, and C.-H. Lee, "Design and optimization of prosthetic foot by using polylactic acid 3D printing," *J. Mech. Sci. Technol.*, vol. 31, no. 5, pp. 2393–2398, May 2017, doi: 10.1007/s12206-017-0436-2.
[68] "Expert Tips for 3D Printing with PLA - Materials Guide." /support/materials-guide/pla/ (accessed Apr. 11, 2019).
[69] "Nylon 6 (PA) — Polyamide 6." https://www.rtpcompany.com/products/product-guide/nylon-6-pa-polyamide-6/ (accessed Jan. 27, 2020).
[70] "Strength to cost ratio analysis of FDM Nylon 12 3D Printed Parts," *Procedia Manuf.*, vol. 26, pp. 753–762, Jan. 2018, doi: 10.1016/j.promfg.2018.07.086.
[71] V. Solouki Bonab and I. Manas-Zloczower, "Chemorheology of thermoplastic polyurethane and thermoplastic polyurethane/carbon nanotube composite systems," *Polymer*, vol. 99, pp. 513–520, Sep. 2016, doi: 10.1016/j.polymer.2016.07.043.
[72] "Average height of men and women worldwide," *Worlddata.info*. https://www.worlddata.info/average-bodyheight.php (accessed Nov. 08, 2020).
[73] T. K. Uchida and S. L. Delp, *Biomechanics of Movement*, 1st ed. 2019.
[74] S. F. Tyson and H. A. Thornton, "The effect of a hinged ankle foot orthosis on hemiplegic gait: objective measures and users' opinions," *Clin. Rehabil.*, vol. 15, no. 1, pp. 53–58, Feb. 2001, doi: 10.1191/026921501673858908.

[75] T. S. Keller, A. M. Weisberger, J. L. Ray, S. S. Hasan, R. G. Shiavi, and D. M. Spengler, "Relationship between vertical ground reaction force and speed during walking, slow jogging, and running," *Clin. Biomech. Bristol Avon*, vol. 11, no. 5, pp. 253–259, Jul. 1996, doi: 10.1016/0268-0033(95)00068-2.
[76] 14:00-17:00, "ISO/WD 4549," *ISO*. https://www.iso.org/cms/render/live/en/sites/isoorg/contents/data/standard/08/00/80065.html (accessed Oct. 30, 2020).
[77] 14:00-17:00, "ISO 10328:2016," *ISO*. https://www.iso.org/cms/render/live/en/sites/isoorg/contents/data/standard/07/02/70205.html (accessed Apr. 15, 2020).
[78] 14:00-17:00, "ISO 10328:2016-Prosthetics — Structural testing of lower-limb prostheses — Requirements and test methods," *ISO*. https://www.iso.org/cms/render/live/en/sites/isoorg/contents/data/standard/07/02/70205.html (accessed Mar. 30, 2020).
[79] M. L. Heng, Y. K. Chua, H. K. Pek, P. Krishnasamy, and P. W. Kong, "A novel method of measuring passive quasi-stiffness in the first metatarsophalangeal joint," *J. Foot Ankle Res.*, vol. 9, no. 1, p. 41, Oct. 2016, doi: 10.1186/s13047-016-0173-2.
[80] "Cheetah 3D Printer Filament (95A)," *NinjaTek*. https://ninjatek.com/shop/cheetah/ (accessed Jul. 01, 2021).
[81] Bayer Material Science, *Snap-Fit Joints for Plastics-A Design Guide*. Pittsburg, 2013.
[82] "TPU 95A | Ultimaker," *Ultimaker.com*. http://ultimaker.com/en/resources/49917-tpu-95a (accessed Feb. 21, 2020).
[83] T. A. Lin, C.-W. Lou, and J.-H. Lin, "The Effects of Thermoplastic Polyurethane on the Structure and Mechanical Properties of Modified Polypropylene Blends," *Appl. Sci.*, vol. 7, no. 12, Art. no. 12, Dec. 2017, doi: 10.3390/app7121254.
[84] tleto, "Polyurethane Coefficient of Friction," *Gallagher Custom Polyurethane Molding*, Sep. 07, 2018. https://gallaghercorp.com/polyurethane-coefficient-of-friction/ (accessed Apr. 15, 2020).
[85] S. G. Trevino, W. L. Buford, T. Nakamura, A. J. Wright, and R. M. Patterson, "Use of a Torque-Range-of-Motion Device for Objective Differentiation of Diabetic from Normal Feet in Adults," *Foot Ankle Int.*, vol. 25, no. 8, pp. 561–567, Aug. 2004, doi: 10.1177/107110070402500809.
[86] H. J. Qi and M. C. Boyce, "Stress-Strain Behavior of Thermoplastic Polyurethane," p. 51.
[87] S. Xiong, R. S. Goonetilleke, C. P. Witana, and E. Y. L. Au, "Modelling foot height and foot shape-related dimensions," *Ergonomics*, vol. 51, no. 8, pp. 1272–1289, Aug. 2008, doi: 10.1080/00140130801996147.
[88] "Meaning of Clearance and Tolerance, by EPI Inc." http://www.epi-eng.com/mechanical_engineering_basics/clearance_and_tolerance.htm (accessed Jul. 02, 2021).
[89] "Dimensional accuracy of 3D printed parts," *3D Hubs*. https://www.3dhubs.com/knowledge-base/dimensional-accuracy-3d-printed-parts/ (accessed Feb. 22, 2021).
[90] *Fundamentals of Machine Component Design*, 5 edition. Hoboken, NJ: Wiley, 2011.
[91] *Shigley's Mechanical Engineering Design*, 10 edition. New York, NY: McGraw-Hill Education, 2014.
[92] "QA1 BJDL5 Quick Disconnect Ball Joint, Carbon Steel, 5/16-24 Thread," *Speedway Motors*. https://www.speedwaymotors.com/QA1-BJDL5-Quick-Disconnect-Ball-Joint-Carbon-Steel-5-16-24-Thread,260897.html (accessed Feb. 02, 2021).
[93] "AISI 1045 Steel, cold drawn, 19-32 mm (0.75-1.25 in) round." http://www.matweb.com/search/DataSheet.aspx?MatGUID=cbe4fd0a73cf4690853935f52d910784&ckck=1 (accessed Jun. 07, 2021).
[94] Z. I. Syed, "Stress analysis of welded gusseted frames," Master of Science, Iowa State University, Digital Repository, Ames, 2011. doi: 10.31274/etd-180810-1278.
[95] "AISI 1018 Steel, cold drawn." http://www.matweb.com/search/DataSheet.aspx?MatGUID=3a9cc570fbb24d119f08db22a53e2421 (accessed Mar. 23, 2021).

[96] Thingiverse.com, "Cover leg prosthesis by jorge22." https://www.thingiverse.com/thing:3121435 (accessed Nov. 30, 2020).
[97] "Haquno Resistance Loop Exercise Bands for Home Fitness, Stretching, Strength Training, Physical Therapy, Workout Bands, Pilates Flexbands, Set of 5 Green, Blue, Yellow, red, Black: Amazon.ca: Sports & Outdoors." https://www.amazon.ca/gp/product/B08CXR96BF/ref=ppx_yo_dt_b_asin_title_o03_s01?ie=UTF8&psc=1 (accessed Jun. 15, 2021).
[98] K. Elleuch, R. Elleuch, and H. Zahouani, "Comparison of elastic and tactile behavior of human skin and elastomeric materials through tribological tests," *Polym. Eng. Sci.*, vol. 46, no. 12, pp. 1715–1720, 2006, doi: https://doi.org/10.1002/pen.20637.
[99] "Sealer and Release Agent Reference Guide," *Smooth-On, Inc.* https://www.smooth-on.com/page/sealers-releases/ (accessed Dec. 31, 2020).
[100] "Nylon 230 Spec," *TAULMAN3D*. http://taulman3d.com/nylon-230-spec.html (accessed Feb. 01, 2021).
[101] "Everything you need to know about Nylon 3D printing," *MakerBot*, Apr. 30, 2020. https://www.makerbot.com/stories/design/nylon-3d-printing/ (accessed Jan. 18, 2021).
[102] "Onyx," *Markforged*. http://support.markforged.com/hc/en-us/articles/209934486-Onyx (accessed Feb. 25, 2020).
[103] "Artillery® Sidewinder X1 SW-X1 3D Printer 300x300x400mm Large Plus Size High Precision Dual Z axis TFT Touch Screen," *Artillery 3D Printer*. https://artillery3d.com/products/artillery-sidewinder-x1-sw-x1-3d-printer-300x300x400mm-large-plus-size-high-precision-dual-z-axis-tft-touch-screen (accessed Jan. 21, 2021).
[104] "Ultimaker Cura: Powerful, easy-to-use 3D printing software," *ultimaker.com*. https://ultimaker.com/software/ultimaker-cura (accessed Jan. 22, 2021).
[105] "3D Printing Overhang: How to 3D Print Overhangs," *All3DP*, May 14, 2019. https://all3dp.com/2/3d-printing-overhang-how-to-master-overhangs-exceeding-45/ (accessed Jan. 19, 2021).
[106] V. Kuznetsov, A. Solonin, O. Urzhumtsev, R. Schilling, and A. Tavitov, *Strength of PLA Components Fabricated with Fused Deposition Technology Using a Desktop 3D Printer as a Function of Geometrical Parameters of the Process*. 2018. doi: 10.20944/preprints201803.0036.v1.
[107] "The effect of Extrusion Width on Strength and Quality of 3D prints," *CNC Kitchen*. https://www.cnckitchen.com/blog/the-effect-of-extrusion-width-on-strength-and-quality-of-3d-prints (accessed Feb. 01, 2021).
[108] "Infill settings," *Ultimaker Support*. https://support.ultimaker.com/hc/en-us/articles/360012607079-Infill-settings (accessed Jan. 19, 2021).
[109] "Support settings," *Ultimaker Support*. https://support.ultimaker.com/hc/en-us/articles/360012612779-Support-settings (accessed Jan. 19, 2021).
[110] K. Moromizato, R. Kimura, H. Fukase, K. Yamaguchi, and H. Ishida, "Whole-body patterns of the range of joint motion in young adults: masculine type and feminine type," *J. Physiol. Anthropol.*, vol. 35, no. 1, p. 23, Oct. 2016, doi: 10.1186/s40101-016-0112-8.
[111] D. A. Nawoczenski, J. F. Baumhauer, and B. R. Umberger, "Relationship Between Clinical Measurements and Motion of the First Metatarsophalangeal Joint During Gait*," *JBJS*, vol. 81, no. 3, pp. 370–6, Mar. 1999.
[112] C. Tudor-Locke, M. M. Brashear, P. T. Katzmarzyk, and W. D. Johnson, "Peak Stepping Cadence in Free-Living Adults: 2005–2006 NHANES," *J. Phys. Act. Health*, vol. 9, no. 8, pp. 1125–1129, Nov. 2012, doi: 10.1123/jpah.9.8.1125.

Appendix A

MatLab Code

A.1 Image Digitizer

```
% Andrea Baldi, 10/01/2015

clear all;
close all;

% Select the figure you want to digitize
filename = uigetfile('Select a SPECTRUM file'); %open spec file

% Read image
image=imread(filename);

% Averages the RGB components of the image and plot
imageave=sum(image./size(image,3),3);
screen_size = get(0,'ScreenSize');
f1 = figure(1);
imshow(imageave,[]);
set(f1,'Position',[0 0 screen_size(3) screen_size(4)]);

% Define your axes limits
prompt = {'Enter xmin:','Enter xmax:','Enter ymin:','Enter ymax:'};
dlg_title = 'Input parameters';
num_lines = 1;
def = {'','','',''};
answer = inputdlg(prompt,dlg_title,num_lines,def);
xmin=str2num(answer{1});
xmax=str2num(answer{2});
ymin=str2num(answer{3});
ymax=str2num(answer{4});

% Check if any axis is in log scale
buttonx = questdlg('Is the x-axis in log scale?');
buttony = questdlg('Is the y-axis in log scale?');

% Select xmin, xmax, ymin, ymax
title(['Select xmin = ',num2str(xmin)]);
```

```
[x0(1),y0(1)]=ginput(1);
title(['Select xmax = ',num2str(xmax)]);
[x0(2),y0(2)]=ginput(1);
title(['Select ymin = ',num2str(ymin)]);
[x0(3),y0(3)]=ginput(1);
title(['Select ymax = ',num2str(ymax)]);
[x0(4),y0(4)]=ginput(1);
title('Now click on the data points and press enter when done');

% Select npoints on the plot
[x,y]=ginput(10000);
close

% Coordinate transformations
if strcmp(buttonx,'No')==1;
    output(:,1)=[(x-x0(1))/(x0(2)-x0(1))].*(xmax-xmin)+xmin;
else if strcmp(buttonx,'No')==0;
        output(:,1)=exp([(x-x0(1))/(x0(2)-x0(1))].*log(xmax/xmin)+log(xmin));
    end
end
if strcmp(buttony,'No')==1;
    output(:,2)=[(y-y0(3))/(y0(4)-y0(3))].*(ymax-ymin)+ymin;
else if strcmp(buttony,'No')==0;
        output(:,2)=exp([(y-y0(3))/(y0(4)-y0(3))].*log(ymax/ymin)+log(ymin));
    end
end

% Plot result
figure
if strcmp(buttony,'No')==1;
    plot(output(:,1),output(:,2),'-o')
else if strcmp(buttony,'No')==0;
        semilogy(output(:,1),output(:,2),'-o')
    end
end

% Save results
button = questdlg('Do you want to save the digitized data as a txt file?')
if strcmp(button,'Yes')==1
    prompt = {'Write file name without extension:'};
    dlg_title = '';
    num_lines = 1;
    def = {''};
    answer = inputdlg(prompt,dlg_title,num_lines,def);
    dlmwrite([answer{1},'.txt'],output,'\t');
end
```

A.2 Gimput2

```
function  [X,Y,BUTTON,SCALEMAT] = ginput2(varargin)
%GINPUT2   Graphical input from mouse with zoom, pan, plot and scaling.
%
%   SYNTAX:
```

```
%                       XY = ginput2;
%                       XY = ginput2(DoScale);          true or false
%                       XY = ginput2(...,PlotOpt);      '.r' for example
%                       XY = ginput2(...,'KeepZoom');   vs. 'UnZoom'
%                       XY = ginput2(N,...);
%                       XY = ginput2(...);
%                    [X,Y] = ginput2(...);
%              [X,Y,BUTTON] = ginput2(...);
%     [X,Y,BUTTON,SCALEMAT] = ginput2(...);
%
%   INPUT:
%     DoScale    - Single logical specifying whether the IMAGE should be
%                  interactively scaled (georeferenced), or it can be the
%                  2x4 SCALEMAT matrix for automatically scaling.
%                  DEFAULT: false (do not scales/georeferences)
%     PlotOpt    - String and/or parameter/value pairs specifying the drawn
%                  points optional inputs (see PLOT for details).
%                  DEFAULT: 'none' (do not plot any point)
%     'KeepZoom' - When finishing selection by default the zoom is
%                  restored. By using this option this feature is ignored.
%                  DEFAULT: 'UnZoom' (restores original axis limits)
%     N          - Number of points to be selected. One of 0,1,2,...,Inf
%                  DEFAULT: Inf (selects until ENTER or ESCAPE is pressed)
%
%   OUTPUT:
%     XY        - [X(:) Y(:)] axis coordinate(s).
%     X         - X-coordinate(s).
%     Y         - Y-coordinate(s).
%     BUTTON    - Last pressed button.
%     SCALEMAT  - 2x4 matrix specifying the coordinates of two different
%                 points (1) and (2) in the Image coordinates (pixels) and
%                 the User coordinates (data):
%                                                Point 1     Point 2
%                   Image coord (pixels):     [ (I1x,I1y)   (I2x,I2y)
%                   User  coord (data)  :       (U1x,U1y)   (U2x,U2y) ]
%                 to be use for scaling/georeferencing.
%
%   DESCRIPTION:
%     This program uses MATLAB's GINPUT function to get the coordinates
%     of a mouse-selected point in the current figure (see GINPUT for
%     details), but with five major improvements:
%                  1. ZOOMING  (left click)
%                  2. PANNING  (dragging mouse)
%                  3. DELETING (last selected point)
%                  4. PLOTING  (temporarily the selected points)
%                  5. SCALING or GEOREFERENCE IMAGES.
%     The differences are:
%      a) Obviously, the SCALEOPT and PlotOpt optional arguments.
%      b) When click is made outside the axes, it is ignored.
%      c) When LEFT-click, ZOOM-IN is performed right into the selected
%         point (PANNING).
%      d) When RIGHT-click, the point is selected (normal).
%      e) When DOUBLE-click, ZOOM-OUT is done.
%      f) When MIDDLE-click, ZOOM-RESET is done (see ZOOM for details).
%      g) When dragging while pressed left-click PAN is done (until the
%         button is released).
%      h) When pressed any KEY follows the next rules:
```

```
%          A) If ENTER is pressed, the selection is terminated. If no point
%             was already selected, the outputs are empty's.
%          B) If BACKSPACE key is pressed, the last selected point is
%             deleted and the selection continues.
%          C) If SPACEBAR the mouse current position or NANs coordinates
%             are saved, depending whether the mouse was inside or outside
%             any of the current figure axes, respectively. In this latter
%             case, the selection is NOT counted as one of the N points.
%             Besides, when drawing the color is changed. Then, the outputs
%             may not be of length N.
%
%   NOTE:
%     * Optional inputs use its DEFAULT value when not given or [].
%     * Optional outputs may or not be called.
%     * String inputs may be shortened, as long as they are unambiguous.
%       Case is ignored.
%     * The function can be used for interactively digitalize/vectorize
%       RASTER images with:
%       >> ginput(true)
%     * The function can be used only as a georeference function with
%       >> ginput2(0,true)
%     * The scale/georeference only works when the current axes has an
%       IMAGE type children (see Image for details).
%     * The x and y data from axes and image are changed when scale/
%       georeference is used.
%     * The drawn points are deleted from the graphics once the selection
%       is finished.
%     * The priority of the inputs are: N, then SCALEOPT and finally
%       PlotOpt. If the first (integer) is missing, the next is taken into
%       account (logical or 2x4 matrix) and so on.
%
%   EXAMPLE:
%     % Selects until ENTER is pressed:
%         xy = ginput2;
%     % Selects 5 points:
%         [x,y] = ginput2(5);
%     % Gets pressed button:
%         [x,y,button] = ginput2(1);
%     % Scales image and select 4 points temporarily coloring them in
%       black. Besides to not ZOOM OUT at the end:
%         imagesc(peaks(40))
%         [x,y,button,scalemat] = ginput2(4,true,'k*','KeepZoom');
%         hold on, plot(x,y,'or'), hold off
%
%   SEE ALSO:
%     GINPUT, PLOT.
%
%
%   ---
%   MFILE:   ginput2.m
%   VERSION: 3.1 (Nov 12, 2009) (<a
href="matlab:web('http://www.mathworks.com/matlabcentral/fileexchange/authors
/11258')">download</a>)
%   MATLAB:  7.7.0.471 (R2008b)
%   AUTHOR:  Carlos Adrian Vargas Aguilera (MEXICO)
%   CONTACT: nubeobscura@hotmail.com
```

```
%   REVISIONS:
%   1.0      Released. (Jul 09, 2008)
%   2.0      Changed default YESERROR value and fixed a bug there. Changed
%            behavior when N==1. Fixed bug with zoom out. Changed default
%            selection keys. Changed default selection click mouse: from
%            left one to the right one. (Jun 08, 2009)
%   2.1      Fixed bugs related with points deletion. Added new 'KeepZoom'
%            feature. (Aug 20, 2009)
%   3.0      Now it PANs when dragging. Updated help. (Nov 05, 2009)
%   3.1      Now returns when N==1 and pressed not predefined KEYS or one
%            of DELECTION or RETURN buttons. (Nov 12, 2009)

%   DISCLAIMER:
%   ginput2.m is provided "as is" without warranty of any kind, under the
%   revised BSD license.

%   Copyright (c) 2008-2009 Carlos Adrian Vargas Aguilera


% INPUTS CHECK-IN
% ---------------------------------------------------------------------------

% PARAMETERS
% Defaults:
X        = [];
Y        = [];
BUTTON   = [];
SCALEMAT = [];
N        = Inf;
DoScale  = false;
PlotOpt  = {'none'};
UnZoom   = 'UnZoom';
% Constants KEYs (on my personal keyboard):
DOUBLECLICK    =   0;
LEFTCLICK      =   1;
MIDDLECLICK    =   2;
RIGHTCLICK     =   3;
BACKSPACE      =   8;
ESCAPE         =  27;
LEFTARROW      =  28;
RIGHTARROW     =  29;
UPARROW        =  30;
DOWNARROW      =  31;
SPACEBAR       =  32;
DELETE         = 127;
ASCII          = [ ...
                    33:64  ...  UP-KEYS
                    65:90  ...  UP-LETTERS
                    91:96  ... LOW-KEYS
                    97:122 ... LOW-LETTERS
                   123:126 ... LOW-KEY
                   161:255 ...     FOREING
                   ];
% Functionality:
% NOTE: I left all this KEYs because the user may use this special case for
% other special purposes outside this function.
```

```
% % First version default:
% % SELECTS   = [LEFTCLICK ASCII ESCAPE LEFTARROW RIGHTARROW ...
% %              UPARROW DOWNARROW SPACEBAR DELETE];
% % ZOOMIN    = RIGHTCLICK;
SELECTS   = [RIGHTCLICK SPACEBAR]; % Selection  buttons
DELETES   = BACKSPACE;             % Deletion   buttons
FINISHES  = [];                    % Finishes   buttons
ZOOMIN    = LEFTCLICK;             % ZOOM(2)    buttons
ZOOMRESET = MIDDLECLICK;           % ZOOM RESET buttons
ZOOMOUT   = DOUBLECLICK;           % ZOOM OUT   buttons
% Other parameters
secpause  = 0.3;    % Seconds to wait for double-click response.
YESERROR  = false;  % If there is an error with GINPUT, it tells to display
                    % an ERROR or a WARNING message.

% Checks number of inputs:
if nargout>4
 error('CVARGAS:ginput2:tooManyOutputs',...
  'At most 4 outputs are allowed.')
end

% Checks N:
if ~isempty(varargin) && ~isempty(varargin{1}) && ...
  isfloat(varargin{1})
 N           = round(abs(varargin{1}(1))); % Forced unique, positive
 varargin(1) = [];                         % integer.
end

% Checks DoScale:
if ~isempty(varargin) && ~isempty(varargin{1}) && ...
   ((islogical(varargin{1})) || (ndims(varargin{1})==2 && ...
    all(size(varargin{1})==[2 4])))
 DoScale     = varargin{1};
 varargin(1) = [];
end

% Checks UnZoom:
if ~isempty(varargin)
 if ~isempty(varargin{1}) && ischar(varargin{1})
  if     strncmpi(varargin(1),'UnZoom'  ,max(length(varargin{1}),2))
   UnZoom = 'UnZoom';
   varargin(1) = [];
  elseif strncmpi(varargin(1),'KeepZoom',max(length(varargin{1}),2))
   UnZoom = 'KeepZoom';
   varargin(1) = [];
  end
 elseif (length(varargin)>1) && ~isempty(varargin{end}) && ...
     ischar(varargin{end})
  if     strncmpi(varargin(end),'UnZoom'  ,max(length(varargin{1}),2))
   UnZoom = 'UnZoom';
   varargin(end) = [];
  elseif strncmpi(varargin(end),'KeepZoom',max(length(varargin{1}),2))
   UnZoom = 'KeepZoom';
   varargin(end) = [];
  end
 end
```

```
end

% Checks PlotOpt:
if ~isempty(varargin) && ~isempty(varargin{1})
 PlotOpt = varargin;
end
clear varargin

% Checks DoScale:
if ~islogical(DoScale)
 SCALEMAT = DoScale;
 DoScale = true;
end

% SCALES/GEOREFERENCE?:
if DoScale
 method = 'linear';
 extrap = 'extrap';
 ha     = gca;
 hi     = findobj(get(ha,'Children'),'Type','image');
 axes(ha)
 if ~isempty(hi)
  hi    = hi(1);
  xlim  = get(ha,'XLim');
  ylim  = get(ha,'YLim');
  zlim  = get(ha,'ZLim');
  z     = repmat(max(zlim),1,5);
  xdata = get(hi,'XData');
  ydata = get(hi,'YData');
  if isempty(SCALEMAT) % interactively
   I1x = round(min(xdata)); I2x = round(max(xdata));
   I1y = round(min(ydata)); I2y = round(max(ydata));
   % Default (equal):
   U1x = I1x; U2x = I2x;
   U1y = I1y; U2y = I2y;
   hgeo     = [];
   dlgTitle = 'Georeference image';
   lineNo   = 1;

   while true
    % Selects first corner:
    theans = ...
          questdlg('Select the first corner (1 of 2):',dlgTitle,'OK','OK');
    if ~strcmp(theans,'OK'), return, end
    pause(secpause)

    [I1x,I1y] = ginput2(1,false,'none','UnZoom');
    I1x       = round(I1x);
    I1y       = round(I1y);
    if ~ishandle(ha), return, end
    if (ha==gca) && ~isempty(I1x) && ~isnan(I1x)
     axis(ha,[xlim ylim])
     hgeo(1) = line([xlim NaN I1x I1x],[I1y I1y NaN ylim],z,'color','m');
     prompt  = {'X-coordinate at 1st corner:',...
                'Y-coordinate at 1st corner:'};
     def     = {int2str(I1x),int2str(I1y)};
```

```
  answer  = inputdlg(prompt,dlgTitle,lineNo,def);
  answer  = str2num(char(answer{:}));
  break
 end
end
axes(ha)

% Checks inputs:
if ~isempty(answer) && isfloat(answer) && (length(answer)==2) && ...
                                                    all(isfinite(answer))
 U1x = answer(1); U1y = answer(2);
 secondcorner = true;
else
 secondcorner = false;
 warning('CVARGAS:ginput2:incorrectGeoreference',...
         'Ignored incorrect georeference corners.')
end

while secondcorner
 % Selects second corner:
 theans = ...
      questdlg('Select the second corner (2 of 2):',dlgTitle,'OK','OK');
 if ~strcmp(theans,'OK'), return, end
 pause(secpause)

 [I2x,I2y] = ginput2(1,false,'none','UnZoom');
 I2x       = round(I2x);
 I2y       = round(I2y);
 if ~ishandle(ha), return, end
 if (ha==gca) && ~isempty(I2x) && ~isnan(I2x) && ...
   (I2x~=I1x) && (I2y~=I1y)
  axis(ha,[xlim ylim])
  hgeo(2) = line([xlim NaN I2x I2x],[I2y I2y NaN ylim],z,'color','c');
  prompt  = {'X-coordinate at 2nd corner:',...
             'Y-coordinate at 2nd corner:'};
  def     = {int2str(I2x),int2str(I2y)};
  answer  = inputdlg(prompt,dlgTitle,lineNo,def);
  answer  = str2num(char(answer{:}));
  break
 end
end
axes(ha)

% Checks inputs:
if secondcorner && ~isempty(answer) && isfloat(answer) && ...
                      (length(answer)==2) && all(isfinite(answer))
 U2x = answer(1); U2y = answer(2);
else
 warning('CVARGAS:ginput2:incorrectGeoreference',...
         'Ignored incorrect georeference corners.')
end

% Deletes corner's lines:
if any(ishandle(hgeo))
 delete(hgeo(ishandle(hgeo)))
end
```

```
   % Scale matrix:
    SCALEMAT = [I1x I1y I2x I2y; U1x U1y U2x U2y];
  else
   % Continue
  end
 else
  warning('CVARGAS:ginput2:noImageFound',...
   'No image found in the current axes to georeference.')
 end

 % OK, set the scaling then:
 if ~isempty(SCALEMAT)
  xdata = interp1(SCALEMAT(1,[1 3]),SCALEMAT(2,[1 3]),xdata,method,extrap);
  ydata = interp1(SCALEMAT(1,[2 4]),SCALEMAT(2,[2 4]),ydata,method,extrap);
  xlim2 = interp1(SCALEMAT(1,[1 3]),SCALEMAT(2,[1 3]),xlim ,method,extrap);
  ylim2 = interp1(SCALEMAT(1,[2 4]),SCALEMAT(2,[2 4]),ylim ,method,extrap);
  set(hi,'XData',xdata);
  set(hi,'YData',ydata);
  set(ha,'XLim' ,sort(xlim2,'ascend'));
  set(ha,'YLim' ,sort(ylim2,'ascend'));
  % Reverses axis directions:
  if diff(xlim)*diff(xlim2)<1
   if strcmp(get(ha,'XDir'),'normal')
    set(ha,'XDir','reverse')
   else
    set(ha,'XDir','normal')
   end
  end
  if diff(ylim)*diff(ylim2)<1
   if strcmp(get(ha,'YDir'),'normal')
    set(ha,'YDir','reverse')
   else
    set(ha,'YDir','normal')
   end
  end
 end
 axis(ha,'normal')

end

% DRAWS?:
if strcmpi(PlotOpt{1},'none')
 yesdraw = false;
else
 yesdraw = true;
end
% Optional parameters:
if yesdraw
 hpoints  = [];
 % Check for linestyle color:
 yescolor     = true;
 Nplotopt     = length(PlotOpt);
 yeslinestyle = rem(Nplotopt,2);
 if yeslinestyle % Given LineStyle
  for k = 1:length(PlotOpt{1})
```

```
   switch lower(PlotOpt{1}(k))
    case 'y', yescolor = false; break
    case 'm', yescolor = false; break
    case 'c', yescolor = false; break
    case 'r', yescolor = false; break
    case 'g', yescolor = false; break
    case 'b', yescolor = false; break
    case 'w', yescolor = false; break
    case 'k', yescolor = false; break
    otherwise, % no color specified
   end
  end
 end
 if ~yescolor && (Nplotopt*yeslinestyle~=1)
  for k = yeslinestyle+1:2:Nplotopt    % Given 'Color'
   if strncmpi(PlotOpt{k},'co',2), yescolor = false; break, end
  end
 end
 if yescolor
  contnan  = 1;
  colors   = get(gca,'ColorOrder');
  ncolors  = size(colors,1);
  color    = colors(1,:);
 end
end


% ------------------------------------------------------------------------
% MAIN
% ------------------------------------------------------------------------

cont       = 0;
alim.ha    = [];
alim.la    = {};
undoPtrFig = [];

while cont<N     % Principal loop

 % GINPUT:
 try
  [x,y,button] = ginput(1);
 catch % Changed for compatibility.
  % GINPUT error:
  if YESERROR
     error('CVARGAS:ginput2:executionError',lasterr)
  else
   warning('CVARGAS:ginput2:executionError',lasterr)
   if nargout<2  % Fixed BUG 29 SEP, 2008
    X = [X Y];
   end
   return
  end
 end

 % Axes clicked:
 ha = gca;
```

```
% Gets limits:
if ~any(alim.ha==ha)
 alim.ha(end+1) = ha;
 alim.la{end+1} = axis;
end

% Sets zoom:
zlim = getappdata(ha,'zoom_zoomOrigAxesLimits');
if isempty(zlim) % Fixed BUG, SEP 2008
 zoom reset
 zlim = getappdata(ha,'zoom_zoomOrigAxesLimits');
end

% Checks if DOUBLE clicks:
pause(secpause) % Gives time for response
if strcmp(get(gcf,'selectiontype'),'open')
 button = DOUBLECLICK;
end

% Checks if ENTER or FINISHES button:
if isempty(button) || ismember(button,FINISHES)
 % Finishes selection:
 if (N==1) && isempty(X) % New feature v3.1
  BUTTON = button;
 end
 break
end

% Checks if DELETION button:
if ismember(button,DELETES)
 if ~isempty(X)
  inan = isnan(X(end));
  if yesdraw
   if ~inan
    % Deletes last drawn point:
    if ~isempty(hpoints) && ishandle(hpoints(end)) % Fixed bug Aug 2009
     delete(hpoints(end)), hpoints(end) = [];
    end
   elseif yescolor
    % Change color as necessary:
    contnan = contnan-1;
    color   = colors(mod(contnan-1,ncolors)+1,:);
   end
  end
  % Deletes the last selected point:
  X(end)      = [];
  Y(end)      = [];
  BUTTON(end) = [];
  % Checks if the last point was NaN:
  if ~inan
   cont = cont-1;
  end
 elseif N==1
  % Finishes selection: New feature v3.1
  BUTTON = button;
```

```
  break
 end
 continue
end

% Checks if ZOOM OUT button:
if ismember(button,ZOOMOUT)
 undoPtrFig = gcf;
 setptr(undoPtrFig,'glassminus')
 zoom out
 continue
end

% Checks if ZOOM RESET button:
if ismember(button,ZOOMRESET)
 zoom reset
 continue
end

% Checks if the mouse was inside an axes of the current figure;
lim     = axis;
outside = x<lim(1) || x>lim(2) || y<lim(3) || y>lim(4);

% Checks if ZOOM IN with PAN:
if ismember(button,ZOOMIN) && ~outside
 % Dragging rectangle:
 undoPtrFig = gcf;
 setptr(undoPtrFig,'closedhand')
 rbbox
 ydrag = get(gca,'CurrentPoint');
 xdrag = ydrag(1,1)-x;
 ydrag = ydrag(1,2)-y;
 % Do the PANNING:
 if  any(abs([xdrag ydrag])>eps*1000000)
  % Only PAN (dragging):
  lim(1:4) = lim(1:4) - [xdrag xdrag ydrag ydrag];
  axis(lim)
 else
  % PAN (centers the last point) and ZOOM in:
  setptr(undoPtrFig,'glassplus')
  lim = [x+diff(lim(1:2))/2*[-1 1] y+diff(lim(3:4))/2*[-1 1]];
  axis(lim)
  zoom(2)
 end
 continue
end

% Checks if SELECTS button:
if ismember(button,SELECTS)

 % Sets NaNs if outside the axes:
 if outside
  if ~isnumeric(N)
   % Change color:
   if yesdraw && yescolor
    contnan = contnan+1;
```

```
    color   = colors(mod(contnan-1,ncolors)+1,:);
   end
   % Adds NaNs but the point counters do not take it into account:
   X      = [X;      NaN];
   Y      = [Y;      NaN];
   BUTTON = [BUTTON; button];
  else
   % Ignores the point
  end
 else
  % Draws the result:
  if yesdraw
   % Search for last point:
   x0 = []; y0 = []; z0 = [];
   inan = isnan([NaN; X; NaN]);
   if ~inan(end-1)
    inan        = find(inan);
    nlastpoints = inan(end)-inan(end-1)-1;
    npoints     = length(hpoints);
    range       = npoints-nlastpoints+1:npoints;
    hlastaxes   = get(hpoints(range),'Parent');
    if iscell(hlastaxes), hlastaxes  = cell2mat(hlastaxes); end
    [loc,loc] = ismember(ha,hlastaxes);
    if loc
     x0 = get(hpoints(range(loc)),'XData');
     y0 = get(hpoints(range(loc)),'YData');
     z0 = get(hpoints(range(loc)),'ZData');
    end
   end
   holdon = ishold;
   if ~holdon, hold on, end
    h = plot([x0 x],[y0 y],PlotOpt{:});
    % Elevates the value:
    z = get(ha,'ZLim'); z = z(2);
    set(h,'Zdata',[z0 z])
    % Sets the color:
    if yescolor
     set(h,'Color',color)
    end
    hpoints = [hpoints; h];
   if ~holdon, hold off, end
   % Restores limits:
   axis(lim)
  end

  % Centers the selected point if ZOOM-IN: 29 SEP,2008
  if all((lim~=zlim))
   lim = [x+diff(lim(1:2))/2*[-1 1] y+diff(lim(3:4))/2*[-1 1]];
   axis(lim)
  end

  % Saves the result:
  X      = [X;      x];
  Y      = [Y;      y];
  BUTTON = [BUTTON; button];
  cont   = cont+1;
```

```
  end
  continue
 end

 % Checks if any other button pressed inside the axes:
 if ~outside
  X      = [X;      x];
  Y      = [Y;      y];
  BUTTON = [BUTTON; button];
  cont   = cont+1;
 else
  if N==1 % New feature v3.1
   BUTTON = button;
   break
  end
  % ignores the selection
 end

end

% Returns pointer.
if ~isempty(undoPtrFig) && ishandle(undoPtrFig)
 setptr(undoPtrFig,'arrow')
end

% Deletes drawn points if still exist:
if yesdraw && any(ishandle(hpoints))
 delete(hpoints(ishandle(hpoints)))
end

% Returns original limits.
if ~strcmp(UnZoom,'KeepZoom') && ~isempty(alim.ha)
 alim.ha(~ishandle(alim.ha)) = [];
 for k = 1:length(alim.ha)
  temp = axis(alim.ha(k));
  if ~all(temp(1:4)==alim.la{k}(1:4))
   axis(alim.ha(k),alim.la{k})
  end
 end
end


% OUTPUTS CHECK-OUT
% ---------------------------------------------------------------------

if nargout<2
 X = [X Y];
end


% [EOF]   ginput2.m
```

A.3 Getdata

```
open(CMiFUp.fig');

a = get(gca,'Children');
xdata = get(a, 'XData');
ydata = get(a, 'YData');
zdata = get(a, 'ZData');
```

Appendix B

Component Drawings

All foot components are dimensioned for a FL of 270 mm.

B.1 Ball Stud

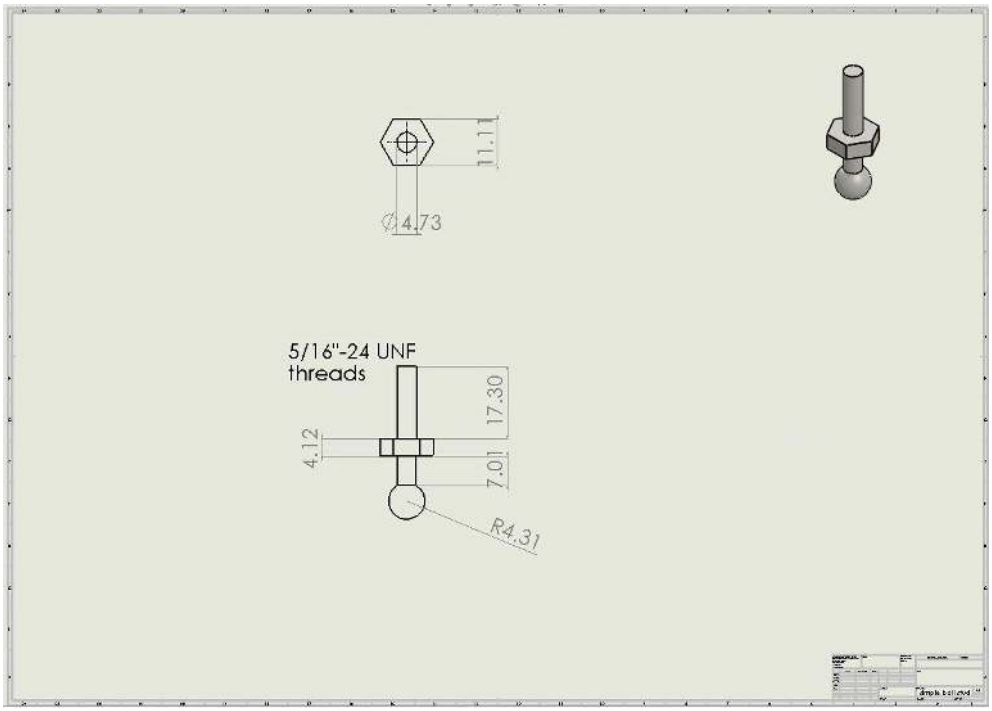

B.2 Shank Shaft

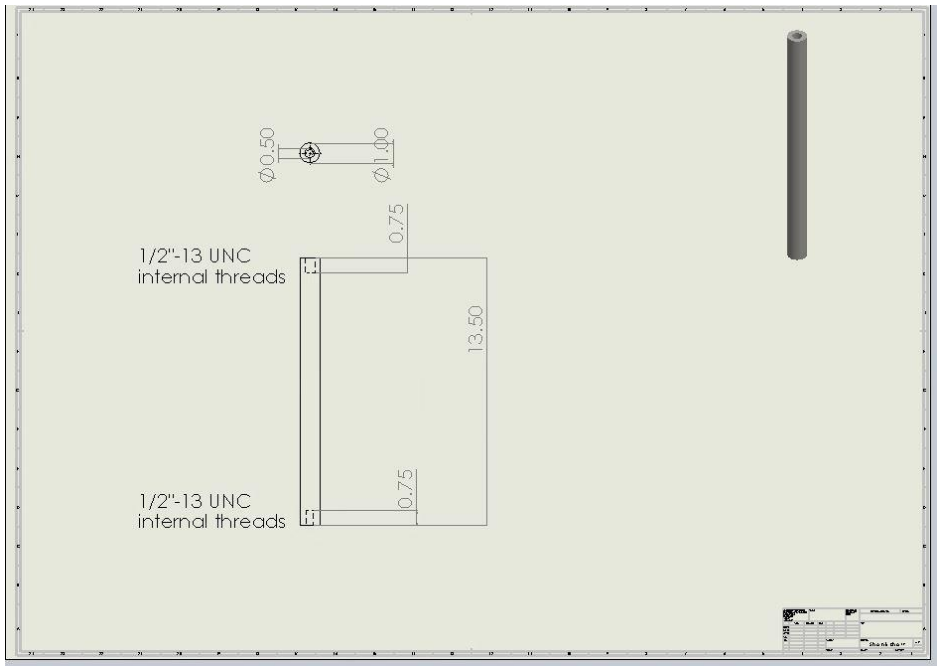

B.3 Shank Cover

B.3.1 Shank Cover Back

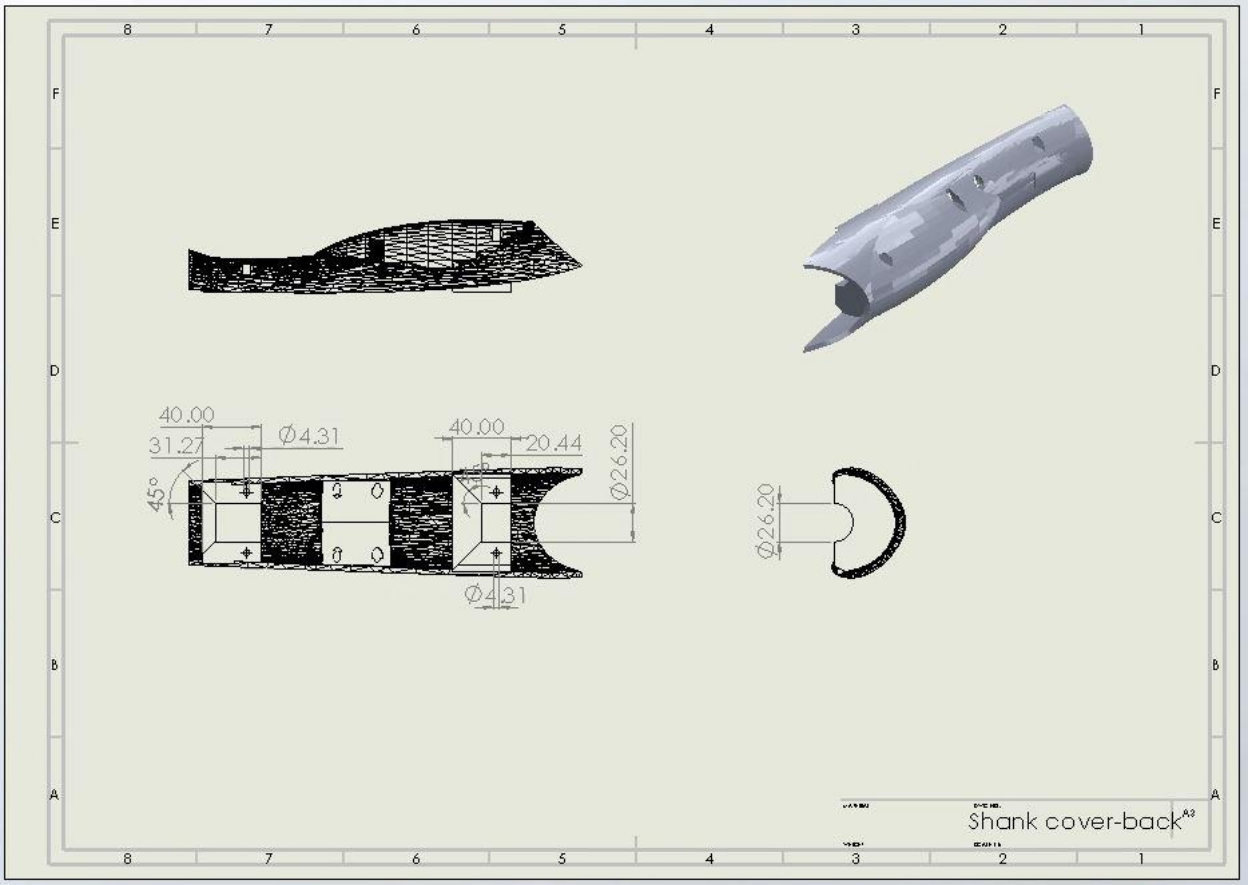

Global variables	Value
“PLA-PLA.tol”	0.6
“PLA-Metal.tol”	0.8

Sketch	Equations	Value
D1@Bottom anchor sketch	= “PLA-Metal.tol” + 25.4	26.20 mm
D1@Top anchor sketch	= “PLA-Metal.tol” +25.4	26.20 mm
D1@Top bolt sketch	= 3.5052 + “PLA-Metal.tol”	4.31 mm
D1@Bottom hex nut sketch	= 7.8 mm + “PLA-Metal.tol”	8.60 mm
D1@Top hex nut sketch	= “PLA-Metal.tol” +7.80	8.60 mm
D5@Bottom bolt sketch	= “PLA-Metal.tol” + 3.50542	4.31 mm

B.3.2 Shank Cover Front

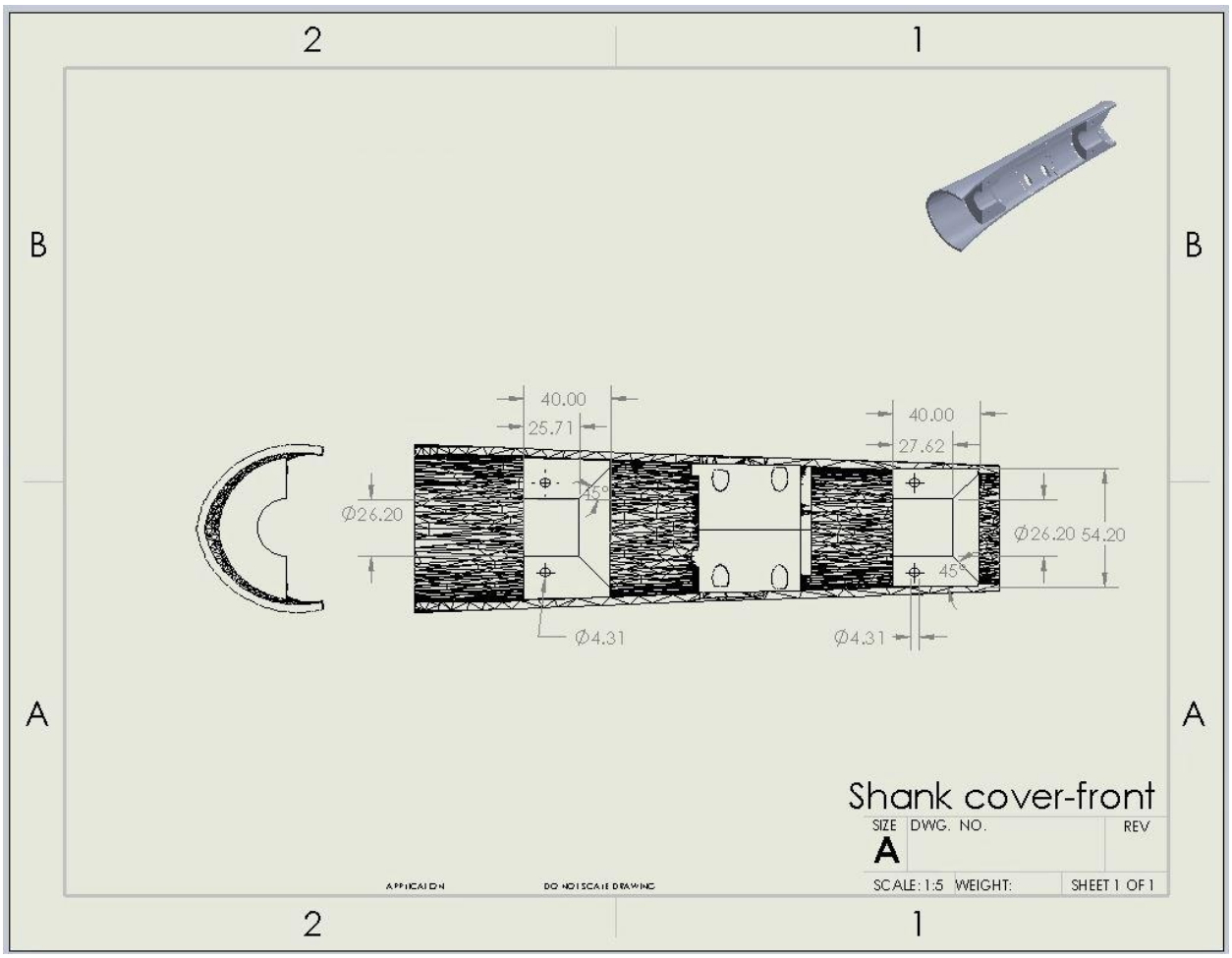

Global variables	Value
"PLA-PLA.tol"	0.6
"PLA-Metal.tol"	0.8

Sketch	Equations	Value
D1@Bottom bolt sketch	= 3.5052 + "PLA-Metal.tol"	4.31 mm
D3@Bottom anchor sketch	= 14.00	14.00 mm
D1@Top anchor sketch	= "PLA-Metal.tol" +25.4	26.20 mm
D3@Top bolt sketch	= "PLA-Metal.tol" + 3.5052	4.31 mm
D1@Bolt head sketch	= 8.00	8.00 mm
D1@Bottom anchor sketch	= "PLA-Metal.tol" + 25.4	26.20 mm

B.4 Top Adapter

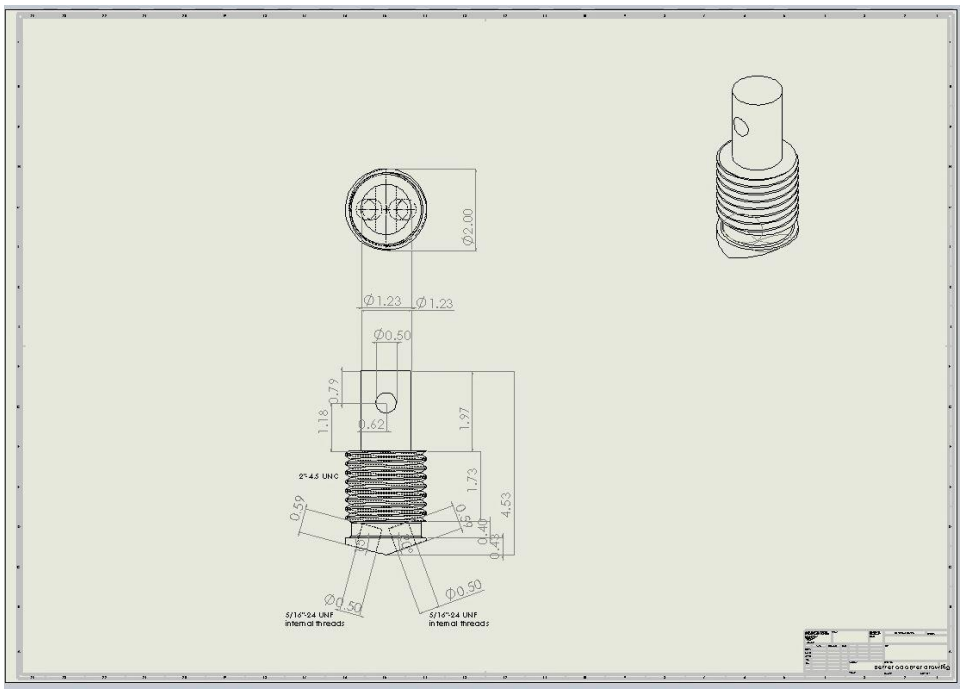

B.5 Bottom adapter

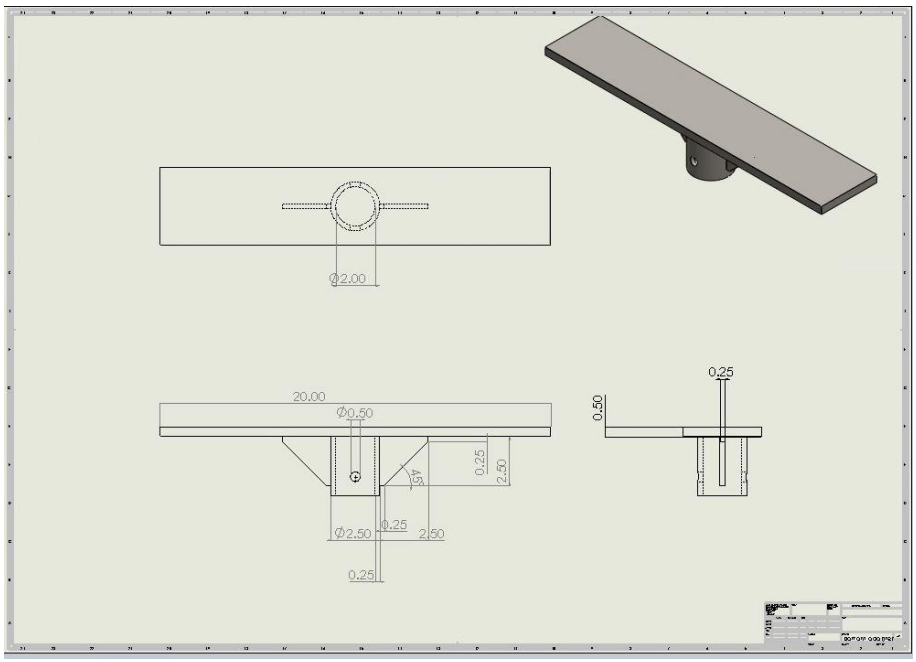

B.6 Adapter Collars

B.6.1 Collar-Heel

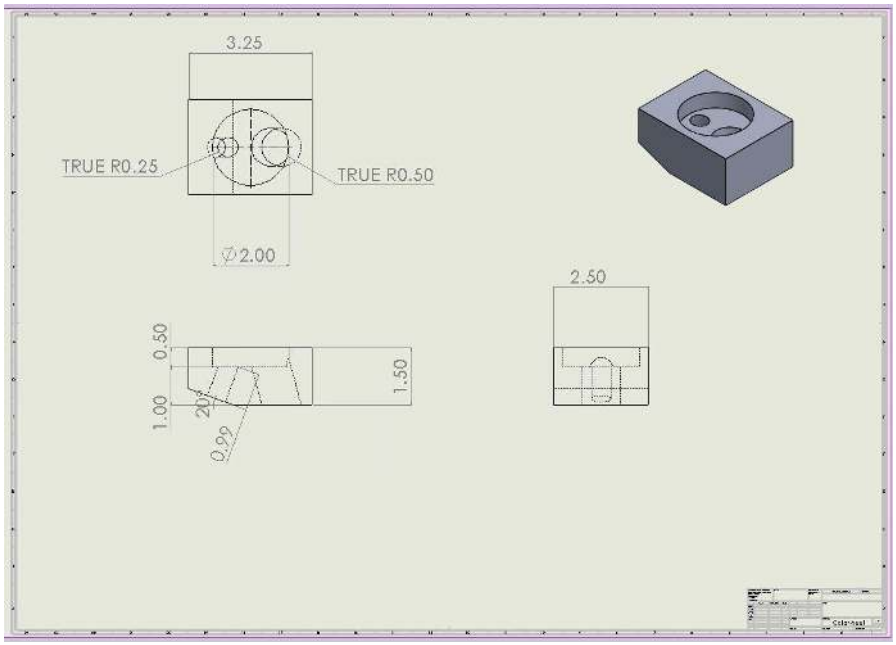

B.6.2 Collar-Forefoot

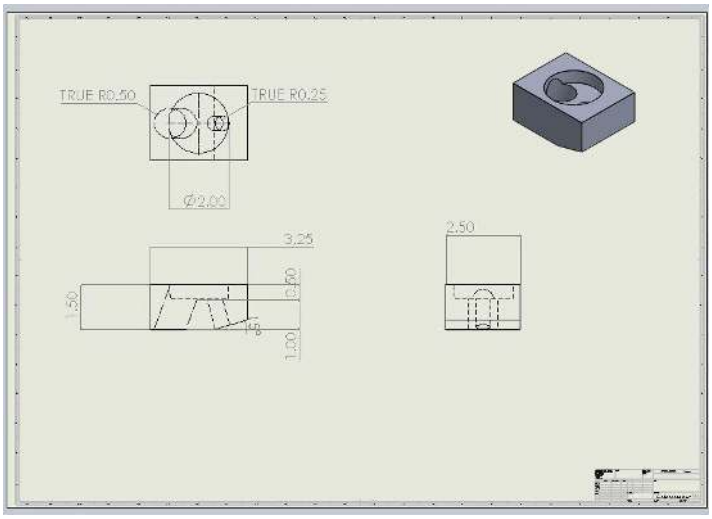

B.7 Heel Base

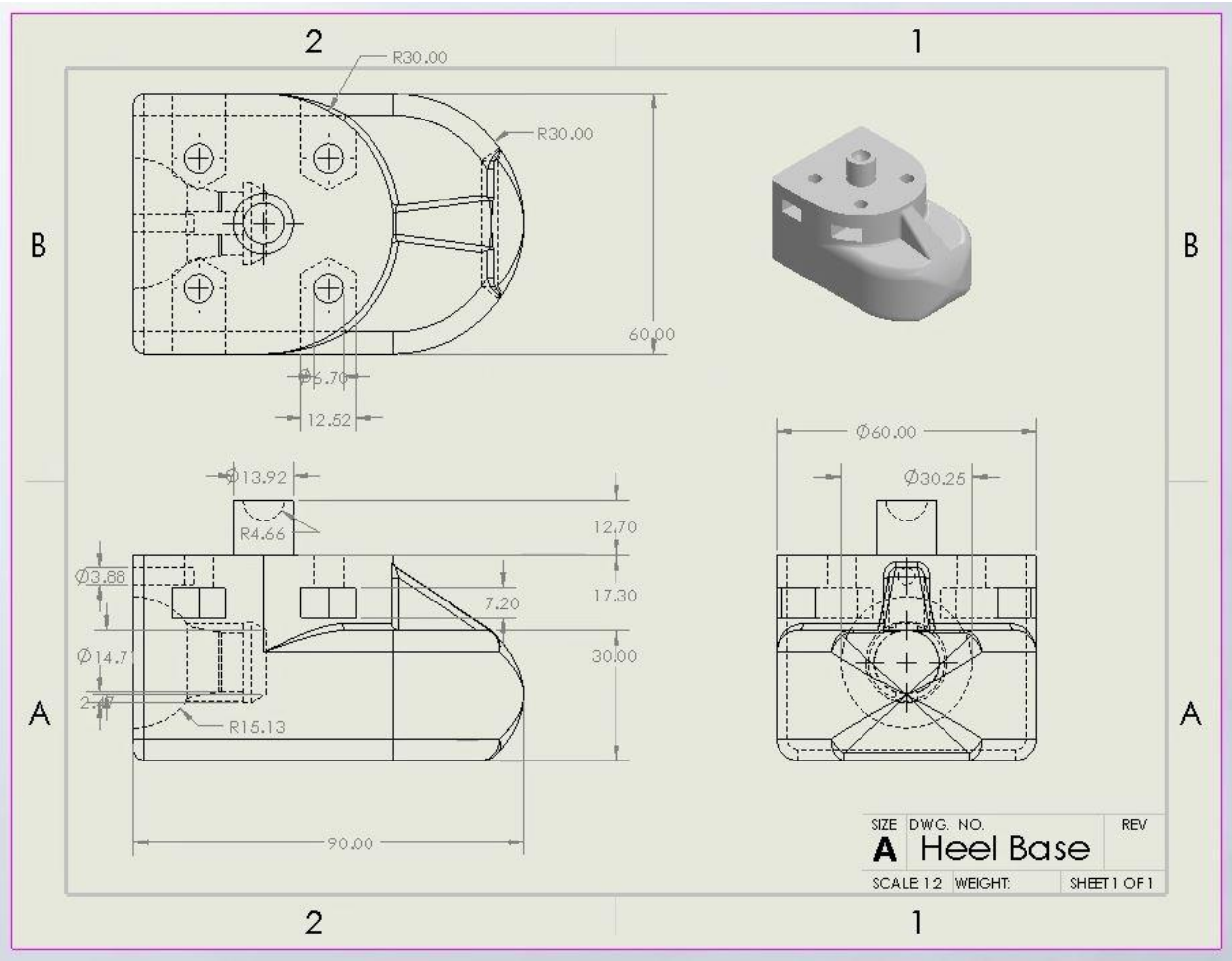

Global variables	Value (mm)
“BallRadius”	4.305
“FootLength”	270
“Alpha”	15
“Nylon-Metal.tol”	0.7
“Nylon-Nylon.tol”	0.5
“Nylon-TPU.tol”	0.3

Sketch	Equations	Value
D1@Shank ball sketch	= “FootLength” * (1 / (4.5 * 2))	30.00 mm
D1@Main body extrusion	= “FootLength” * (1 / 4.5)	60.00 mm
D2@Shank ball sketch	= “BallRadius” + (“Nylon-Metal.tol” / 2)	4.66 mm
D5@Lower half sketch	= “FootLength” * (1 / 18)	15.00 mm
D1@Pinhole	= “FootLength” * (1 / 6.3553)	42.50 mm
D1@Plate connection sketch	= “FootLength” * (1 (4.5 * 2))	30.00 mm
D2@Plate connection sketch	= “FootLength” * (2 / 36)	15.00 mm
D1@Connector hole sketch	= “FootLength” * (1 / 18)	15.00 mm
D1@Force direction	= “alpha”	15.0 deg
D1@Main body sketch	= “FootLength” * (11 / 36)	82.50 mm
D2@Main body sketch	= “FootLength” * (1 / 9)	30.00 mm
D1@Lower half sketch	= “FootLength” * (1 / 9)	30.00 mm
D2@Lower half sketch	= “FootLength” * (11 / 36)	82.50 mm
D6@Lower half sketch	= “FootLength” * (1 / 36)	7.50 mm
D1@Top half round cut	= “FootLength” * (1 / 9)	30.00 mm
D1@Ball socket sketch	= “FootLength” * (1 / 36)	7.50 mm
D1@Top half round cut sketch	= “FootLength” * (1 / (4.5 * 2))	30.00 mm
D2@Bottom half round cut sketch	= “FootLength” * (1 / 5)	54.00 mm
D1@Bottom half round cut sketch	= “FootLength” * (1 / 9)	30.00 mm
D2@Top half round cut sketch	= “FootLength” * (1 / 4.5)	60.00 mm
D3@Top half round cut sketch	= “FootLength” * (1 / 9)	30.00 mm
D1@Top plate pins cut	= “FootLength” * (1 / 13.5)	20.00 mm
D3@Connector hole sketch	= (14.56 + (“Nylon-TPU.tol” / 2)) /2	7.36 mm
D6@Connector hole sketch	= 3.47 / 2	1.74 mm
D10@Connector hole sketch	= “D6@Connector hole sketch”	1.74 mm
D1@Hex nut cut	= (2 * “Nylon-Metal.tol”) + 11.12 mm	12.52 mm
D3@Pinhole	= “Nylon-Metal.tol” + 3.175	3.88 mm
D2@Connector hole sketch	= (“Nylon-TPU.tol” / 2) + 15.5	15.65 mm
D7@Connector hole sketch	= 2.002 mm	2.00 mm
D9@Connector hole sketch	= (“Nylon-TPU.tol”) + 7.00 mm	7.30 mm
D1@Bolt hole cut	= 5.80mm + (“Nylon-Metal.tol” * 2)	7.20 mm
D2@Ball socket sketch	= ((“FootLength”) / 9) + (“Nylon-Nylon.tol” / 2)	30.25 mm
D1@IN-Eve pin hole	= 13.0mm + “Nylon-Metal.tol”	13.75 mm
D1@Rail cut	= “Nylon-TPU.tol” + 4.85	5.15 mm
D2@Pin 9-11 sketch	= “FootLength” * (1 / 4)	67.50 mm
D3@Pin 9-11 sketch	= “FootLength” * (1 / 13.5)	20.00 mm
D1@Pin 15 sketch	= “FootLength” * (1 / 36)	7.50 mm
D1@Pin 21-22 sketch	= “FootLength” * (1 / 18)	15.00 mm
D1@Heel-connection	= (10.71 – 3 – (“Nylon-Nylon.tol” * 1.5)) * 2	13.92 mm
D4@Plate connection sketch	= (“Nylon-Metal.tol” / 2) + 6.35 mm	6.70 mm

B.8 Heel plate

B.8.1 Heel plate front

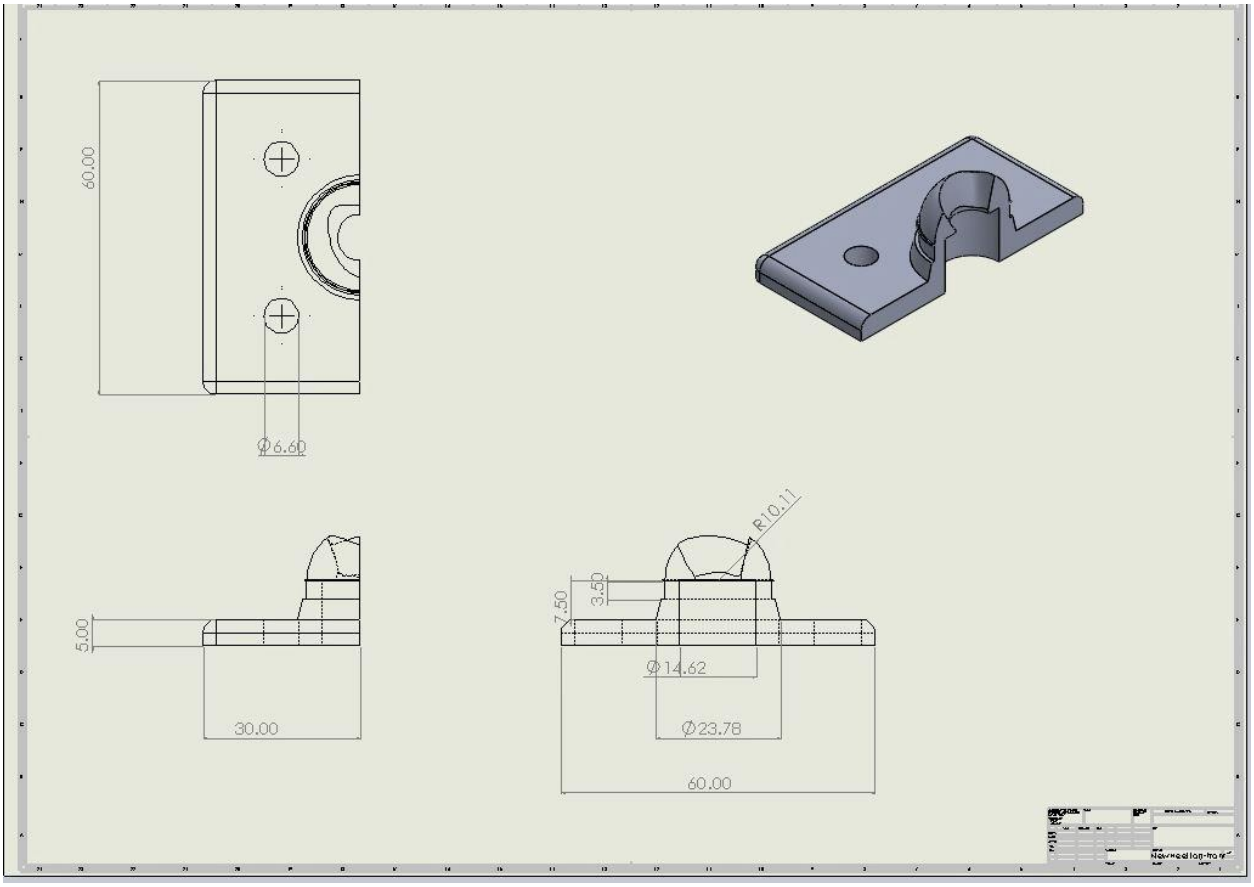

Global variables	Value
“max.rad”	10.11
“ballrad”	4.305
“neck.rad”	2.6
“Heel.Eve”	20.8
“Heel.Inv”	32.4
“FL”	270
“heel.Dors”	20
“heel.Plant”	50
“Nylon-Metal.tol”	0.7
“Nylon-Nylon.tol”	0.5
“Nylon-TPU.tol”	0.3

Sketch	Equations	Value
D1@Dome sketch	= “max.rad”	10.11 mm
D2@Dome sketch	= ballrad”	4.31 mm
D3@Sagittal sketch	= “neck.rad”	2.60 mm
D1@Frontal sketch	= “max.rad”	10.11 mm
D4@Frontal sketch	= “neck.rad”	2.60 mm
D6@Frontal sketch	= “ballrad”	4.31 mm
D1@Bolt and circular cut	= “FL” * (1 / 9)	30.00 mm
D2@Bolt and circular cut	= “FL” * (2 / 9)	60.00 mm
D5@Bolt and circular cut	= “D1@Bolt and circular cut” / 2	15.00 mm
D6@Bolt and circular cut	= “FL” * (1 / 9)	30.00 mm
D1@Ball diameter	= 2 * (“ballrad” + (“Nylon-Metal.tol / 4))	8.96 mm
D1@Sagittal sketch	= “heel.Dors”	20.0 deg
D2@Sagittal sketch	= “heel.Plant”	50.0 deg
D5@Sagittal sketch	= “ballrad”	4.31 mm
D1@Stem diameter	= 3 – (“Nylon-Nylon.tol” / 2)	2.75 mm
D4@Sagittal sketch	= “neck.rad”	2.60 mm
D5@Frontal sketch	= “neck.rad”	2.60 mm
D1@Smallest ball diameter	= “ballrad” * 2 – (“Nylon-Metal.tol” / 2)	8.26 mm
D2@Frontal sketch	= “Heel.Inv”	32.4 deg
D3@Frontal sketch	= “Heel.Eve”	20.8 deg
D7@Bolt and circular cut	= (“Nylon-Metal,tol” / 2) + 6.35 mm	6.70 mm

B.8.2 Heel plate back

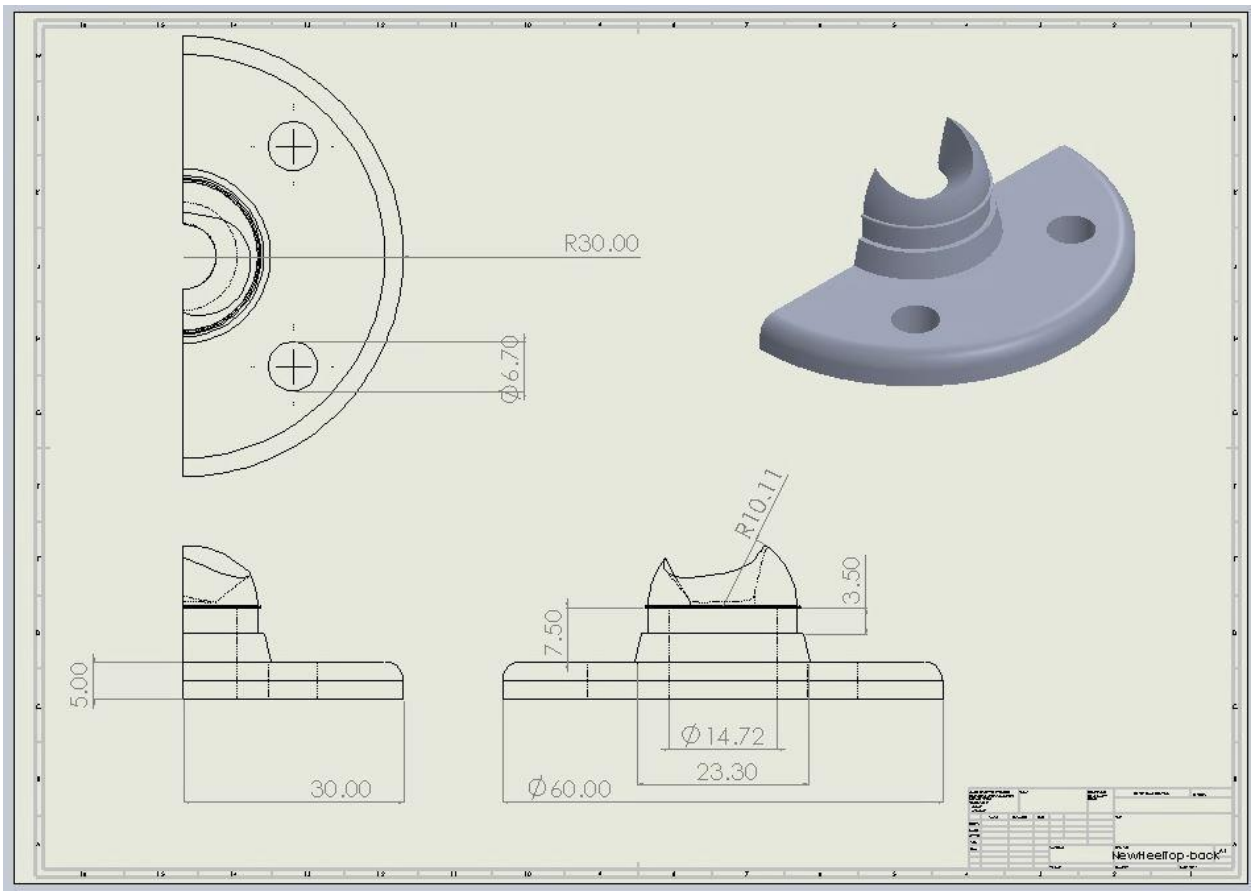

Global variables	Value
“max.rad”	10.11
“ballrad”	4.305
“neck.rad”	2.6
“Heel.Eve”	20.8
“Heel.Inv”	32.4
“FL”	270
“heel.Dors”	20
“heel.Plant”	50
“Nylon-Metal.tol”	0.7
“Nylon-Nylon.tol”	0.5
“Nylon-TPU.tol”	0.3

Sketch	Equations	Value
D1@Dome sketch	= “max.rad”	10.11 mm
D2@Dome sketch	= ballrad”	4.31 mm
D3@Sagittal sketch	= “neck.rad”	2.60 mm
D1@Frontal sketch	= “max.rad”	10.11 mm
D4@Frontal sketch	= “neck.rad”	2.60 mm
D6@Frontal sketch	= “ballrad”	4.31 mm
D1@Bolt and circular cut	= “FL” * (1 / 9)	30.00 mm
D2@Bolt and circular cut	= “FL” * (2 / 9)	60.00 mm
D5@Bolt and circular cut	= “D1@Bolt and circular cut” / 2	15.00 mm
D6@Bolt and circular cut	= “FL” * (1 / 9)	30.00 mm
D1@Ball diameter	= 2 * (“ballrad” + (“Nylon-Metal.tol / 4))	8.96 mm
D1@Sagittal sketch	= “heel.Dors”	20.0 deg
D2@Sagittal sketch	= “heel.Plant”	50.0 deg
D5@Sagittal sketch	= “ballrad”	4.31 mm
D1@Stem diameter	= 3 – (“Nylon-Nylon.tol” / 2)	2.75 mm
D4@Sagittal sketch	= “neck.rad”	2.60 mm
D5@Frontal sketch	= “neck.rad”	2.60 mm
D1@Smallest ball diameter	= “ballrad” * 2 – (“Nylon-Metal.tol” / 2)	8.26 mm
D1@Stem extension	= 7.7	7.70 mm
D2@Frontal sketch	= “Heel.Inv”	32.4 deg
D3@Frontal sketch	= “Heel.Eve”	20.8 deg
D7@Bolt and circular cut	= (“Nylon-Metal,tol” / 2) + 6.35 mm	6.70 mm

B.9 Midfoot

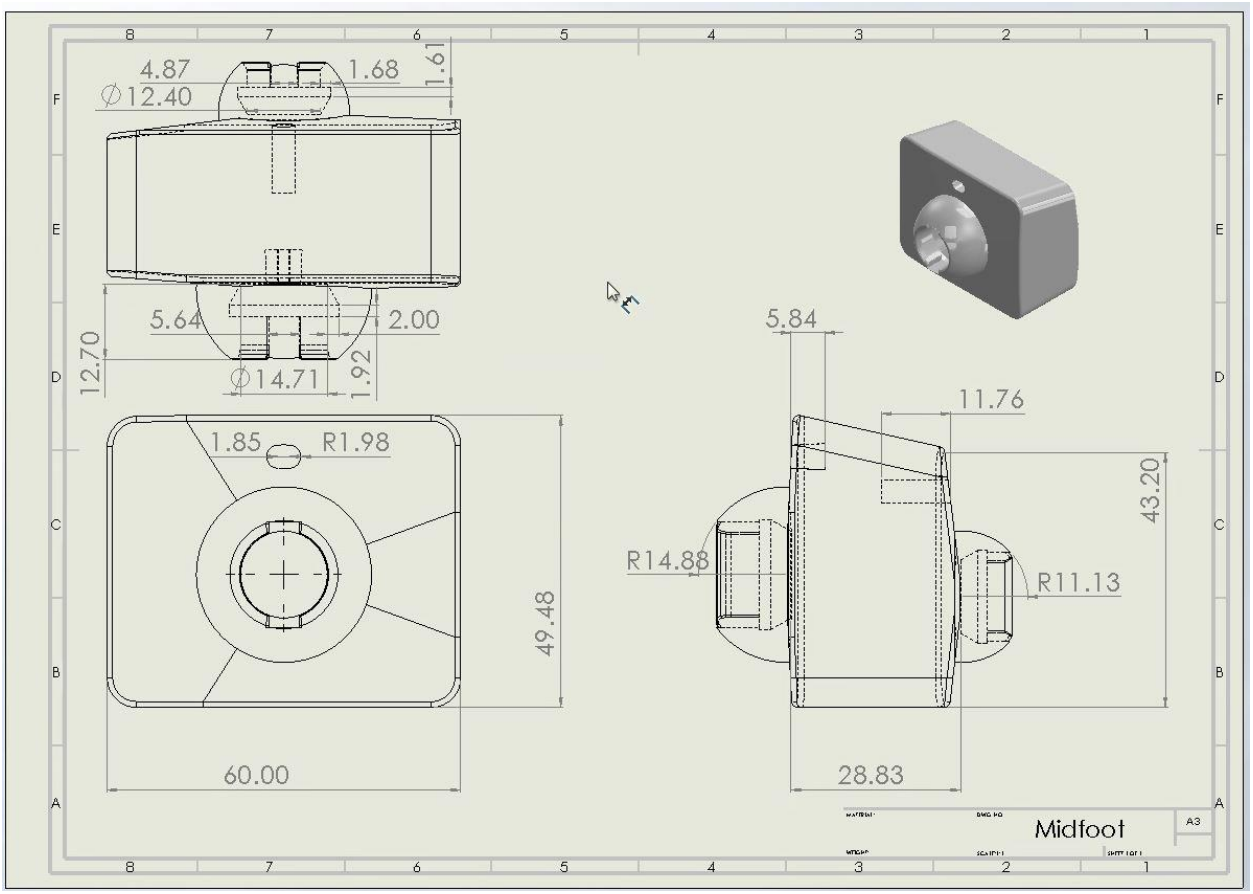

Global variables	Value
“FootLength”	270
“HeelAbd”	0.5
“HeelAdd”	3.8
“HeelPLant”	2.24
“HeelInv”	3.2
“HeelEve”	3.5
“HeelDors”	2.24
“ForeAdd”	6.45
“foreAbd”	1.98
“ForePlant”	6.12
“ForeDors”	6.47
“Nylon-Metal.tol”	0.7
“Nylon-Nylon.tol”	0.5
“Nylon-TPU.tol”	0.3

Sketch	Equations	Value
D1@Overall body sketch	= “FootLength” * (1 / 4.5)	60.00 mm
D2@Overall body sketch	= “FootLength” * (1/ 9)	30.00 mm
D1@Overall body extruding	= “FootLength” * (1 / 5.4)	50.00 mm
D1@HM abd cut	= “HeelAbd” + “Nylon-Nylon.tol”	1.0 deg
D1@HM add cut	= “HeelAdd” + “Nylon-Nylon.tol”	4.3 deg
D1@HM plant cut	= “FootLength” * (1 / 18)	15.00 mm
D2@HM plant cut	= “FootLength” * (1 / 12)	22.50 mm
D3@HM plant cut	= “HeelPlant” + “Nylon-Nylon.tol”	2.74 deg
D1@HH E-I cut Sketch	= “FootLength” * (1 / 6.353)	42.50 mm
D2@HM E-I cut Sketch	= “FootLength” * (1 / 12)	22.50 mm
D3@HM E-I cut Sketch	= “HeelInv” – “Nylon-Metal.tol”	2.5 deg
D4@HM E-I cut Sketch	= “HeelEve” – “Nylon-Metal.tol”	2.8 deg
D1@HM dors cut	= “FootLength” * (1 / 12)	22.50 mm
D2@HM dors cut	= “FootLength” * (1 / 18)	15.00 mm
D3@HM dors cut	= “HeelDors” + “Nylon-Nylon.tol”	2.74 deg
D1@Slope cut	= “FootLength” * (1 / 9)	30 mm
D2@Slope cut	= “FootLength” * (1 / 40.5)	6.67 mm
D1@MF add	= “FootLength” * (1 / 18)	15.00 mm
D2@MF add	= “ForeAdd” + “Nylon-Nylon.tol”	6.95 deg
D1@MF plant	= “FootLength” * (1 / 14.4)	18.75 mm
D2@MF plant	= “ForePlant” + “Nylon-Nylon.tol”	6.62 deg
D2@MF dorsi	= “FootLength” * (1 / 14.4)	18.75 mm
D3@MF dorsi	= “ForeDors” + “Nylon-Nylon.tol”	6.97 deg
D1@MF ball sketch	= “FootLength” * (1 / 12) – (“Nylon-Nylon.tol” / 2)	22.25 mm
D1@MF dorsi	= “FootLength” * (1 / 18)	15.00 mm
D1@HM heel E-I cut	= “Nylon-Metal.tol” + 6	6.70 mm
D7@HM connector sketch	= (14.56 + (“Nylon-TPU.tol” / 2)) / 2	7.36 mm
D3@MF connector	= 1.684	1.68 mm
D4@MF connector	= 2.92 / 2	1.46 mm
D7@MF connector	= 2.92 / 2	1.46 mm
D5@MF connector	= (“Nylon-TPU.tol”) + 5.84	6.14 mm
D5@HM E-I cut sketch	= (“Nylon-Metal.tol” + 3.75) / 2	1.94 mm
D1@MF E-I pinhole	= “FootLength” * (3.25 / 24)	36.56 mm
D2@MF E-I pinhole	= (“Nylon-Metal.tol”) + 3.175	3.88 mm
D1@HM connector sketch	= (“Nylon-TPU.tol” / 2) + 15.5	15.65 mm
D4@HM connector sketch	= 2.002	2.00 mm
D6@HM connector sketch	= (“Nylon-TPU.tol”) +7.00	7.30 mm
D6@MF connector	= (“Nylon-TPU.tol” / 2) + 11.25	11.40 mm
D1@MF E-I pin cut	= 13.00 + “Nylon-Metal.tol”	13.70 mm
D8@MF connector	= (12.25 + (“Nylon-TPU.tol” / 2)) / 2	6.20 mm
D1@HM ball sketch	= (“FootLength” * (1 / 9)) – (“Nylon-Nylon.tol” / 2)	29.75 mm
D1@HM rail	= 4.85 + (“Nylon-TPU.tol”)	5.15 mm
D1@MF rail	= “Nylon-TPU.tol” + 4.08	4.38 mm
D1@Pin 7-8 sketch	= “FootLength” * (1 / 18)	15.00 mm
D1@Pin 14	= “FootLength” * (1 / 12)	22.50 mm
D1@MF abd	= “ForeAbd” + “Nylon-Nylon.tol”	2.5 deg
D3@MF entrance enlargement sketch	= ("Nylon-TPU.tol" / 2) + ("FootLength" / 24) + ("FootLength" / 18) - 2.40	24.00 mm

D3@MF entrance enlargement sketch	= (12.25 + (“Nylon-TPU.tol” / 2)) / 2 – 0.5	5.70 mm
D3@MF entrance enlargement sketch	= “FootLength” * (1 / 14.4)	18.75 mm

B.10 Forefoot

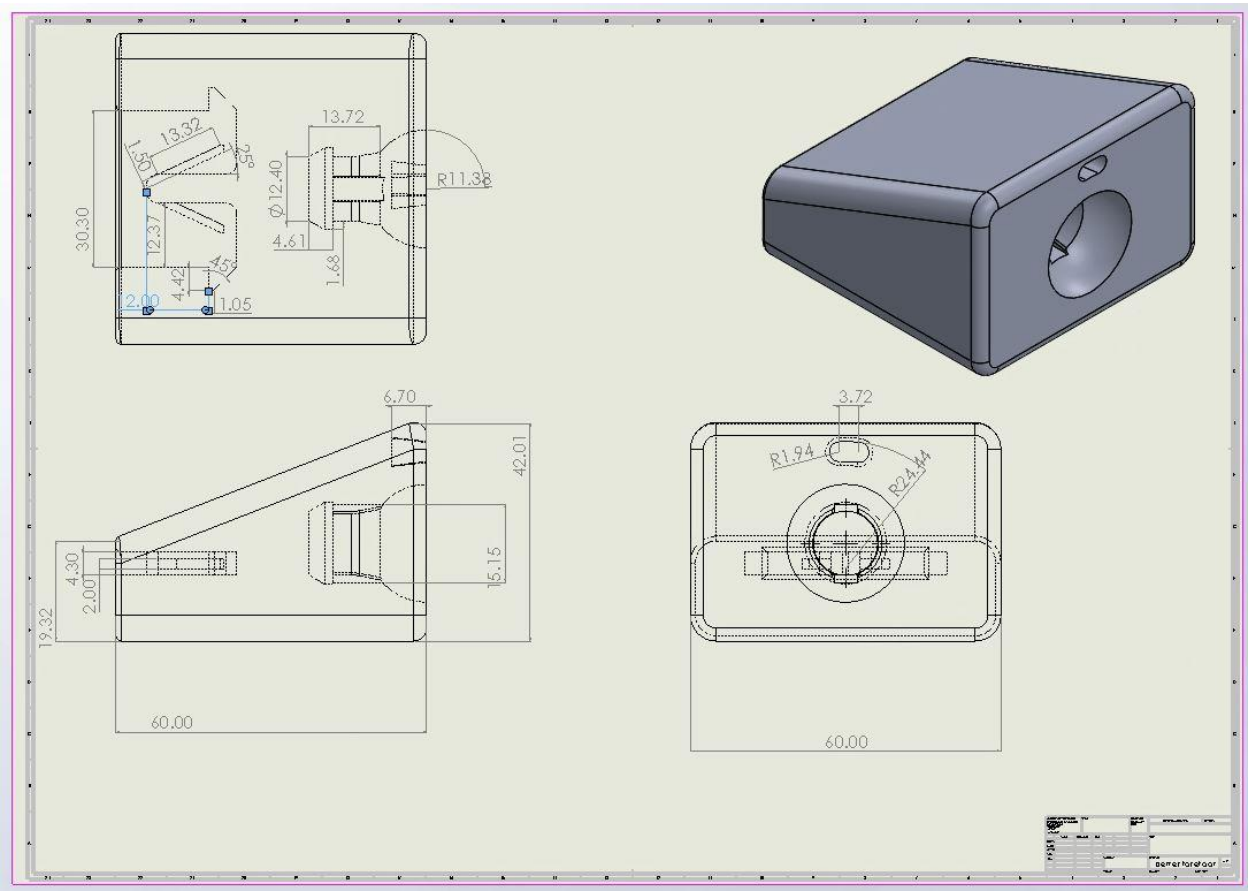

Global variables	Value
“FootLength”	270
“MF_Inv”	7.03
“MF_Eve”	3.47
“Nylon-Metal.tol”	0.7
“Nylon-Nylon.tol”	0.5
“Nylon-TPU.tol”	0.3

Sketch	Equations	Value
D1@Main body sketch	= “FootLength” * (1 / 13.5)	20.00 mm
D3@Main body sketch	= “FootLength” * (1 / 4.5)	60.00 mm
D4@Main body sketch	= “FootLength” * (13 / 81)	43.33 mm
D1@Main body	= “FootLength” * (1 / 4.5)	60.00 mm
D1@Eve-Inv groove sketch	= “FootLength” * (3.25 / 24)	36.56 mm
D2@Eve-Inv groove sketch	= “FootLength” * (1 / 12)	22.50 mm
D3@Eve-Inv groove sketch	= “MF_Inv” – “Nylon-Nylon.tol”	6.53 deg
D4@Eve-Inv groove sketch	= “MF_Eve” – “Nylon-Nylon.tol”	2.97 deg
D5@Eve-Inv groove sketch	= (“Nylon-Metal.tol” + 3.175) / 2	1.94 mm
D1@MF-EI groove	= “Nylon-Metal.tol” + 6	6.70 mm
D1@MF socket sketch	= “FootLength” * (1 / 36)	7.50 mm
D2@MF socket sketch	= “FootLength” * (1 / 12) + (“Nylon-Nylon.tol”) / 2	22.75 mm
D1@MF connector hole sketch	= “FootLength” * (1 / 24)	11.25 mm
D3@MF connector hole sketch	= (12.25 + (“Nylon-TPU.tol” / 2)) / 2	6.20 mm
D4@MF connector hole sketch	= 11.25 + (“Nylon-TPU.tol” / 2)	11.40 mm
D7@MF connector hole sketch	= 5.84 + “Nylon-TPU.tol”	6.14 mm
D2@MF connector hole sketch	= 1.684	1.68 mm
D1@FT plane setter	= “FootLength” * (1 / 18)	15.00 mm
D2@FT hole sketch	= 30 + “Nylon-TPU.tol”	30.30 mm
D3@FT hole sketch	= “Nylon-TPU.tol” + 5.28	5.58 mm
D4@FT hole sketch	= “Nylon-TPU.tol” + 12	12.30 mm
D7@FT hole sketch	= “Nylon-TPU.tol”	0.30 mm
D8@FT hole sketch	= 4.42	4.42 mm
D9@FT hole sketch	= (“Nylon-TPU.tol” / 2) + 10.422 + 1.8	12.37 mm
D1@FT connector hole	= 4 + “Nylon-TPU.tol”	4.30 mm
D1@MF rail sketch	= 4.08 + “Nylon-TPU.tol”	4.38 mm
D1@Pin 13 Sketch	= “FootLength” * (1 / 9)	30.00 mm
D1@Pin 5-6 Sketch	= “FootLength” * (1 / 9)	30.00 mm

B.11 Toes

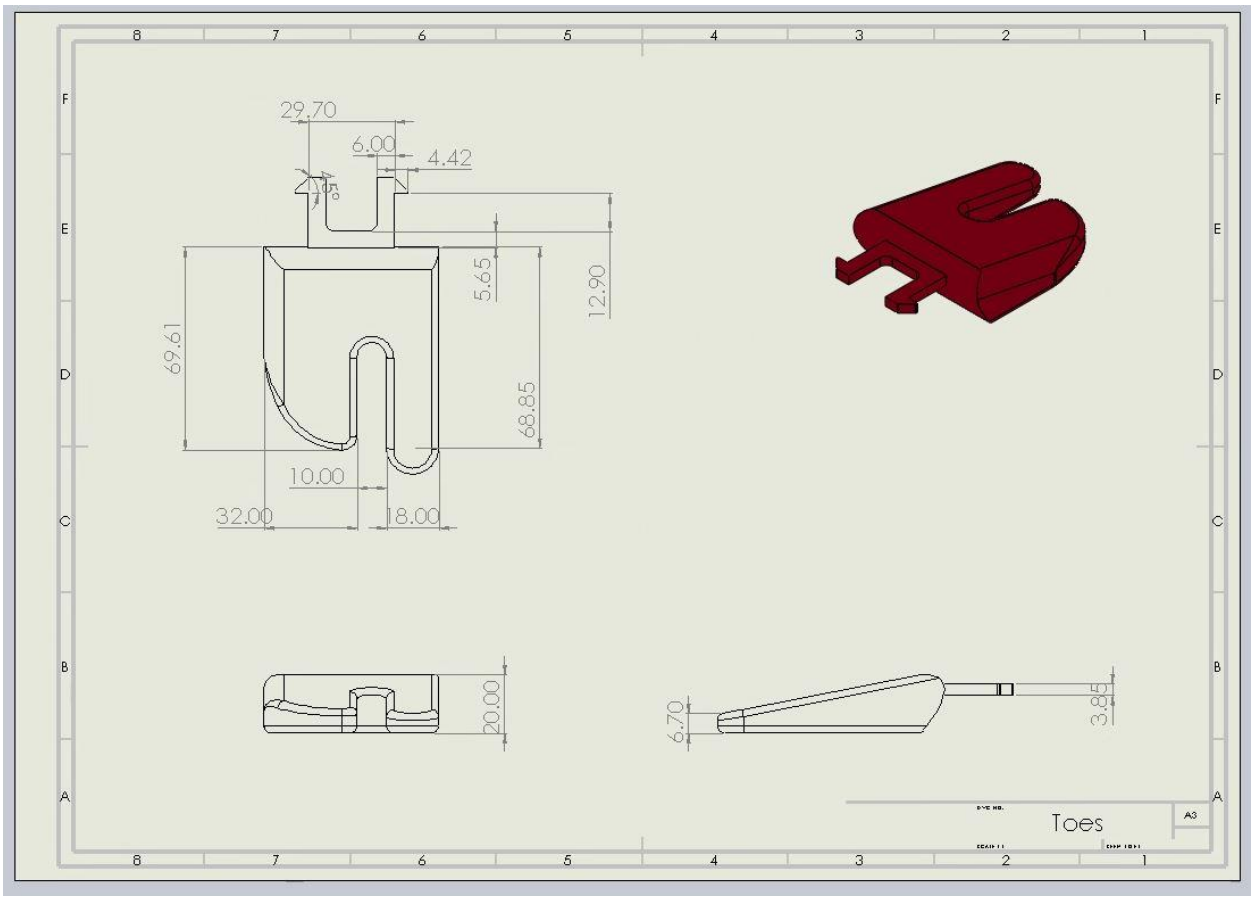

Global variables	Value
“FootLength”	270
“Nylon-Metal.tol”	0.7
“Nylon-Nylon.tol”	0.5
“Nylon-TPU.tol”	0.3

Sketch	Equations	Value
D1@Main body extrusion	= “FootLength” / 13.5	20.00 mm
D2@Toe slope sketch	= “FootLength” * (1 / 3.375) + 1	81.00 mm
D7@Main body sketch	= “FootLength” * (1 / 4.5)	60.00 mm
D2@Main body sketch	= “FootLength” * (1 / 9)	30.00 mm
D3@Main body sketch	= “FootLength” * (1 / 6.75)	40.00 mm
D4@Main body sketch	= “FootLength” * (1 / 30)	9.00 mm
D6@Main body sketch	= “FootLength” * (1 / 30)	10.00 mm
D8@Main body sketch	= “FootLength” * (1 / 30)	30.00 mm
D1@Toe-fore connector	= 4.00 – (“Nylon-TPU.tol” / 2)	3.85 mm
D5@Main body sketch	= “FootLength” * (37 / 540)	18.50 mm
D1@FT plane height sketch	= “FootLength” * (1 / 18)	15.00 mm
D1@FT curved surface	= “FootLength” * (pi / 108)	7.85 mm
D2@FT curved surface	= “FootLength” * (1 / 18)	15.00 mm
D1@Main body sketch	= “FootLength” * (1 / 18)	30.00 mm
D1@FT connector sketch	= 30.00 – (“Nylon-TPU.tol”)	29.70 mm
D3@FT connector sketch	= 4.42	4.42 mm
D6@FT connector sketch	= 1.00 – (“Nylon-TPU.tol” / 2)	0.85 mm
D8@FT connector sketch	= (1.0 * Nylon-TPU.tol”) + 5.28	5.58 mm
D2@FT connector sketch	= Nylon-TPU.tol”	0.30 mm
D9@FT connector sketch	= 12.00 + (2 * “Nylon-TPU.tol”)	12.60 mm
D9@Main body sketch	= “FootLength” * (1 / 8.5)	31.76 mm
D1@Toe slope sketch	= “FootLength” * (1 / 65)	4.15 mm
D2@Pin 2-4	= “FootLength” * (1 / 18)	15.00 mm
D1@ Pin 12	= “FootLength” * (1 / 10)	27.00 mm
D1@Pin 2-4	= “FootLength” * (1 / 36)	7.50 mm
D4@Pin 2-4	= “FootLength” * (1 / 15)	18.00 mm

B.12 Connectors

B.12.1 HM Annular Connectors

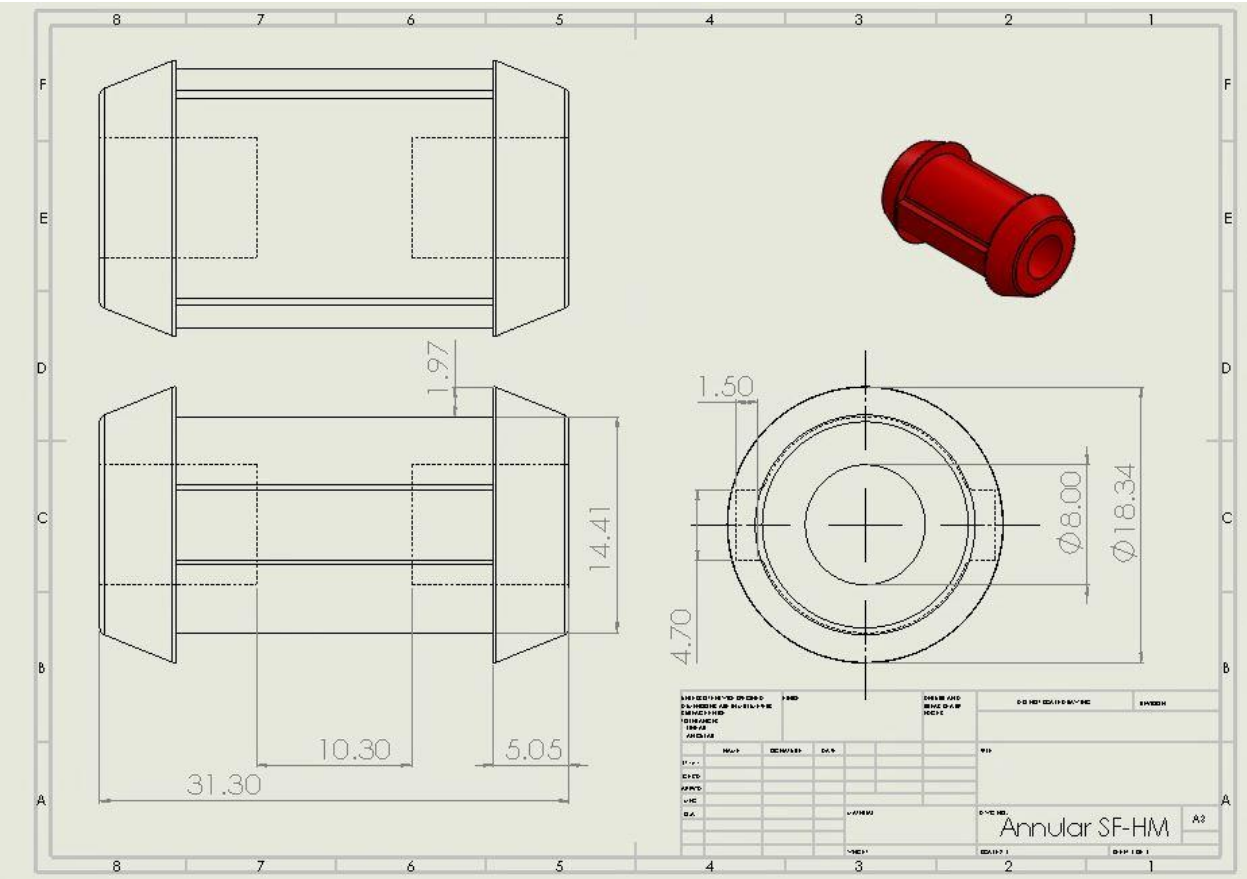

Global variables	Value
“FootLength”	270
“Nylon-Metal.tol”	0.7
“Nylon-Nylon.tol”	0.5
“Nylon-TPU.tol”	0.3

Sketch	Equations	Value
D1@Main body	= 15.5 + (“Nylon-TPU.tol” / 2)	15.65 mm
D3@Notch sketch	= “FootLength” * (1.2 / 18) – 1	17.00 mm
D2@Notch sketch	= 4.004 / 2	2.00 mm
D5@Notch sketch	= “D1@Sketch2” * 2 – (“Nylon-TPU.tol” / 2)	6.64 mm
D1@Main body sketch	= 14.56 mm – (“Nylon-TPU.tol” / 2)	14.41 mm
D1@Rail sketch	= 4.85 mm – (“Nylon-TPU.tol” / 2)	4.70 mm

B.12.2 MF Annular Connectors

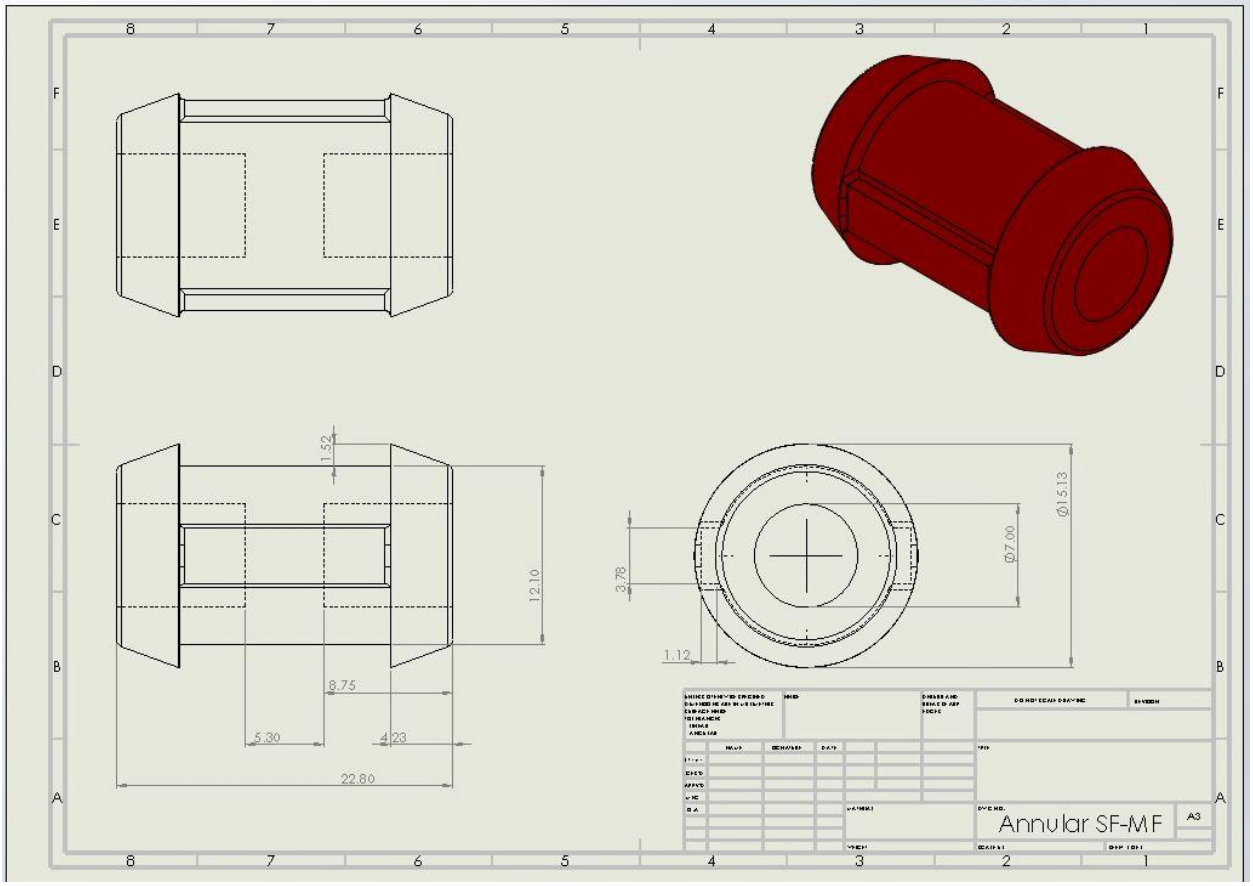

Global variables	Value
“FootLength”	270 mm
“Nylon-Metal.tol”	0.7
“Nylon-Nylon.tol”	0.5
“Nylon-TPU.tol”	0.3

Sketch	Equations	Value
D1@Main body sketch	= 12.25 – (“Nylon-TPU.tol” / 2)	12.10 mm
D1@Main body	= 11.25 + (“Nylon-TPU.tol” * 0.5)	11.40 mm
D1@Notch sketch	= “FootLength” * (1.2 / 24) – 1	12.50 mm
D2@Notch sketch	= 1.685 mm – (“Nylon-TPU.tol” / 2)	1.54 mm
D7@Notch sketch	= “D5@Sketch2” * 2 – (“Nylon-TPU.tol”)	5.54 mm
D1@Rail sketch	= 4.08 – (“Nylon-TPU.tol”)	3.78 mm

B.13 Mould

B.13.1 Mould Front

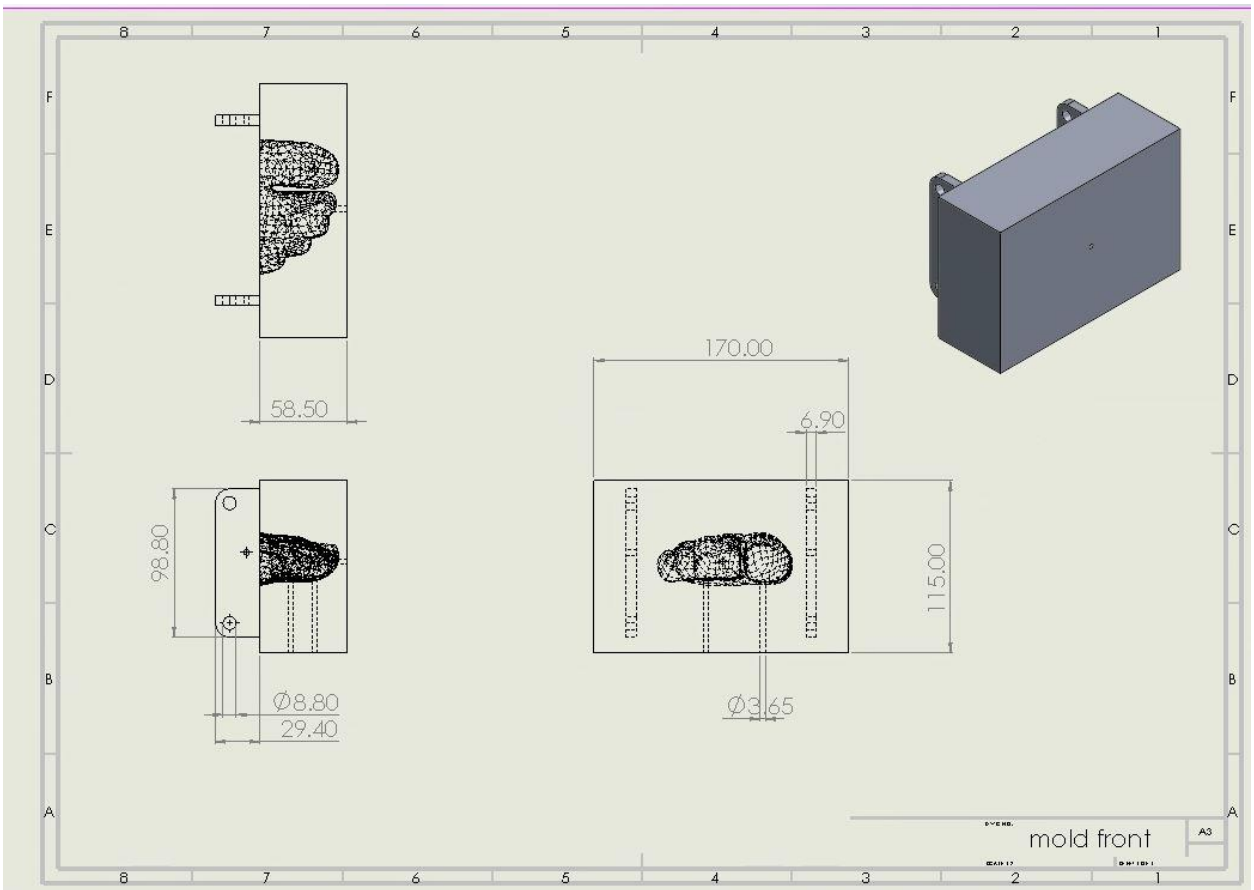

Global variables	Value
“PLA-Metal.tol”	0.8
“PLA-PLA.tol”	0.6
“pin-dia”	3.25
“Cover.length”	272.08

Sketch	Equations	Value
D1@A-1 sketch	= “pin.dia” + “PLA-Metal.tol” / 2	3.65 mm
D3@B-2 sketch	= “pin.dia” + “PLA-Metal.tol” / 2	3.65 mm
D1@T-18 sketch	= “pin.dia” + “PLA-Metal.tol” / 2	3.65 mm
D1@L and M sketch	= “pin.dia” + “PLA-Metal.tol” / 2	3.65 mm
D3@Leaf-lock sketch	= 10.00 – “PLA-PLA.tol”	9.40 mm
D1@Leaf-lock sketch	= 10.00 – “PLA-PLA.tol”	9.40 mm
D1@Leaf-lock extrusion	= 7.50 – “PLA-PLA.tol”	6.90 mm
D2@T-18 sketch	= “Cover.length” * (22.9085571 / 272.08)	22.91 mm
D3@T-18 sketch	= “Cover.length” * (3.1225513 / 272.08)	3.12 mm
D3@A-1 sketch	= “Cover.length” * (3.7592336 / 272.08)	3.76 mm
D2@A-1 sketch	= “Cover.length” * (15.67434921 / 272.08)	15.67 mm
D2@B-2 sketch	= “Cover.length” * (34.12435025 / 272.08)	34.12 mm
D1@B-2 sketch	= “Cover.length” * (317635478 / 272.08)	31.76 mm
D1@Main body sketch	= (“Cover.length” * 0.20215) + 3.5	58.50 mm
D1@bolt hole sketch	= PLA-Metal.tol” + 8.00	8.80 nn

B.13.2 Mould Back Left

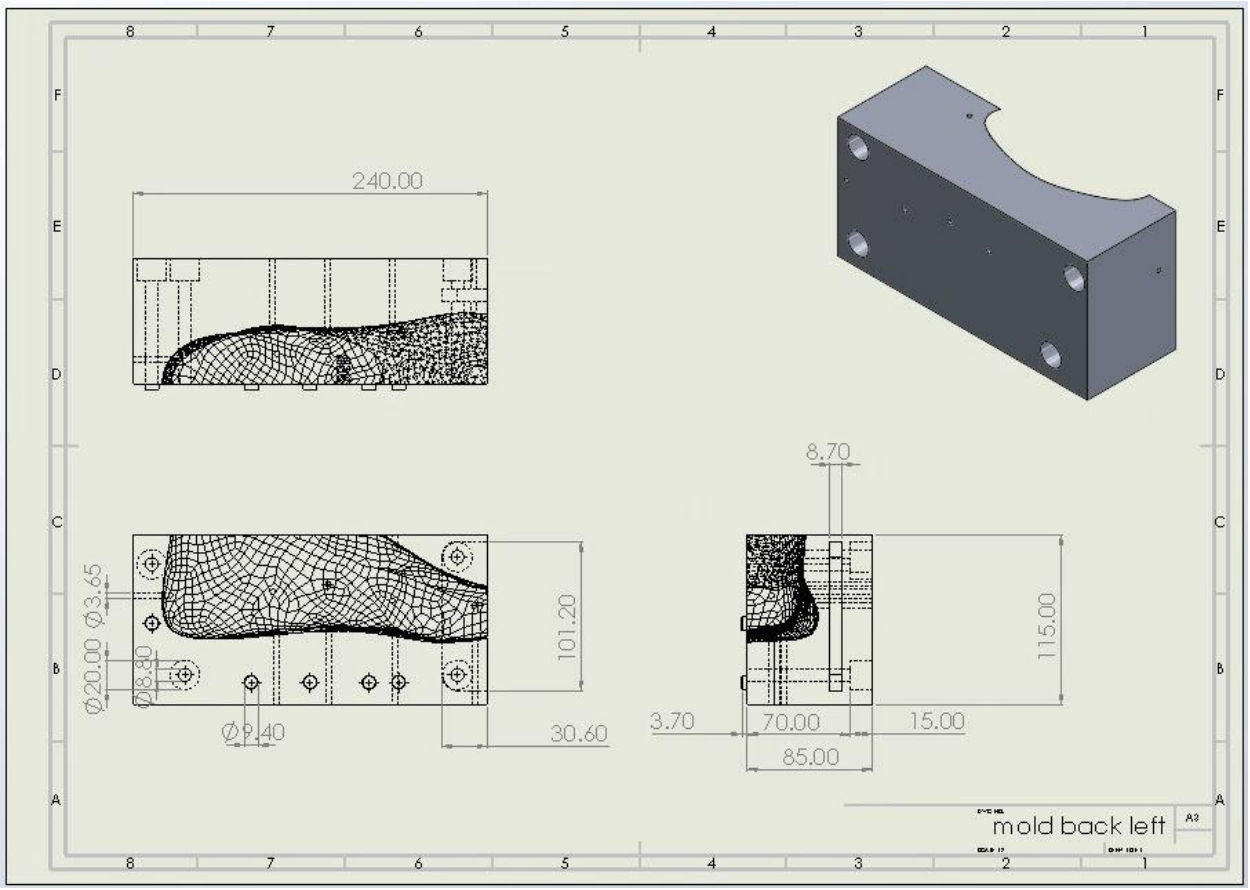

Global variables	Value
“PLA-Metal.tol”	0.8
“PLA-PLA.tol”	0.6
“pin-dia”	3.25
“Cover.length”	272.08

Sketch	Equations	Value
D1@Leaf-lock sketch	= (10 + “PLA-PLA.tol”)	10.60 mm
D2@Leaf-lock sketch	= (10 + “PLA-PLA.tol”)	10.60 mm
D1@Leaf-lock hole	= (“PLA-PLA.tol” * 2) + 7.5	8.70 mm
D1@Alignment bump sketch	= 10 – “PLA-PLA.tol”	9.40 mm
D1@U-21 sketch	= “pin-dia” + (“PLA-Metal.tol” / 2)	3.65 mm
D1@L-12 medial sketch	= “pin-dia” + (“PLA-Metal.tol” / 2)	3.65 mm
D1@N-13 medial sketch	= “pin-dia” + (“PLA-Metal.tol” / 2)	3.65 mm
D1@P-14 medial sketch	= “pin-dia” + (“PLA-Metal.tol” / 2)	3.65 mm
D1@R-15 medial sketch	= “pin-dia” + (“PLA-Metal.tol” / 2)	3.65 mm
D3@C-3 sketch	= “pin-dia” + (“PLA-Metal.tol” / 2)	3.65 mm
D3@E-5 sketch	= “pin-dia” + (“PLA-Metal.tol” / 2)	3.65 mm
D3@G-7 sketch	= “pin-dia” + (“PLA-Metal.tol” / 2)	3.65 mm
D3@I-9 sketch	= “pin-dia” + (“PLA-Metal.tol” / 2)	3.65 mm
D1@Alignment bump extrusion	= 5.00 + “PLA-Metal.tol”	4.20 mm
D1@Corner bolt sketch	= “PLA-Metal.tol” + 8.00	8.80 mm
D3@U-21 sketch	= “Cover.length” * (9.72642976 / 272.08)	9.73 mm
D2@U-21 sketch	= “Cover.length” * (15.23827947 / 272.08)	15.24 mm
D2@R-15 medial sketch	= “Cover.length” * (74.59979381 / 272.08)	74.60 mm
D3@R-15 medial sketch	= “Cover.length” * (12.72642976 / 272.08)	12.23 mm
D3@P-14 medial sketch	= “Cover.length” * (17.52643458 / 272.08)	17.53 mm
D2@P-14 medial sketch	= "Cover.length" * (112.13396871 / 272.08)	112.13 mm
D2@N-13 medial sketch	= "Cover.length" * (155.52996497 / 272.08)	155.53 mm
D3@N-13 medial sketch	= "Cover.length" * (6.28250265 / 272.08)	6.28 mm
D2@L-12 medial sketch	= ("Cover.length" * (213.85915275 / 272.08)) – 2.5	211.36 mm
D3@L-12 medial sketch	= "Cover.length" * (2.88832489 / 272.08)	2.89 mm
D1@I-9 sketch	= "Cover.length" * (19.22391232 / 272.08)	19.22 mm
D1@G-7 sketch	= "Cover.length" * (112.53995601 / 272.08)	112.54 mm
D2@G-7 sketch	= "Cover.length" * (15.45053454 / 272.08)	15.45 mm
D1@E-5 sketch	= "Cover.length" * (157.66641551 / 272.08)	157.67 mm
D2@E-5 sketch	= "Cover.length" * (19.34830776 / 272.08)	19.35 mm
D2@I-9 sketch	= "Cover.length" * (77.32681614 / 272.08)	77.33 mm
D1@C-3 sketch	= ("Cover.length" * (215.09664134 / 272.08)) – 3.5	211.60 mm
D2@C-3 sketch	= "Cover.length" * (24.03493266 / 272.08)	24.03 mm
D1@W-23 sketch	= “pin.dia” + (“PLA-Metal.tol” / 2)	3.65 mm
D1@Main body sketch	= “Cover.length” * (0.8821)	240.00 mm

B.13.3 Mould Back Right

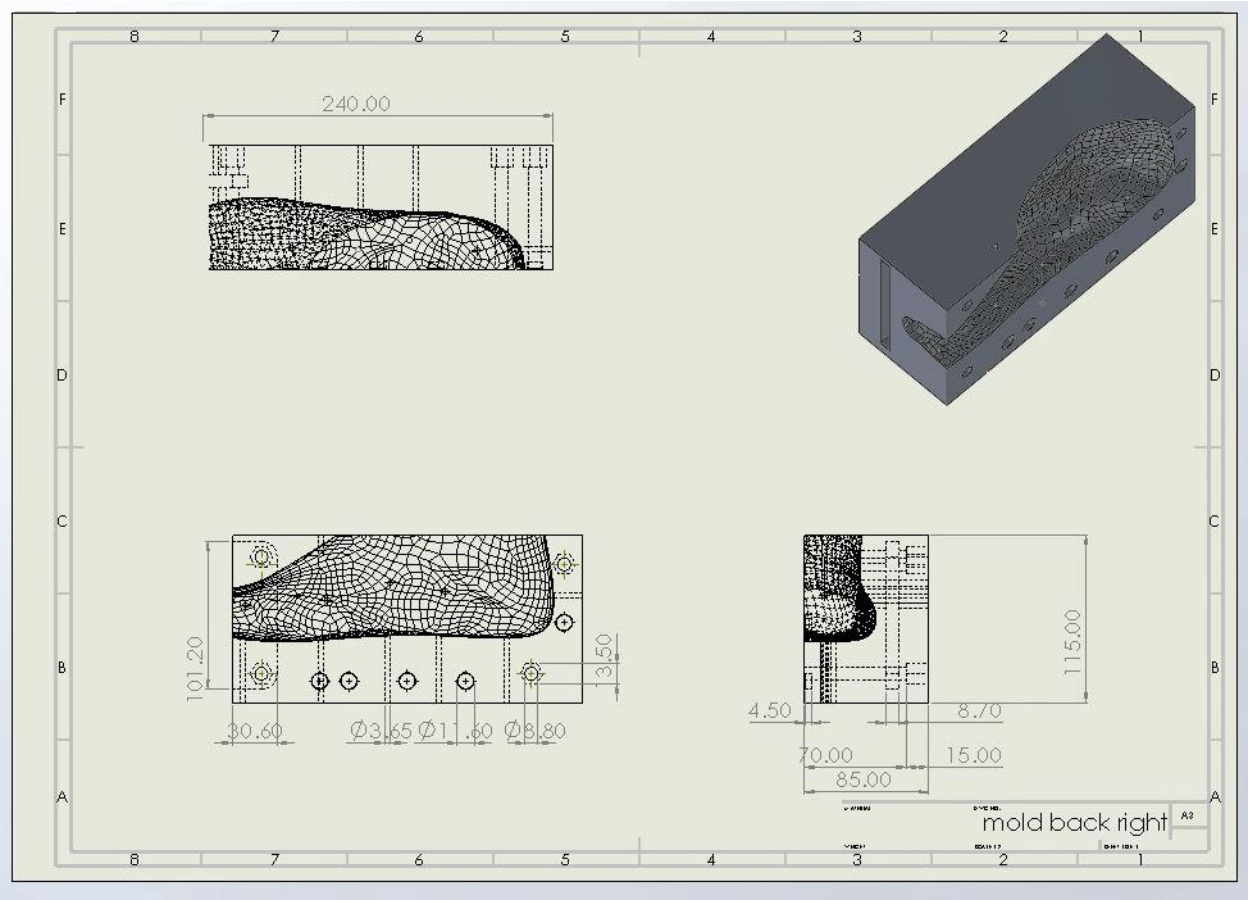

Global variables	Value
“PLA-Metal.tol”	0.8
“PLA-PLA.tol”	0.6
“pin-dia”	3.25
“Cover.length”	272.08

Sketch	Equations	Value
D1@Connector wing sketch	= “PLA-PLA.tol” + 10	10.60 mm
D1@Connector wing cut	= (2 * “PLA-PLA.tol”) + 7.5	8.70 mm
D6@Guiding bumps sketch	= “PLA-PLA.tol” + 10	10.60 mm
D1@V-22 sketch	= “pin.dia” + “PLA-Metal.tol” / 2	3.65 mm
D1@M-12 lateral sketch	= “pin.dia” + “PLA-Metal.tol” / 2	3.65 mm
D1@O-13 lateral sketch	= “pin.dia” + “PLA-Metal.tol” / 2	3.65 mm
D1@Q-14 lateral sketch	= “pin.dia” + “PLA-Metal.tol” / 2	3.65 mm
D1@S-15 lateral sketch	= “pin.dia” + “PLA-Metal.tol” / 2	3.65 mm
D1@D-4 sketch	= “pin.dia” + “PLA-Metal.tol” / 2	3.65 mm
D3@F-6 sketch	= “pin.dia” + “PLA-Metal.tol” / 2	3.65 mm
D1@H-8 sketch	= “pin.dia” + “PLA-Metal.tol” / 2	3.65 mm
D3@J-10 sketch	= “pin.dia” + “PLA-Metal.tol” / 2	3.65 mm
D3@K-11 sketch	= “pin.dia” + “PLA-Metal.tol” / 2	3.65 mm
D1@nut sketch	= “PLA-Metal.tol” + 12.70	13.50 mm
D7@bolt sketch	= “PLA-Metal.tol” + 8.00	8.80 mm
D2@K-11 bolt	= “Cover.length” * (14.10289458 / 272.08)	14.10 mm
D1@K-11 sketch	= “Cover.length” * (32.0722084 / 272.08)	32.07 mm
D2@J-10 sketch	= “Cover.length” * (20.75466192 / 272.08)	20.75 mm
D1@J-10 sketch	= “Cover.length” * (78.8073449 / 272.08)	78.81 mm
D3@H-8 sketch	= “Cover.length” * (14.53413143 / 272.08)	14.53 mm
D2@H-8 sketch	= “Cover.length” * (113.67148981 / 272.08)	113.67 mm
D2@F-6 sketch	= “Cover.length” * (15.27454718 / 272.08)	15.27 mm
D1@F-6 sketch	= “Cover.length” * (158.95991843 / 272.08)	158.96 mm
D2@D-4 sketch	= (“Cover.length” * (216.57716921 / 272.08)) – 3.5	213.08 mm
D3@D-4 sketch	= “Cover.length” * (15.94363364 / 272.08)	15.94 mm
D3@V-22 sketch	= “Cover.length” * (9.73533114 / 272.08)	9.74 mm
D2@V-22 sketch	= “Cover.length” * (14.74486064 / 272.08)	14.74 mm
D2@M-12 lateral sketch	= (“Cover.length” * (21356988876 / 272.08)) -2.5	211.07 mm
D3@M-12 lateral sketch	= “Cover.length” * (2.89696319 / 272.08)	2.90 mm
D2@Q-14 lateral sketch	= “Cover.length” * (111.84467365 / 272.08)	111.84 mm
D3@Q-14 lateral sketch	= “Cover.length” * (17.93540422 / 272.08)	17.94 mm
D2@O-13 lateral sketch	= “Cover.length” * (155.24067456 / 272.08)	155.24 mm
D3@O-13 lateral sketch	= “Cover.length” * (6.29114202 / 272.08)	6.29 mm
D1@X-24 sketch	= “pin.dia” + (“PLA-Metal.tol” / 2)	3.65 mm
D1@Main body sketch	= “Cover.length” * 0.8821	240.00 mm
D5@Guiding bumps sketch	= “Cover.length” * (0.1471)	40.02 mm
D1@Guiding bumps sketch	= “Cover.length” * (0.2940)	79.99 mm

Appendix C

Bill of Materials

Table C-1: 3D printing filament spools

Name	Description	Quantity	Price (CAD)
Nylon filament	1 kg spool of Nylon 230, 1.75 mm width	1	$ 59.95
TPU filament	0.5 kg Cheetah 95A TPU Filament - Sapphire Blue - 1.75mm	1	$ 59.95
PLA filament	Generic 1 kg, 1.75 mm PLA	1	$ 39.95

Table C-2: Main foot components

Name	Description	Quantity	Price CAD (each)	Part Number
Ball stud	QuickDisconnect™ ball stud and socket with 5/16”-24 threads	1	$ 4.96	GTIN 721BJDL5
Heel plate bolt	¼”-20 threads, 3/4” long threads, grade 5, plain finish	4	$ 0.21	UNSPSC 31161501
Heel plate washer	0.734” OD, ¼” ID, plain finish low carbon steel	4	$ 0.05	UNSPSC 31161807
Heel plate nut	¼”-20 internal threads, wrench size 7/16” grade 5, plain finish	4	$ 0.06	UNSPSC 31161727
Heel plate zip tie	Nylon cable ties, 5 ½” length, 3.50 mm wide	1	$ 2.49	Item # 8634-971
SH elastic	Haquno resistance band, heavy band (11-14 kg)	1	$ 13.99	ASIN B08CXR96BF
Shank cover bolt (top)	#6-32 threads, 2” long, zinc finish steel	2	$ 0.08	UNSPSC 31161504
Shank cover bolt (bottom)	#6-32 threads, 1-½”, zinc finish steel	2	$ 0.05	UNSPSC 31161504
Shank cover nut	#6-32 internal threads, wrench size 5/16”, zing finish	4	$ 0.05	UNSPSC 31161727
E-I pin	1/8” diameter, 3 ft long	2	$ 3.79	#061-6100-0
Mould bolt	5/16”-18 threads, 6” long, grade 5 steel, zinc finish	4	$ 4.28	UNSPSC 31161620
Mould nut	5/16” internal threads, wrench size ½”, grade 5 steel, zinc finish	4	$ 0.11	UNSPSC 31161727
Wrapping material	Press’n Seal Wrap™ by Glad	1	$4.99	N/A
Silicone rubber	Mold Star 30™	1 pint	$ 45.00	N/A
Release agent	200 Ease Release™	1 can	$18.50	N/A
Collar screw	Zinc Yellow-Chromate Plated Hex Head Screw, Grade 8 Steel, 1/2"-13 Thread Size, 1-3/4" Long	1	$ 10.90	92620A718
Top Adapter threaded rod	High-Strength Steel Threaded Rod, 1/2"-13 Thread Size, 1-1/2" Long	2	$ 4.53	90322A146
Collar washer	Grade 9 Steel Washer, Zinc Yellow-Chromate Plated, 1/2" Screw Size, 1.092" OD	10	$ 7.65	90850A300

Table C-3: Metal for machined components

Name	Description	Quantity	Price (CAD)
Top adapter raw material	Hot drawn 44W steel, 2” diameter, 4.6” long	1	$ 6.24
Top adapter hex nut	2”-4.5 internal threads, wrench size 3-1/8”	1	$ 12.50
Bottom adapter plate	Cold drawn 1018 steel, flat bar, 4” by 0.375” by 8.35”	1	$ 12.84
Bottom adapter gusset material	Cold drawn 1018 steel, flat bar, 2.00” by 0.25” by 4”	1	$ 1.61
Bottom adapter cylinder	Cold drawn 1018 steel, round bar, 2.50” OD, 3” long	1	$ 11.11
Shank shaft rod	1” OD, 0.5” ID, steel 1045 hot drawn.	1	$ 17.23
Mould pin	2 ½” long nails, 3.25 mm diameter flat head, pack of 100	1	$ 6.28
Collar	1.5” by 2.5” by 3.25” flat bar ASTM 1018 steel	2	$ 9.31

Appendix D

FDM Printer Setting Details

All settings used on a Artillery Sidewinder X1 FDM printer and Cura version 4.8.1.

D.1 Sidewinder X1

Layer resolution	0.1 mm
Frame	Aluminum extrusion
XYZ positioning accuracy	0.05 mm, 0.05 mm, 0.1 mm
Printing filament	PLA, ABS, TPU, flexible materials
Filament diameter	1.75 mm
Nozzle diameter	0.4 mm
Machine dimensions	550 x 405 x 640 mm
Machine dimensions with spool holder	550 x 405 x 870 mm
Machine weight	14 kg
Maximum print speed	150 mm/s
Maximum travel speed	250 mm/s
Build volume	300 x 300 x 400
Extruder type	Titan extruder (direct drive)
Maximum build plate temperature	130°C
Power requirements	100 V / 220 V
	650 W max
Connectivity	USB, TF card, USB stick
Control board	MKS Gen L
Nozzle type	Volcano

D.2 Nylon

Quality	
Layer height	0.2 mm
Initial layer height	0.2 mm
Line width	0.6 mm
Wall line width	0.6 mm
Outer wall line width	0.6 mm
Inner wall(s) line width	0.6 mm
Top/bottom line width	0.6 mm
Infill line width	0.6 mm
Initial layer line width	100.0 %

Shell	
Wall thickness	1.8 mm
Wall line count	2
Top/bottom thickness	0.8 mm
Top thickness	0.8 mm
Top layers	4
Bottom thickness	0.8 mm
Bottom layers	4
Optimize wall printing order	Yes
Fill gaps between walls	Everywhere
Horizontal expansion	0 mm
Enable ironing	No

Infill	
Infill density	85 %
Infill line distance	2.1176 mm
Infill pattern	Cubic
Infill line multiplier	1
Infill overlap percentage	30.0 %
Infill layer thickness	0.2 mm
Gradual infill steps	0

Material	
Printing temperature	235 °C
Printing temperature initial layer	235 °C
Initial printing temperature	235 °C
Final printing temperature	235 °C
Build plate temperature	60 °C
Build plate temperature initial layer	60 °C
Flow	100 %

Speed	
Print speed	60.0 mm/s
Infill speed	60.0 mm/s
Wall speed	30.0 mm/s
Outer wall speed	30.0 mm/s
Inner wall speed	30.0 mm/s
Top/bottom speed	30.0 mm/s
Support speed	30.0 mm/s
Travel speed	150.0 mm/s
Initial layer speed	20.0 mm/s
Skirt/brim speed	20.0 mm/s
Enable acceleration control	No
Enable jerk control	No

Travel	
Enable retraction	Yes
Retract at layer change	No
Retraction distance	2 mm
Retraction speed	25 mm/s
Combing mode	Off
Z hop when retracted	Yes
Z hop only over printed parts	No
Z hop height	0.2 mm

Cooling	
Enable print cooling	No

Support	
Generate support	Yes
Support structure	Normal
Support placement	Touching build plate
Support overhang angle	56 °
Support pattern	Zig Zag
Support density	10 %
Support Z distance	0.4 mm
Support X/Y distance	1.2 mm
Support horizontal expansion	0 mm
Support infill layer thickness	0.2 mm
Gradual support infill steps	0
Enable support interface	Yes
Enable support roof	Yes
Enable support floor	Yes
Support interface thickness	1.0 mm
Support interface density	90%
Support interface pattern	Concentric

Build plate adhesion	
Build plate adhesion type	Brim
Brim width	8.0 mm
Brim line count	14
Brim only on outside	Yes

D.3 TPU

D.3.1 Toes (with support)

Quality	
Layer height	0.2 mm
Initial layer height	0.2 mm
Line width	0.6 mm
Wall line width	0.6 mm
Outer wall line width	0.6 mm
Inner wall(s) line width	0.6 mm
Top/bottom line width	0.6 mm
Infill line width	0.6 mm
Initial layer line width	100.0 %

Shell	
Wall thickness	1.8 mm
Wall line count	2
Top/bottom thickness	0.8 mm
Top thickness	0.8 mm
Top layers	4
Bottom thickness	0.8 mm
Bottom layers	4
Optimize wall printing order	Yes
Fill gaps between walls	Everywhere
Horizontal expansion	0 mm
Enable ironing	No

Infill	
Infill density	100 %
Infill line distance	0.6 mm
Infill pattern	Concentric
Infill line multiplier	1
Infill layer thickness	0.2 mm
Gradual infill steps	0

Material	
Printing temperature	235 °C
Printing temperature initial layer	235 °C
Initial printing temperature	235 °C
Final printing temperature	235 °C
Build plate temperature	60 °C
Build plate temperature initial layer	60 °C
Flow	100 %

Speed	
Print speed	60.0 mm/s
Infill speed	60.0 mm/s
Wall speed	30.0 mm/s
Outer wall speed	30.0 mm/s
Inner wall speed	30.0 mm/s
Top/bottom speed	30.0 mm/s
Support speed	30.0 mm/s
Travel speed	150.0 mm/s
Initial layer speed	20.0 mm/s
Skirt/brim speed	20.0 mm/s
Enable acceleration control	No
Enable jerk control	No

Travel	
Enable retraction	Yes
Retract at layer change	No
Retraction distance	2 mm
Retraction speed	25 mm/s
Combing mode	Off
Z hop when retracted	Yes
Z hop only over printed parts	No
Z hop height	0.2 mm

Cooling	
Enable print cooling	Yes
Fan speed	100.0 %
Regular fan speed	100.0 %
Maximum fan speed	100.0 %
Regular/maximum fan speed threshold	10 s
Initial fan speed	0 %
Regular fan speed at height	0.96 mm
Regular fan speed at layer	3
Minimum layer time	10 s
Minimum speed	10 mm/s
Lift head	No

Support	
Generate support	Yes
Support structure	Normal
Support placement	Touching build plate
Support overhang angle	56 °
Support pattern	Zig Zag
Support density	10 %
Support Z distance	0.4mm
Support X/Y distance	1.2 mm
Support horizontal expansion	0 mm
Support infill layer thickness	0.2 mm
Gradual support infill steps	0
Enable support interface	Yes
Enable support roof	Yes
Enable support floor	Yes
Support interface thickness	1.0 mm
Support interface density	90%
Support interface pattern	Concentric

Build plate adhesion	
Build plate adhesion type	Brim
Brim width	8.0 mm
Brim line count	14
Brim only on outside	Yes

D.3.2 Annular Connectors (no support)

Quality	
Layer height	0.2 mm
Initial layer height	0.2 mm
Line width	0.6 mm
Wall line width	0.6 mm
Outer wall line width	0.6 mm
Inner wall(s) line width	0.6 mm
Top/bottom line width	0.6 mm
Infill line width	0.6 mm
Initial layer line width	100.0 %

Shell	
Wall thickness	1.8 mm
Wall line count	2
Top/bottom thickness	0.8 mm
Top thickness	0.8 mm
Top layers	4
Bottom thickness	0.8 mm
Bottom layers	4
Optimize wall printing order	Yes
Fill gaps between walls	Everywhere
Horizontal expansion	0 mm
Enable ironing	No

Infill	
Infill density	100 %
Infill line distance	0.6 mm
Infill pattern	Concentric
Infill line multiplier	1
Infill layer thickness	0.2 mm
Gradual infill steps	0

Material	
Printing temperature	235 °C
Printing temperature initial layer	235 °C
Initial printing temperature	235 °C
Final printing temperature	235 °C
Build plate temperature	60 °C
Build plate temperature initial layer	60 °C
Flow	100 %

Speed	
Print speed	60.0 mm/s
Infill speed	60.0 mm/s
Wall speed	30.0 mm/s
Outer wall speed	30.0 mm/s
Inner wall speed	30.0 mm/s
Top/bottom speed	30.0 mm/s
Support speed	30.0 mm/s
Travel speed	150.0 mm/s
Initial layer speed	20.0 mm/s
Skirt/brim speed	20.0 mm/s
Enable acceleration control	No
Enable jerk control	No

Travel	
Enable retraction	Yes
Retract at layer change	No
Retraction distance	2 mm
Retraction speed	25 mm/s
Combing mode	Off
Z hop when retracted	Yes
Z hop only over printed parts	No
Z hop height	0.2 mm

Cooling	
Enable print cooling	Yes
Fan speed	100.0 %
Regular fan speed	100.0 %
Maximum fan speed	100.0 %
Regular/maximum fan speed threshold	10 s
Initial fan speed	0 %
Regular fan speed at height	0.96 mm
Regular fan speed at layer	3
Minimum layer time	10 s
Minimum speed	10 mm/s
Lift head	No

Support	
Generate support	No

Build plate adhesion	
Build plate adhesion type	Brim
Brim width	8.0 mm
Brim line count	14
Brim only on outside	Yes

D.4 PLA settings

D.4.1 Mold Back Left

Quality	
Layer height	0.32 mm
Initial layer height	0.32 mm
Line width	0.6 mm
Wall line width	0.6 mm
Outer wall line width	0.6 mm
Inner wall(s) line width	0.6 mm
Top/bottom line width	0.6 mm
Infill line width	0.6 mm
Initial layer line width	100.0 %

Shell	
Wall thickness	1.8 mm
Wall line count	2
Top/bottom thickness	1.28 mm
Top thickness	1.28 mm
Top layers	3
Bottom thickness	1.28 mm
Bottom layers	3
Optimize wall printing order	Yes
Fill gaps between walls	Everywhere
Horizontal expansion	0 mm
Enable ironing	No

Infill	
Infill density	5 %
Infill line distance	12.0 mm
Infill pattern	Gyroid
Infill line multiplier	1
	30.0 %
Infill layer thickness	0.32 mm
Gradual infill steps	0

Material	
Printing temperature	200 °C
Printing temperature initial layer	200 °C
Initial printing temperature	200 °C
Final printing temperature	200 °C
Build plate temperature	60 °C
Build plate temperature initial layer	60 °C
Flow	100 %

Speed	
Print speed	60.0 mm/s
Infill speed	60.0 mm/s
Wall speed	30.0 mm/s
Outer wall speed	30.0 mm/s
Inner wall speed	30.0 mm/s
Top/bottom speed	30.0 mm/s
Support speed	30.0 mm/s
Travel speed	150.0 mm/s
Initial layer speed	20.0 mm/s
Skirt/brim speed	20.0 mm/s
Enable acceleration control	No
Enable jerk control	No

Travel	
Enable retraction	Yes
Retract at layer change	No
Retraction distance	2 mm
Retraction speed	25 mm/s
Combing mode	Off
Z hop when retracted	Yes
Z hop only over printed parts	No
Z hop height	0.2 mm

Cooling	
Enable print cooling	Yes
Fan speed	100.0 %
Regular fan speed	100.0 %
Maximum fan speed	100.0 %
Regular/maximum fan speed threshold	10 s
Initial fan speed	0 %
Regular fan speed at height	0.96 mm
Regular fan speed at layer	3
Minimum layer time	10 s
Minimum speed	10 mm/s
Lift head	No

Support	
Generate support	Yes
Support structure	Normal
Support placement	Everywhere
Support overhang angle	56 °
Support pattern	Zig Zag
Support density	10 %
Support Z distance	0.64 mm
Support X/Y distance	1.2 mm
Support horizontal expansion	0 mm
Support infill layer thickness	0.2 mm
Gradual support infill steps	0
Enable support interface	Yes
Enable support roof	Yes
Enable support floor	Yes
Support interface thickness	1.0 mm
Support interface density	90%
Support interface pattern	Concentric

Build plate adhesion	
Build plate adhesion type	Brim
Brim width	8.0 mm
Brim line count	14
Brim only on outside	Yes

D.4.2 PLA Settings for Mould Front, Mould Back Right

Quality	
Layer height	0.32 mm
Initial layer height	0.32 mm
Line width	0.6 mm
Wall line width	0.6 mm
Outer wall line width	0.6 mm
Inner wall(s) line width	0.6 mm
Top/bottom line width	0.6 mm
Infill line width	0.6 mm
Initial layer line width	100.0 %

Shell	
Wall thickness	1.8 mm
Wall line count	2
Top/bottom thickness	1.28 mm
Top thickness	1.28 mm
Top layers	3
Bottom thickness	1.28 mm
Bottom layers	3
Optimize wall printing order	Yes
Fill gaps between walls	Everywhere
Horizontal expansion	0 mm
Enable ironing	No

Infill	
Infill density	5 %
Infill line distance	12.0 mm
Infill pattern	Gyroid
Infill line multiplier	1
	30.0 %
Infill layer thickness	0.32 mm
Gradual infill steps	0

Material	
Printing temperature	200 °C
Printing temperature initial layer	200 °C
Initial printing temperature	200 °C
Final printing temperature	200 °C
Build plate temperature	60 °C
Build plate temperature initial layer	60 °C
Flow	100 %

Speed	
Print speed	60.0 mm/s
Infill speed	60.0 mm/s
Wall speed	30.0 mm/s
Outer wall speed	30.0 mm/s
Inner wall speed	30.0 mm/s
Top/bottom speed	30.0 mm/s
Support speed	30.0 mm/s
Travel speed	150.0 mm/s
Initial layer speed	20.0 mm/s
Skirt/brim speed	20.0 mm/s
Enable acceleration control	No
Enable jerk control	No

Travel	
Enable retraction	Yes
Retract at layer change	No
Retraction distance	2 mm
Retraction speed	25 mm/s
Combing mode	Off
Z hop when retracted	Yes
Z hop only over printed parts	No
Z hop height	0.2 mm

Cooling	
Enable print cooling	Yes
Fan speed	100.0 %
Regular fan speed	100.0 %
Maximum fan speed	100.0 %
Regular/maximum fan speed threshold	10 s
Initial fan speed	0 %
Regular fan speed at height	0.96 mm
Regular fan speed at layer	3
Minimum layer time	10 s
Minimum speed	10 mm/s
Lift head	No

Support	
Generate support	No

Build plate adhesion	
Build plate adhesion type	Brim
Brim width	8.0 mm
Brim line count	14
Brim only on outside	Yes

D.4.3 Shank Covers: Back and Front

Quality	
Layer height	0.32 mm
Initial layer height	0.32 mm
Line width	0.6 mm
Wall line width	0.6 mm
Outer wall line width	0.6 mm
Inner wall(s) line width	0.6 mm
Top/bottom line width	0.6 mm
Infill line width	0.6 mm
Initial layer line width	100.0 %

Shell	
Wall thickness	1.8 mm
Wall line count	3
Top/bottom thickness	1.28 mm
Top thickness	1.28 mm
Top layers	4
Bottom thickness	1.28 mm
Bottom layers	4
Optimize wall printing order	Yes
Fill gaps between walls	Everywhere
Horizontal expansion	0 mm
Enable ironing	No

Infill	
Infill density	15 %
Infill line distance	12.0 mm
Infill pattern	Cubic
Infill line multiplier	1
	30.0 %
Infill layer thickness	0.32 mm
Gradual infill steps	0

Material	
Printing temperature	200 °C
Printing temperature initial layer	200 °C
Initial printing temperature	200 °C
Final printing temperature	200 °C
Build plate temperature	60 °C
Build plate temperature initial layer	60 °C
Flow	100 %

Speed	
Print speed	60.0 mm/s
Infill speed	60.0 mm/s
Wall speed	30.0 mm/s
Outer wall speed	30.0 mm/s
Inner wall speed	30.0 mm/s
Top/bottom speed	30.0 mm/s
Support speed	30.0 mm/s
Travel speed	150.0 mm/s
Initial layer speed	20.0 mm/s
Skirt/brim speed	20.0 mm/s
Enable acceleration control	No
Enable jerk control	No

Travel	
Enable retraction	Yes
Retract at layer change	No
Retraction distance	2 mm
Retraction speed	25 mm/s
Combing mode	Off
Z hop when retracted	Yes
Z hop only over printed parts	No
Z hop height	0.2 mm

Cooling	
Enable print cooling	Yes
Fan speed	100.0 %
Regular fan speed	100.0 %
Maximum fan speed	100.0 %
Regular/maximum fan speed threshold	10 s
Initial fan speed	0 %
Regular fan speed at height	0.96 mm
Regular fan speed at layer	3
Minimum layer time	10 s
Minimum speed	10 mm/s
Lift head	No

Support	
Generate support	Yes
Support structure	Normal
Support placement	Touching Buildplate
Support overhang angle	43 °
Support pattern	Zig Zag
Support density	10 %
Support Z distance	0.64 mm
Support X/Y distance	1.2 mm
Support horizontal expansion	0 mm
Support infill layer thickness	0.32 mm
Gradual support infill steps	0
Enable support interface	Yes
Enable support roof	Yes
Enable support floor	Yes
Support interface thickness	1.6 mm
Support interface density	90%
Support interface pattern	Concentric

Build plate adhesion	
Build plate adhesion type	Brim
Brim width	8.0 mm
Brim line count	14
Brim only on utside	Yes

Appendix E

Results

E.1 Motion Graphs

E.1.1 Initial Test Block

E.1.1.1 SH block motion

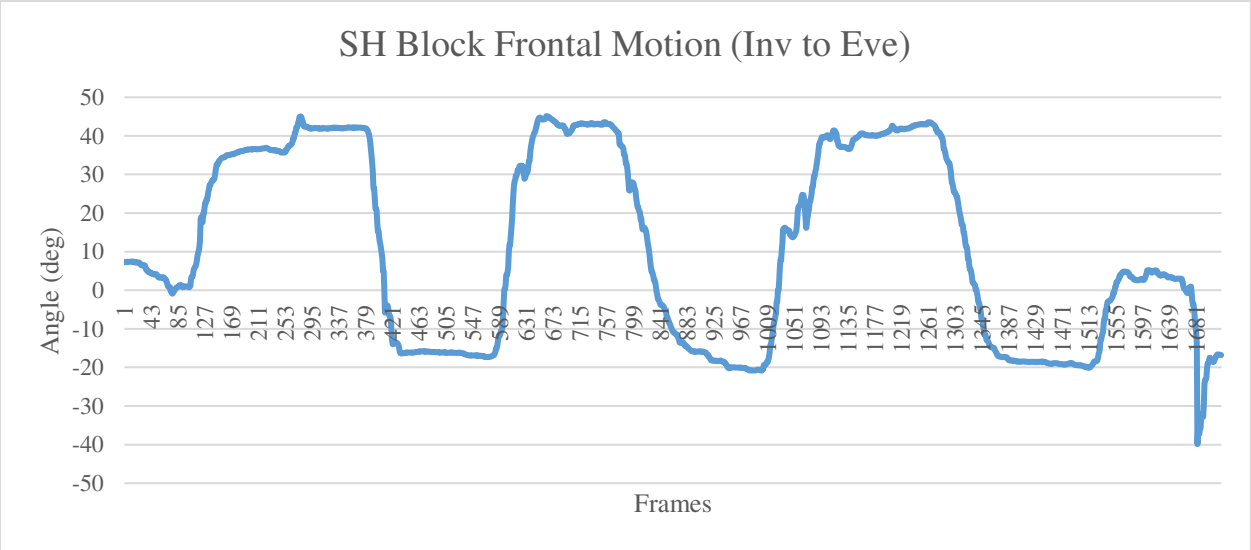

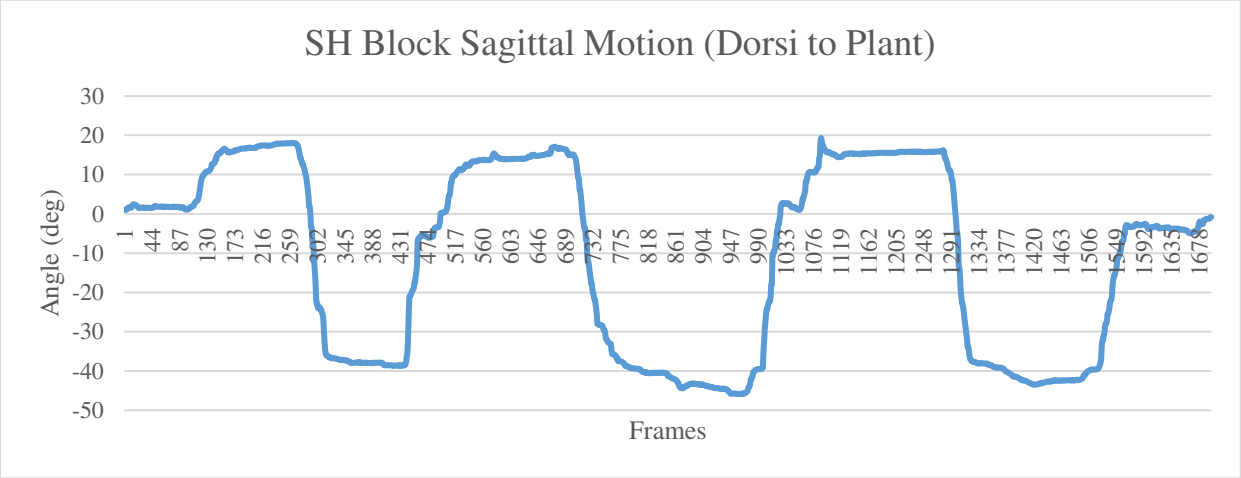

E.1.1.2 HM Block Motion

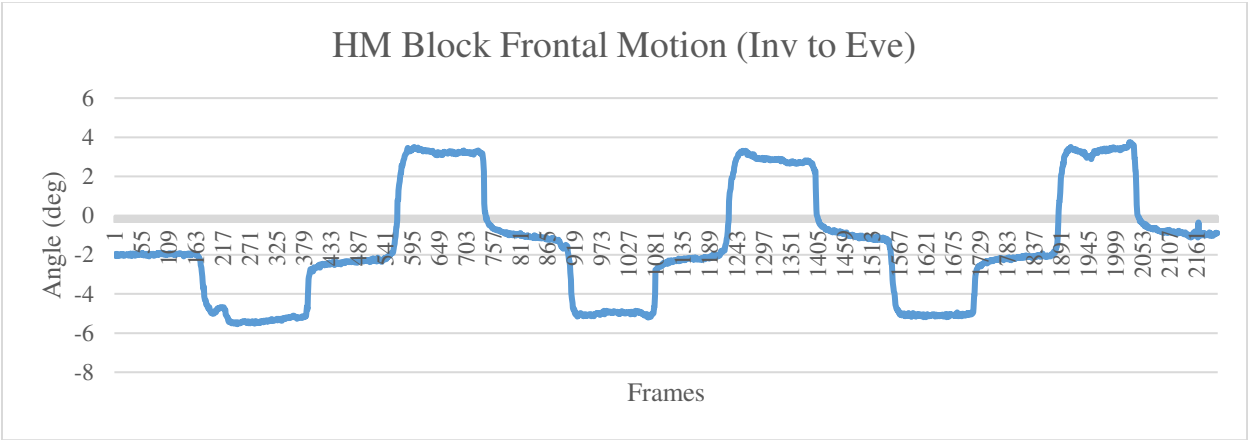

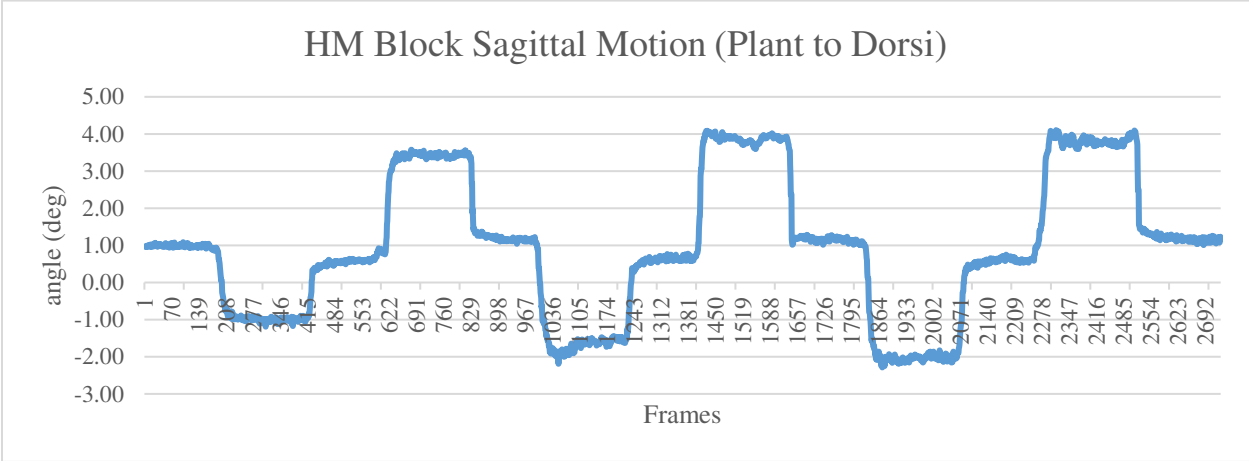

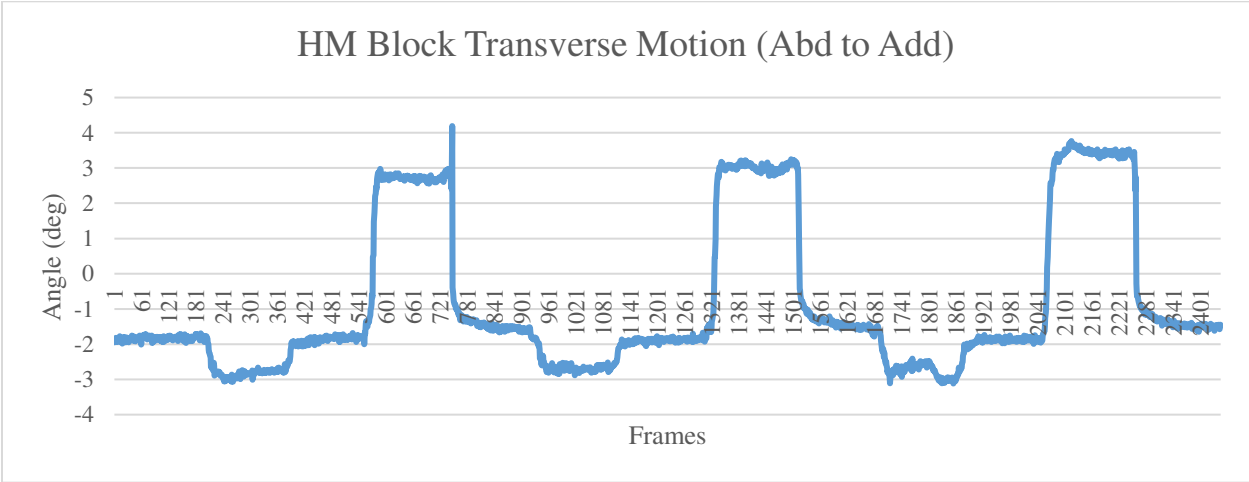

E.1.1.3 MF Block Motion

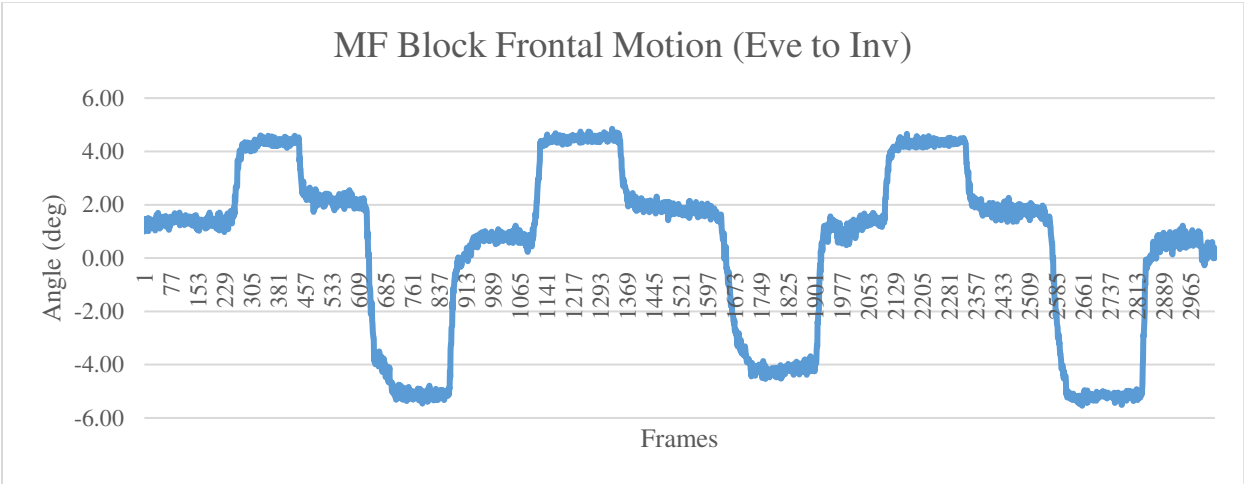

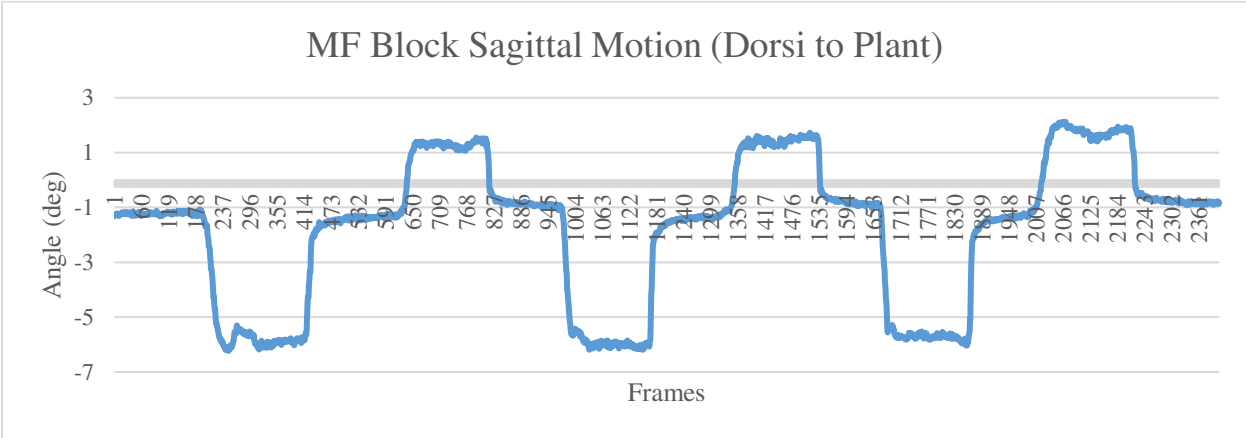

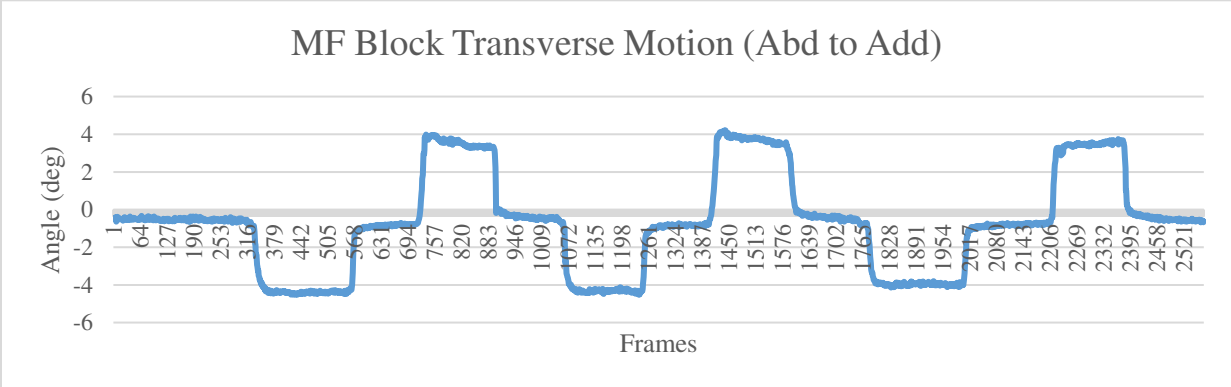

E.1.1.4 FT block Motion

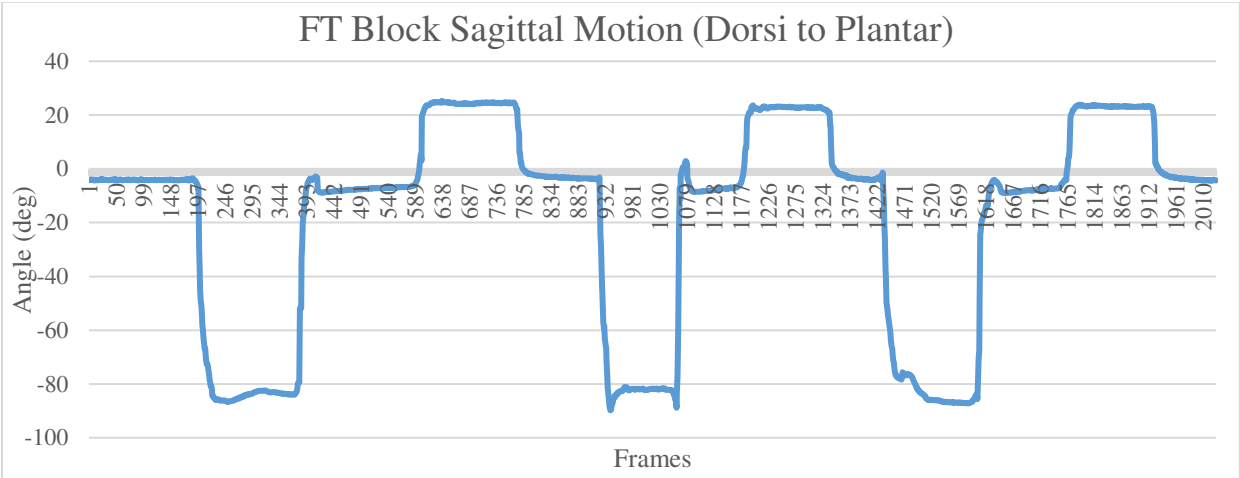

E.1.2 SLL pre-cast

E.1.2.1 SH Joint

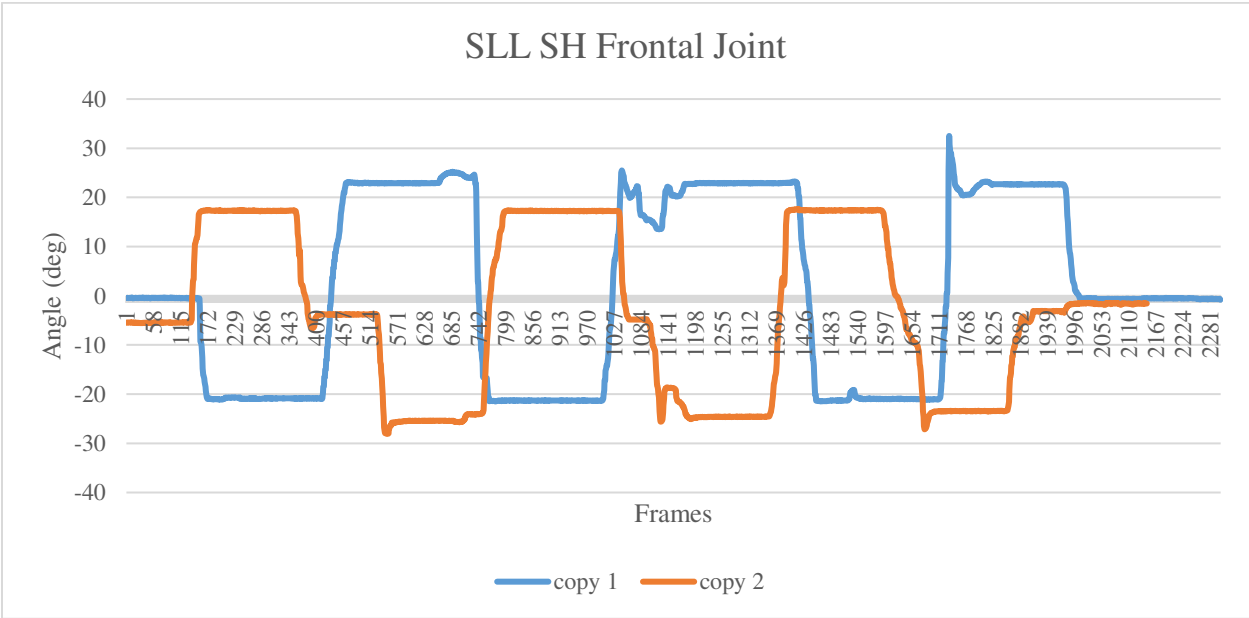

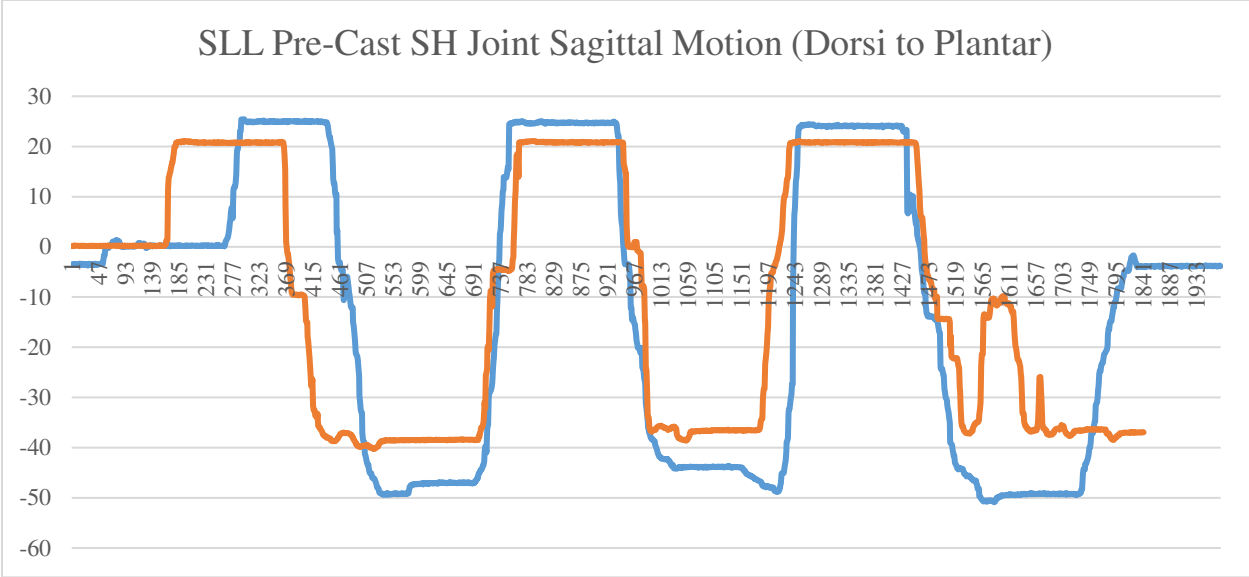

E.1.2.2 HM Joint

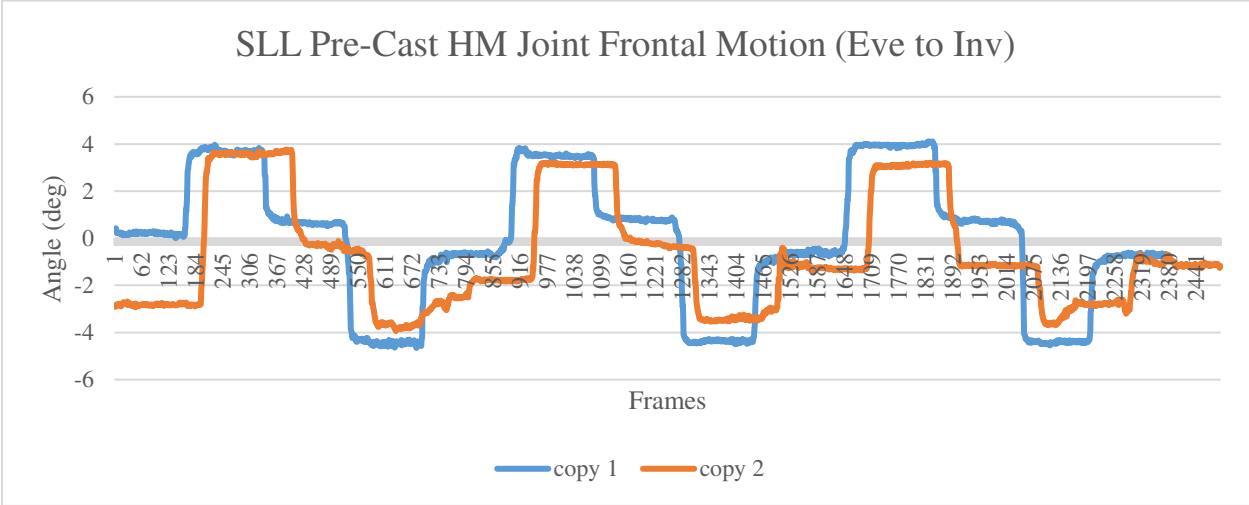

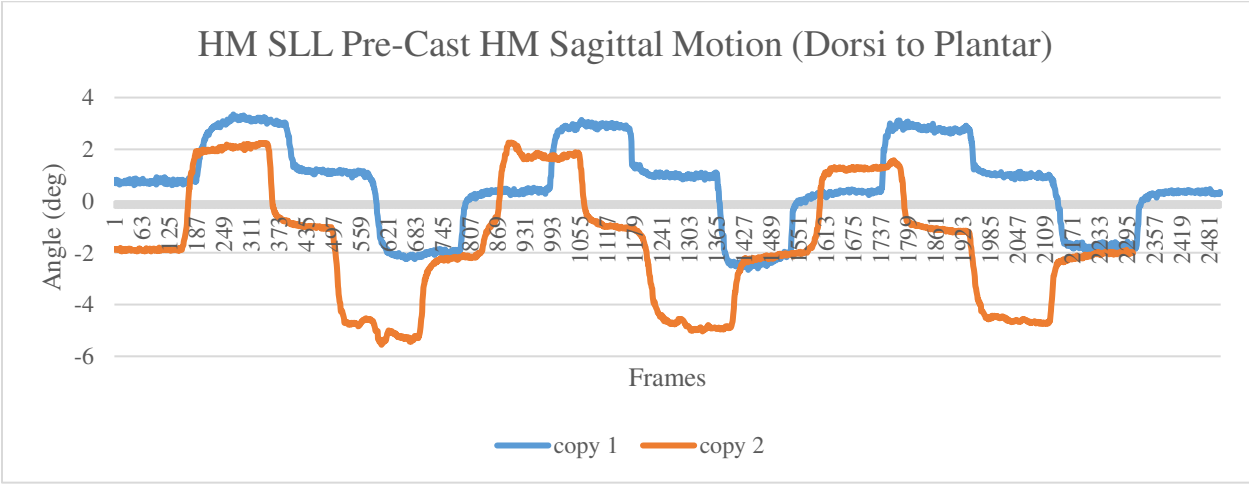

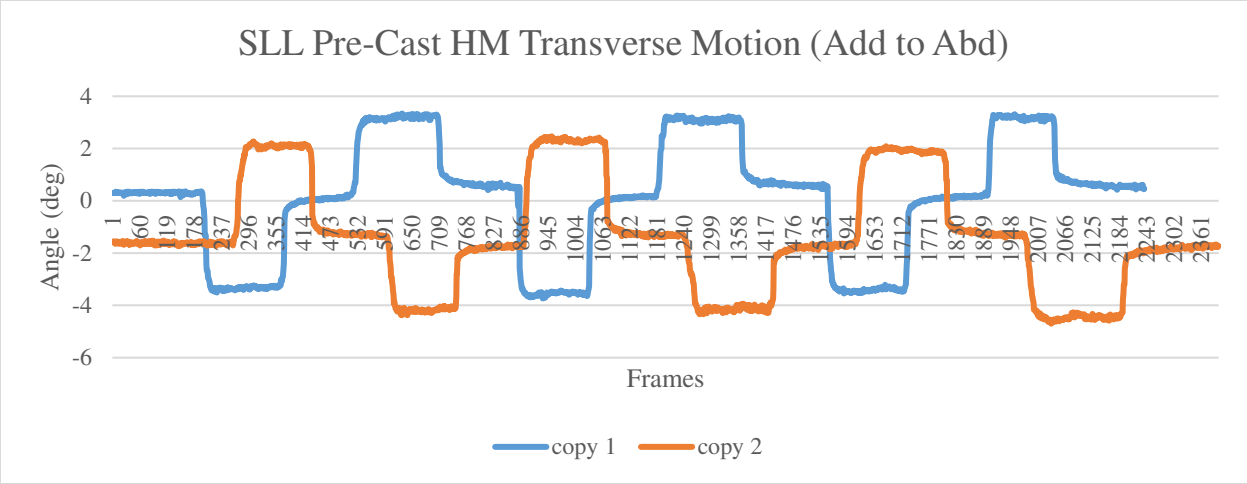

E.1.2.3 MF Joint

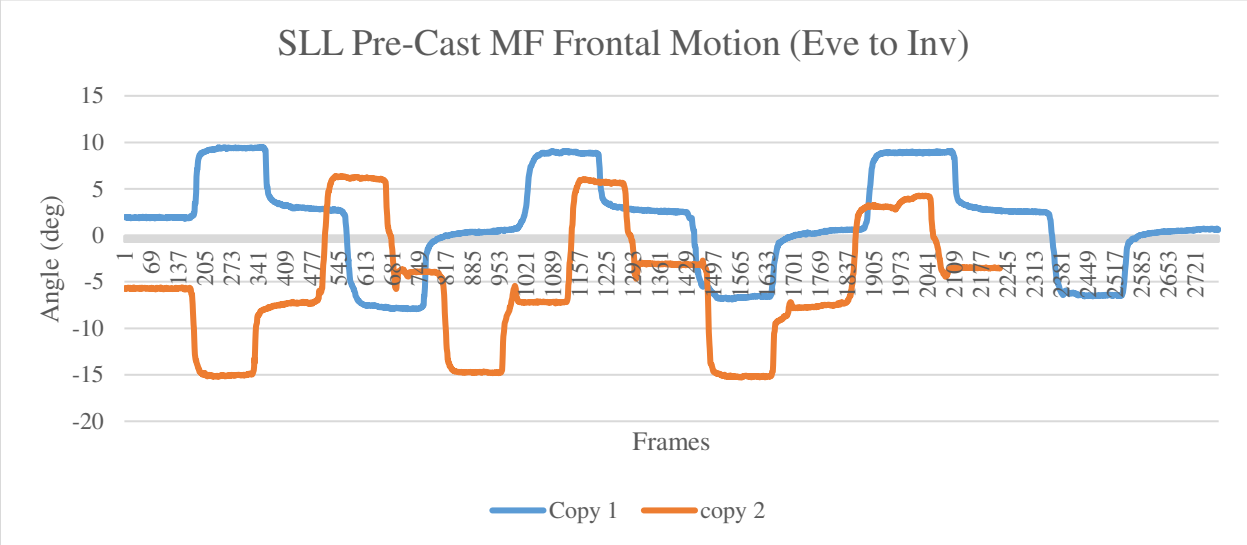

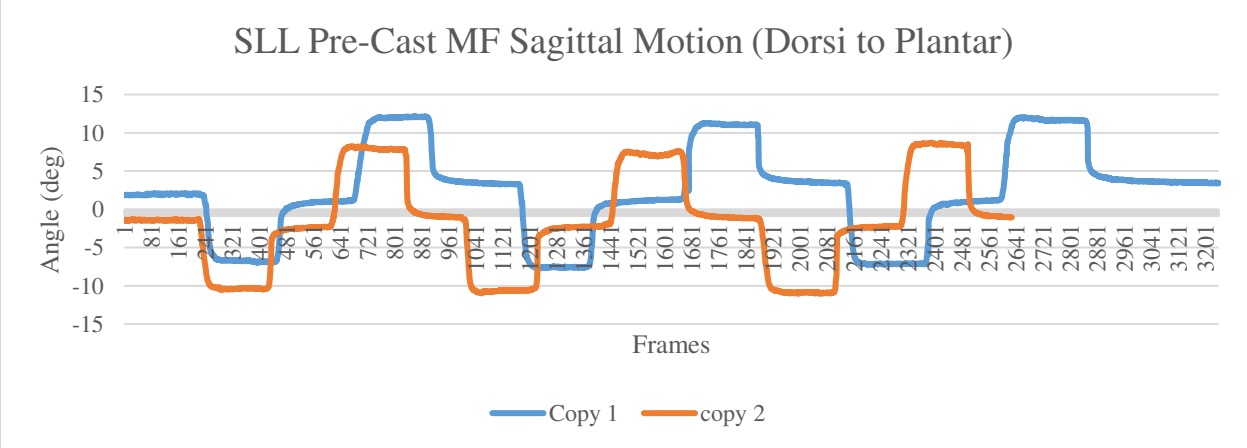

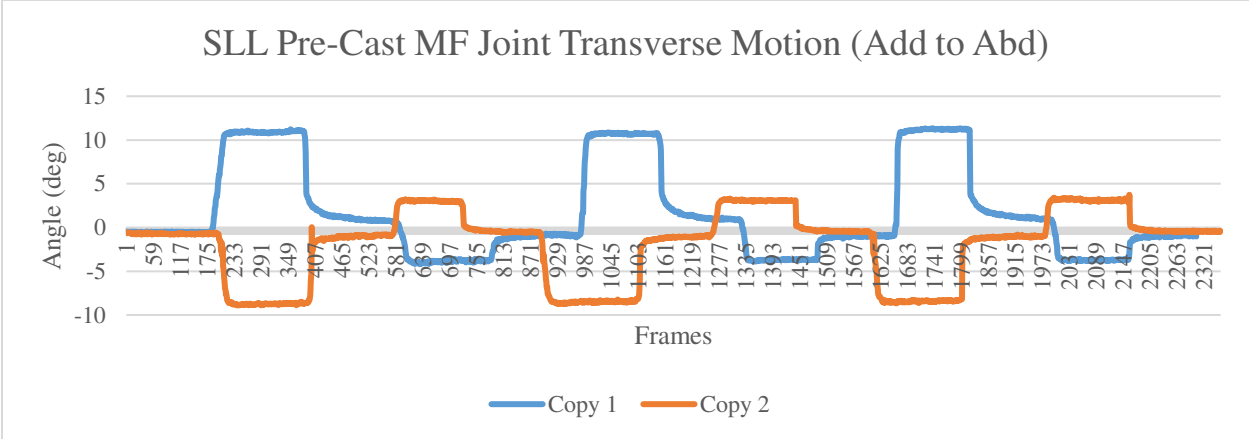

E.1.2.4 FT Joint

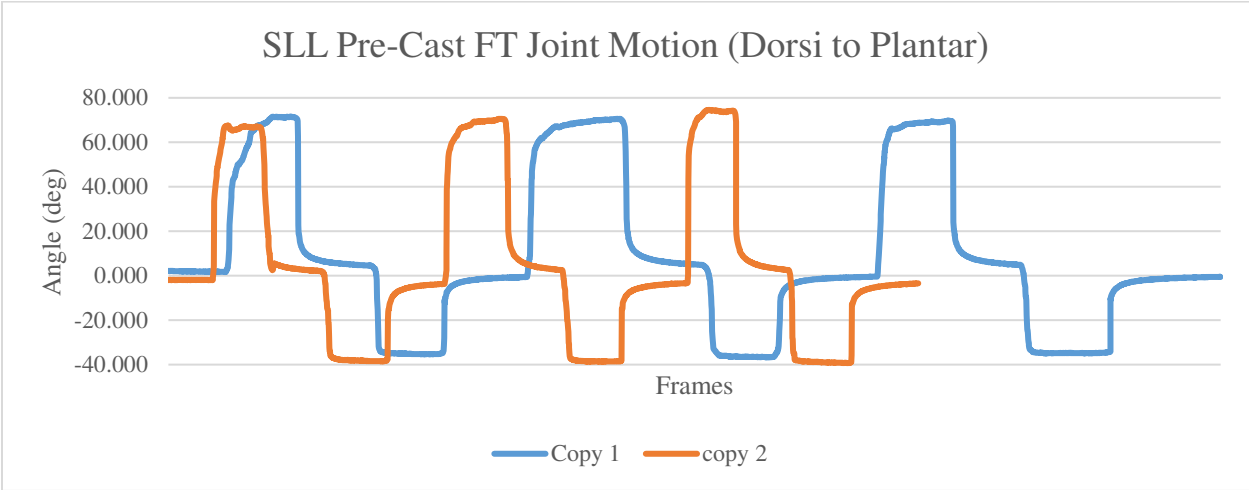

E.1.3 SLL Post-Cast

E.1.3.1 SH Joint

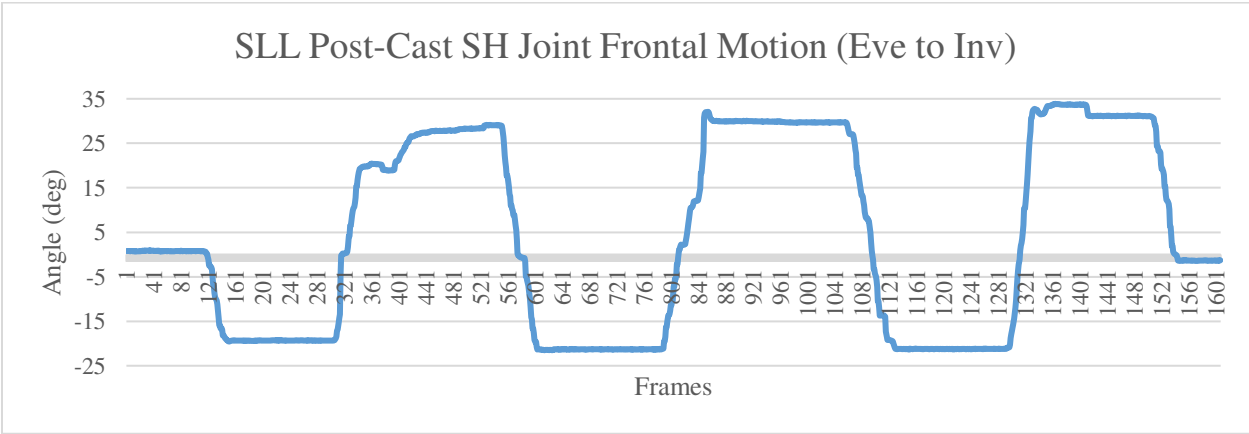

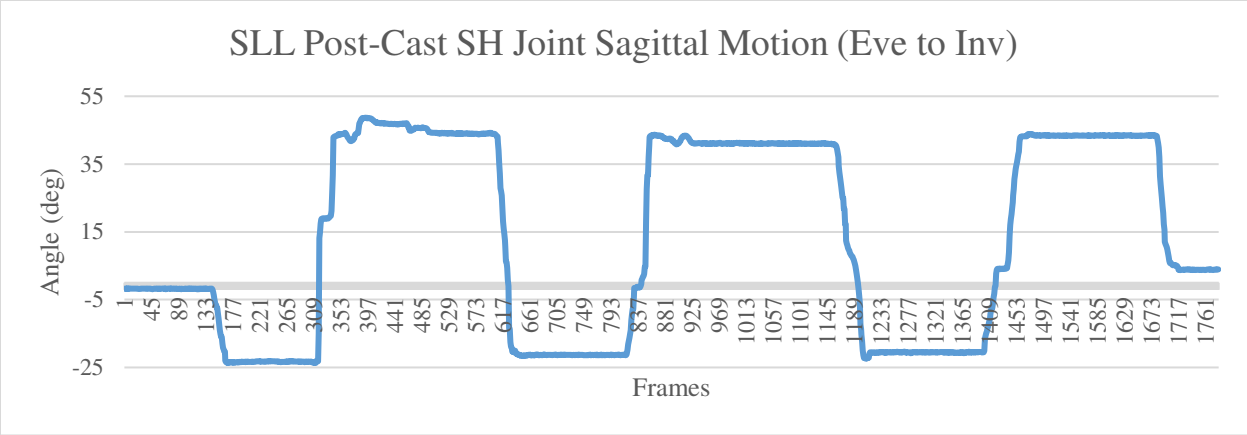

E.1.3.2 HM Joint

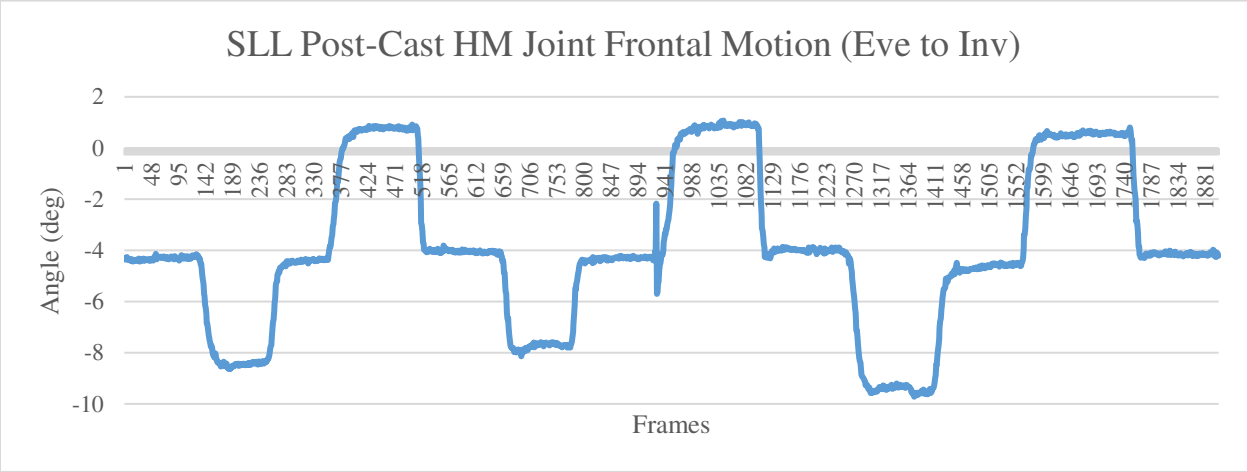

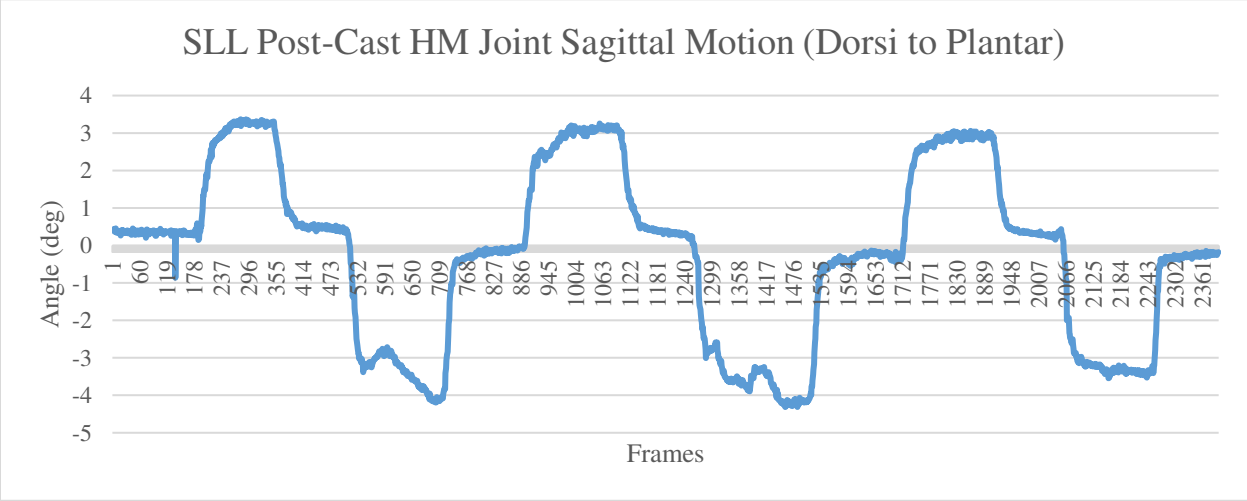

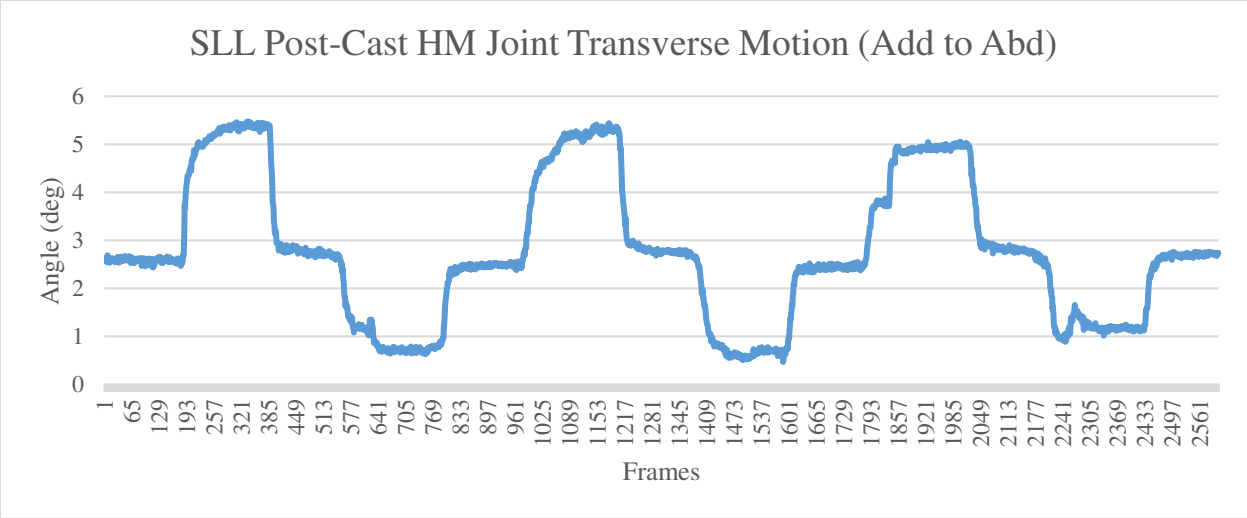

E.1.3.3 MF Joint

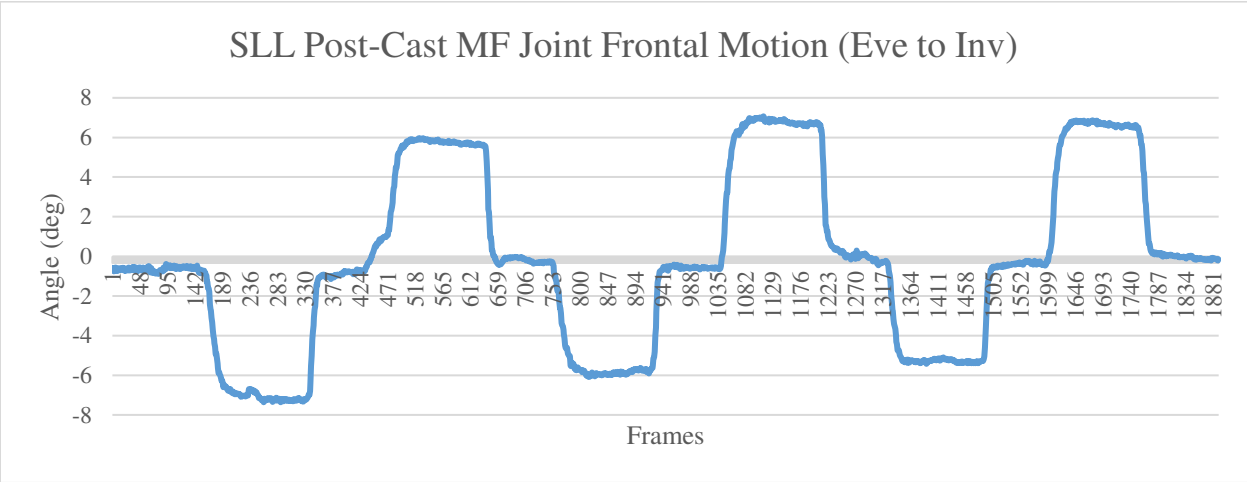

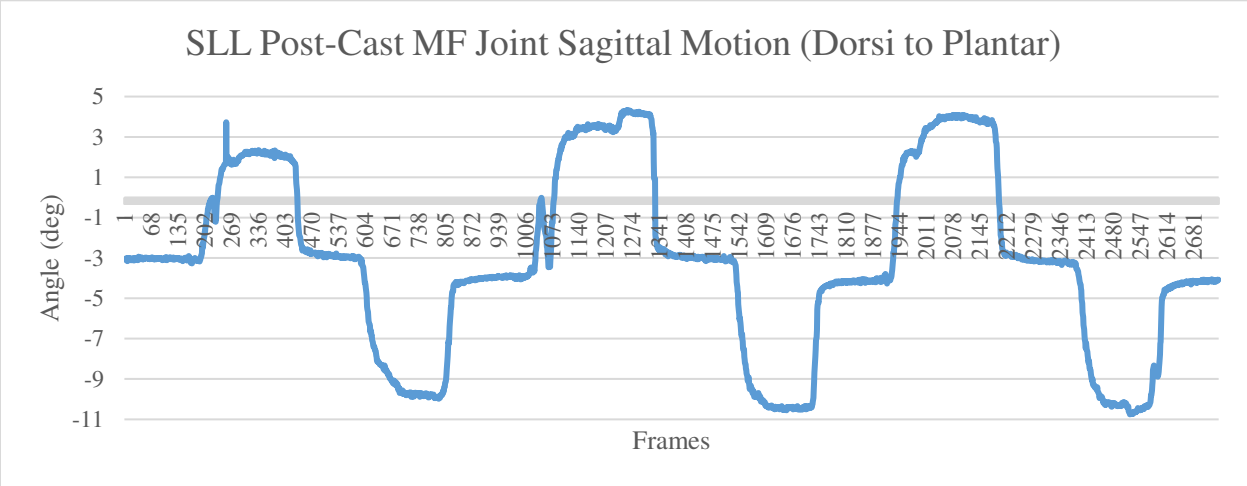

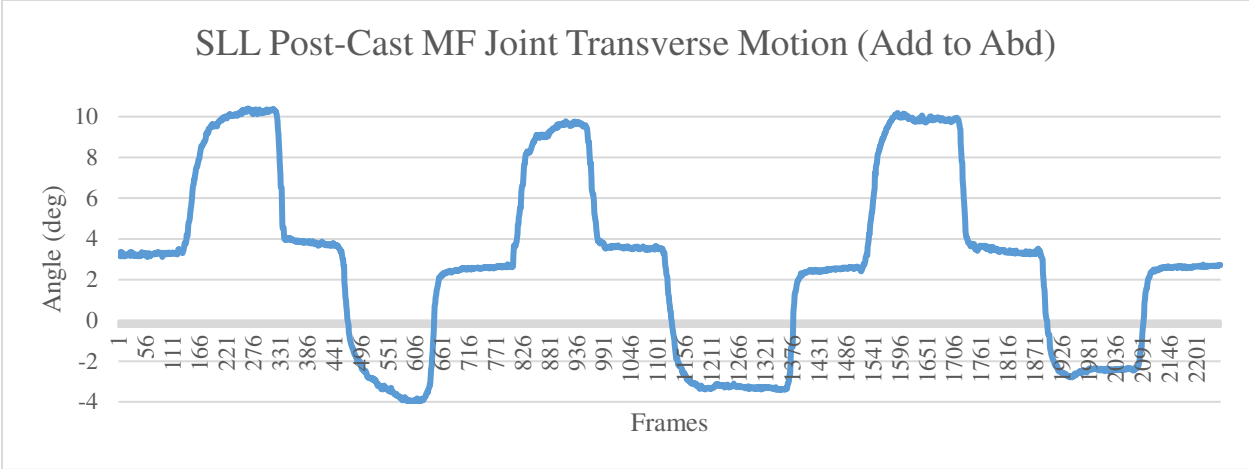

E.1.3.4 FT Joint

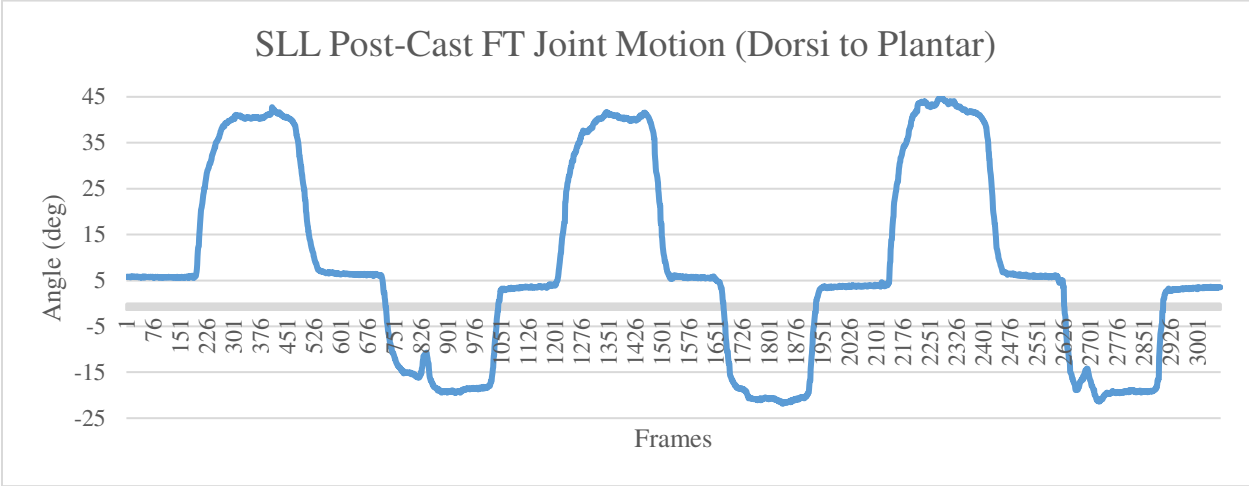

Appendix F

LabView block diagrams

F.1.1 Static Load Testing

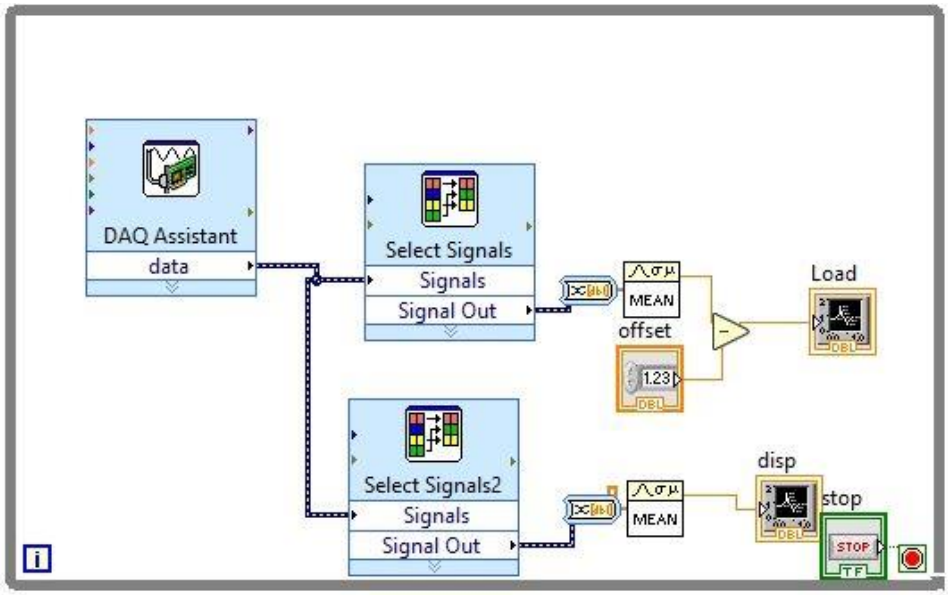

F.1.2 Cyclic Load Testing